Studies on edge mode transport in quantum Hall, quantum spin Hall and quantum anomalous Hall samples

By

Arjun Mani

PHYS11201504002

National Institute of Science Education and Research

Jatni, Odisha - 752050, India

A thesis submitted to the

Board of Studies in Physical Sciences

In partial fulfillment of requirements

for the Degree of

DOCTOR OF PHILOSOPHY

of

HOMI BHABHA NATIONAL INSTITUTE

December, 2018

Homi Bhabha National Institute

Recommendations of the Viva Voce Committee

As members of the Viva Voce Committee, we certify that we have read the dissertation prepared by **Arjun Mani** entitled **"Studies on edge mode transport in quantum Hall, quantum spin Hall and quantum anomalous Hall samples"** and recommend that it may be accepted as fulfilling the thesis requirement for the award of Degree of Doctor of Philosophy.

Chairman - Dr. Sanjay Swain	7/12/18 — Date
Guide / Convener - Dr. Colin Benjamin	07.12.2018 — Date
Member 1 - Dr. V. Ravi Chandra	07-12-2018 — Date
Member 2 - Dr. Kartikeswar Senapati	07/12/2018 — Date
Member 3- Dr. Satchidananda Rath	07/12/18 — Date
External Member - Dr. Santanu K. Maiti	07/12/2018 — Date
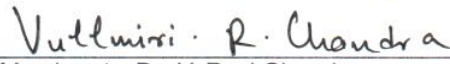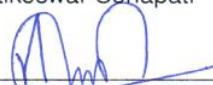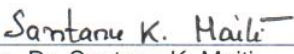
Final approval and acceptance of this thesis is contingent upon the candidate's submission of the final copies of the thesis to HBNI.

I hereby certify that I have read this thesis prepared under my direction and recommend that it may be accepted as fulfilling the thesis requirement.

Date: Bhubaneswar

Place: 07.12.2018

Dr. Colin Benjamin

STATEMENT BY AUTHOR

This dissertation has been submitted in partial fulfillment of requirements for an advanced degree at Homi Bhabha National Institute (HBNI) and is deposited in the Library to be made available to borrowers under rules of the HBNI.

Brief quotations from this dissertation are allowable without special permission, provided that accurate acknowledgement of source is made. Requests for permission for extended quotation from or reproduction of this manuscript in whole or in part may be granted by the Competent Authority of HBNI when in his or her judgment the proposed use of the material is in the interests of scholarship. In all other instances, however, permission must be obtained from the author.

Arjun Mani

Arjun Mani

DECLARATION

I, Arjun Mani, hereby declare that the investigation presented in the thesis has been carried out by me. The work is original and has not been submitted earlier as a whole or in part for a degree/diploma at this or any other Institution/University.

Arjun Mani

Arjun Mani

List of Publications arising from the thesis

Journal

1. "Are quantum spin Hall edge modes more resilient to disorder, sample geometry and inelastic scattering than quantum Hall edge modes?" Arjun Mani, Colin Benjamin, J. Phys.: Condens. Matter, (2016), 28, 145303.

2. "Fragility of Nonlocal Edge-Mode Transport in the Quantum Spin Hall State", Arjun Mani, Colin Benjamin, Phys. Rev. Applied, (2016), 6, 014003.

3. "Probing helicity and the topological origins of helicity via non-local Hanbury-Brown and Twiss correlations", Arjun Mani, Colin Benjamin, Scientific Reports, (2017), 7: 6954.

4. "Strained graphene based highly efficient quantum heat engine operating at maximum power", Arjun Mani, Colin Benjamin, Phys. Rev. E, (2017), 96, 032118.

5. "Role of helical edge modes in the chiral quantum anomalous Hall state", Arjun Mani, Colin Benjamin, Scientific Reports, (2018), 8: 1335.

6. "Helical thermoelectrics and refrigeration", Arjun Mani, Colin Benjamin, Phys. Rev. E, (2018), 97, 022114.

7. "Are thermal fluctuations the sole reason for finite longitudinal resistance in quantum anomalous Hall experiments?", Arjun Mani, Colin Benjamin, J. Phys.: Condens. Matter,

(2018), 30, 37LT01.

Submitted (undergoing peer review)

8. "Designing a highly efficient graphene quantum spin heat engine", Arjun Mani, Colin Benjamin, arXiv:1707.07159.

Conferences

1. Presented a poster at "International Workshop on Emergent Phenomena in Quantum Hall Systems", TIFR Mumbai, Jan 2016.

2. Presented a poster at "School on Nanoscale Transport" at HRI, India, Feb 2016.

3. Presented a poster at "International School and Symposium on Nanoscale Transport and photonics", Atsugi Kanagawa, Japan, Nov 2017.
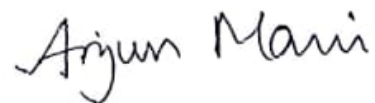
Arjun Mani

Arjun Mani

Dedicated
to
My Well Wishers

Abstract

Quantum Hall (QH) edge modes appear in a 2-dimensional electron gas at high magnetic fields and at low temperatures. These edge modes are topologically protected (immune to backscattering) and are chiral (unidirectional). Quantum spin Hall (QSH) edge modes appear in topological insulators due to large spinorbit coupling and at low temperatures. These edge modes are spin polarized, helical and are topologically protected too. Another cousin brother quantum anomalous Hall (QAH) edge modes appear in magnetically doped topological insulators due to high spinorbit coupling and again in absence of magnetic field. Edge modes are quite promising candidates for low power information processing due to their dissipation-less transport. They could also be useful for converting waste heat into useful work due to their high degree of coherence when used in quantum heat engines. Thus it is quite important to probe these topological states by disorder and inelastic scattering to check their susceptibility to these. It is also important to distinguish these edge modes from one another, which can be probed via nonlocal resistance as well as nonlocal HBT noise cross correlation measurements. In some recent experiments it has been shown that QAH edge modes always come with the additional baggage of quasi helical QSH edge modes. Quasi helical QSH edge modes are prone to backscattering. If QAH edge modes are also prone to back scattering then they are trivial otherwise topological. The topological nature of QAH edge modes can be checked via conductance measurements in presence of disorder and inelastic scattering. Further, we will discuss the performance

of 2-terminal chiral (QH) and 3-terminal helical (QSH) edge mode based quantum heat engines and refrigerators. Along with charge thermoelectric properties we will discuss the spin thermoelectric properties in a QSH heat engine. For better understanding of these edge mode based heat engines, we will compare their performance against ballistic mode based heat engines, e.g., in 2-terminal monolayer graphene. A magnetic impurity introduced along with strain can generate spin thermoelectric effects in graphene. As time reversal symmetry is not broken in 2-terminal and 3-terminal QSH systems, these heat engines can also efficiently work as quantum refrigerators too in different parameter space. Graphene and QSH based spin heat engines and refrigerators exceed in their performance over other quantum heat engines and quantum refrigerators in generating huge power and efficiency.

Acknowledgments

Foremost, I would like to express my sincere gratitude to my advisor Dr. Colin Benjamin for the continuous support of my Ph.D. study and research, for his patience, motivation, enthusiasm, and immense knowledge. His guidance helped me in all the time of research and writing of this thesis. I could not have imagined having a better advisor and mentor for my Ph.D. study.

Besides my advisor, I would like also to thank the rest of the mentors of my thesis committee: Dr. S. Swain, Dr. V. R. Chandra, Dr. K. Senapati, and especially Dr. S. Rath.

My sincere thanks also goes to the Chairperson of School of Physical Sciences, Dean of Academics Dr. H. Mohapatra and all the staff members of School of Physical sciences, for their immense support throughout my research.

I thank my fellow labmates in condensed matter theoretical Group: Subhajit Pal, Gour Jana, Joydev De, Abhilash Patra, Bikash Patra, Rita Maji, and Subrata Jana, for the stimulating discussions, for the sleepless nights we were working together before deadlines, and for all the fun we have had in the last three and half years. In particular, I am grateful to Prof. Asmita Sengupta and Dr. Ashis Bhattacharyya at Visva-Bharati University for enlightening me to the first glance of research.

Last but not the least, I would like to thank my family: my parents Ratan Mani and Reba Mani and my elder brother Kunal Mani, for supporting me spiritually throughout my life.

Synopsis

Studies on edge mode transport in quantum Hall, quantum spin Hall and quantum anomalous Hall samples

Abstract

Quantum Hall (QH) edge modes appear in a 2-dimensional electron gas at high magnetic fields and low temperature, these edge modes are chiral (unidirectional). Quantum spin Hall (QSH) edge modes appear in topological insulators at low temperature and these edge modes are helical (topological) and protected by time reversal (TR) symmetry. QSH edge modes can also appear in a trivial insulator too but as is to be expected these are not protected by TR symmetry. These latter edge modes are identified as trivial or quasi-helical QSH edge modes. In a magnetic topological insulator at low temperature and in presence of no net magnetic field another cousin brother of QH edge modes appears, these are quantum anomalous Hall (QAH) edge modes. We study these edge modes, QH (topological), QSH(topological), QSH (trival) and QAH (topological) edge modes, in presence of disorder and inelastic scattering with spin-flip scattering via the conductance and noise. Further, we have checked the potential applicability of helical (topological) edge modes to convert heat energy to electrical energy to work as a heat engine or as a refrigerator and compared the

result with that of heat engines and refrigerators based on ballistic modes in monolayer graphene system.

Research questions we address

Our purpose is four fold: 1. To identify first how resilient these edge modes are to disorder and inelastic scattering, 2. How to distinguish between trivial and topological helical edge modes, 3. How to be sure of the topological nature of quantum anomalous Hall edge modes and finally 4. How do these chiral and helical edge modes stack up against each other as well as against ballistic modes as regards their application in quantum heat engines and refrigerators.

Part A (comprising chapters 2, 3, 4): Edge mode transport in QH, QSH and QAH samples

On the surface of 2D Topological insulators occur 1D quantum spin Hall edge modes with Dirac like dispersion. Unlike quantum Hall(QH) edge modes which occur at high magnetic fields in 2DEGs, the occurrence of quantum spin Hall(QSH) edge modes is because of spin-orbit scattering in the bulk of the material. These QSH edge modes are spin dependent and chiral- opposite spins move in opposing directions. Electronic spin has larger decoherence and relaxation time than charge- in view of this its expected that QSH edge modes will be more robust to disorder and inelastic scattering than QH edge modes which are charge dependent and spin unpolarized. However, we notice no such advantage accrues to QSH edge modes when subjected to same degree of contact disorder and/or inelastic scattering

in similar setups as QH edge modes. In fact we observe QSH edge modes are more susceptible to inelastic scattering and contact disorder than QH edge modes[1]. Further, while a single disordered contact has no effect on QH edge modes it leads to a finite charge Hall current in case of QSH edge modes and thus vanishing of pure QSH effect. For more than a single disordered contact while QH states continue to remain immune to disorder, QSH edge modes become more susceptible- the Hall resistance for QSH effect changes sign with increasing disorder. In case of many disordered contacts with inelastic scattering included while quantization of Hall edge modes holds, for QSH edge modes- a finite charge Hall current still flows. For QSH edge modes in the inelastic scattering regime we distinguish between two cases: with spin-flip and without spin-flip scattering. Finally, while asymmetry in sample geometry can have a deleterious effect on QSH case it has no impact in QH case. Another interesting effect of this dichotomy between chiral QH and helical QSH edge modes becomes apparent when one deals with non-local transport. Now it is well known that non-local currents and voltages are better able at withstanding the deleterious effects of dephasing than local currents and voltages in nanoscale systems. This hypothesis is known to be true in QH set-ups. We test this hypothesis in a four terminal QSH set up wherein we compare the local resistance measurement with the non-local one. In addition to inelastic scattering induced dephasing we also test resilience of the resistance measurements in the aforesaid set-ups to disorder and spin-flip scattering. We find the axiom that non-local resistance is less affected by the detrimental effects of disorder and dephasing to be in general untrue for QSH case[2]. This has important consequences since it has been widely communicated that non-local transport through edge channels in topological insulators will have potential applications in low power information processing. Unlike QH chiral edge modes which always occur in topological systems, helical edge modes may arise in a trivial insulator too. These trivial helical or quasi-helical edge modes are not topologically protected and therefore need to be distinguished from helical edge modes arising due

to topological reasons. Earlier conductance measurements were used to identify these helical states, in this chapter we report on the advantage of using the non local shot noise as a probe for the helical nature of these states as well as to reveal their topological or otherwise origin and compare them with the chiral quantum Hall states. We see that in similar set-ups affected by same degree of disorder and inelastic scattering, non local shot noise "HBT" correlations can be positive for helical edge modes but are always negative for the chiral quantum Hall edge modes. Further, while trivial helical edge modes exhibit negative non-local "HBT" charge correlations, topological helical edge modes can show positive non-local "HBT" charge correlation[3]. We also study the non-local spin correlations and Fano factor for clues as regards both the distinction between chirality/helicity as well as the topological/trivial dichotomy for helical edge modes. The trivial versus topological conundrum is not restricted to QSH samples alone. Quantum anomalous Hall(QAH) edge modes, which arise from QSH edge modes via the introduction of ferromagnetism into topological insulators, also are subject to the trivial/topological conundrum. A fair way to be sure of the topological character of QAH edge modes is by testing them against disorder and inelastic scattering. The test reveals uniquely transport via topological QAH edge modes does not result in quantized Hall resistances while transport via the trivial counterparts does[4]. In a recent work[5], this deviation of longitudinal and Hall conductance from the topological quantization is explained as a finite temperature effect. In our work[6], we have shown that finite temperature is not the sole reason to have this deviation, a finite disorder and presence of inelastic scattering also can give rise to this deviation.

Part B (comprising chapters 5, 6 and Appendix): Edge modes vs ballistic modes in designing quantum heat engines and refrigerators

Finally, we explore the distinction between quantum heat engines designed via chiral and helical edge modes. We further probe how quantum heat engines delineated via edge modes stack up against those conceived using ballistic modes. Using a strained graphene monolayer as a template for highly ballistic mode of transport we show its operation as a highly efficient quantum heat engine delivering maximum power[7]. The efficiency and power of the proposed device exceeds that of recent proposals. The reason for these excellent characteristics is that strain enables complete valley separation in transmittance through the device, implying that increasing strain leads to very high Seebeck coefficient as well as lower conductance. This proposed device works as a charge heat engine which converts heat energy to charge currents efficiently. Next we introduce a magnetic impurity, a Delta like potential, to our strained monolayer graphene device to generate spin currents along with a charge currents on applying a temperature bias at one of its terminals [8]. We have shown that a huge charge as well as spin thermoelectric figure of merit can be generated in our proposed device, which shows the potential of our device to work as not only a charge heat engine but as a spin heat engine too. We have also shown that our proposed device can also generate a pure spin current on application of a temperature bias. In addition, since time-reversal symmetry is unbroken in our system, the proposed strained graphene quantum heat engines can also act as a high performance refrigerator[7, 8]. To compare the output power and efficiency generated in these ballistic mode devices to that of edge modes devices, we have proposed a three terminal QSH heat engine[9]. This QSH heat engine in presence of quantum point contacts generates a energy dependent transmission which is the prerequisite to generate thermoelectric effects. We have shown

that this three terminal QSH heat engine outperforms our two terminal strained graphene heat engines based on ballistic modes. The advantage of a three terminal heat engine over a two terminal one is that in a three terminal heat engine the separate flow of electric and heat currents can be modulated through different terminals to give more accessibility to control these thermoelectric properties and generate a large power and efficiency for both charge and spin currents. A multi-terminal QSH heat engine does not break time reversal (TR) symmetry unlike multi-terminal QH heat engine and thus it can work both as a charge/spin heat engine as well as a charge/spin refrigerator.

Theoretical Methods used

The Landauer-Buttiker formalism[10, 11] has been the workhorse for mesoscopic transport problems and we adopt it here to calculate the conductance and Hall resistances used in this thesis. To include inelastic scattering we use the energy equilibration approach as has been applied in Ref. [12] as also inelastic scattering via a voltage probe as has been pioneered by Buttiker[13]. Nonlocal shot noise calculations follow the template set up by the works of Buttiker and Texier [14, 15]. Thermoelectric Seebeck and Peltier coefficients for both charge as well as spin are calculated using approaches due to some works by Bauer and Seifert[16, 17]. Thermoelectric properties for QSH systems are calculated by following the approach of Sanchez and Sothmann [18].

Relevance for Science

Edge modes hold great promise for low power information processing as well as in topological quantum computation[56]. Understanding the nature of these edge modes is crucial in applications in thermoelectrics. This thesis helps to shed a light on the promise held out by these edge modes and on how far these are capable of delivering on these hoped for applications. Our studies on quantum spin Hall edge modes especially reveals that they are not as immune to disorder and/or inelastic scattering compared to their quantum Hall counterparts. However, quantum spin Hall edge modes since they do not break time reversal symmetry are more geared towards potential applications in quantum thermoelectrics than quantum Hall edge modes.

List of Figures

List of Tables

Contents

1. Introduction

"Beyond the edge of the world there's a space where emptiness and substance neatly overlap, where past and future form a continuous, endless loop. And, hovering about, there are signs no one has ever read, chords no one has ever heard."

– Haruki Murakami, *Kafka on the Shore*

Ever since the discovery of electromagnetism by H.C. Orsted in 1820, the scientific community has put great interest in studying current carrying samples in presence of magnetic fields. There have been many important discoveries due to the dynamics of electrons in presence of a magnetic field. One of those discoveries is the observation of transverse charge voltage generated in a conductor with a magnetic field applied perpendicular to the sample by Edwin Hall in 1879[19]. This is called classical Hall effect. After more than a century, in 1980 the quantization of this transverse Hall voltage was observed in a two dimensional electron gas(2DEG) but at very low temperatures. This is the quantum version of classical Hall effect and is called quantum Hall (QH) effect. Another brother of the Hall family was discovered by Russian physicists M.I. Dyakonov and V.I. Perel in 1971, when they discovered that a transverse spin voltage is generated in a two dimensional conductor but in absence of magnetic field. This discovery is known as the classical spin Hall effect [20]. The quantum version of this effect was proposed by the two groups Kane, Mele[21] and Bernevig, Zhang[22] independently in 2006 and experimentally observed by the Molenkamp

group in 2007[23]. This is the quantum spin Hall (QSH) effect. Unlike quantum Hall effect, quantum spin Hall effect arises in absence of magnetic field due to spin-orbit interaction. There is still one more member of the the Hall family left which is the quantum anomalous Hall (QAH) effect. In quantum anomalous Hall effect too the quantized charge Hall voltage is observed similar to quantum Hall effect but in absence of magnetic field. Quantum Hall, quantum spin Hall and quantum anomalous Hall effects all seen in 2 dimensional samples have one thing in common- the existence of 1D edge modes [24]. Although, the origin of these 1D edge modes are different in the three cases. In quantum Hall, for example, 1D edge modes arise at high magnetic fields but in quantum spin Hall case the edge modes arise at zero magnetic fields because of bulk spin orbit effects in 2D topological insulators [25, 26]. In quantum anomalous Hall case 1D edge modes arise in absence of magnetic field but with doping of magnetic adatoms in 2D topological insulator or a ferromagnetic topological insulator. In quantum Hall case 1D edge modes are chiral (see Fig. 1.1(a)), i.e., at one edge of the sample electrons move in one direction and at the other edge of the sample electrons move in opposite direction. In quantum spin Hall case, the edge modes are chiral not only with respect to edge but also spin (see Fig. 1.1(b)). For example, if at the top edge of the topological insulator spin up electrons are moving in one direction, then spin down electrons are moving in the opposite direction at the same edge and at the bottom edge vice-versa. In QAH case, 1D edge modes are chiral, similar to QH case, but spin polarized (see Fig. 1.1(c)), i.e., either spin up chiral edge modes are moving in the system or spin down chiral edge modes depending on the spontaneous magnetization direction of the ferromagnetic topological insulator. In Fig. 1.1 (d) the distinguishing property of an edge mode is highlighted. An edge mode will never backscatter from an impurity placed in the sample. This is the main difference between a ballistic mode and an edge mode. A ballistic mode will scatter from an impurity while an edge mode because of its provenance as explained in the next sections won't. Of course, edge mode transport in QSH samples
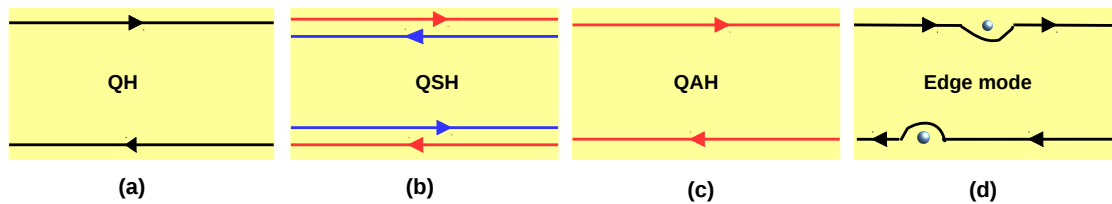
Figure 1.1: (a) Chiral quantum Hall edge mode, (b) helical quantum spin Hall edge modes, (c) chiral spin polarized quantum anomalous Hall edge mode and (d) the distinguishing property of an edge mode is highlighted. An edge mode will never backscatter from a non-magnetic impurity placed in the sample. Black solid line denotes spin unpolarized edge mode, red solid line denotes spin up edge mode and blue solid line denotes spin down edge mode.

will be impacted by magnetic impurities which may lead to spin flip scattering. However, edge modes be they QH, QSH or QAH are all protected against non-magnetic impurities, ballistic modes aren't and therein lies the importance of edge modes. In this chapter the origin of QH, QSH and QAH edge modes are discussed first, e.g., how these edge modes appear at low temperature in 2DEG's and topological insulators? The characteristics of these edge modes are then discussed following thus the Landauer-Buttiker formalism is applied to derive the Hall, 2-terminal, longitudinal and non-local resistances in ideal 6 terminal QH, QSH and QAH samples. The importance of these edge modes and the reason for studying these edge modes is discussed next. The application of these edge modes in thermoelectrics to design efficient quantum heat engines and quantum refrigerators forms an important part of this thesis. An introduction to quantum heat engines and quantum refrigerators is given next. Finally, the chapter concludes with an overview of the complete thesis.

1.1 Quantum Hall Effect

Quantum Hall effect is one of the most important discoveries of the 1980s[27]. It is observed in a two-dimensional electron system at low temperatures and high magnetic field. The Hall
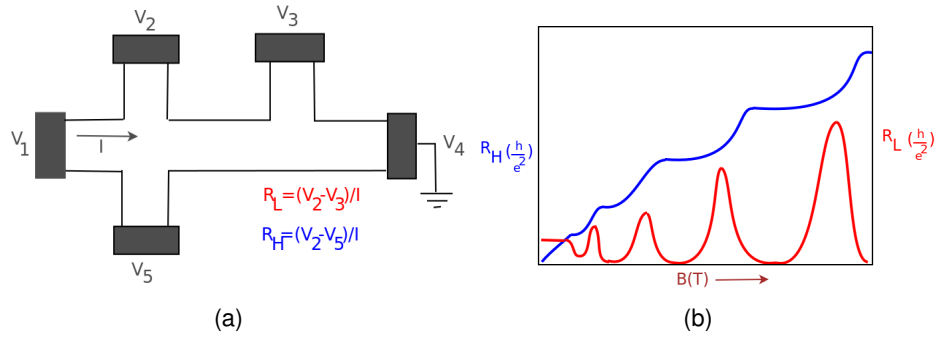
Figure 1.2: (a)Rectangular Hall bar with magnetic field applied in the z-direction perpendicular to the plane of the conductor, (b) Schematic of measured longitudinal resistance $R_L = \frac{(V_2 - V_3)}{I_1}$ and Hall resistance $R_H = \frac{(V_2 - V_6)}{I_1}$ in units of h/e^2 for the conductor shown in (a) as function of magnetic field (B) in Tesla.

conductance of a 2D sample is-

$$\sigma = \frac{I_{channel}}{V_{Hall}} = \nu \frac{e^2}{h}, \tag{1.1}$$

where $I_{channel}$ is the channel current, V_{Hall} is the Hall voltage developed, e is the elementary charge and h is Planck's constant. ν is known as the filling factor, it can take either integer 1,2,3,...for integer quantum Hall effect (QHE) or fractional values 1/2,1/3, 1/4, 2/3 ,.... for fractional quantum Hall effect (FQHE). Integer quantum Hall effect or quantum Hall (QH) effect is described by single particle Hamiltonian and it is well understood. However, FQHE is complicated and it needs electron-electron interactions to describe it properly. Besides in two-dimensional electron gas, QH effect has been studied in other systems too like graphene[28, 30, 29, 31], square lattice model [32], etc, with interesting twists. The quantization of the Hall resistance and characteristics of the longitudinal resistance in presence of magnetic field, is discussed next.

Shubnikov deHaas Oscillations

At high magnetic field the longitudinal resistance in a two dimensional electron gas (2DEG) shows oscillatory behaviour with increase of the magnetic field, while Hall resistance exhibits

plateaus corresponding to the minima in the longitudinal resistance[32, 33] (see Fig. 1.2(b)). These oscillations in the longitudinal resistance are known as Shubnikov-deHaas (or SdH) oscillations. To understand these features one has to understand the formation of Landau levels which is a quantum mechanical effect. The main reason for the SdH oscillations is the breaking of the step like density of states for the 2DEG at zero magnetic field (B)-

$$N_s(E) = \frac{m}{\pi\hbar^2}\vartheta(E - E_s),\tag{1.2}$$

into a sequence of peaks spaced by $\hbar\omega_c$ at high magnetic fields (see Fig. 1.3(a)),

$$N_s(E,B) = \frac{2eB}{h}\sum_{n=0}^{\infty}[\delta(E - E_s - (n + \frac{1}{2})\hbar\omega_c)].\tag{1.3}$$

Here, $\omega_c = eB/m$ is the cyclotron frequency and B is the applied magnetic field in perpendicular direction in Eq. (1.3). It is shown in Fig. 1.3(a). The different values of n refer to different Landau levels. The density of states of a 2DEG thus depends on the magnetic field. When one changes the magnetic field the peaks in the density of states also change and the longitudinal resistivity $\rho_{xx} = R_L$(for 2DEG) completes one oscillation (see Fig. 1.2(b)) while the Fermi energy passes through the center of one Landau level to the center of the next Landau level. The longitudinal resistivity ρ_{xx} is minimum whenever the Fermi energy lies between two Landau levels because in the bulk there are no states so that electrons on the upper edge of 2DEG can't deflect to the lower edge of 2DEG, but there are edge states that carry current (see Fig. 1.3(b)). The Fermi energy crosses Landau levels only at the edges of the conductor if it lies between Landau levels. Thus due to the absence of backscattering, the longitudinal resistivity ρ_{xx} goes to zero, whenever Fermi energy is between two Landau levels. It is maximum when the Fermi energy coincides with any Landau level. Next the Schroedinger equation is solved for electrons in presence of magnetic field and a confining potential and it is shown how the 1D chiral spin unpolarized edge states arise only at the
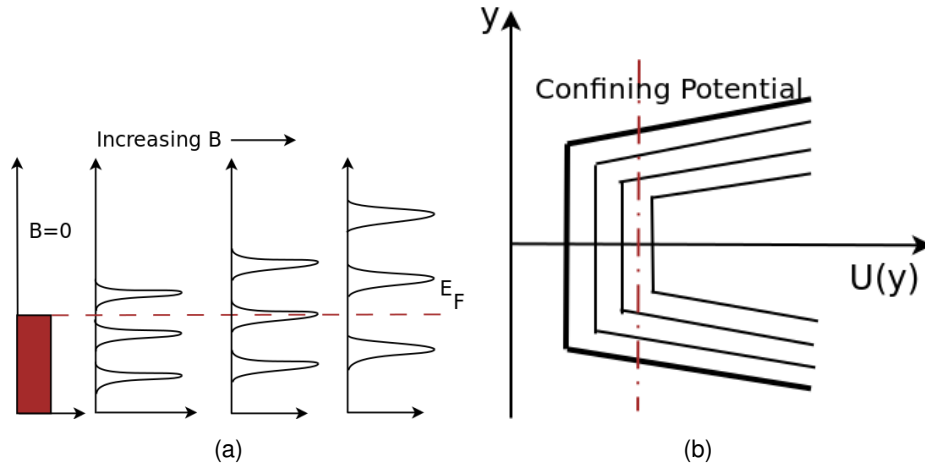
Figure 1.3: (a) Schematic of Density of states $N_S(E,B)$ vs. energy E for a 2DEG in a magnetic field. (b) Confining potential $U(y)$ vs y and Landau Levels with Fermi energy (maroon line).

edges of the conductor.

1.1.1 How do quantum Hall edge modes arise?

Consider a rectangular conductor that is uniform in the x-direction and has some transverse confining potential $U(y)$ [33]. The motion of electrons in such a conductor is described by the effective mass equation[33]-

$$\left[E_s + \frac{(i\hbar\nabla + eA)^2}{2m} + U(y) \right] \psi(x,y) = E\psi(x,y),$$ (1.4)

where $E_s = E_c + E_z$. E_z is the cut-off energy in the z direction, m is the effective mass of electron and E_c is the band-edge energy (bulk). $U(y)$ is the confining potential in the y direction. A constant magnetic field B in the z-direction perpendicular to the plane of the conductor is present. This can be represented by a vector potential of the form- $A_x = -By, A_y = 0$. Thus, Eq. (1.4) can be written as -

$$\left[E_s + \frac{(p_x + eBy)^2}{2m} + \frac{p_y^2}{2m} + U(y) \right] \psi(x,y) = E\psi(x,y),$$ (1.5)

Where $p_x = -i\hbar \frac{\partial}{\partial x}$ and $p_y = -i\hbar \frac{\partial}{\partial y}$. The solutions of Eq. (1.5) can be expressed in the form of plane waves, L is the length of conductor over which the wave-functions are normalized,-

$$\psi(x,y) = \frac{1}{\sqrt{L}} exp[ikx] \chi(y), \tag{1.6}$$

where $\chi(y)$ satisfies the equation-

$$\left[E_s + \frac{(\hbar k + eBy)^2}{2m} + \frac{p_y^2}{2m} + U(y) \right] \chi(y) = E\chi(y). \tag{1.7}$$

For any arbitrary potential there is no analytical solution. However, if $U(y)$ is a parabolic potential such as-

$$U(y) = \frac{1}{2} m \omega_o^2 y^2, \tag{1.8}$$

where ω_o is the strength of confining potential. Then substituting $y_k = \frac{\hbar k}{eB}$, $\omega_c = eB/m$, and $\omega_{co}^2 = \omega_c^2 + \omega_o^2$, Eq. (1.7) reduces to-

$$\left[E_s + \frac{1}{2} m \frac{\omega_o^2 \omega_c^2}{\omega_{co}^2} y_k^2 + \frac{p_y^2}{2m} + \frac{1}{2} m \omega_{co}^2 \left[y + \frac{\omega_c^2}{\omega_{co}^2} y_k \right]^2 \right] \chi(y) = E\chi(y). \tag{1.9}$$

This equation is similar to a 1D Schrödinger equation with parabolic potential, so the solution of Eq. (1.9) is-

$$\chi_{n,k}(y) = u_n \left[q + \frac{\omega_c^2}{\omega_{co}^2} q_k \right], \quad u_n(q) = exp[-q^2/2] H_n(q), \tag{1.10}$$

with $q = \sqrt{m\omega_c/\hbar} y$, $H_n(q)$ is the Hermite polynomial, n is the Landau Level and $q_k = \sqrt{m\omega_c/\hbar} y_k$, the Landau level energies then are-

$$E(n,k) = E_s + \frac{1}{2} m \frac{\omega_o^2 \omega_c^2}{\omega_{co}^2} y_k^2 + \left(n + \frac{1}{2} \right) \hbar \omega_{co} = E_s + \left(n + \frac{1}{2} \right) \hbar \omega_{co} + \frac{\hbar^2 k^2}{2m} \frac{\omega_o^2}{\omega_{co}^2}. \tag{1.11}$$
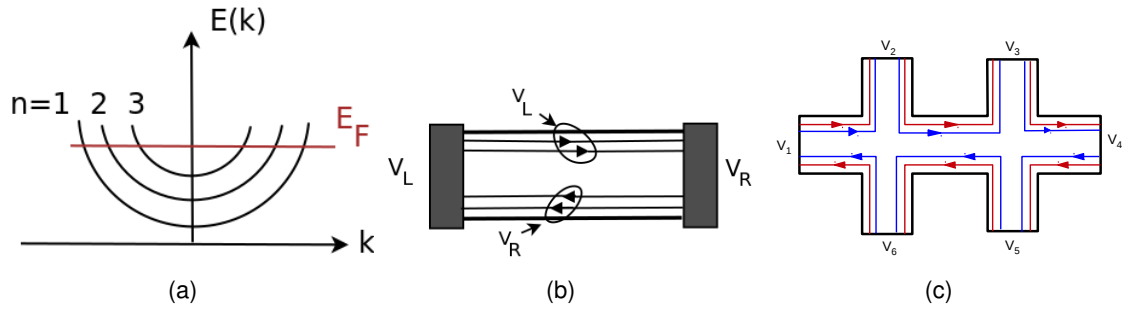
Figure 1.4: (a) Magneto-electric subbands in a parabolic potential: Dispersion relation, $E(k)$ vs. k for different subbands indexed by n. (b) A conductor in the quantum Hall regime. The edge states carrying current to the right are in equilibrium with the left contact while those carrying current to the left are in equilibrium with the right contact, (c) a six terminal ideal QH bar (both spin up and down edge modes move in the same direction). Red solid line denotes spin up edge mode, while blue solid line denotes spin down edge mode.

The velocity of an electron in any one of the Landau levels is thus-

$$\upsilon(n,k) = \frac{1}{\hbar}\frac{\partial E(n,k)}{\partial k} = \frac{\hbar k}{m}\frac{\omega_o^2}{\omega_{co}^2}. \tag{1.12}$$

The centroid of a Landau level eigenstate is located at $y = -y_k$, with

$$y_k = \frac{\hbar k}{eB} = \upsilon(n,k)\frac{\omega_o^2 + \omega_c^2}{\omega_c\omega_o^2}. \tag{1.13}$$

From Eq. (1.13) we can see that the position of the Landau level depends on the velocity of electrons in these states. As magnetic field is increased, the states carrying current in the $+x$ direction shift to one side of the conductor while states carrying current in the $-x$ direction will shift to the other side. Increasing the magnetic field, the overlap between the states going in opposite directions will be reduced. Due to this divided highway for the two groups of states going in opposite directions, backscattering cannot take place even in presence of sample impurities leading to edge mode transport exclusively. Next the current carried by each of these edge states is calculated from their dispersion relation.

Current carried by each edge mode

Depending on the position of Fermi energy in the $E(k)$ vs k plot (see Fig. 1.4(a)), one can check how many edge modes will be present in a quantum Hall conductor. It is because below the Fermi energy all Landau levels are filled while above it all are empty at zero temperature. So, only those Landau levels which have cut-off energy (ε_n) below the Fermi energy will carry current. The number of Landau levels M below Fermi energy E_F carrying current is-

$$M(E_F) = \sum_N \vartheta(E_F - \varepsilon_n), \text{ with } \quad \varepsilon_n = E(n, k = 0) \tag{1.14}$$

is the cut-off energy for n^{th} Landau level see Eq. (1.11). Consider a single edge mode whose $+k$ states are occupied with probability given by Fermi function $f^+(E)$. Now a 2DEG with N being the electron density per unit length, of length L carries a current Nev. The electron density associated with a single k state in a conductor of length L is $(1/L)$. Thus current I^+ of the $+k$ states is-

$$I^+ = \frac{e}{L} \sum_{n,k} \upsilon f^+(E) = \frac{e}{L} \sum_{n,k} \frac{1}{\hbar} \frac{\partial E}{\partial k} f^+(E). \tag{1.15}$$

Similarly, the current I^- of the $-k$ states is-

$$I^- = \frac{e}{L} \sum_{n,k} \upsilon f^-(E) = \frac{e}{L} \sum_{n,k} \frac{1}{\hbar} \frac{\partial E}{\partial k} f^-(E), \tag{1.16}$$

where f^- is probability of occupation of $-k$ states. Assuming periodic boundary condition and converting the sum into the integral -

$$\sum_k \quad \to \quad 2 \text{ (for spin) } \frac{L}{2\pi} \int dk, \quad \text{one has-}$$

$$I^+ = \frac{2e}{h} \sum_n \int_{\varepsilon_n}^{\infty} f^+(E)dE \text{ and } \quad I^- = \frac{2e}{h} \sum_n \int_{\varepsilon_n}^{\infty} f^-(E)dE.$$

$$\text{Thus } I = I^+ - I^- = \frac{2e}{h} \int_{\mu_R}^{\mu_L} (f^+(E) - f^-(E))M(E_F)dE, \tag{1.17}$$

is the net current in the 2DEG. From Eq. (1.17) one can conclude that current carried by each edge mode per unit energy by a occupied state is $2e/h$, which is equal to 80 nA/meV. If M is constant over a range of energy, i.e., $\mu_L > E > \mu_R$, then at zero temperature Fermi functions are just step functions and one has-

$$I = \frac{2e^2}{h}M\frac{(\mu_L - \mu_R)}{e} = \frac{2e^2}{h}M(V_L - V_R) \quad \text{(with, } V_i = \frac{\mu_i}{e}), i = L, R, \tag{1.18}$$

where μ_L and μ_R are the chemical potential of the left and right reservoir respectively (Fig. 1.4(b)). If T is the probability for an electron injected at one end contact to transmit to the other end contact. Then Eq. (1.18) becomes-

$$I = \frac{2e^2}{h}MT(V_1 - V_2) \text{ with } \quad G = \frac{2e^2}{h}MT. \tag{1.19}$$

Eq. (1.19) is applicable for 2-terminal systems. For multi-terminal systems one has to follow the Landauer-Buttiker formalism, which is discussed below.

1.1.2 Landauer-Buttiker formalism for quantum Hall systems

Landuaer-Buttiker formula for an N terminal QH system at zero temperature is a generalization of the two terminal case, see [10]-

$$I_i = \sum_{j \neq i} (G_{ji}V_i - G_{ij}V_j) = \frac{2e^2 M}{h} \sum_{j=1, j \neq i}^{N} (T_{ji}V_i - T_{ij}V_j), \qquad (1.20)$$

herein V_i is the voltage at i^{th} contact, I_i is the current flowing out of that contact, M is the number of edge modes, T_{ij} is the transmission probability from j^{th} to i^{th} contact and G_{ij} is the associated conductance. In this thesis the phrase terminal/contact/probe represents the same thing a metallic reservoir for electrons.

1.1.2.1 Distinguishing between voltage and current contacts

A voltage contact is used to measure the potential difference between any two points within the conductor, while current contact is used to measure the current through those points of the conductor. Due to the difference in their use, a voltage contact has to be designed so as not to disturb the potential distribution of the sample and to draw no net current. On the other hand a current contact has to be designed so as to draw maximum current through it. A voltage contact differs from a current contact in the sense that the net current through a voltage contact is always zero while for current contact it is finite and equal to current in sample. The potential of a voltage contact is floating because this floating potential is adjusted in such a way that the current entering to a voltage contact is always equal to the current coming out of it and thus cancelling the net current through it. On the other hand for current contacts the potential is fixed from external source either to a finite value or to zero, i.e., grounded. A contact regardless of whether its a voltage or a current contact may be ideal (i.e., reflectionless) or disordered. A disordered contact as is wont is not reflectionless. Edge modes as shown earlier are impervious to non-magnetic impurities

placed in the sample. However, both ballistic, as well as edge modes, are scattered by disordered contacts[10, 12].

1.1.3 Edge mode transport in an ideal quantum Hall sample

An ideal six terminal QH sample is shown in Fig. 1.4(c). Herein all contacts are ideal, i.e., the transmission probability of an electron through that contact is unity (reflection is zero). The current voltage relations can be derived from the conductance matrix below:

$$
G = -\frac{2e^2 M}{h}
\begin{pmatrix}
-1 & 0 & 0 & 0 & 0 & 1 \\
1 & -1 & 0 & 0 & 0 & 0 \\
0 & 1 & -1 & 0 & 0 & 0 \\
0 & 0 & 1 & -1 & 0 & 0 \\
0 & 0 & 0 & 1 & -1 & 0 \\
0 & 0 & 0 & 0 & 1 & -1
\end{pmatrix},
\tag{1.21}
$$

where the diagonal elements $G_{ii} = \sum_{j=1, j\neq i}^{6} G_{ji} = \frac{2e^2}{h} \sum_{j=1, j\neq i}^{N} T_{ji}$ and the non-diagonal elements $G_{ij} = \frac{2e^2}{h} T_{ij}$ (for $j \neq i$). The diagonal element, for example, $G_{11} = \frac{2e^2}{h} \sum_{j=1, j\neq i}^{6} T_{j1}$. M represents the total no. of modes while a factor 2 is introduced due to the spin degeneracy of the electrons. In setup as shown in Fig. 1.4(c), $M = 1$ to avoid clutter. From Fig. 1.4(b) we see that there is transmission of electrons only between the adjacent contacts in clockwise direction, i.e., transmission probability for an electron from contact i to $i+1$ (for $i = 1-5$ and $T_{16} = 1$) is unity, while rest of the transmission probabilities are zero. The diagonal conductance G_{11} thus reduces to $\frac{2e^2}{h} M T_{21} = \frac{e^2}{h} M$ (since $T_{21} = 1$). Similarly, rest of the probabilities can be derived. Substituting I_2, I_3, I_5, and $I_6 = 0$ (since contacts $2, 3, 5$ and 6 are voltage contacts) and choosing reference potential $V_4 = 0$, we have $V_1 = V_2 = V_3$ and $V_4 = V_5 = V_6 = 0$. When a voltage bias is applied across contacts 1 and 4 (see

Fig. 1.4(c)) and the response (potential drop) is measured between the same two probes then it is called local resistance measurement and again when voltage bias is applied across contacts 1 and 2 but response is measured far away across contacts 5 and 4 (see Fig. 1.4(c)), it is called non-local resistance measurement. The local resistance measured then is defined as $R_{2T} = R_{14,14} = \frac{V_1 - V_4}{I_1}$, where contacts 1 and 4 are both current and voltage contacts simultaneously. Non-local set-up resistance measurement is defined as $R_{NL} = R_{12,54} = \frac{V_5 - V_4}{I_1}$, where the current is measured across contacts 1 and 2, and resistance is measured far away between voltages contacts 5 and 4. In QH sample shown in Fig. 1.4(c) local or 2-terminal resistance is $\frac{h}{2e^2 M}$ and non-local resistance is zero. The Hall resistance $R_H = R_{14,26} = \frac{h}{2e^2} \frac{1}{M}$, while longitudinal resistance $R_L = R_{14,23} = 0$. The Hall and 2-terminal resistances are quantized in units of M and the longitudinal and non-local resistances vanish for an ideal QH sample with ideal (reflection less) contacts.

1.1.4   Why do we study quantum Hall systems?

Quantum Hall edge modes are well known for their dissipation less transport even in presence of sample disorder. Due to the robustness of QH edge modes to disorder, they are ideal candidates for low power information processing and transport[34, 35]. There are many other applications of QH edge modes such as- 1) the quantization of the Hall resistance is so accurate with accuracy of parts per million, that it has been used in metrology as a resistance standard, 2) the quantized Hall effect is also used to measure the universal constants like fine structure constant $\alpha = \frac{e^2}{\hbar c}$, Plank's constant h and electronic charge e, 3) quantum heat engines based on quantum Hall edge modes have a higher performance characteristic than most other quantum heat engines[18, 36]. Our aim in this thesis is to probe QH edge modes in six terminal Hall bar in presence of disorder placed at contacts and check its susceptibility to contact disorder. Further, including inelastic scattering within the sample one can check its effect on Hall, longitudinal, 2-terminal and

non-local resistances. Extending this approach to a N terminal quantum Hall bar one can obtain a generalized formula for all the resistances, such that just by knowing the number of terminals and strength of disorder, one can derive all the resistances $(R_H, R_{2T}, R_L, R_{NL})$. Moreover, performing non-local Hanbury Brown and Twiss (HBT) correlations measurement on the QH edge modes one can differentiate them from the QSH edge modes, which is discussed in chapter 3. Our study on QH edge modes in presence of disorder and inelastic scattering to find its characteristics can be useful in order to understand their use in low power information transport and other purposes more wisely.

1.2   Quantum Spin Hall Effect

The quantum spin Hall (QSH) state with1D spin polarized helical edge state is a topological state of matter that exists in certain two dimensional semi-conducting or insulating material with a quantized spin Hall conductance and vanishing charge Hall conductance. It is topological as it has gapless edge states and is robust to sample disorder. The QSH state was proposed by Kane, Mele and Bernevig, Zhang independently in Refs. [21, 22]. The QSH state can be viewed as two copies of the QH state with opposite Hall conductances. The QSH state in graphene, proposed by Kane, Mele could not be observed due to the very small spin-orbit interaction in graphene. The QSH state does not break time reversal (TR) symmetry while QH state breaks it. This can be shown in a simple way as follows. In QH case Hall current is given by $j_x = \sigma_{xy} E_y$ (for a 2D conductor lying in $x - y$ plane, j_x is the current in x direction, E_y is the applied electric field in the y direction and σ_{xy} is the Hall conductivity) wherein j_x is odd under TR symmetry, but E_y is not, so $\sigma_{xy} \neq 0$ breaks TR symmetry. In QSH case the spin Hall current is given by $j_x^s = \sigma_{xy}^s E_y$ where j_x^s is even under TR symmetry, so $\sigma_{xy}^s \neq 0$ is consistent with TR symmetry. QH case can be compared to a free-way(single-way highway) where if one has to go in opposite direction it has to go
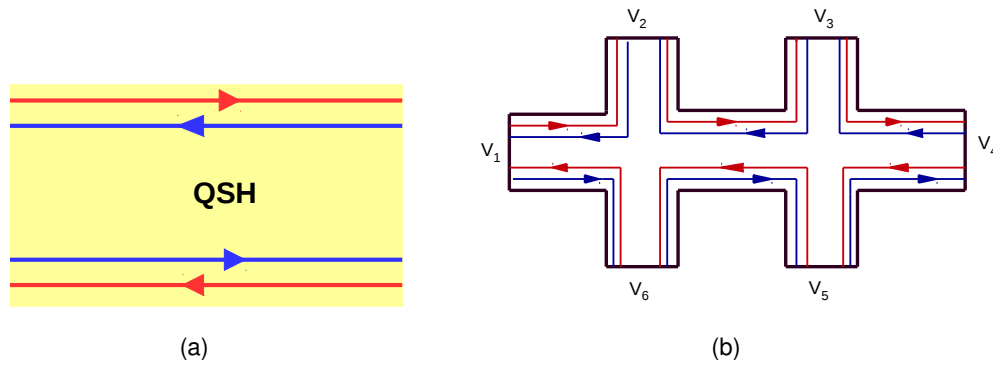
Figure 1.5: (a) Spin-momentum locked quantum spin Hall edge modes, (b) an ideal six terminal QSH bar. Red solid line denotes spin up edge mode while blue solid line denotes spin down edge mode.

in a different lane (chiral) (Fig. 1.4(b)). Due to this chiral traffic rule electrons are forced to avoid impurities, and follow the same direction. But QSH case can be considered as two copies of QH states one for each spin (helical) (Figs. 1.5(a, b)). Here backscattering is suppressed by another traffic rule- helical traffic rule. If an electron has to backscatter it has to flip its spin which breaks the TR symmetry. If TR symmetry is conserved, as is the case with non-magnetic impurity, there will be no backscattering.

1.2.1 How do quantum spin Hall edge modes arise?

Efforts to see quantum spin Hall effect in graphene were unrealized because in graphene the spin orbit coupling is very small[37, 38]. Soon afterwards Bernevig, Hughes and Zhang[39] predicted a quantum phase transition in HgTe/CdTe quantum wells from a trivial insulator phase to a QSH phase controlled by the thickness d of the quantum well. The idea behind the transition is as follows- CdTe has a normal band structure (see Fig. 1.6 (a)) with the valence band lying below the conduction band. On the other hand, HgTe has an inverted band structure with valence band lying above the conduction band (see Fig. 1.6 (b)) due to strong spin orbit coupling. Starting from bulk bands, one can consider different behaviours for thin and thick quantum wells, whose band structures are determined by confinement, as

schematically shown in Fig. 2 of Ref. [40]. When the central layer of HgTe is thin, the energy bands align in a normal ordering, similar to the ones of CdTe. On the other hand, when the width of HgTe is above a critical thickness d_c, due to confinement, the energy bands will be aligned in the inverted regime, similar to bulk HgTe. The change of sign of band gap from positive (Trivial insulator) to negative (Topological insulator) is the necessary condition to get the edge states which are described in the next section. The transition between normal and inverted regime occurs at the critical thickness $d_c \approx 6.3$ nm for HgTe/CdTe quantum wells[40].

Quantum Spin Hall Edge Modes

The effective model for QSH effect was derived by Bernevig, Hughes and Zhang [41] for a quantum well of HgTe/CdTe -

$$H_{BHZ} = \begin{pmatrix} h(k) & 0 \\ 0 & h(-k)^* \end{pmatrix}, \tag{1.22}$$

$$\text{where} \quad h(k) = \varepsilon(k)I_2 + A(k_x\sigma_x + k_y\sigma_y) + [M - B(k_x^2 + k_y^2)]\sigma_z.$$

In Eq. (1.22), $\varepsilon(k) = C - D(k_x^2 + k_y^2)$, I_2 is a 2×2 unit matrix and σ_j's are the Pauli matrices with $j = x, y, z$. This model is actually a modified two dimensional Dirac equation. A, B, C, D, and M are parameters that are determined by the thickness of the quantum well and other material parameters. The upper block $h(k)$ is for spin up and lower block is for spin down states. The gap parameter M changes sign at the critical thickness d_c denoting a quantum phase transition from a trivial to non-trivial or topological state. If one consider a semi infinite plane of HgTe/CdTe topological insulator with an open boundary condition at $y = 0$, k_x is a good quantum number (in the x direction it has a plane wave solution) but k_y
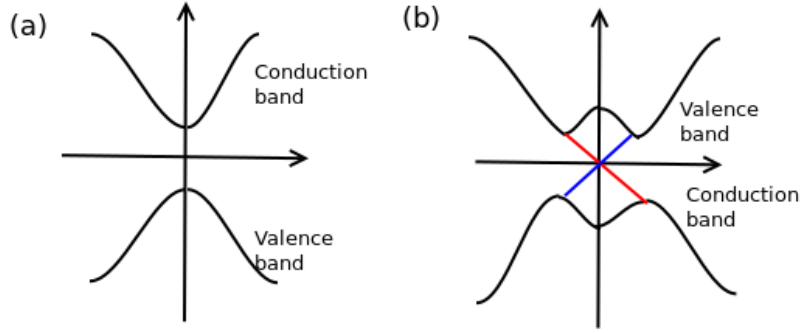
Figure 1.6: Schematic diagram of (a) band gap in trivial insulator, (b) band gap in topological insulator (red and blue lines denote spin up and spin down edge states). For a trivial insulator band gap is positive, i.e., conduction band lies above valence band as in (a). In topological insulator the band gap is negative and conduction band lies below the valence band as in (b).

is given by $-i\partial_y$. The Hamiltonian(1.22) is thus-

$$\mathcal{H}(k_x, -i\partial_y) = \begin{pmatrix} h_\uparrow(k_x, -\partial_y) & 0 \\ 0 & h_\downarrow(k_x, -\partial_y) \end{pmatrix}, \tag{1.23}$$

$$\text{with,} \quad h_\uparrow(k_x, -i\partial_y) = \begin{pmatrix} M - B_+(k_x^2 - \partial_y^2) & A(k_x - \partial_y) \\ A(k_x + \partial_y) & -M + B_-(k_x^2 - \partial_y^2) \end{pmatrix},$$

and $B_\pm = B \pm D$. The eigen value problem for upper and lower blocks can be solved separately, as $h_\uparrow \Psi_\uparrow = E\Psi_\uparrow$ and $h_\downarrow \Psi_\downarrow = E\Psi_\downarrow$. Because the lower block $h^*(-k)$ is the time reversal of the upper block $h(k)$, the solution $\Psi_\downarrow(k_x, y) = \Theta\Psi_\uparrow(k_x, y)$, where $\Theta = -i\sigma_y K$, is a time reversal operator, and K is for complex conjugation. Here we will focus on the upper block of the Hamiltonian,

$$h_\uparrow \Psi_\uparrow = E\Psi_\uparrow. \tag{1.24}$$

Considering a trial wave function -

$$\Psi_\uparrow = \begin{pmatrix} c \\ d \end{pmatrix} e^{\lambda y} \tag{1.25}$$

and substituting this in Eq. (1.24) and using Dirichlet boundary condition $\Psi_\uparrow(k_x, y = 0) = \Psi_\uparrow(k_x, y = \infty) = 0$, we get-

$$\Psi_\uparrow = \begin{pmatrix} \tilde{c}(k_x) \\ \tilde{d}(k_x) \end{pmatrix} (e^{-\lambda_1 y} - e^{-\lambda_2 y}), \tag{1.26}$$

where λ_1 and λ_2 are real and positive. If λ_1 and λ_2 are purely imaginary then we would get a solution that is distributed over the whole space and is a solution for the bulk states. But here we want to look for bound states, which are real. From Eq. (1.26) one can also see that the states are distributed strictly near the edge. So these are edge states. Substituting Eq. (1.26) into Eq. (1.24), we get-

$$E_\uparrow(k_x) = -MD/B + A\sqrt{B_+/B_-}\,k_x + O(k_x^2). \tag{1.27}$$

The effective velocity of the spin-up states thus are-

$$v_\uparrow = \frac{\partial E_+}{\partial k_x} = +sign(B)A\sqrt{\frac{B+D}{B-D}}. \tag{1.28}$$

Since $\Psi_\uparrow(k_x, y)$ is an eigenstate of σ_y with an eigen value $+1$ for $B > 0$ and -1 for $B < 0$, so spin polarization and direction of propagation both are defined by $sign(B)$. As the spin and direction of propagation are coupled, there is spin-momentum locking which is a property of helical edge states. Electrons with opposite spins counter-propagate. Similarly, we can calculate the energy states for lower block in Hamiltonian (1.23)-

$$E_\downarrow(k_x) = -MD/B - A\sqrt{B_+/B_-}\,k_x + O(k_x^2). \tag{1.29}$$

The effective velocity of the spin-down states are-

$$v_\downarrow = \frac{\partial E_-}{\partial k_x} = -sign(B)A\sqrt{\frac{B+D}{B-D}}.$$ (1.30)

Thus we see the velocity of the edge states are opposite- one is positive (1.28) and the other one is negative (1.30). These two states form helical edge states near the boundary (Fig. 1.5(a)).

1.2.2 Landauer-Buttiker formalism for quantum spin Hall systems

Landuaer-Buttiker formula for an N terminal QSH system at zero temperature is a generalization of the Landauer-Buttiker formalism for N terminal QH system, shown in section 1.1.2, and is given as[34, 42]-

$$I_i = \sum_{\substack{j=1 \\ j\neq i}}^{N} (G_{ji}V_i - G_{ij}V_j) = \frac{e^2 M}{h} \sum_{\substack{j=1 \\ j\neq i}}^{N} \sum_{\sigma,\sigma'} [T_{ji}^{\sigma\sigma'}V_i - T_{ij}^{\sigma\sigma'}V_j],$$ (1.31)

where $G_{ij} = \frac{e^2 M}{h} \sum_{\sigma,\sigma'} T_{ij}^{\sigma\sigma'}$ is the conductance between contact j and i, M is the number of edge modes, $T_{ij}^{\sigma\sigma'}$ is the transmission probability for an electron from contact j to contact i with initial spin σ' to final spin σ, V_i is the potential bias at contact i.

1.2.3 Edge mode transport in an ideal quantum spin Hall sample

An ideal six terminal QSH bar is shown in Fig. 1.5(b). The current voltage relations can be derived from the conductance matrix below:

$$G = -\frac{e^2 M}{h}
\begin{pmatrix}
-2 & 1 & 0 & 0 & 0 & 1 \\
1 & -2 & 1 & 0 & 0 & 0 \\
0 & 1 & -2 & 1 & 0 & 0 \\
0 & 0 & 1 & -2 & 1 & 0 \\
0 & 0 & 0 & 1 & -2 & 1 \\
1 & 0 & 0 & 0 & 1 & -2
\end{pmatrix},$$ (1.32)

where the diagonal elements are given as- $G_{ii} = \sum_{j, j \neq i} G_{ji}$ while the off-diagonal elements, for example, $(1,2)^{th}$ element the conductance between contact 2 and 1 is given by $\sum_{\sigma,\sigma'} T_{12}^{\sigma\sigma'}$, similarly the other off-diagonal elements can be written. The diagonal element $G_{11} = \sum_{j=2}^{6} G_{j1}$ where $G_{j1} = \frac{2e^2 M}{h}(T_{j1}^{\uparrow\uparrow} + T_{j1}^{\uparrow\downarrow} + T_{j1}^{\downarrow\uparrow} + T_{j1}^{\downarrow\downarrow}), j = 2,3,4,5,6$ can be calculated as follows- from Fig. 1.5(b) we see that there is transmission of edge modes only between the adjacent contacts (as the contacts are reflection less), say for example, for spin up edge mode from contact i to $i+1$ the transmission is unity (for $i = 1$ to 5 and $T_{61}^{\uparrow\uparrow} = 1$) while for spin down edge mode from contact i to $i-1$ transmission is unity (for $i = 2$ to 6 and $T_{61}^{\downarrow\downarrow} = 1$), rest of the transmission probabilities are zero. Thus G reduces to $\frac{e^2}{h} M(T_{21}^{\uparrow\uparrow} + T_{61}^{\downarrow\downarrow}) = \frac{2e^2}{h} M$ (since transmission probabilities: $T_{21}^{\uparrow\uparrow} = T_{61}^{\downarrow\downarrow} = 1$). Similarly the other diagonal and off diagonal elements of the conductance matrix (Eq. (1.32)) can be calculated. Substituting I_2, I_3, I_5, and $I_6 = 0$ (since contacts $2, 3, 5$ and 6 are voltage probes) and choosing reference potential $V_4 = 0$, we get $V_3 = V_2/2 = V_1/3$ and $V_5 = V_6/2 = V_1/3$. The charge Hall resistance $R_H = R_{14,26} = 0$ obviously and longitudinal resistance is $R_L = R_{14,23} = \frac{h}{e^2}\frac{1}{2M}$, two terminal resistance $R_{2T} = R_{14,14} = \frac{h}{e^2}\frac{3}{2M}$ and non-local resistance $R_{NL} = R_{12,54} = \frac{h}{e^2}\frac{1}{6M}$. Thus, charge Hall resistance vanishes, longitudinal resistance is quantized in units of $2M$ while two terminal and non-local resistances are quantized in units of $\frac{2}{3}M$ and $6M$ respectively.

1.2.4 Why do we study quantum spin Hall systems?

The advantage of quantum spin Hall edge modes over quantum Hall edge modes is that these edge modes arise in absence of magnetic field, while in QH effect edge modes arise at the cost of a large magnetic field. The non-local transport in QSH systems is also a potential candidate for low power information processing due to its dissipation less transport with in the system[34]. Edge modes are also protected by their topological character and thus are robust to disorder within the system as long as it is non-magnetic. We probe QSH

edge modes via disordered contacts and inelastic scattering to find out their resilience and to check if they are as suitable for low power transport as claimed. A reasonable comparison between the QH and QSH edge modes is also desired to show which one can sustain itself better against disorder and inelastic scattering. Further in this thesis the nonlocal shot noise (Hanbury Brown and Twiss correlation)[14, 15] for QSH edge modes are calculated to differentiate them from topological QH edge modes and also from trivial (or quasi-helical) QSH edge modes since there are recent experiments which claim to have observed quasi-helical edge modes in a trivial insulator too[43]. Quasi-helical or trivial QSH edge modes are spin polarized too like helical QSH edge modes but are prone to spin flip scattering unlike helical QSH edge modes which are not. Further, this thesis checks the potential of QSH edge modes in designing charge and spin quantum heat engines and compares their performance with other quantum heat engines such as based on quantum Hall edge modes or ballistic modes in graphene.

1.3   Quantum anomalous Hall effect

Another member of the Hall family is the quantum anomalous Hall (QAH) effect, which again is the quantum version of the classical anomalous Hall effect[44, 45]. In a ferromagnetic topological insulator (doped with magnetic atoms) at low temperatures quantum anomalous Hall edge modes arise in absence of an external magnetic field unlike quantum Hall effect[33, 10]. QAH edge modes are chiral similar to QH edge modes but spin polarized, i.e., these edge modes consist of a particular type of spin- either spin up or spin down depending on direction of the spontaneous magnetization in a ferromagnetic topological insulator. At the upper edge of the sample if spin up electrons are moving in one direction then at the lower edge of the system too spin up electrons are moving in the opposite direction. These edge modes give quantized Hall conductance $\frac{\nu e^2}{h}$ (with $\nu =$integer) and a

vanishing longitudinal resistance (similar to the quantum Hall effect).

1.3.1   How do quantum anomalous Hall edge modes arise?

In a topological insulator quantum spin Hall (QSH) edge modes appear at low temperature due to the inverted band structure. These QSH edge modes are helical, i.e., spin polarized edge modes with opposite chirality. Thus a QSH system can be thought of as two QAH edge states with opposite Hall conductances which exactly cancel each other. If we remove one spin chiral edge mode (i.e., one QAH edge state) from the picture, then we are left with the other spin chiral edge mode, which is nothing but a QAH edge mode with non-vanishing Hall conductance. This is achieved by doping magnetic atoms like Mn atoms within the topological insulator. Here, we theoretically describe the origin of QAH edge modes as follows. The Hamiltonian for a QSH system (e.g., HgTe/CdTe QW structure) can be written as (see Fig. 1 of Ref. [46])-

$$H = \begin{pmatrix} h(k) & 0 \\ 0 & h^*(-k) \end{pmatrix}. \tag{1.33}$$

The Hamiltonian is written in the basis of spin up conduction band $|E_1,\uparrow\rangle$ ($E_1^{\uparrow}$ is the energy of spin up conduction band), spin up valence band $|H_1,\uparrow\rangle$ ($H_1^{\uparrow}$ is the energy of spin up valence band), spin down conduction band $|E_1,\downarrow\rangle$ ($E_1^{\downarrow}$ is the energy of spin down conduction band) and spin down valence band $|H_1,\downarrow\rangle$ ($H_1^{\downarrow}$ is the energy of spin down valence band). The upper block $h(k)$ in Hamiltonian (1.33) is for spin up sub-bands while lower block represents spin down sub-bands, which are time reversal counterparts of each other. If time-reversal
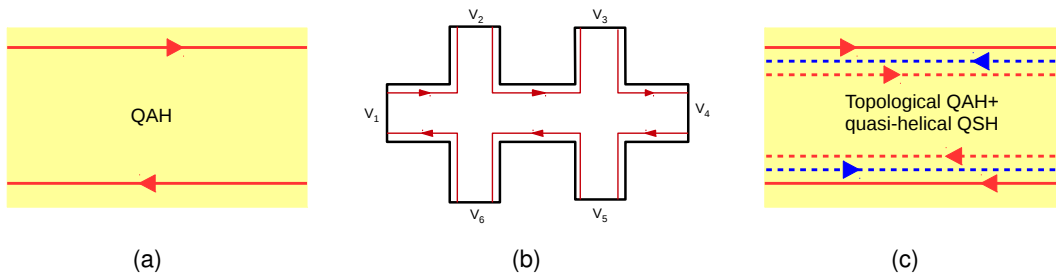
Figure 1.7: (a) Quantum anomalous Hall edge mode, (b) six terminal QAH bar, (c) QAH edge mode along with quasi-helical QSH edge modes. Red solid line denotes spin up topological QAH edge mode while red and blue dashed line denote spin up and spin down quasi-helical QSH edge modes.

symmetry is broken by introducing a magnetic field (represented by Hamiltonian H_s), then-

$$
H_s = \begin{pmatrix} G_E & 0 & 0 & 0 \\ 0 & G_H & 0 & 0 \\ 0 & 0 & -G_E & 0 \\ 0 & 0 & 0 & -G_H \end{pmatrix},
$$
(1.34)

where $2G_E$ is the splitting energy for conduction bands, i.e., $2G_E = E_1^\uparrow - E_1^\downarrow$ and $2G_H$ is the splitting energy for valence bands, i.e., $2G_H = H_1^\uparrow - H_1^\downarrow$. In QSH case opposite spin chiral edge states appear only when there is a inverted band structure. For normal (non-inverted) band structure edge modes do not appear. If one can manipulate the sub-bands such that for up-spin sub-bands the band gap is inverted (generates spin up QAH edge state) and for spin-down sub-band the band gap is normal (no QAH edge state for down-spin) then finally we are left with just a spin-up QAH edge mode. This is the first condition to get a QAH edge state from QSH edge states. The second condition is the the entire system must be in the insulating regime, i.e., conduction band and valence band should not overlap on each other. Both of these conditions are satisfied when $G_E G_H < 0$, i.e., the splitting of valence band and conduction band should be of opposite signs, see also Ref. [45].

1.3.2 Landauer-Buttiker formalism for quantum anomalous Hall edge modes

In QAH case, since edge modes are spin polarized, we can use the Landauer-Buttiker formalism built for QSH case. According to this formalism, for a multi-terminal device at zero temperature, the current at contact i is given as follows[33, 10, 12]:

$$I_i = \sum_{\substack{j=1 \\ j\neq i}}^{N} (G_{ji}V_i - G_{ij}V_j) = \frac{e^2 M}{h} \sum_{\substack{j=1 \\ j\neq i}}^{N} \sum_{\sigma,\sigma'} [T_{ji}^{\sigma\sigma'}V_i - T_{ij}^{\sigma\sigma'}V_j], \qquad (1.35)$$

where $G_{ij} = \frac{e^2 M}{h}\sum_{\sigma,\sigma'} T_{ij}^{\sigma\sigma'}$ is the conductance between terminal j and i, $T_{ij}^{\sigma\sigma'}$ is the transmission probability for an electron from contact j to contact i with initial spin σ' to final spin σ and V_i is the potential bias at contact i.

1.3.3 Edge mode transport in an ideal quantum anomalous Hall sample

An ideal six terminal quantum anomalous hall (QAH) bar is shown in Fig. 1.7(b). The current voltage relations can be derived from the conductance matrix below:

$$G = -\frac{e^2 M}{h} \begin{pmatrix} -1 & 0 & 0 & 0 & 0 & 1 \\ 1 & -1 & 0 & 0 & 0 & 0 \\ 0 & 1 & -1 & 0 & 0 & 0 \\ 0 & 0 & 1 & -1 & 0 & 0 \\ 0 & 0 & 0 & 1 & -1 & 0 \\ 0 & 0 & 0 & 0 & 1 & -1 \end{pmatrix}, \qquad (1.36)$$

where the diagonal elements are given as- $G_{ii} = \sum_{j,j\neq i} G_{ji}$ while the off-diagonal elements, for example, $(1,2)^{th}$ element the conductance between contact 2 and 1 is given by $\sum_{\sigma,\sigma'} T_{12}^{\sigma\sigma'}$, similarly the other off-diagonal elements can be written. The diagonal element $G_{11} = \sum_{j=2}^{6} G_{j1}$ where $G_{j1} = \frac{2e^2 M}{h}(T_{j1}^{\uparrow\uparrow} + T_{j1}^{\uparrow\downarrow} + T_{j1}^{\downarrow\uparrow} + T_{j1}^{\downarrow\downarrow}), j = 2,3,4,5,6$ can be calculated as follows. From Fig. 1.7(b) we see that there is transmission of spin up edge modes

between the adjacent contacts (as the contacts are reflection less) in the clockwise direction only, say for example, for spin up edge mode from contact i to $i+1$ the transmission is unity (for $i=1$ to 5 and $T_{61}^{\uparrow\uparrow}=1$) while for spin down edge mode all the transmission probabilities are zero ($T_{ij}^{\uparrow,\downarrow}=T_{ij}^{\downarrow,\uparrow}=T_{ij}^{\downarrow,\downarrow}=0$ for $i,j=1$ to 6), since there is no spin down edge mode for particular magnetization direction (see Fig. 1.7(b)). Thus G_{11} reduces to $\frac{e^2}{h}MT_{21}^{\uparrow\uparrow}=\frac{e^2}{h}M$ (since transmission probability: $T_{21}^{\uparrow\uparrow}=1$). Similarly the other diagonal and off diagonal elements of the conductance matrix (Eq. (1.36)) can be calculated. M represents the total no. of modes. In setup as shown in Fig. 1.7(b), $M=1$ to avoid clutter. Substituting I_2,I_3,I_5, and $I_6=0$ (since contacts $2,3,5$ and 6 are voltage probes) and choosing reference potential $V_4=0$, we get $V_1=V_2=V_3$ and $V_4=V_5=V_6=0$. Thus, the Hall resistance $R_H=R_{14,26}=\frac{h}{e^2}\frac{1}{M}$, longitudinal resistance $R_L=R_{14,23}=0$, two terminal resistance $R_{2T}=R_{14,14}=\frac{h}{e^2}\frac{1}{M}$ and the non-local resistance is $R_{NL}=R_{12,54}=0$. The Hall resistance is quantized in units of M and thus both longitudinal and non-local resistances vanish and the two terminal resistance is quantized in units of M.

1.3.4   Why do we study quantum anomalous Hall edge modes?

In some recent experiments, it has been shown that QAH edge modes have finite longitudinal resistance along with quantized Hall resistance[44, 45, 47, 48, 49]. This finite longitudinal resistance leads to a discrepancy because QAH edge modes are chiral, and ideal chiral QAH edge modes should always give vanishing longitudinal resistance as observed in QH case. In Ref. [44], it is shown that presence of a quasi-helical (or, trivial) QSH edge modes along with a topological chiral QAH edge mode satisfies the experimental observation (i.e., finite longitudinal resistance and quantized Hall resistance), see Ref. [44]. The conclusion of QAH experiments such as done in Ref. [44] is that chiral QAH edge modes occur along with quasi-helical QSH edge modes (see Fig. 1.7(c)). This is because chiral QAH edge modes themselves originate from QSH edge modes via doping of magnetic

atoms or/and suppressing one of the spin polarized edge modes. In some other recent works[5], it has been shown that this finite longitudinal resistance can also be described by a single chiral QAH edge modes but at finite temperature, and at zero temperature this longitudinal resistance vanishes. Now it is a moot point whether this finite longitudinal resistance is due to the finite temperature effect on the single chiral QAH edge mode as in Ref. [5] or due to the presence of trivial QSH edge modes[44] along with chiral QAH edge mode. These questions are our motivation to study QAH edge modes. Another important question we concentrate on is what if this topological QAH edge mode along with quasi-helical QSH edge modes loses its topological character in presence of a magnetic impurity. This is very much possible if in the conversion process from QSH edge modes to chiral QAH edge mode via magnetic doping, topological protection of the QAH edge mode is lost. These aforesaid two questions have been answered in chapter 4 of this thesis. This completes the introduction for first part of this thesis which consists of the discussion on origin and properties of the edge modes in QH, QSH and QAH samples.

In the next section an introduction to the second part of this thesis is given which consists of the application of these edge modes in thermoelectrics in chapter 5 and their comparison with thermoelectrics based on ballistic modes in chapter 6. As explained earlier, ballistic modes differ from edge modes in that they are prone to backscattering within the sample while edge modes aren't. However, both ballistic modes and edge modes are perfect transmission channels through any 2DEG. Graphene is the ideal candidate to see these ballistic modes in operation as because it has perfectly conducting transmission channels[50] and pristine graphene is easily available. Thus it is a moot point to check how do ballistic and edge modes stack up against each other in thermoelectric applications. In the next section quantum heat engines and quantum refrigerators are introduced and then the working formulas for the thermoelectric coefficients in the quantum heat engine and quantum refrigerator are derived.

1.4 Application of edge mode transport in thermoelectrics

Quantum Hall and quantum spin Hall edge modes are well known for their dissipation less transport. The chiral motion of electrons in QH systems or the helical motion in QSH systems can be tuned further for the purpose of generating large thermoelectric responses, see Refs. [36, 18]. For thermoelectric applications a quantum system can work in two ways-either as a quantum heat engine or as a quantum refrigerator. The difference between a quantum heat engine or quantum refrigerator and their classical counterparts is that the size of these systems are so small (less than the electron inelastic scattering length) that classical laws break down at these length scales. When a quantum system converts waste heat energy back into electricity (thus generating electrical energy) from the heat current flowing between hot and cold contacts, it is called a quantum heat engine. On the other hand, when the quantum system transfers heat from cold to hot contacts via consuming power from an external source then it is called quantum refrigerator. Another application of edge modes is as a quantum heat diode, i.e., to use the chiral motion of the edge modes to control the flow of heat current. Quantum heat engines are of two types-a) cyclic and b) steady state. Cyclic [51] heat engines are defined by the time dependent parameters like volume, temperature etc, where all of these parameters return to their previous position after one complete cycle in parameter space. Some examples of cyclic heat engines are Carnot engines, Otto engines, etc. On the other hand, steady state heat engines have no time dependent parameter and they do the conversion from heat to work via steady state flows of microscopic particles like electron, phonon, etc [51]. This thesis only deals with steady state heat engines. Next the theoretical framework needed to understand steady state quantum heat engines and quantum refrigerators is discussed.
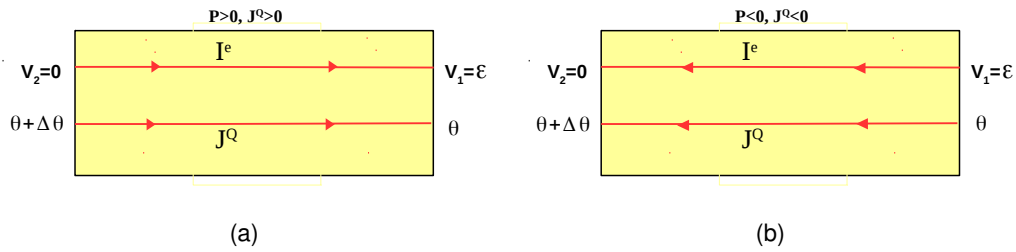
Figure 1.8: (a) Two-terminal quantum heat engine with temperature bias applied at the left contact while potential bias at the right contact. Electric (I^e) and heat (J^Q) currents are flowing from hotter to colder region with output power $\mathcal{P} > 0$ and $J^Q > 0$ (b) A two terminal quantum refrigerator with electric and heat currents flowing from colder to hotter region with $\mathcal{P} < 0$ and $J^Q < 0$.

1.4.1   What are quantum heat engines and quantum refrigerators?

A quantum heat engine converts heat energy given to a system into electrical work, while a quantum refrigerator converts the work done on system into absorbing heat from a low temperature region of the system to dump it onto a higher temperature region. For a system to work as a quantum heat engine, heat energy (J^Q) is given to system, i.e., $J^Q > 0$ (heat energy flows from hot to cold region) and system generates output power ($\mathcal{P}$), i.e., $\mathcal{P} > 0$, see Fig. 1.8(a). To work as a quantum refrigerator external work (power) is done on the system, i.e., $\mathcal{P} < 0$ and system absorbs heat energy from cold region and dumps it onto a hotter region, i.e., $J^Q < 0$ (heat energy flows from lower to higher temperature region), see Fig. 1.8.(b). These sign conventions must be followed for a system to either work as a heat engine or as a refrigerator. Next the main working formulas for a general two terminal system to work as a quantum heat engine or a quantum refrigerator are derived. To do this one considers a two dimensional system connected to two reservoirs at the two ends as shown in Fig. 1.8. In the linear transport regime, electric and heat current in the system are linearly proportional to the applied biases such as electric bias $\mathcal{E}$ or thermal bias $\Delta\theta$. This linear dependence can be expressed in terms of Onsager matrix as shown

below[52, 53, 36]-

$$\begin{pmatrix} I^e \\ J^Q \end{pmatrix} = \begin{pmatrix} L^{11} & L^{12} \\ L^{21} & L^{22} \end{pmatrix} \begin{pmatrix} \mathcal{E} \\ \Delta\theta \end{pmatrix},$$ (1.37)

where I^e and J^Q are the electric and heat currents, the Onsager coefficients L^{11} and L^{22} are related to the electric and thermal conductances while the non-diagonal coefficients (L^{12} and L^{21}) are related to the Seebeck and Peltier coefficients. The Seebeck coefficient is defined as the potential difference generated across the system due to unit temperature difference $\Delta\theta$, while the Peltier coefficient is defined as the heat current generated due to unit potential bias applied to the system[51, 52]. They are expressed as-

$$S = -\frac{L^{12}}{L^{11}} \quad \text{and} \quad P = \frac{L^{21}}{L^{11}}.$$ (1.38)

The Onsager matrix (in Eq. (1.37)) relating the electric and heat currents to potential bias and temperature difference can be written as [52, 54]-

$$\begin{pmatrix} L^{11} & L^{12} \\ L^{21} & L^{22} \end{pmatrix} = \begin{pmatrix} \mathcal{L}^0 & \mathcal{L}^1/e\theta \\ \mathcal{L}^1/e & \mathcal{L}^2/e^2\theta \end{pmatrix},$$ (1.39)

wherein, $\mathcal{L}^\alpha = G_0 \int_{-\infty}^{\infty} d\varepsilon (-\frac{\partial f}{\partial \varepsilon}) \rho(\varepsilon)(\varepsilon - \mu)^\alpha T(\varepsilon),$ (1.40)

here $G_0 = (e^2/\hbar)(W/\pi^2)$, $\mathcal{L}^0 = G$ is conductance of system with sample width W [55], ε the energy of the electron, $\rho(\varepsilon)$ the density of states, f the Fermi-Dirac distribution, μ is Fermi energy, θ is the temperature of colder terminal and $T(\varepsilon)$ the transmission probability for electrons through the system at electronic energy ε. Once one knows the energy dependent transmission function $T(\varepsilon)$ for any system, one can calculate the Onsager coefficients L^{ij} using Eq. (1.40) and thus calculate the thermoelectric coefficients such as the Seebeck coefficient, Peltier coefficient, thermal conductance. In the following subsection the maximum output power generated in a quantum heat engine and the efficiency at that

maximum output power are discussed.

1.4.2 Quantum heat engine: power and efficiency

The output power [53] generated for a general quantum heat engine system is given as-

$$\mathcal{P} = -I^e\mathcal{E} = -(L^{11}\mathcal{E} + L^{12}\Delta\theta)\mathcal{E}, \tag{1.41}$$

which is maximized by $\frac{d\mathcal{P}}{d\mathcal{E}} = 0$, at $\mathcal{E} = -\frac{L^{12}}{2L^{11}}\Delta\theta$ which gives the maximum power as-

$$P_{max} = \frac{1}{4}\frac{(L^{12})^2}{L^{11}}(\Delta\theta)^2 = \frac{1}{4}S^2 G(\Delta\theta)^2. \tag{1.42}$$

The efficiency at maximum power is defined as the ratio of maximum power to the heat current transported and is-

$$\eta(\mathcal{P}_{max}) = \frac{\mathcal{P}_{max}}{J^Q} = \frac{\eta_c}{2}\frac{\theta L^{12^2}}{2L^{11}L^{22} - L^{12}L^{21}} = \frac{\eta_c}{2}\frac{GS^2\theta/\kappa}{2 + GS^2\theta/\kappa}, \tag{1.43}$$

at $\mathcal{E} = -\frac{L^{12}}{2L^{11}}\Delta\theta = \frac{S}{2}\Delta\theta$, which is the condition for maximum power and κ is the thermal conductance, defined as-

$$\kappa = \frac{L^{11}L^{22} - L^{12}L^{21}}{L^{11}}. \tag{1.44}$$

Similarly, efficiency η is the ratio of output power to heat current transported[53]-

$$\eta = \frac{\mathcal{P}}{j^Q} = \frac{(L^{11}\mathcal{E} + L^{12}\Delta\theta)\mathcal{E}}{(L^{21}\mathcal{E} + L^{22}\Delta\theta)} = \frac{-(\mathcal{E} - S\Delta\theta)\mathcal{E}}{(\theta S\mathcal{E} - (\frac{\kappa}{G} + \theta S^2)\Delta\theta)}. \tag{1.45}$$

To calculate maximal efficiency we need to find the relation between $\mathcal{E}$ and $\Delta\theta$, substituting $\frac{d\eta}{d\mathcal{E}} = 0$ in Eq. (1.45), with the condition $j^Q > 0$, gives-

$$\mathcal{E} = \frac{L^{22}}{L^{21}}\left(-1 + \sqrt{\frac{L^{11}L^{22} - L^{12}L^{21}}{L^{11}L^{22}}}\right)\Delta\theta \text{ and } \eta_{max} = \eta_c\frac{\sqrt{ZT+1}-1}{\sqrt{ZT+1}+1}, \quad (1.46)$$

wherein $\eta_c = \frac{\Delta\theta}{\theta}$ is the Carnot efficiency and ZT is the figure of merit, a dimensionless quantity, defined as-

$$ZT = \frac{GS^2\theta}{\kappa}. \quad (1.47)$$

Eqs. (1.46), (1.47) define the operational characteristics of a quantum heat engine based on charge transport. However, quantum heat engines can also operate via spin transport[16]. In chapters 5 and 6 we discuss both charge and spin based quantum heat engines.

1.4.3   Why do we study quantum heat engines?

In nanostructured electronics such as microchips or integrated circuits used in computers, a lot of heat energy is produced due to Joule heating and other processes. This generation of heat increases the temperature of the system and thus can interrupt the smooth working of the system. A large amount of energy in these systems is completely wasted in the form of heat, which is called waste heat energy. A system which can convert this waste heat energy to useful work by generating electric current in the quantum regime, is a quantum heat engine. To design an efficient quantum heat engine in linear response regime we need a material with large Seebeck coefficient, large electrical conductivity and small thermal conductivity. Since these quantities are inter related, if one tries to increase the Seebeck coefficient, electrical conductivity reduces and vice versa. This is why, it is very difficult to increase the performance of quantum heat engines beyond a certain limit. The aim in this

thesis is to design quantum heat engines working at high efficiency and maximum output power as compared to other quantum heat engines.

1.4.4 Quantum refrigerator: cooling power and coefficient of performance

For a general two terminal system to work as a quantum refrigerator, we need to define two quantities- a) coefficient of performance (COP) and b) cooling power. COP is defined as the ratio of the heat energy absorbed (J^Q) from the colder region to the work done the system ($\mathcal{P}$). On the other hand cooling power is the heat energy absorbed from the colder region. These quantities are expressed as follows-

$$\text{COP: } \eta^r = \frac{J^Q}{\mathcal{P}}, \qquad \text{Cooling power} = -J^Q, \tag{1.48}$$

where $J^Q < 0$ and $\mathcal{P} < 0$ (since J^Q is always negative, to plot cooling power as a positive quantity a minus sign is taken before J^Q). COP of the system can be set to maximum via $\frac{d\eta^r}{d\mathcal{E}} = 0$, which gives the maximum COP (considering $J^Q < 0$ and $\mathcal{P} < 0$) at [53]-

$$\mathcal{E} = -\frac{L^{22}}{L^{21}}\left(1 + \sqrt{\frac{det\mathbb{L}}{L^{11}L^{22}}}\right)\Delta\theta, \text{where } \mathbb{L} = \begin{pmatrix} L^{11} & L^{12} \\ L^{21} & L^{22} \end{pmatrix}, \tag{1.49}$$

and $det\mathbb{L}$ refers to determinant of Onsager matrix $\mathbb{L}$. The maximum COP and the cooling power J^Q are -

$$
\begin{aligned}
\eta^{r,max} &= \frac{\eta_c^r}{x}\frac{\sqrt{y+1}-1}{\sqrt{y+1}+1}, \quad \text{with } y = \frac{L^{21}L^{12}}{det\mathbb{L}}, \quad x = \frac{L^{12}}{\theta L^{21}}, \\
\text{and } J^Q(\eta^{r,max}) &= L^{22}\left(\sqrt{\frac{det\mathbb{L}}{L^{11}L^{22}}}\right)\Delta\theta,
\end{aligned}
\tag{1.50}
$$

where, $\eta_c^r = \theta/\Delta\theta$ is the Carnot efficiency of refrigerators. Here we see that for a system to work as a good quantum refrigerator (large COP) the asymmetric parameter (x), i.e., ratio of Seebeck to Peltier coefficient should be equal to or less than unity. As asymmetric parameter x increases from one to ∞, coefficient of performance of the refrigerator reduces to zero.

1.4.5   Why do we study quantum refrigerators?

An efficient quantum refrigerator is useful in cooling down a quantum system below the temperature of its surroundings. For quantum systems to work efficiently it has to be close to zero degree Kelvin. This is done by quantum refrigerators. The aim of this thesis is to analyse the thermoelectric properties of chiral or helical edge modes so as to design efficient quantum refrigerators. Comparing the performance of these quantum refrigerators based on edge modes to other quantum refrigerators like those based on ballistic modes in graphene helps in designing better quantum refrigerators. This is because in both cases electron transport occurs with almost zero scattering in the coherent transport regime. This completes the introduction for second part of this thesis.

1.5   This thesis

In this thesis, some important scattering problems are addressed in the mesoscopic transport regime. The length of the systems considered in this thesis is small such that electrons are not affected by inelastic scattering. Inelastic scattering between edge modes is introduced phenomenologically which realistically takes place via electron- electron scattering at low temperature or electron-phonon scattering at high temperature[33]. In chapter 2 the effect of disordered contacts and inelastic scattering on QH and QSH edge modes is considered and the robustness or otherwise of these edge modes are compared.

Chapter 2 is based on Refs. [1, 2]. In chapter 3 the topological helical QSH edge modes are distinguished from the topological chiral QH edge modes via non-local Hanbury-Brown and Twiss (HBT) noise correlations. Chapter 3 is based on Ref. [3]. In the same chapter the topological origin of the helical QSH edge modes is also discussed via non-local HBT noise measurements. Chapter 4 addresses, the question, whether topological protection of QAH edge modes is sustained during the evolution of QAH edge modes from QSH edge modes or not and its consequences. Chapter 4 is based on Refs. [4, 6]. In chapters 5, 6 the focus is on the application of these edge modes in thermoelectrics. In chapter 5 quantum heat engines and quantum refrigerators based on QSH edge modes are studied. Chapter 5 is based on Ref. [9]. In chapter 6 charge as well as spin based quantum heat engines and quantum refrigerators are discussed, which operate with ballistic modes in graphene. A comparison is made between the quantum heat engines and quantum refrigerators based on edge modes (discussed in chapter 5) to that based on ballistic modes in graphene (discussed in chapter 6). Chapter 6 is based on Refs. [7, 8]. In chapter 7 this thesis concludes with a summary of all the chapters and a perspective on future endeavours. Finally, the Mathematica programs used to plot the various thermoelectric coefficients are given in the Appendix (Chapter 8), first for the QSH heat engine (described in Chapter 5) in section 8.1 and then for the graphene spin heat engine (described in Chapter 6) in section 8.2.

2. Effect of disorder and inelastic scattering on quantum Hall and quantum spin Hall edge modes

"When you ask people, 'What's the opposite of fragile?,' they tend to say robust, resilient, adaptable, solid, strong. That's not it. The opposite of fragile is something that gains from disorder."

– Nassim Nicholas Taleb

2.1 Introduction

It is widely known that transport along edge modes in a quantum Hall (QH) setting is resilient to disorder[10]. In lieu of this, one can ask the question whether in a quantum spin Hall (QSH) bar the QSH edge modes will be more/less resilient to the twin effects of disorder and inelastic scattering- the bane of any phenomena which relies on complete quantum coherence. The expectation is that since QSH edge modes are spin dependent and spin has longer relaxation times than charge, the spin Hall edge modes would be far more robust to disorder and inelastic scattering. However, contrary to expectations one sees in this chapter not only that there is no added advantage of QSH edge modes as against QH edge

modes, its rather a disadvantage. QSH edge modes are far more susceptible to disorder and inelastic scattering than QH edge modes. This is of possible relevance to the use of QSH edge modes in spintronics and quantum computation applications[56] as also in setups wherein QSH edge modes are utilized to generate Majorana fermions[57, 58].

The aim of this chapter is to compare the quantization of Hall and longitudinal resistance seen in ideally contacted QH or QSH sample as shown in sections 1.1.3 and 1.2.3 of the introduction of this thesis and investigate how this quantization is affected by disordered contacts, inelastic scattering and the number of contacts. A disordered contact in contrast to an ideal contact does not have a transmission probability of one. Further, as sample size increases edge modes will be affected by inelastic scattering, in case inelastic scattering length $l_{in} < L$ (length of sample). There is no inter edge scattering, what inelastic scattering does is to equilibrate the populations of edge states with each other on same side of the sample[10, 12]. This is the case for inelastic scattering in QH samples.

In QSH samples on the other hand one has spin-up and spin-down edge modes and equilibration might happen at the same edge between spin up and spin down edge modes in effect with spin flip scattering. In absence of spin flip scattering also edge modes will equilibrate due to inelastic processes like electron-electron or electron-phonon scattering, however this time spin-up edge modes will equilibrate only with spin-up and not spin-down, similarly for spin-down edge modes. The edge states once equilibrated remain in equilibrium[10]. In contrast to an earlier work[59] which predicted quantized values of conductance in the presence of strong disorder for topological insulator edge modes in the chapter it is shown that quantization of longitudinal conductance and Hall conductance is lost even when a single contact is disordered. Of course, one has to caveat the aforesaid statement since Ref. [59] considers disorder in the sample itself but in the cases considered in this chapter, disorder is confined to the contacts only. The effect of random magnetic fluxes on QSH edge modes has been considered earlier[60] wherein it was concluded that

spin Hall edge modes are localized in their presence. Localization of QSH edge modes has also been predicted for non-magnetic disorder in the sample, see Ref. [61]. This chapter discusses the effects of both disordered contacts and inelastic scattering on Hall resistance, non-local resistance, 2-terminal resistance and longitudinal resistance in QH and QSH samples. There is a special focus on non-local resistance because of two factors, which we outline below.

2.1.1   Importance of non-local measurement

Non-local conductance measurement can distinguish between chiral and helical edge conduction [34]. In a multi-terminal Hall sample, local or 2-terminal resistance for QH case is $\frac{h}{2e^2 M}$ and for QSH case is $\frac{h}{2e^2 M}$. So measuring the local resistance one can't distinguish between chiral(QH) and helical(QSH) edge modes, while non-local resistance for helical(QSH) edge mode transport is $\frac{h}{4e^2 M}$ for a 4-terminal sample and for chiral(QH) edge mode transport is zero. Non-local transport is not affected by the bulk conduction but local transport is affected by bulk conduction. To confirm edge mode conduction within a sample non-local measurement is used rather than local measurement. Non-local transport in helical(QSH) regime is dissipation less and this heat generation due to ohmic dissipation in logic gates based on semiconductor design can be considerably reduced by using non-local transport in helical(QSH) regime along-with improved performance[34].

2.1.2   Resilience of non-local measurement

In a remarkable experiment conducted in Ref. [62] and theoretically analysed in Ref. [63], an Aharonov-Bohm ring based four-probe set up was considered, in it was shown that the non-local resistance is less affected by dephasing than the local two-probe resistance. This chapter tries to answers the question, whether in a QSH bar the non-local resistance will be

adversely affected by the twin effects of disorder and inelastic scattering-the bane of any phenomena which relies on complete quantum coherence. In this chapter it is shown that non-local edge state transport in the QSH case is quite susceptible to disorder and even a single disordered probe can change the non-local resistance. Although it is well known that spin flip scattering adversely affects the non-local transport in QSH case[59], in this chapter, it is seen that non-spin flip scattering with disorder and inelastic scattering can greatly affect the non-local transport too. The reason for looking into this case is because of a point made in the abstract of Ref. [34]- that non-local transport through edge channels in topological insulators will have potential applications in low power information processing. In this chapter it is shown that this statement is not true in presence of disorder and/or inelastic scattering with or without spin flip processes.

2.1.3   This chapter

The structure of this chapter is as follows. First the effect of disordered contacts is discussed on QH and QSH edge mode transport in section 2.2. Then the effect of inelastic scattering is included to see its effect in section 2.3. The focus is on the effects of disorder and inelastic scattering on both local and non-local edge mode transport. Next the discussion on disorder and inelastic scattering is extended to N terminal QH/QSH samples in section 2.4. Then a comparison is made in section 2.5 in two Tables 2.1, 2.2 comparing the resilience of edge mode transport in both QH and QSH samples to both disorder and inelastic scattering. Finally this chapter concludes in section 2.6 with a perspective.

2.2   Effect of disordered contacts

A disordered contact can be thought of as an ideal contact with a disordered region separating the reservoir and the sample. The contact can be treated in the same way as the
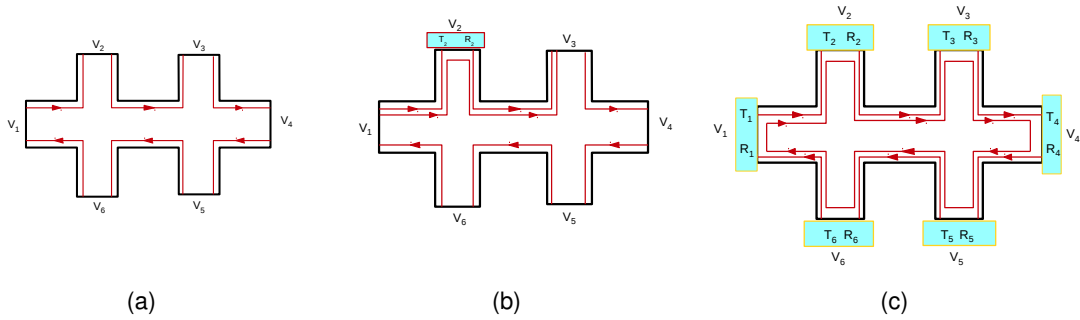
Figure 2.1: QH (a) ideal case, (b) single contact disordered case, (c) all contacts disordered case. Maroon solid line denotes chiral spin unpolarized QH edge modes. Edge modes are transmitted through a disordered contact i with transmission probability $T_i = 1 - D_i$ and reflection probability $R_i = D_i$ while D_i being the strength of disorder at contact i.

two-terminal sample, where the total transmission and reflection probabilities for electrons coming from the sample are T and R[12, 10] respectively. An ideal contact is reflection less thus $T = 1, R = 0$ while if a contact is disordered with strength D, then its reflection probability is $R = D$ while its transmission probability is $T = 1 - D$.

2.2.1 Quantum Hall sample with single disordered contact

The ideal case without any disorder is represented in Fig. 2.1(a) for six terminal QH sample. The current voltage relation and conduction matrix are shown in Eqs. (1.20), (1.21) in chapter 1- Introduction. The resistances for the ideal case have also been calculated in section 1.1.3 of chapter 1. We do not repeat it here and start with the case of single disordered contact. QH sample with single disordered contact is shown in Fig. 2.1(b). Here contact 2 is disordered with transmission probability T_2 and reflection probability R_2. The strength of disorder at contact 2- D_2 is related to the reflection and transmission probabilities by the relation- $T_2 = (1 - D_2)$ and $R_2 = D_2$. Depending on the disorder strength D_2 only a fraction of the edge modes will transmit through the disordered contact. Landuaer-Buttiker

formula for an 6 terminal QH system at zero temperature is given as[10]-

$$I_i = \sum_{\substack{j=1 \\ j \neq i}}^{6} (G_{ji}V_i - G_{ij}V_j) = \frac{2e^2 M}{h} \sum_{\substack{j=1, \\ j \neq i}}^{6} (T_{ji}V_i - T_{ij}V_j), \qquad (2.1)$$

herein V_i is the voltage at i^{th} contact and I_i is the current flowing out of that contact, M is

the number of edge modes, T_{ij} is the transmission probability from j^{th} to i^{th} contact and G_{ij}

is the associated conductance. The conduction matrix for six terminal QH sample relating

the currents to the voltages is -

$$G = -\frac{2e^2}{h} \begin{pmatrix} -M & 0 & 0 & 0 & 0 & M \\ T_2 & -T_2 & 0 & 0 & 0 & 0 \\ R_2 & T_2 & -M & 0 & 0 & 0 \\ 0 & 0 & M & -M & 0 & 0 \\ 0 & 0 & 0 & M & -M & 0 \\ 0 & 0 & 0 & 0 & M & -M \end{pmatrix}, \qquad (2.2)$$

where the diagonal elements $G_{ii} = \sum_{j=1, j \neq i}^{6} G_{ji} = \frac{2e^2}{h} \sum_{j=1, j \neq i}^{N} T_{ji}$ and the non-diagonal ele-

ments $G_{ij} = \frac{2e^2}{h} T_{ij}$ (for $j \neq i$). For example, the diagonal element $G_{11} = \frac{2e^2}{h} M \sum_{j=1, j \neq i}^{6} T_{j1}$,

M represents the total no. of modes while a factor 2 is introduced due to the spin degeneracy

of the electrons. In setup as shown in Fig. 2.1(b), $M = 1$ to avoid clutter. From Fig. 2.1(b) we

see that an electron coming out of contact 1 can either transmit into the contact 2 with prob-

ability $T_2 = (1 - D_2)$ or it can reflect to contact 3 with probability $R_2 = D_2$ (since contact 2 is

disordered). So the $(1,1)^{th}$ element of the conduction matrix G reduces to $\frac{2e^2}{h} M (T_{21} + T_{31})$

(since there is no transmission from contact 1 to 4 or 5 or 6, so $T_{41} = T_{51} = T_{61} = 0$). Thus,

$G_{11} = \frac{2e^2}{h} M (T_2 + R_2) = \frac{2e^2}{h} M$. Similarly rest of the transmission probabilities T_{ij}'s can be

derived. Substituting $I_2, I_3, I_5,$ and $I_6 = 0$ (since contact $2, 3, 5, 6$ are voltage probes and

current through voltage probe is zero) and choosing reference potential $V_4 = 0$, we get

$V_1 = V_2 = V_3$, and $V_4 = V_5 = V_6 = 0$. Thus, as done in section 1.1.3 for an ideal contact, for a single disordered contact we get the Hall resistance $R_H = R_{14,26} = \frac{h}{2e^2}\frac{1}{M}$, longitudinal resistance $R_L = R_{14,23} = 0$, two terminal resistance $R_{2T} = R_{14,14} = \frac{h}{2e^2}\frac{1}{M}$ and non-local resistance $R_{NL} = R_{12,54} = 0$. We see the Resistance characteristics are completely independent of the strength of disorder. Similar to the case of ideal contacts, the Hall resistance is quantized in units of M and both the longitudinal and non-local resistances vanish while the 2-terminal resistance is also quantized in units of M.

2.2.2   Quantum Hall sample with all disordered contacts

The case of all disordered contacts is shown in Fig. 2.1(c). All the contacts of the six terminal QH sample are disordered with strength D_i ($i = 1, 2, 3, 4, 5, 6$). Disorder strength D_i is related to the reflection and transmission probabilities R_i and T_i by the relation $T_i = (1 - D_i)M$ and $R_i = D_i M$. The current voltage relations can be derived from the conductance matrix below:

$$
G = -\frac{2e^2 M}{h}
\begin{pmatrix}
-T_{11} & T_{12} & T_{13} & T_{14} & T_{15} & T_{16} \\
T_{21} & -T_{22} & T_{23} & T_{24} & T_{25} & T_{26} \\
T_{31} & T_{32} & -T_{33} & T_{34} & T_{35} & T_{36} \\
T_{41} & T_{42} & T_{43} & -T_{44} & T_{45} & T_{46} \\
T_{51} & T_{52} & T_{53} & T_{54} & -T_{55} & T_{56} \\
T_{61} & T_{62} & T_{63} & T_{64} & T_{65} & -T_{66}
\end{pmatrix}.
\tag{2.3}
$$

M is the total number of edge modes in the sample. In setup as shown in Fig. 2.1(c), $M = 1$. To avoid clutter only one mode is shown. In the above matrix T_{15} say is defined as the total

transmission probability from contact 5 to contact 1 and can be calculated explicitly as-

$$
\begin{aligned}
T_{15} &= (1-D_5)D_6(1-D_1)M + (1-D_5)D_6^2 D_1 D_2 D_3 D_4 D_5(1-D_1)M + ..., \\
T_{15} &= (1-D_5)D_6(1-D_1)M[1 + D_1 D_2 D_3 D_4 D_5 D_6 + ...], \\
T_{15} &= \frac{(1-D_5)D_6(1-D_1)M}{1 - D_1 D_2 D_3 D_4 D_5 D_6}.
\end{aligned}
\tag{2.4}
$$

The Eq. (2.4) can be understood as follows- An electron starting from contact 5 has probability $1 - D_5$ to be transmitted from contact 5. Since we are interested in the probability of its reaching contact 1, it has to be reflected from contact 6 with probability D_6 and finally it is transmitted to contact 1 with probability $1 - D_1$. However, this is the shortest of the many paths possible for an electron starting from 5 to reach 1, another path can be that of an electron starting from contact 5 with probability $1 - D_5$ and since we are interested in the probability of its reaching contact 1, it has to be reflected from contact 6 with probability D_6 and then reflected from contact 1 with probability D_1, similarly with probability D_2 it will be reflected from contact 2, with probability D_3 from contact 3, with probability D_4 from contact 4, with probability D_5 from contact 5 again get reflected with probability D_6 from contact 6 and finally get transmitted into contact 1, this is the second shortest path possible, similarly one can sum over all the other paths leading to an infinite series, which can be summed to yield the total probability per mode for transmission from contact 5 to 1 as in Eq. (2.4). Similarly all the other transmission probabilities in Eq. (2.3) can be explained. Since currents I_2, I_3, I_5 and $I_6 = 0$ as these are voltage probes and choosing reference potential $V_4 = 0$, we solve the Eqs. (1.20), (2.3) and calculate the Hall, longitudinal and 2-terminal resistances. So, the Hall resistance $R_H = R_{14,26} = \frac{h}{2e^2}\frac{1}{M}$, longitudinal resistance $R_L = R_{14,23} = 0$, two terminal resistance $R_{2T} = R_{14,14} = \frac{h}{2e^2 M}\frac{1-D_1 D_4}{(1-D_1)(1-D_4)}$. Further, for the non-local measurement currents I_3, I_4, I_5 and $I_6 = 0$ as these are voltage probes and choosing reference potential $V_2 = 0$ we get the non-local resistance $R_{NL} = R_{12,54} = 0$, see
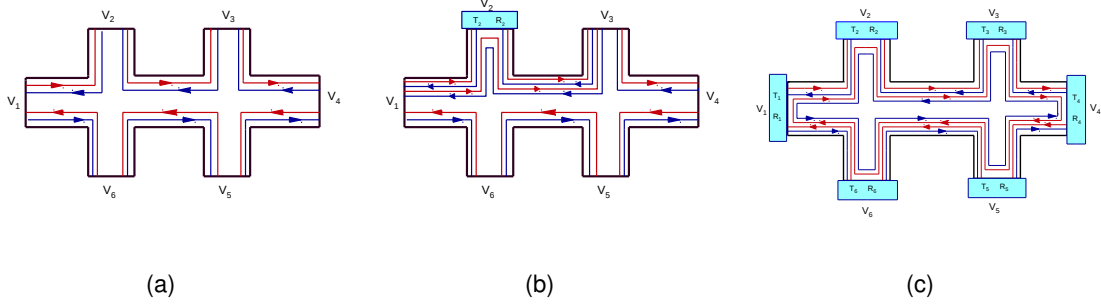
Figure 2.2: QSH (a) ideal case: Contacts are reflection-less, (b) single contact disordered case (R_2, T_2 represent the reflection and transmission probability of edge modes from and into contact 2), (c) all contacts disordered case. Red solid line denotes spin up edge mode while blue solid line denotes spin down edge mode.

Figs. 2.3(a,b). The Hall, longitudinal and non-local resistances are all ideally quantized and do not deviate from their ideal results however the 2-terminal (local) resistance does deviate when more than one contact is disordered as in Figs. 2.3(a,b). This also shows that non-local resistance is not affected by disorder unlike the local resistance agreeing with what was observed in the AB ring in Ref. [62]. Next we discuss the effect of single contact disorder and all contacts disorder on QSH edge modes.

2.2.3 Quantum spin Hall sample with single disordered contact

The ideal case without any disorder is represented in Fig. 2.2(a). The current voltage relations and conduction matrix are shown in Eqs. (1.31), (1.32) in chapter 1- Introduction. The resistances for the ideal case have also been calculated in section 1.2.3 of chapter 1. We do not repeat it here and start with the case of single disordered contact. This case is represented in Fig. 2.2(b), only a single contact 2 is disordered. Landuaer-Buttiker formula for an 6 terminal QSH system at zero temperature is given as[34, 42]-

$$I_i = \sum_{\substack{j=1 \\ j \neq i}}^{6} (G_{ji}V_i - G_{ij}V_j) = \frac{e^2 M}{h} \sum_{\substack{j=1 \\ j \neq i}}^{6} \sum_{\sigma, \sigma'} [T_{ji}^{\sigma\sigma'} V_i - T_{ij}^{\sigma\sigma'} V_j], \qquad (2.5)$$

where $G_{ij} = \frac{e^2 M}{h} \sum_{\sigma,\sigma'} T_{ij}^{\sigma\sigma'}$ is the conductance between terminal j and i, M is the number of edge modes, $T_{ij}^{\sigma\sigma'}$ is the transmission probability for an electron from contact j to contact i with initial spin σ' to final spin σ and V_i is the potential bias at contact i. The conduction matrix for six terminal QSH sample relating the currents to the voltages is -

$$
G = -\frac{e^2}{h}
\begin{pmatrix}
-2M & T_2 & R_2 & 0 & 0 & M \\
T_2 & -2T_2 & T_2 & 0 & 0 & 0 \\
R_2 & T_2 & -2M & M & 0 & 0 \\
0 & 0 & M & -2M & M & 0 \\
0 & 0 & 0 & M & -2M & M \\
M & 0 & 0 & 0 & M & -2M
\end{pmatrix},
\tag{2.6}
$$

where the diagonal elements $G_{ii} = \sum_{j,j\neq i} G_{ji} = \frac{e^2 M}{h} \sum_{j=1, j\neq i, \sigma, \sigma'}^6 T_{ji}^{\sigma\sigma'}$. The off-diagonal elements $(i,j)^{th}$ element which is the conductance between contact j and i is given by $\sum_{\sigma,\sigma'} T_{ij}^{\sigma\sigma'}$. To understand the effect of single disordered contact we first look at the diagonal element $G_{11} = \sum_{j=2}^6 G_{j1}$ where $G_{j1} = \frac{e^2 M}{h}(T_{j1}^{\uparrow\uparrow} + T_{j1}^{\uparrow\downarrow} + T_{j1}^{\downarrow\uparrow} + T_{j1}^{\downarrow\downarrow}), j = 2,3,4,5,6$. From Fig. 2.2(b), we see that an spin up electron after coming out of contact 1 can either transmit to contact 2 with probability T_2, thus $T_{21}^{\uparrow\uparrow} = T_2 = 1 - D_2$ or can reflect from contact 2 with probability $R_2 = D_2$ and then enter contact 3 thus $T_{31}^{\uparrow\uparrow} = R_2 = D_2$ while a spin down electron can directly transmit from contact 1 to contact 6 with transmission probability of unity, thus $T_{61}^{\uparrow\uparrow} = 1$. Thus G_{11} in Eq. (2.5) reduces to $\frac{e^2}{h}M(T_{21}^{\uparrow\uparrow} + T_{31}^{\uparrow\uparrow} + T_{61}^{\downarrow\downarrow})$ (since rest of the transmission probabilities from contact 1 to other contacts are zero, see Fig. 2.2(b)). So, $G_{11} = \frac{e^2}{h}M(T_2 + R_2 + 1) = 2\frac{e^2}{h}M$. Similarly, rest of the elements of the conduction matrix G can be derived. Substituting $I_2, I_3, I_5,$ and $I_6 = 0$ (since contacts $2,3,5,6$ are voltage probes) and choosing reference potential $V_4 = 0$, we derive $V_5 = V_6/2 = V_1/3$. So, the Hall resistance $R_H = R_{14,26} = \frac{h}{2e^2M}\frac{D_2}{3+2D_2}$, longitudinal resistance $R_L = R_{14,23} = \frac{h}{2e^2M}\frac{3}{3+2D_2}$, 2-terminal resistance $R_{2T} = R_{14,14} = \frac{h}{2e^2M}\frac{9+3D_2}{3+2D_2}$. Further, for the non-local measurement

currents I_3, I_4, I_5 and $I_6 = 0$ as these are voltage probes and choosing reference potential $V_2 = 0$ we get the non-local resistance $R_{NL} = R_{12,54} = \frac{h}{2e^2M} \frac{1}{6+4D_2}$. Thus all of the calculated resistances Hall , longitudinal, 2-terminal and non-local lose their quantization and are dependent on disorder. Notice that these quantities are all influenced by disorder in contrast to the QH case in which they are immune to disorder.

2.2.4 Quantum spin Hall sample with all disordered contacts

The case for all disordered contacts is an extension of the case of single disordered contact as represented in Fig. 2.2(c). Herein we consider all the contacts to be disordered in general. The current voltage relations can be derived from the conductance matrix below:

$$
G = -\frac{e^2M}{h}
\begin{pmatrix}
-T_{11} & T_{12} & T_{13} & T_{14} & T_{15} & T_{16} \\
T_{21} & -T_{22} & T_{23} & T_{24} & T_{25} & T_{26} \\
T_{31} & T_{32} & -T_{33} & T_{34} & T_{35} & T_{36} \\
T_{41} & T_{42} & T_{43} & -T_{44} & T_{45} & T_{46} \\
T_{51} & T_{52} & T_{53} & T_{54} & -T_{55} & T_{56} \\
T_{61} & T_{62} & T_{63} & T_{64} & T_{65} & -T_{66}
\end{pmatrix}.
\tag{2.7}
$$

$2M$ represents the total number of modes. In setup as shown in Fig. 2.2(c), $M = 1$ to avoid clutter and only a single pair of spin up and spin down modes are shown. In the above matrix T_{15}-the total transmission probability from contact 5 to 1, in contrast to that for QH case (Eq. (2.4)) can be written explicitly as

$$
T_{15} = \frac{[(1-D_5)D_6(1-D_1) + (1-D_5)D_4D_3D_2(1-D_1)]M}{1 - D_1D_2D_3D_4D_5D_6}.
\tag{2.8}
$$

The reason being there are two spin polarized edge modes which are moving in opposite directions, the spin up polarized edge mode contributes to T_{15} via the first term while the

spin down polarized edge mode contributes via the second term. So the total probability per mode for transmission from contact 5 to 1 is as defined above in Eq. (2.8). Similarly all other transmission probabilities occurring in the above matrix can be explained. Substituting I_2, I_3, I_5, and $I_6 = 0$ as these are voltage probes and choosing reference potential $V_4 = 0$, we solve the above matrix and calculate the Hall, longitudinal and 2-terminal resistances. Further, for the non-local measurement currents I_3, I_4, I_5 and $I_6 = 0$ as these are voltage probes and choosing reference potential $V_2 = 0$ we get the non-local resistance R_{NL}. Since the expressions for these are quite large we write down the expressions for $D_1 = D_2 = D_3 = D_u$, $D_4 = D_5 = D_6 = D_l$ for Hall resistance and for equally disordered contacts $D_i = D$ ($i = 1, 2, 3, 4, 5, 6$) for rest of the resistances and also analyse them via plots as in Figs. 2.3(a, b).

$$
\begin{aligned}
R_H &= \frac{(D_u - D_l)(1 + 2D_u - D_l(2 + D_u))}{6(1 + D_l)(1 + D_u)(1 - D_l D_u)} = 0 \quad \text{(when } D_u = D_l\text{)},\\
R_{2T} &= \frac{h}{2e^2}\frac{(3 - D(2 - 3D))}{2(1 - D^2)}, \quad R_L = 3R_{NL} = \frac{h}{2e^2}\frac{(1 - D)}{2(1 + D)}.
\end{aligned}
\tag{2.9}
$$

As previously noted for QH case in section 2.2.2, we see that the difference between QH and QSH is also quite stark when it comes to more than one disordered contact too. In QH case, while the Hall and longitudinal resistances do not deviate from ideal quantized values for QSH case these deviate from their ideal quantized values. In fact for a particular choice as in Fig. 2.3(a), the Hall current for spin Hall edge modes not only is finite it changes sign indicating the complete breakdown of the quantum spin Hall effect via disorder. Further in Fig. 2.3(b), we see while non-local resistance for QH case is quantized the same for QSH case deviates from its ideal quantized value indicating that QSH edge modes are much more fragile than QH edge modes. The local 2-terminal resistance in both case is affected by disorder as shown in Fig. 2.3(b).
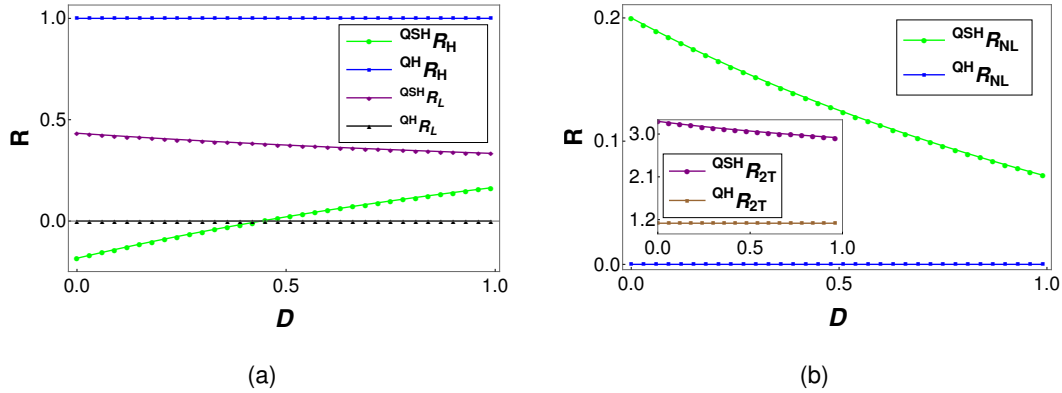
Figure 2.3: (a) Comparison of Hall and longitudinal resistances (in units of $h/2e^2$) in QH and QSH samples with parameters: $D_1 = D_6 = 0.2$, $D_2 = D_3 = D_4 = 0.5$, $D_5 = D$, (b) Comparison of local and non-local resistance in QH and QSH samples with same parameters as in (a).

2.3 Effect of inelastic scattering

Inelastic scattering is not restricted to contacts but is all pervasive and comes into picture when the sample length exceeds the inelastic scattering length. Furthermore, inelastic scattering may be accompanied by spin-flip scattering too. In the cases we consider in this chapter, the length of the sample for single disordered contact in both QH (section 2.2.1) and QSH (section 2.2.3) cases are less than inelastic scattering length. For all disordered contacts in both QH (section 2.2.2) and QSH (section 2.2.4) cases the length of sample is less than inelastic scattering length. However, for all disordered contacts in both QH and QSH cases the length of the sample may be less than inelastic scattering length and that we are considering below. In this thesis the term "probe" and "contact" mean the same- a metallic reservoir.

2.3.1 Quantum Hall sample with both disordered contacts and inelastic scattering

The case of QH edge modes in presence of all disordered contacts and with inelastic scattering included has been dealt with before in Refs. [10, 12]. We can look at Fig. 2.4(a)

where we consider the length between disordered contacts is larger than inelastic scattering length. On the occasion of an inelastic scattering event happening the edge states originating from different contacts with different energies are equilibrated to a common potential. In Fig. 2.4(a), one can see that electrons coming from contacts 1 and 6 are equilibrated to potential V_1'. If as before contacts 1 and 4 are chosen to be the current contacts then no current flows into the other voltage probe contacts. Lets say a current $\frac{e^2}{h}T_2V_1'$ enters contact 2 while current $\frac{e^2}{h}T_2V_2$ leaves contact 2, and since contact 2 is a voltage probe net current has to be zero, implying $V_2 = V_1'$. The same thing happens at contact 3 and along the lower edge where states are equilibrated to V_4'.

Now we write the current voltage relations in continuous fashion, eschewing our earlier method of writing it in matrix form to avoid clutter as there are not only the 6 potentials $V_1 - V_6$, we also have the equilibrated potentials $V_1' - V_6'$.

$$
\begin{aligned}
I_1 &= \frac{2e^2}{h}T_1(V_1 - V_6'), \\
I_i &= \frac{2e^2}{h}T_i(V_i - V_{i-1}'), \text{ for } i = 2,3,4,5,6.
\end{aligned}
\tag{2.10}
$$

By putting the condition of net current into voltage probe contacts $2,3,4,5$ to be zero we get the following relations between the contact potentials: $V_2 = V_1', V_3 = V_2', V_5 = V_4',$ and $V_6 = V_5'$. Further, due to the equilibration the net current just out of contact 2 is the sum $\frac{2e^2}{h}(T_2V_2 + R_2V_1')$ and this should be equal to $\frac{2e^2}{h}MV_2'$ which is the equilibrated potential due to inelastic scattering at contact 3. Thus, $\frac{2e^2}{h}(T_2V_2 + R_2V_2) = \frac{2e^2}{h}MV_2'$, or $V_2 = V_2'$, as $T_2 + R_2 = M$ the total no. of edge modes in the system. Thus all the upper edges are equilibrated to same potential $V_1' = V_2 = V_2' = V_3 = V_3'$.

Similarly for the equilibrated potentials at the lower end we get $V_4' = V_5 = V_5' = V_6 = V_6'$. So, the Hall resistance $R_H = R_{14,26} = \frac{h}{2e^2}\frac{1}{M}$, longitudinal resistance $R_L = R_{14,23} = 0$, 2-terminal resistance $R_{2T} = R_{14,14} = \frac{h}{2e^2}\frac{M^2 - R_1R_4}{MT_1T_4}$. Further, for the non-local measurement currents
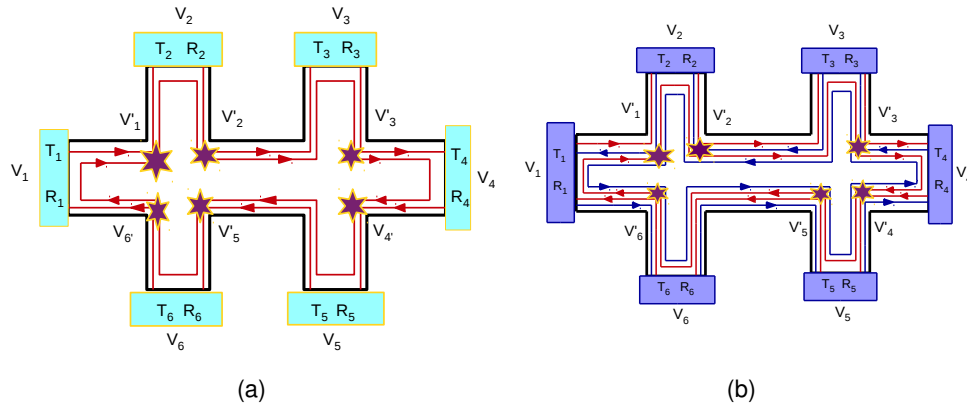
Figure 2.4: (a) QH system, (b) QSH system: with all contacts disordered and inelastic scattering. Violet color starry blobs indicate equilibration of the edge modes via inelastic scattering.

I_3, I_4, I_5 and $I_6 = 0$ as these are voltage probes and choosing reference potential $V_2 = 0$ we get $V_3 = V_3' = V_4 = V_4' = V_5 = V_5' = V_6 = 0$ and the non-local resistance $R_{NL} = R_{12,54} = 0$. The quantum Hall edge mode conductance apart from the 2-terminal case remains quantized even when all contacts are disordered with inelastic scattering included.

2.3.2   Quantum spin Hall sample with both disordered contacts and inelastic scattering

The case of QSH edge modes in presence of completely disordered contacts and with inelastic scattering included can be understood by extending the approach of section 2.3.1 to QSH edge modes. We can look at Fig. 2.4(b) where we consider the length between disordered contacts is larger than inelastic scattering length. On the occasion of an inelastic scattering event happening the edge states originating from different contacts with different energies are equilibrated to a common potential as in QH case. In Fig. 2.4(b), one can see that electrons coming from contacts 1 and 6 are equilibrated to potential V_1'. If as before contacts 1 and 4 are chosen to be the current contacts then no current flows into the other voltage probe contacts. Lets say a current $\frac{e^2}{h}(T_2 V_1' + T_2 V_2')$ enters contact 2, the first part $\frac{e^2}{h} T_2 V_1'$ is the spin-up component while the second part $\frac{e^2}{h} T_2 V_2'$ is the spin-down component

moving in exactly the opposite direction. Similarly, the current $\frac{e^2}{h}2T_2V_2$ leaves contact 2 and

since contact 2 is a voltage probe net current has to be zero, implying $V_2 = (V_1' + V_2')/2$.

The same thing happens at contact 3 and along the lower edge.

Now we write the current voltage relations in continuous fashion, eschewing our earlier

method of writing it in matrix form to avoid clutter as there are not only the 6 potentials

$V_1 - V_6$, we also have the equilibrated potentials $V_1' - V_6'$.

$$
\begin{aligned}
I_1 &= \frac{e^2}{h}T_1(2V_1 - V_1' - V_6'), \\
I_i &= \frac{e^2}{h}T_i(2V_i - V_{i-1}' - V_i'), \text{ for } i = 2,3,4,5,6.
\end{aligned}
\tag{2.11}
$$

By putting the condition of net current into voltage probe contacts $2,3,4,5$ to be zero we get

the following relations between contact potentials: $V_2 = (V_1' + V_2')/2, V_3 = (V_2' + V_3')/2, V_5 =$

$(V_4' + V_5')/2$ and $V_6 = (V_5' + V_1')/2$. Further, due to the equilibration the net spin-up current

out of contact 2 is the sum $\frac{e^2}{h}(T_2V_2 + R_2V_1')$ and the net spin-down current out of contact 3

is the sum $\frac{e^2}{h}(T_3V_3 + R_3V_3')$ and this should be equal to $\frac{e^2}{h}2MV_2'$ which is the net current

out of V_2'- the equilibrated potential due to inelastic scattering between contacts 2 and

3. Similarly, we can write the net spin polarized currents into and out of the equilibrated

potentials. Since there are 6 equilibrated potentials we will have six such equations. The

origin of the first equation has already been explained above herein below we list all of

them:

$$
\begin{aligned}
\frac{e^2}{h}(T_iV_i + R_iV_{i-1}') + \frac{e^2}{h}(T_{i+1}V_{i+1} + R_{i+1}V_{i+1}') &= \frac{e^2}{h}2MV_i', \text{ for } i = 2,3,4,5, \\
\frac{e^2}{h}(T_1V_1 + R_1V_6') + \frac{e^2}{h}(T_2V_2 + R_2V_2') &= \frac{e^2}{h}2MV_1', \\
\frac{e^2}{h}(T_1V_1 + R_1V_6') + \frac{e^2}{h}(T_6V_6 + R_6V_5') &= \frac{e^2}{h}2MV_6'.
\end{aligned}
\tag{2.12}
$$

Solving the above six equations, gives the equilibrated potentials $V_i', i = 1,..6$ in terms of
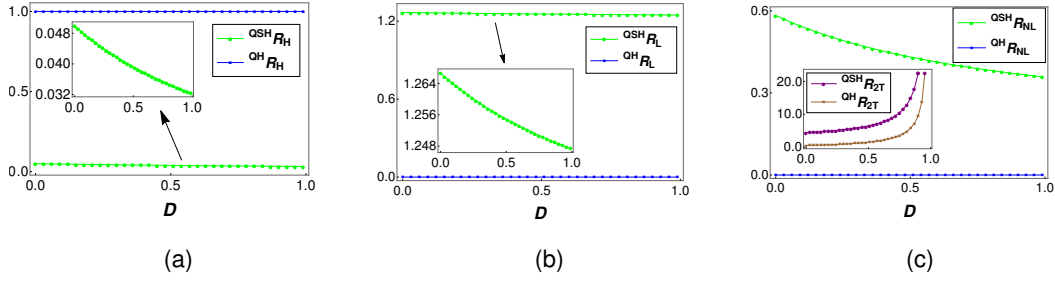
Figure 2.5: QH and QSH samples with all disordered contacts and inelastic scattering. (a) Hall, (b) longitudinal, (c) 2-terminal and non-local resistances (in units of $h/2e^2$) with parameters $D_l = 0.8$, $D_u = 0.5$, $D_c = D$, $M = 1$.

the contact potentials $V_i, i = 1, ..6$. Substituting the obtained $V_i', i = 1, ..6$ in Eq. (2.11), we can derive the necessary resistances. For the non-local measurement currents I_3, I_4, I_5 and $I_6 = 0$ as these are voltage probes and choosing reference potential $V_2 = 0$ we get the non-local resistance R_{NL} as below. We specially consider the case wherein $D_c = D_1 = D_4$, $D_u = D_2 = D_3$, $D_l = D_5 = D_6$ and we have-

$$
\begin{aligned}
R_H &= R_{14,26} = \frac{h}{2e^2 M} \frac{(D_l - D_u)}{3 + 2D_l + D_u(2 + D_l) + D_c(2 + D_l + D_u)}, \\
R_L &= R_{14,23} = \frac{h}{e^2 M} \frac{(3 + 2D_c + D_l)}{3 + 2D_l + D_u(2 + D_l) + D_c(2 + D_l + D_u)}, \\
R_{2T} &= R_{14,14} = \frac{h}{e^2 M} \frac{(4D_c^2 - (3 + D_l)(3 + D_u))}{(-1 + D_c)(3 + 2D_l + D_u(2 + D_l) + D_c(2 + D_l + D_u))}, \\
R_{NL} &= R_{12,54} = \frac{h}{4e^2 M} \frac{(2 + D_c + D_l)(2 + D_c + D_u)}{(1 + D_c)(3 + 2D_u + D_l(2 + D_u) + D_c(2 + D_l + D_u))}.
\end{aligned} \tag{2.13}
$$

Here D_c denotes disorder in current contacts while $D_u(D_l)$ represent disorder in contacts at upper(lower) edge. When disorder in contacts at upper and lower edge are unequal one sees finite charge Hall conductance and thus pure QSH effect vanishes. This is unlike what happens in this case for QH edge modes not only quantum Hall conductance is resilient to disorder and inelastic scattering it retains its quantization and the longitudinal resistance a measure of voltage drop across the sample remains zero. So unlike in case of QH edge modes where inelastic scattering restores Hall quantization in presence of all disordered

contacts regardless of whether their strengths are equal or not, in case of QSH inelastic scattering also fails to restore the pure QSH effect in presence of unequal disorder. In Figs. 2.5(a, b) we plot the Longitudinal and Hall resistances for QH and QSH cases. One can see from the insets how the QSH case is dependent on disorder while QH case remains untroubled by disorder. The disorder dependent behaviour of the nonlocal QSH resistance comes out clearly in Fig. 2.5 (c). For the disorder parameters considered, the nonlocal resistance monotonically decreases, while the local resistance, on the other hand increases with increasing disorder. In Fig. 2.5(c) we also see that while for QSH case the non-local resistance loses its quantization, QH case remains quantized with vanishing non-local resistance.

2.4   Generalization to N contacts

Till now we have only discussed six terminal QH and QSH samples in presence of disorder in section 2.2 and in presence of both disorder and inelastic scattering in section 2.3. To study the effects of number of contacts on the Hall, longitudinal, 2-terminal and non-local resistances we extend the previous discussions to N terminals in both QH and QSH samples. First we consider the case of ideal contacts for QH and QSH samples and finally we include disorder and inelastic scattering to study its effect on the N terminal QH and QSH samples.

2.4.1   N terminal quantum Hall sample with ideal contacts

The ideal case is represented in Fig. 2.6(a). The current voltage relations can be derived from the current voltage equation:
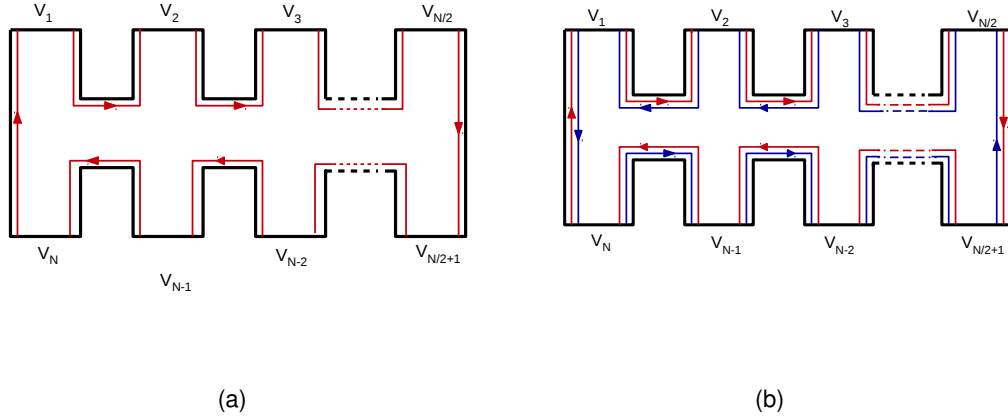
Figure 2.6: (a) N terminal QH bar with ideal contacts, (b) N terminal QSH bar with ideal contacts.

$$
\begin{pmatrix} I_1 \\ I_2 \\ .. \\ I_{k-1} \\ I_k \\ I_{k+1} \\ .. \\ I_{N-1} \\ I_N \end{pmatrix} = -\frac{2e^2 M}{h} \begin{pmatrix} -1 & 0 & .. & 0 & 0 & 0 & .. & 0 & 1 \\ 1 & -1 & .. & 0 & 0 & 0 & .. & 0 & 0 \\ .. & .. & .. & .. & .. & .. & .. & .. & .. \\ 0 & 0 & .. & -1 & 0 & 0 & .. & 0 & 0 \\ 0 & 0 & .. & 1 & -1 & 0 & .. & 0 & 0 \\ 0 & 0 & .. & 0 & 1 & -1 & .. & 0 & 0 \\ .. & .. & .. & .. & .. & .. & .. & .. & .. \\ 0 & 0 & .. & 0 & 0 & 0 & .. & -1 & 0 \\ 0 & 0 & .. & 0 & 0 & 0 & .. & 1 & -1 \end{pmatrix} \begin{pmatrix} V_1 \\ V_2 \\ .. \\ V_{k-1} \\ V_k \\ V_{k+1} \\ .. \\ V_{N-1} \\ V_N \end{pmatrix},
$$

(2.14)

where the diagonal elements $G_{ii} = \sum_{j=1,j\neq i}^{N} G_{ji} = \frac{2e^2}{h}\sum_{j=1,j\neq i}^{N} T_{ji}$ and the non-diagonal elements $G_{ij} = \frac{2e^2}{h} T_{ij}$ (for $j \neq i$). The diagonal element, for example, $G_{11} = \frac{2e^2}{h}\sum_{j=1,j\neq i}^{N} T_{j1}$. M represents the total no. of modes while a factor 2 is introduced due to the spin degeneracy of the electrons. In setup as shown in Fig. 2.6(a), $M = 1$ to avoid clutter. From Fig. 2.6(a) we see that there is transmission of electrons only between the adjacent contacts in clockwise direction, i.e., transmission probability for an electron from contact i to $i+1$ (for

$i = 1 - (N-1)$ and $T_{1N} = 1$) is unity, while rest of the transmission probabilities are zero. The diagonal conductance G_{11} reduces to $\frac{2e^2}{h} M T_{21} = \frac{2e^2}{h} M$ (since $T_{21} = 1$). Similarly rest of the probabilities are derived. Substituting I_2, I_3, I_{k-1} and $I_{k+1}, ..I_N = 0$ and choosing reference potential $V_N = 0$, we derive $V_1 = V_2 = ... = V_{k-1}$ and $V_k = ... = V_{N-1} = V_N = 0$. So, the Hall resistance $R_H = R_{1k,ij} = \frac{h}{2e^2} \frac{1}{M}$, with $1 \leq i < k \leq j \leq N$, then longitudinal resistance $R_L = R_{1k,ij} = 0$, with $1 \leq i, j < k$ and two terminal resistance $R_{2T} = R_{1k,1k} = \frac{h}{2e^2} \frac{1}{M}$ with $1 \leq i, j < N$. Further, for the non-local measurement currents $I_3, I_4, ..., I_k, .., I_{N-1}$ and $I_N = 0$ as these are voltage probes and choosing reference potential $V_2 = 0$ we get $V_3 = V_4 = ... = V_k = ... = V_N = 0$ and the non-local resistance $R_{NL} = R_{12,ij} = 0$ with $2 < j < i \leq N$. The case of a single disordered probe as was done for 6 terminal case in section 2.2.3 can be easily calculated and the resistances-Hall, Longitudinal and two terminal are identical to the ideal case with disorder having no impact. Importantly the quantization of Hall resistance is independent of any asymmetry in number of contacts at upper and lower edge while as we will see below in case of QSH edge modes this is not the case.

2.4.2 N terminal quantum spin Hall sample with ideal contacts

The ideal case is represented in Fig. 2.6(b). The current voltage relations can be derived from the current voltage equation:

$$
\begin{pmatrix} I_1 \\ I_2 \\ .. \\ I_{k-1} \\ I_k \\ I_{k+1} \\ .. \\ I_{N-1} \\ I_N \end{pmatrix} = -\frac{e^2 M}{h}
\begin{pmatrix}
-2 & 1 & .. & 0 & 0 & 0 & .. & 0 & 1 \\
1 & -2 & .. & 0 & 0 & 0 & .. & 0 & 0 \\
.. & .. & .. & .. & .. & .. & .. & .. & .. \\
0 & 0 & .. & -2 & 1 & 0 & .. & 0 & 0 \\
0 & 0 & .. & 1 & -2 & 1 & .. & 0 & 0 \\
0 & 0 & .. & 0 & 1 & -2 & .. & 0 & 0 \\
.. & .. & .. & .. & .. & .. & .. & .. & .. \\
0 & 0 & .. & 0 & 0 & 0 & .. & -2 & 1 \\
1 & 0 & .. & 0 & 0 & 0 & .. & 1 & -2
\end{pmatrix}
\begin{pmatrix} V_1 \\ V_2 \\ .. \\ V_{k-1} \\ V_k \\ V_{k+1} \\ .. \\ V_{N-1} \\ V_N \end{pmatrix} ,
$$

$$(2.15)$$

where the diagonal elements $G_{ii} = \sum_{j=1, j \neq i}^{N} G_{ji}$ and the off-diagonal elements, for example, $(1,2)^{th}$ element which is the conductance between contact 2 and 1 is given by $\sum_{\sigma,\sigma'} T_{12}^{\sigma\sigma'}$, similarly for the other off-diagonal elements. The diagonal element $G_{11} = \sum_{j=2}^{N} G_{j1}$ where $G_{j1} = \frac{2e^2 M}{h}(T_{j1}^{\uparrow\uparrow} + T_{j1}^{\uparrow\downarrow} + T_{j1}^{\downarrow\uparrow} + T_{j1}^{\downarrow\downarrow}), j = 2 - N$. From Fig. 2.6(b) we see that there is transmission of edge modes only between the adjacent contacts (as the contacts are reflection less), say for example, for spin up edge mode from contact i to $i+1$ the transmission is unity (for $i = 1 - (N-1)$ and $T_{N1}^{\uparrow\uparrow} = 1$) while for spin down edge mode from contact i to $i-1$ transmission is unity (for $i = 2 - N$ and $T_{N1}^{\downarrow\downarrow} = 1$), rest of the transmission probabilities are zero. Thus $(1,1)^{th}$ element of the conduction matrix G reduces to $\frac{e^2}{h}M(T_{21}^{\uparrow\uparrow} + T_{N1}^{\downarrow\downarrow}) = \frac{2e^2}{h}M$ (Since the transmission probabilities $T_{21}^{\uparrow\uparrow} = T_{N1}^{\downarrow\downarrow} = 1$). Substituting I_2, I_3, I_{k-1} and $I_{k+1}, ..I_N = 0$ and choosing reference potential $V_N = 0$, we derive $V_i = (i-1)V_2 - (i-2)V_1$, where $1 \leq i \leq k$ with $V_2 = \frac{2k-N-2}{k-1}V_1$. Similarly, $V_i = -(N-i)V_1$, where $k \leq i \leq N$.

So, the Hall resistance-

$$R_H = R_{1k,ij} \quad = \quad \frac{h}{e^2 M} \frac{(i-1)(2k-N-2)}{N}, \text{with} 1 \leq i \leq k, \tag{2.16}$$

longitudinal resistance-

$$R_L = R_{1k,ij} \quad = \quad \frac{h}{e^2 M} (\frac{j-i}{N})(1-k+N), \text{with } 1 \leq i,j < k \tag{2.17}$$

and two terminal resistance $R_{2T} = R_{1k,1k} = \frac{h}{e^2 M} \frac{k-1}{N}(1-k+N)$, with $1 \leq i,j \leq N$. Further, for the non-local measurement currents $I_3, I_4, ..., I_k, .., I_{N-1}$ and $I_N = 0$ as these are voltage probes and choosing reference potential $V_2 = 0$ we get non-local resistance $R_{NL} = R_{12,ij}$-

$$R_{NL} = R_{12,ij} = \frac{h}{e^2 M}(\frac{i-j}{N}), \text{with } 2 \leq j < i \leq N. \tag{2.18}$$

Surprisingly, a finite charge Hall current flows even when there is no disorder. It arises only due to asymmetry between number of contacts at upper and lower edge. This number asymmetry has no role as far as QH edge modes are concerned.

2.4.3 Effect of inelastic scattering

We have already shown in section 2.3.1 for QH and in section 2.3.2 for QSH that in presence of inelastic scattering for both QH and QSH samples (six terminal) there are no multiple paths from one contact to another, thus the resistances remain quantized for QH (except 2-terminal resistance) while they lose their quantization in QSH. So next we discuss the N terminal generalization for QH and then for QSH samples.
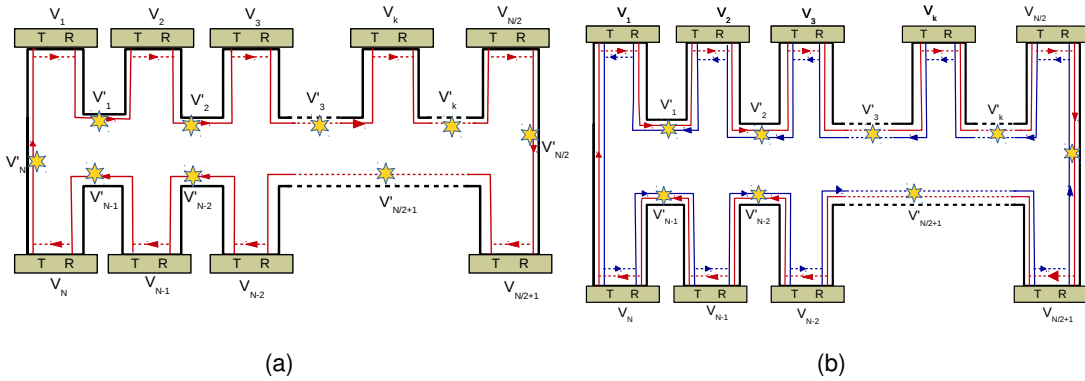
Figure 2.7: N terminal (a) QH sample, (b) QSH sample with all equally disordered contacts and inelastic scattering.

2.4.3.1 Quantum Hall sample with N disordered contacts and inelastic scattering

The completely disordered case with inelastic scattering is represented in Fig. 2.7(a) for N terminal QH sample. Here all the contacts are disordered, i.e., $D_i \neq D_j, i, j = 1...N$ and $i \neq j$. It does not matter whether the contacts are equally disordered or not. The disorder strengths D_i's can be written in terms of the T_i's- the number of transmitted edge modes. So, $T_i = (1 - D_i)$ and $R_i = D_i$. We can look at the Fig. 2.7(a) where we consider that the length between disordered contacts is larger than inelastic scattering length. On the occasion of an inelastic scattering event happening the edge states originating from different contacts with different energies are equilibrated to a common potential. In Fig. 2.7(a), one can see that electrons coming from contact 1 and N are equilibrated to potential V_1'. If as before contacts 1 and k are chosen to be the current contacts then no current flows into the other voltage probe contacts. Lets say a current $\frac{2e^2}{h}MT_2V_1'$ enters contact 2 while current $\frac{2e^2}{h}MT_2V_2$ leaves contact 2, and since contact 2 is a voltage probe net current has to be zero, implying $V_2 = V_1'$. The same thing happens at contact 3 and along the lower edge where states are equilibrated to V_k'. Now we write the current voltage relations in continuous fashion, eschewing our earlier method of writing it in matrix form to avoid clutter as there

are not only the N potentials $V_1 - V_N$, we also have the equilibrated potentials $V_1' - V_N'$.

$$
\begin{aligned}
I_1 &= \frac{2e^2}{h} T_1 (V_1 - V_N'), \\
I_k &= \frac{2e^2}{h} T_k (V_k - V_{k-1}'), \quad \text{for } k = 2 - N.
\end{aligned}
$$
(2.19)

By putting the condition of net current into voltage probe contacts $2, 3, ... k-1, k+1 ..., N$ to be zero we get the following relations between the contact potentials: $V_2 = V_1', V_3 = V_2', ... V_{k-1} = V_{k-2}',$ and $V_{k+1} = V_k', ..., V_N = V_{N-1}'$. Further, due to the equilibration the net current just out of contact 2 is the sum $\frac{2e^2}{h} M (T_2 V_2 + R_2 V_1')$ and this should be equal to $\frac{2e^2}{h} M V_2'$ which is the equilibrated potential due to inelastic scattering between contacts 2 and 3. Thus, $\frac{2e^2}{h} M (T_2 V_2 + R_2 V_2) = \frac{2e^2}{h} M V_2'$, or $V_2 = V_2'$, as $T_2 + R_2 = 1$. Thus all the upper edges are equilibrated to same potential $V_1' = V_2 = V_2' = V_3 = V_3' = V_1 = ... = V_{k-1} = V_{k-1}'$. Similarly for the equilibrated potentials at the lower edge we get $V_k' = V_{k+1} = V_{k+1}' = ... = V_N = V_N' = 0$, as $V_N = 0$. So, the Hall resistance $R_H = R_{1k,ij} = \frac{h}{2e^2} \frac{1}{M}$ with $1 < i < k < j \leq N$, longitudinal resistance $R_L = R_{1k,ij} = 0$ with $1 < i, j < k$ and two terminal resistance $R_{2T} = R_{1k,1k} = \frac{h}{2e^2} \frac{M^2 - R_1 R_k}{M T_1 T_k}$. Further, for the non-local measurement currents $I_3, I_4, ... I_k, ..., I_N = 0$ as these are voltage probes and choosing reference potential $V_2 = 0$ we get the non-local resistance $R_{NL} = R_{12,ij} = 0$ with $2 < j < i < N$. Thus sample geometry has no role in this case.

2.4.3.2   Quantum spin Hall sample with N disordered contacts and inelastic scattering

The completely disordered case with inelastic scattering is represented in Fig. 2.7(b). Here both the voltage as well as current probe contacts are disordered, i.e., $D_i = D_j, i, j = 1...N$. To simplify the calculation- all the contacts are considered equally disordered. The disorder strengths D's can be written in terms of the T's- the transmission probabilities

of transmitted edge modes. So, $T_i = T = (1 - D_i) = (1 - D)$ and $R_i = R = D_i = D$. In Fig. 2.7(b), we consider the length between disordered contacts to be larger than the inelastic scattering length. On the occasion of an inelastic scattering event happening the edge states originating from different contacts with different energies are equilibrated to a common potential. In Fig. 2.7(b), one can see that electrons coming from contact 1 and N are equilibrated to potential V_1'. If as before contacts 1 and k are chosen to be the current contacts then no current flows into the other voltage probe contacts. Lets say a current $\frac{e^2}{h} M(T_2 V_1' + T_2 V_2')$ enters contact 2, the first part $\frac{e^2}{h} M T_2 V_1'$ is the spin-up component while the second part $\frac{e^2}{h} M T_2 V_2'$ is the spin-down component moving in exactly the opposite direction. Similarly, the current $\frac{e^2}{h} M 2 T_2 V_2$ leaves contact 2, and since contact 2 is a voltage probe net current has to be zero, implying $V_2 = (V_1' + V_2')/2$. The same thing happens at contacts $3, 4..k - 1$ and along the lower edge.

Now we write the current voltage relations in continuous fashion, and as before eschewing our earlier method of writing it in matrix form to avoid clutter as there are not only the N potentials $V_1 - V_N$, we also have the equilibrated potentials $V_1' - V_N'$.

$$
\begin{aligned}
I_1 &= \frac{e^2}{h}(2TV_1 - T(V_1' + V_N')), \\
I_k &= \frac{e^2}{h}(2TV_k - T(V_{k-1}' + V_k')), \quad \text{for } k = 2 - N.
\end{aligned}
\tag{2.20}
$$

Further, due to the equilibration the net current just out of contact 2 is the sum $\frac{e^2}{h} M(TV_2 + RV_1' + RV_3' + TV_3)$ and this should be equal to $\frac{e^2}{h} 2MV_2'$ which is the equilibrated potential due to inelastic scattering between contacts 2 and 3. Similarly for the net current just out of kth contact is the sum $\frac{e^2}{h} M(TV_k + RV_{k-1}' + RV_{k+1}' + TV_{k+1})$ and this should be equal to $\frac{e^2}{h} 2MV_k'$ which is the equilibrated potential due to inelastic scattering between contacts k and $k + 1$. By putting the condition of net current into voltage probe contacts $2, 3, ...k - 1, k + 1..., N$ to be zero we get the following relations between the contact potentials:

$V_i' = (i-1)V_2' - (i-2)V_1'$ with $2 \le i \le (k-1)$ and $V_i' = -(2N - 2i - 1)V_N'$ with $k \le i \le N$.

So, the Hall resistance with $j = N - i + 2$ is given as-

$$R_H = R_{1k,ij} = \frac{h}{e^2 M} \frac{2(i-1)(2k - N - 2)}{(1+D)N} \text{ with } 1 < i < k < j \le N$$

and if we consider $k = N/2 + 1$, i.e., a symmetric sample (with equal no of contacts at the lower and upper edge) then $R_H = 0$. So sample geometry (number asymmetry between contacts at upper and lower edge) has a direct bearing on whether one sees a pure spin Hall effect or it is contaminated by a charge current. Further in symmetric case although there is no charge Hall current- it is seen only when all the contacts are equally disordered, i.e., quantum spin Hall effect is restored. If on the other hand contacts are not equally disordered as seen in 6 terminal case in section 2.3.2 $R_H \ne 0$ even in presence of inelastic scattering. So unlike in case of quantum Hall edge modes where inelastic scattering restores Hall quantization in presence of all disordered contacts regardless of their strengths are equal or not, in case of quantum spin Hall inelastic scattering also fails to restore the pure quantum spin Hall effect in presence of unequal disorder.

Next, longitudinal resistance-

$$R_L = R_{1k,ij} = \frac{h}{e^2 M} \frac{(j-i)2(1 - k + N)}{(1+D)N} \text{ with } 2 < i, j < k$$

and finally the two terminal resistance

$$R_{2T} = R_{1k,1k} = -\frac{h}{e^2 M} \frac{2[(k-1)(k - N - 1) - D(1 + k^2 + 2N - k(N+2))]}{(1-D)(1+D)N}.$$

Further, for the non-local measurement currents $I_3, I_4, ... I_k, ..., I_N = 0$ as these are voltage probes and choosing reference potential $V_2 = 0$ we get the non-local resistance $R_{NL} = R_{12,ij} = \frac{h}{e^2 M} \frac{2(i-j)}{(1+D)N}$, with $3 \le i, j \le N$. The N-terminal results reduce to the 6 terminal

case of equal number of probes at the upper and lower edge (symmetric case) in all cases confirming the results obtained as before. Further they shed light on the asymmetric case wherein probes on upper and lower edge are unequal. Asymmetry has no role as far as quantum Hall edge modes are concerned but in case of quantum spin Hall edge modes they have a non-trivial role, even destroying the pure quantum spin Hall effect, regardless of whether there is disorder or not.

2.5 Comparison of QH edge mode with QSH edge mode in presence of disorder and/or inelastic scattering

The robustness of QH and QSH edge modes are compared in Tables 2.1 and 2.2 for a six terminal QH or QSH sample in presence of disorder and inelastic scattering. In QH sample for ideal case the Hall resistance is quantized to $h/(2e^2)M$, longitudinal, non-local resistances are zero and 2-terminal resistance is quantized to $h/(2e^2)M$, see Tables 2.1, 2.2. In QSH sample for ideal case the Hall resistance is zero, longitudinal, non-local and 2-terminal resistances are quantized to $h/(2e^2)M$, $h/(6e^2)M$ and $3h/(2e^2)M$ respectively. In presence of single disordered contact it can be seen that while in QH sample R_H, R_L, R_{NL} and R_{2T} all remain quantized and unaffected by the disorder, in QSH sample Hall resistance is finite ($hD_2/(2e^2)M(3+D_2)$), longitudinal resistance is $3h/(2e^2)M(3+D_2)$, non-local resistance is $h/(2e^2)M(3+D_2)$ and finally 2-terminal resistance is $3h(3+D_2)/(2e^2)M(3+D_2)$. Thus all the resistances become dependent on disorder even if single contact is disordered. In presence of all the disordered contacts for QH sample R_H, R_L and R_{NL} continued to remain unaffected,only R_{2T} becomes dependent on disorder as shown in Table 2.2. In QSH sample they continued to remain affected by disorder, see Tables 2.1 and 2.2. With inclusion of inelastic scattering in the sample for QH case all the resistances remain unchanged from the all disordered contacts case while for QSH case all the resistances

continued to remain affected as before, see Tables 2.1 and 2.2.

Table 2.1: How do the quantum spin Hall edge modes compare with quantum Hall edge modes in a six terminal Hall bar?

	QH Edge Modes		QSH Edge Modes	
	R_H	R_L	R_H	R_L
Ideal Case	$\frac{h}{2e^2}\frac{1}{M}$	0	0	$\frac{h}{2e^2M}$
Single disordered probe	$\frac{h}{2e^2}\frac{1}{M}$	0	$\frac{h}{2e^2M}\frac{D_2}{3+2D_2}$	$\frac{h}{2e^2M}\frac{3}{3+2D_2}$
Two or more disordered probes	$\frac{h}{2e^2}\frac{1}{M}$	0	Disorder dependent (Fig. 2.3(a))	Disorder dependent (Fig. 2.3(a))
Disorder+inelastic scattering	$\frac{h}{2e^2}\frac{1}{M}$	0	Disorder dependent (Fig. 2.5(a))	Disorder dependent (Fig. 2.5(b))

Table 2.2: How do QH and QSH edge modes compare vis a vis their proclivity to disorder, inelastic and spin-flip scattering in non- local and local set-ups?

	QH Edge Modes		QSH Edge Modes	
	R_{NL}	R_{2T}	R_{NL}	R_{2T}
Ideal Case	0	$\frac{h}{2e^2}\frac{1}{M}$	$\frac{h}{e^2M}\frac{1}{6}$	$\frac{3h}{2e^2M}$
Single disordered probe	0	$\frac{h}{2e^2}\frac{1}{M}$	$\frac{h}{2e^2M}\frac{1}{3+2D_2}$	$\frac{h}{2e^2M}\frac{3(3+D_2)}{(3+2D_2)}$
Two or more disordered probes	0	$\frac{h}{2e^2}\frac{(1-D_1D_4)}{(1-D_1)(1-D_4)M}$	Disorder dependent (Fig. 2.3(b))	Disorder dependent (Fig. 2.3(b))
Disorder+inelastic scattering	0	$\frac{h}{2e^2}\frac{(1-D_1D_4)}{(1-D_1)(1-D_4)M}$	Disorder dependent (Fig. 2.5(c))	Disorder dependent (Fig. 2.5(c))

2.6   Conclusion

The aim of this chapter was to check the robustness of QH and QSH edge modes to the

twin effects of disorder and inelastic scattering- the bane of any phenomena in mesoscopic

physics. It was also expected that non-local transport regime is less affected by disorder

and inelastic scattering than the local transport regime, which is known to be true for

quantum ballistic transport[62, 63]. This question was addressed in this chapter whether

this hypothesis is true for QH and QSH regime too or not. It is seen that in QH regime non-local transport is not affected by disorder and inelastic scattering unlike local transport (see Table 2.2) while in QSH regime non-local and local both are affected by disorder and inelastic scattering. Thus the hypothesis regarding- "non-local transport regime is less affected by disorder and inelastic scattering than the local transport regime" is true for QH regime but untrue in QSH regime. How do increasing number of terminals in QH and QSH system affect the Hall, longitudinal, 2-terminal and non-local resistance in presence of disorder and inelastic scattering was also addressed in this chapter. It was observed that while in QH system, increasing number of terminals had no effect on the various resistances, it severally affected the same in QSH systems. The various resistances are calculated using Landauer-Buttiker formalism as done in Refs. [66, 11, 10] too. It was also seen in this chapter that while in QH regime Hall resistance, longitudinal resistance and non-local resistance retain their quantization even in presence of disorder and inelastic scattering (see Table 2.1), in QSH regime they become non-quantized even in presence of a single disordered contact. This result raises questions regarding the usefulness of non-local QSH transport in low-power information processing as reported in several works[34]. This also shows that the widely used quantized non-local conductance as a tool to detect helical edge mode transport has serious deficiencies especially in presence of disorder and inelastic scattering. In short, the non-local conductance in helical (QSH) edge mode transport does not retain its quantization and so would be unable to detect helicity in presence of contact disorder and inelastic scattering. Further, since QSH edge modes are considered to be useful in a host of other areas ranging from topological quantum computation[56] (braiding of majorana fermions) to searching for novel spin dependent effects, this chapter casts a shadow of doubt as regards their utility in such applications.

3.   Probing Helical edge modes and their topological origins

"The noise is the signal"

– Rolf Landauer

"I think there's something strangely musical about noise."

– Trent Reznor

"In the beginning, there was noise. Noise begat rhythm, and rhythm begat everything else."

– Mickey Hart

3.1   Introduction

In presence of a magnetic field and at low temperatures, chiral quantum Hall (QH) edge modes appear in a 2 dimensional electron gas[10, 33]. In such systems, edge modes flow in a manner (shown in Fig. 3.1(a), left panel) such that at the top edge electrons only move in one direction to the right. At the other, i.e., bottom edge electrons flow to the left in exactly opposite direction, this is called the chiral traffic rule. At low temperatures and in Mercury Telluride/Cadmium Telluride (HgTe/CdTe) heterostructure's[25] with strong

spin-orbit coupling quantum spin Hall (QSH) edge modes appear. Herein spin of the electron is locked to its momentum. If at the top edge of the sample spin up electrons are moving in one direction (say, right) then spin down electrons are moving in the opposite direction (left), and at the bottom edge vice versa. Thus a new traffic rule comes into effect-helical traffic rule and these edge modes are helical[25], see Fig. 3.1(a) (middle panel). To scatter, in the opposite direction an electron has to flip its spin. This is prohibited by time reversal(TR) symmetry as QSH samples obey TR symmetry in contrast to QH samples which don't. However, it is not always that the origin of helical edge modes in QSH samples is topological, recently there have been cases[43] where spin-momentum locked quasi-helical edge modes appear but these are not topologically protected. It has to be pointed out that the spin momentum locking among quasi-helical edge modes does not survive non-magnetic disorder and intra-edge backscattering comes into effect. These are termed trivial or quasi-helical edge modes and are shown in Fig. 3.1(a) (right panel).

The reason it is necessary to probe helicity is because the QSH state is a new state of matter- it is a topologically ordered phase in absence of magnetic field. This unique state of matter has to be experimentally and rigorously probed such that its existence is proved beyond doubt. Secondly, the confusion regarding the origin of helical edge states whether its really topological and therefore protected from sample disorder and inelastic scattering or its due to some trivial reason and thus of non-topological origin is a current topic of interest as evidenced by the recent works in this field[43, 64].

There are different methods for distinguishing helicity from chirality. The usual way to probe the existence of chiral/helical edge modes is via conductance measurements in multi terminal transport experiments[34, 65]. Lets consider an elementary set-up as in Fig. 3.1(b)(left panel)- a two terminal conductor with contacts 1 and 3 as source and sink. Herein, the words terminal/contact/probe imply the same thing a metallic reservoir for electrons. If a third probe is added in between contacts 1 and 3 as a voltage probe
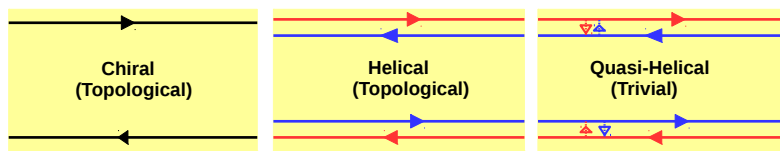
(a)
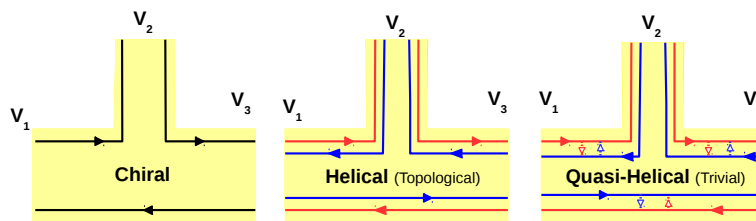
(b)

Figure 3.1: (a) Chiral vs helical(Topological) vs quasi-helical (Trivial), (b) 3-terminal chiral, helical(Topological) and quasi-helical (Trivial) bar. Black solid line denotes spin unpolarized QH edge mode, while red and blue solid line denote spin up and spin down QSH edge modes. Arrows between two edge modes at the same edge denote intra-edge spin flip scattering among them.

(Fig. 3.1(b) (left panel)) then for QH sample one edge mode enters probe 2 from source and another edge mode goes out from it. So to maintain net current zero at probe 2 its potential is adjusted to potential of the source, and the two terminal conductance of the sample remains same as before (without voltage probe 2). This can be understood from Landauer-Buttiker formalism[10, 33], since current through voltage probe- $I_2 = G_{21}(V_2 - V_1) = 0$, it leads to $V_1 = V_2$. The total conductance of the QH sample (chiral-topological) is then $2\frac{e^2}{h}$. The conductance of the QH sample does not change with addition of an extra voltage probe. But in QSH sample (helical-topological) (Fig. 3.1(b) (middle panel)) one edge mode enters the voltage probe from source and two edge modes come out of the voltage probe. The current through voltage probe- $I_2 = G_{21}(V_2 - V_1) + G_{23}(V_2 - V_3) = 0$ leads to $I_2 = G(2V_2 - V_1 - V_3) = 0$, $\Rightarrow V_2 = V_1/2$, where $G_{21} = G_{23} = G$ and $V_3 = 0$. Thus potential of voltage probe is adjusted to half of the potential of the source[98]. In QSH (helical-topological) samples the conductance is reduced by adding a voltage probe and is $\frac{3}{2}\frac{e^2}{h}$. Measuring the conductance with the inclusion of a voltage probe one can differentiate between the topological helical and chiral edge modes. Now what about quasi-helical (trivial) edge modes since these are not topologically protected and therefore are susceptible to intra-edge scattering Fig. 3.1(b)(right panel). At the top edge the electronic edge mode with spin-up (shown in red) has a finite probability of spin-flip scattering and reversing its path, the same thing happens for the spin-down electron (shown in blue). The small arrows in between the quasi-helical (trivial) edge modes indicates this process. The three terminal conductance for the quasi-helical (trivial) case then is $\frac{3}{2}\frac{e^2}{h}(1-f)$, where f is the probability of intra-edge scattering- a measure of the vulnerability of trivial quasi-helical edge modes to disorder and inelastic scattering. In clean samples where the probability of intra-edge scattering(f) is expected to be small, relying on conductance measurement alone may not be wise. Therefore in this chapter the focus is on the noise in particular the non-local Hanbury-Brown and Twiss (HBT) correlations [3].

In this chapter it is assumed that the trivial quasi-helical edge modes, in absence of any disorder, are similar to the topological helical edge modes and are spin-momentum locked. In other words- helical, up-spin edge modes at same edge have exactly opposite momentum to down-spin edge modes.

The subject of this chapter on distinguishing topological chiral and helical edge modes and determining whether the origin of the helical edge modes is topological or not via non-local HBT correlations has been dealt with in Ref. [3]. In chapter 2 the distinct attributes of chiral QH and helical QSH topological edge modes have been explored. Further, few more papers [70, 71, 72, 73] have explored the topic of helical vs. chiral edge modes using superconductors[70], with polarized STM tips[73], with corner junctions[72] and finally exploiting the Rashba coupling[71]. All these works while relying on different systems have a common conductance measurement which acts as the arbiter of helicity. Since in quantum spin Hall systems spin is locked to momentum, relying on just conductance measurements is risky, wherein detecting degree of spin polarization in samples exposed to disorder and spin-flip scattering will be tricky. In this chapter the aim is to use the Hanbury-Brown and Twiss or shot-noise correlations to probe the presence of helical edge modes and determine its origins whether topological or not. Non-local shot noise correlations on the other hand are seen to use the disorder and/or inelastic scattering present as a resource in being better able to differentiate between chirality and helicity and also between trivial and topological edge modes.

The theoretical examination of noise in QSH systems has mostly focused on the effect of electron-electron (e-e) interactions on the current-current correlations within a helical Luttinger liquid model describing the QSH state. Further these studies are in presence of a quantum point contact (QPC) in a QSH bar, as in Refs. [74, 75, 76]. There are also few papers on current-current correlation studied via the scattering matrix approach or other than helical Luttinger liquid approach, see Refs. [77, 78]. In this chapter zero frequency non-

local shot noise correlations are studied for QSH systems as regards distinguishing chiral versus helical (topological) and quasi-helical (trivial) phases. The focus of the aforesaid references [74, 75, 76, 77, 78] is not on identifying the topological origins of helical edge modes neither on the distinction between chiral and helical edge modes as is the case in this chapter.

However, apart from noise, various research groups around the world have made intriguing attempts at inferring helicity in edge mode transport in QSH systems via the conductance. A very recent proposal concerns a π shift seen in the conductance measurement of a QSH system[80]. This method also has an inherent weakness in that such a π shift is only observed when backscattering is absent. This implies presence of disorder will trip this method up rendering it un-fructuous. Another interesting proposal aims to use a Hong-Ou-Mandel interferometer[81] with QSH/QH edge modes which uses noise and proposes to use the dip in noise at zero power as a probe for helicity. However, this dip is shown as function of the time delay between two sources in the interferometer and its magnitude is compared for chiral and helical cases. These dips are affected by number of edge modes making the clear cut differentiation difficult. Further, no comment is made on the presence of disorder and inelastic scattering. Another work which includes disorder[82] and tries to distinguish between chiral and helical edge modes via a quantization of the conductance measurement obviates the weakness of Refs. [80, 81] but has an inherent weakness in that- with disorder the quantization vanishes. An interesting proposal which also uses the noise correlations[83] to distinguish between chiral and helical edge modes in presence of disorder purports to be better than[82] but then it again would be difficult to experimentally realize with current technology because of its reliance on QPC's. Another related work concerns the amount of net spin tunnelling between edge states and this can be also used as an arbiter for helicity[84], however herein too effects of disorder and inelastic scattering are not dealt with, finally a related work suggests the use of noise[76] and uses a

four terminal QPC to probe the helicity versus chirality dilemma, however herein too the dependence on QPC's will hamper any experimental realization. Further, the distinction between chiral and helical cases is via a difference in magnitude of the noise while a better arbiter is the sign which we will focus on in this chapter and will aim to surmount the challenges in the above proposals. On the question of topological helical vs. trivial quasi-helical edge modes there have been a couple of experimental papers[43] which have shown that quasi-helical edge modes do exist in trivial insulator but only a single theoretical work has dealt with this problem. In Ref. [85], the authors propose a method to distinguish between the two which relies on the addition of two non-magnetic impurities in an other wise clean QSH sample. The occurrence of localized zero modes identifies the topological origin of the helical edge modes. Notwithstanding the complexity of the method this approach also will be hard to fashion experimentally since detecting zero modes is a non-trivial task. Further, while local shot noise correlations have been calculated in some recent works with QSH samples[77] to our knowledge this is the first time[3] wherein both the non-local charge and spin shot noise correlations have been used as a probe of helicity and its topological origins and also to discriminate between chiral and helical edge modes. In 1950, R. Hanbury Brown and R. Twiss found out the diameter of radio stars via a intensity-intensity correlation experiment[86, 10]. The fermionic analogue of this famous experiment was realized in Refs. [87, 88] for a 2DEG in the chiral QH regime. The Hanbury Brown and Twiss (HBT) or shot noise correlations were shown to be completely anti-correlated meaning fermions are in obedience to Paulli exclusion principle. These correlations also go by the name of shot noise which measures the correlations between fluctuations of the current[15]. In this chapter it is shown that while there is no distinction between charge and spin noise correlations for topological helical edge modes, they are completely different for trivial quasi-helical edge modes enabling an effective discrimination between the topological or trivial origins of these edge modes.

3.1.1 This chapter

The structure of this chapter is as follows, beginning with "What is noise?" in section 3.2 the focus is on types of noise- thermal noise in section 3.2.1 and shot noise in section 3.2.2. Next, the focus is on measurement of HBT correlations in a multi-terminal QH sample in section 3.2.3 and in QSH sample in section 3.2.4. Next the focus is on the effect of disorder in section 3.3, first for chiral QH case the non-local HBT correlations are calculated for two disordered contacts in section 3.3.1, then for all disordered contacts in section 3.3.2. Next the focus is on the topological helical QSH case, wherein both non-local charge and spin correlations are calculated. Similar to chiral QH case, the non-local HBT correlations for two disordered contacts are calculated in section 3.3.3, then the case of all disordered contacts is discussed in section 3.3.4. Further, inelastic scattering is added to the set-ups discussed previously in section 3.4, first for two disordered contacts in QH system in section 3.4.1 and and then for all disordered contacts in section 3.4.2. In all these cases it is seen that non-local HBT correlations are always negative for QH systems. Then the focus is on a well known theoretical work[14] and its subsequent experimental implementation[68] and it is explained in section 3.4.3 why there is a difference between Refs. [14, 68] and the results in sections 3.4.1 and 3.4.2. In this chapter, deliberately QPC's are removed from the QH or QSH systems discussed, since the focus is on obtaining positive correlations in helical QSH samples, wherein due to Dirac nature of the edge states experimental implementation with QPC's is difficult. Like the QH case, inelastic scattering is added to the QSH set-up in section 3.5. First for two disordered contacts in section 3.5.1 and finally for all disordered contacts in section 3.5.2. It is seen that the non-local charge correlations can be positive in presence of inelastic scattering for QSH samples.

Next the focus is on the question of distinguishing topological helical from trivial quasi-helical edge modes in section 3.6. In section 3.6 first the case of trivial quasi-helical edge modes is discussed in presence of two disordered contacts and inelastic scattering in section 3.6.1.

Then the ratio of HBT noise to current (Fano factor) is calculated for both topological and trivial QSH samples as well as to distinguish between chiral QH and helical QSH samples in section 3.6.2. Finally the chapter concludes with a summary of the results in Tables 3.1 and 3.2 and with a perspective on future endeavours.

3.2   What is Noise?

Noise is any unwanted signal or sound that mixes with the desired signal. It disturbs people or makes it difficult to identify the original signal (sound). Conversations of other people, road traffic sounds may be called noise by people not involved in them. For our purpose the fluctuations of an a electrical current will be identified as noise. Noise then is some irregular fluctuations that accompanies any transmitted electrical signal but is not part of it and tends to obscure it. Noise is mainly of two types: a) Thermal Noise (Johnson-Nyquist Noise), b) Shot Noise.

3.2.1   Thermal Noise

The thermodynamic average of the occupation number $\langle n \rangle$ of a conductor is defined as the Fermi-Dirac distribution function f[15]. In a conductor at equilibrium the time averaged probability of occupation of a state is also defined as Fermi-Dirac distribution f. Therefore, the time averaged probability of a state not being occupied is $1 - f$. The fluctuation in the occupation number is then-

$$\langle (\Delta n)^2 \rangle = \langle (n - \langle n \rangle)^2 \rangle = \langle n^2 - 2n\langle n \rangle + \langle n \rangle^2 \rangle = f(1 - f), \qquad (3.1)$$

where $\langle n^2 \rangle$ is equal to $\langle n \rangle$ since due to the Pauli exclusion principle any state can be occupied with occupation number 1 or 0. Thermal noise defined by Eq. (3.1) is finite only

when temperature is finite, at zero temperature it is zero. The fluctuations in the occupation number give rise to equilibrium current fluctuations in the external circuit which are via the fluctuation-dissipation theorem related to the conductance of the system. Thermal noise does not give more information than the conductance measurement about the system but shot noise can[15].

3.2.2 Shot Noise

Shot noise in an electrical conductor is a consequence of the quantization of the charge. Let's say a single particle is incident on a rectangular barrier, either it is transmitted with probability T or reflected with probability $R = 1 - T$. The time averaged occupation number of incident state $\langle n_{in} \rangle$ is unity at zero temperature. The time averaged probability of occupation of a transmitted state $\langle n_T \rangle$ is T and for reflected state $\langle n_R \rangle$ is R. The mean squared fluctuation in the occupation number of incident state is $\langle (\Delta n_{in})^2 \rangle = \langle (n_{in} - \langle n_{in} \rangle)^2 \rangle = 0$. The mean squared auto correlation either in the fluctuations in the transmitted or reflected current is $\langle (\Delta n_T)^2 \rangle = \langle (\Delta n_R)^2 \rangle = TR$. Finally, HBT or shot noise cross correlation between the fluctuations of the reflected and transmitted current is-

$$\langle (\Delta n_T \Delta n_R) \rangle = \langle (n_T - \langle n_T \rangle)(n_R - \langle n_R \rangle) \rangle = -TR, \tag{3.2}$$

where $\Delta n_X = n_X - \langle n_X \rangle$ with $X = in, T, R$. Since the particle in the incident state is either transmitted or reflected, so $\langle n_T n_R \rangle = 0$. From Eq. (3.2) it is evident that the auto correlation $\langle (\Delta n_T)^2 \rangle = \langle (\Delta n_R)^2 \rangle = TR$ is always positive and the cross correlation $\langle (\Delta n_T \Delta n_R) \rangle - TR = -T(1 - T)$ is always negative for fermions[15].

3.2.3 How to measure Hanbury-Brown and Twiss noise in a multiterminal quantum Hall system?

Following the scattering matrix approach one can calculate the shot noise cross correlation $(S_{\alpha\beta})$ between the currents at two contacts α and β from the scattering matrix of a multi terminal QH system[15]-

$$S_{\alpha\beta} = \frac{2e^2}{h} \int dE \sum_{\gamma\lambda} Tr\left\{A^{\alpha}_{\gamma\lambda} A^{\beta}_{\lambda\gamma}\right\} f_{\gamma}(1 - f_{\lambda}), \tag{3.3}$$

where $A^{\alpha}_{\gamma\lambda} = \delta_{\alpha\gamma}\delta_{\alpha\lambda} - s^{\dagger}_{\alpha\gamma}s_{\alpha\lambda}$ is derived from the scattering matrix elements s_{ij} with i,j being the contact indices. In this chapter we only consider four terminal QH systems with $\alpha, \beta = 4, 3$ respectively. f_{γ} is the Fermi-Dirac distribution at contact γ. In this chapter the zero temperature limit is only considered, hence f_{γ} can take values 0 or 1 only.

3.2.4 How to measure Hanbury-Brown and Twiss noise in a multiterminal quantum spin Hall system?

As the edge modes in QSH are spin polarized, so the shot noise cross correlation can be calculated separately for charge as well as spin. The charge shot noise formula is given as follows-

$$S^{ch}_{\alpha\beta} = \sum_{\sigma,\sigma'=\uparrow,\downarrow} S^{\sigma\sigma'}_{\alpha\beta} = S^{\uparrow\uparrow}_{\alpha\beta} + S^{\uparrow\downarrow}_{\alpha\beta} + S^{\downarrow\uparrow}_{\alpha\beta} + S^{\downarrow\downarrow}_{\alpha\beta}. \tag{3.4}$$

The above expression can be easily derived by extending the formalism of section 3.2.3 to spin. The spin shot noise formula is given as-

$$S^{sp}_{\alpha\beta} = S^{\uparrow\uparrow}_{\alpha\beta} - S^{\uparrow\downarrow}_{\alpha\beta} - S^{\downarrow\uparrow}_{\alpha\beta} + S^{\downarrow\downarrow}_{\alpha\beta}, \tag{3.5}$$

(a)   (b)
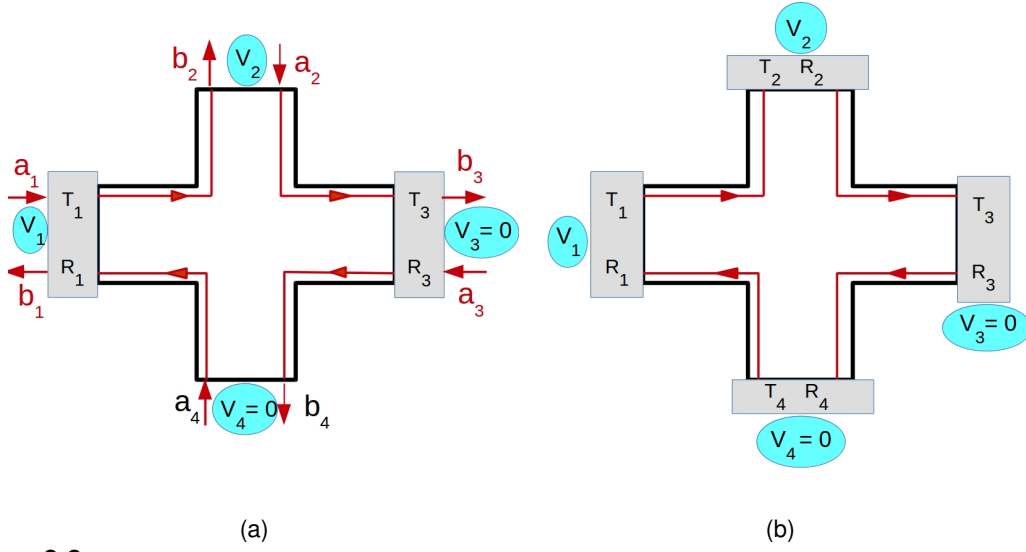
Figure 3.2: Four terminal quantum Hall bar showing chiral edge modes with (a) two disordered contacts, (b) all disordered contacts. Disordered contact: $R_i = D_i$ and $T_i = 1 - D_i$, represents the reflection (transmission) probability of edge modes from and into contact i with the strength of disorder (D_i) in contact i ranging from $0 < R_i(\text{or}, D_i) < 1$. To avoid clutter only a single edge state is shown in (a) and (b).

$$\text{with } S_{\alpha\beta}^{\sigma\sigma'} = \frac{2e^2}{h} \int dE \sum_{\gamma,\gamma'} \sum_{\rho,\rho'=\uparrow,\downarrow} Tr\left[A_{\gamma\gamma'}^{\rho\rho'}(\alpha,\sigma)A_{\gamma'\gamma}^{\rho'\rho}(\beta,\sigma')\right] f_\gamma(1-f_{\gamma'}), \qquad (3.6)$$

herein the $\{m,n\}^{th}$ element of the Buttiker current matrix $A_{\gamma\gamma'}^{\rho\rho'}(\alpha,\sigma)$ is given by[102]-

$$\left[A_{\gamma\gamma'}^{\rho\rho'}(\alpha,\sigma)\right]_{mn} = \delta_{mn}\delta_{\gamma\alpha}\delta_{\gamma'\alpha}\delta^{\sigma\rho}\delta^{\sigma\rho'} - \sum_k \left[s_{\alpha\gamma}^{\sigma\rho\dagger}\right]_{mk}\left[s_{\alpha\gamma'}^{\sigma\rho'}\right]_{kn}.$$

One can clearly see that the equations for charge and spin shot noise differ by a minus sign in front of the opposite spin correlations. This has important consequences since in presence of finite spin-flip scattering the charge and spin shot noise behave in a dis-similar manner unlike the case in absence of spin-flip wherein these are identical.

3.3   Effect of disorder on HBT noise

Herein, we consider the contacts to be disordered in a similar way as described in section 2.2 of chapter 2. A disordered contact can be thought of as an ideal contact with a

disordered region separating the reservoir and the sample. The contact can be treated in the same way as a two-terminal sample, where the total transmission and reflection probabilities for electrons coming from the sample are T and R respectively[12, 10].

3.3.1 Quantum Hall system with two disordered contacts

The case of QH sample with two disordered contacts is depicted in Fig. 3.2(a) with contacts 1 and 3 disordered. The scattering matrix relating the incoming edge states to the outgoing is given as:

$$\begin{pmatrix} b_1 \\ b_2 \\ b_3 \\ b_4 \end{pmatrix} = s \begin{pmatrix} a_1 \\ a_2 \\ a_3 \\ a_4 \end{pmatrix}, \text{with } s = \begin{pmatrix} r_1 & 0 & 0 & t_1 \\ -t_1 & 0 & 0 & r_1 \\ 0 & -t_3 & r_3 & 0 \\ 0 & r_3 & t_3 & 0 \end{pmatrix}, \quad (3.7)$$

$r_i = \sqrt{D_i}$ and $t_i = \sqrt{1 - D_i}$ (D_i is the strength of disorder at contact i) represent the reflection and transmission amplitudes at contact i. For ideal contacts $D_i = 0$ and thus $r_i = 0$ and $t_i = 1$. In Fig. 3.2(a), M, the no. of edge modes is one for clarity. Each element of the total scattering matrix s can be calculated in the following way: suppose an electron incoming in edge state (a_1) can reflect as b_1 edge state with amplitude r_1, thus s_{11} represents scattering of an edge state from contact 1 to itself which is r_1. The way we derive S_{21} is as follows- S_{21} defines the scattering of an electron coming from contact 1 to 2. An electron comes out of a contact with scattering amplitude $-t_1$ and enters contact 2 without reflection. When an electron comes out of a contact, a minus sign is always multiplied with its transmission amplitude, while for an electron entering into a contact no such sign is multiplied. This is just to distinguish forward and backward directions of propagation. This also makes the s-matrix 's' in Eq. (3.7) unitary. Similarly rest of the elements of the scattering matrix s can be derived. The scattering matrix s obeys the unitarity relation $s^\dagger s = s s^\dagger = I$, I being identity matrix, which is the necessary condition for

conservation of current. The equations required to satisfy the scattering matrix to be unitary are $|t_i|^2 + |r_i|^2 = 1$, where $i =$ contact index. Contact 2 is a current probe with $V_2 = 0$ while other potentials $V_1 = V$, $V_3 = V_4 = 0$. Thus all four contacts are basically current probes. Further, $f_1 = 1$ and $f_2 = f_3 = f_4 = 0$ (for $0 < E < eV_1$) at zero temperature, where E is the electronic energy and $f_i = \Theta(eV_i - E)$ Fermi-Dirac distribution at contact i which basically depends on the potential of that contact. Since current is flowing from contact 1 to 2 via edge modes as bias voltage V_1 is applied only at contact 1, and as the edge modes are chiral there is only current flowing between contacts 1 and 2 and not between any other contacts as others are all grounded. From Eq. (3.3) one can calculate the nonlocal HBT cross correlation between contacts 3 and 4 as-

$$
\begin{aligned}
S_{43} &= \frac{2e^2}{h} \int dE \left[A_{12}^4 A_{21}^3 f_1(1-f_2) + A_{13}^4 A_{31}^3 f_1(1-f_3) + A_{14}^4 A_{41}^3 f_1(1-f_4) \right], \\
&= \frac{2e^2}{h} \left[e(V_1 - V_2) A_{12}^4 A_{21}^3 + e(V_1 - V_3) A_{13}^4 A_{31}^3 + e(V_1 - V_4) A_{14}^4 A_{41}^3 \right], \\
&= \frac{2e^2}{h} |eV_1| \left[s_{41}^\dagger s_{42} s_{32}^\dagger s_{31} + s_{41}^\dagger s_{43} s_{33}^\dagger s_{31} + s_{41}^\dagger s_{44} s_{34}^\dagger s_{31} \right] = 0,
\end{aligned}
$$

herein s_{ij} are the elements of scattering matrix (Eq. (3.7)). Thus, the nonlocal correlation S_{43} vanishes for case of two disordered contacts in QH system, see Fig. 3.2(a).

3.3.2 Quantum Hall system with all disordered contacts

The case of all disordered contacts in a QH sample is depicted in Fig. 3.2(b). The scattering matrix relating the incoming and outgoing edge states is given as:

$$
s = \frac{1}{a} \begin{pmatrix} r_1 - r_2 r_3 r_4 & -t_1 t_2 r_3 r_4 & -t_1 t_3 r_4 & -t_1 t_4 \\ -t_1 t_2 & r_2 - r_1 r_3 r_4 & -t_2 t_3 r_1 r_4 & -t_2 t_4 r_1 \\ -t_1 t_3 r_2 & -t_2 t_3 & r_3 - r_1 r_2 r_4 & -t_3 t_4 r_1 r_2 \\ -t_1 t_4 r_3 r_2 & -t_2 t_4 r_3 & -t_3 t_4 & r_4 - r_1 r_2 r_3 \end{pmatrix}, \tag{3.8}
$$

herein $a = 1 - r_1 r_2 r_3 r_4$, arises because of the multiple reflections from disordered contacts[1, 3]. Each element of the total scattering matrix can be calculated in the following way: suppose an electron incoming in edge state (a_1) can reflect as b_1 edge state with amplitude r_1, but then, it can also follow a different path by transmitting through contact 1 and then get reflected at contact 2, then again reflected at 3 and then at 4 after which it transmits through contact 1 into b_1 state. The amplitude for this path is $-t_1 \times r_2 \times r_3 \times r_4 \times t_1 = -t_1^2 r_2 r_3 r_4$. Following this one can also have a third path with amplitude $-t_1^2 r_1 (r_2 r_3 r_4)^2$ and so on. Summing all these terms we get the scattering amplitude from contact 1 to itself, as $(r_1 - r_2 r_3 r_4)/(1 - r_1 r_2 r_3 r_4)$. The origin of minus sign in the transmission amplitudes is same as explained in section 3.3.1. Similarly, rest of the elements of the s matrix of the four terminal QH system can be derived. This matrix satisfies the unitarity relation $s^\dagger s = s s^\dagger = I$. Herein too the potentials are identical to the two disordered contact case-$V_1 = V$, $V_2 = V_3 = V_4 = 0$. Thus, $f_1 = 1$ and $f_2 = f_3 = f_4 = 0$ (for $0 < E < eV_1$) at zero temperature. We can calculate the nonlocal HBT correlation from Eq. (3.3) as shown below-

$$
\begin{aligned}
S_{43} &= \frac{2e^2}{h} \int dE \left[A_{12}^4 A_{21}^3 f_1 (1 - f_2) + A_{13}^4 A_{31}^3 f_1 (1 - f_3) + A_{14}^4 A_{41}^3 f_1 (1 - f_4) \right], \\
&= \frac{2e^2}{h} \left[e(V_1 - V_2) A_{12}^4 A_{21}^3 + e(V_1 - V_3) A_{13}^4 A_{31}^3 + e(V_1 - V_4) A_{14}^4 A_{41}^3 \right], \\
&= \frac{2e^2}{h} |eV_1| \left[s_{41}^\dagger s_{42} s_{32}^\dagger s_{31} + s_{41}^\dagger s_{43} s_{33}^\dagger s_{31} + s_{41}^\dagger s_{44} s_{34}^\dagger s_{31} \right], \\
&= -\frac{2e^2}{h} |eV| \frac{T_1^2 T_3 T_4 R_2^2 R_3}{a^4},
\end{aligned}
$$

wherein we have used the unitarity or conservation of probability condition $|r_i|^2 + |t_i|^2 = R_i + T_i = 1$. Here the correlation depends on the disorder at contacts 2 and 3 which explains why the correlation for two disordered contacts (contacts 1 and 3) case is zero. The nonlocal HBT correlation is negative which is the property of the Fermi-Dirac distribution which directly relates to the antisymmetric wave function of electrons.

(a)   (b)
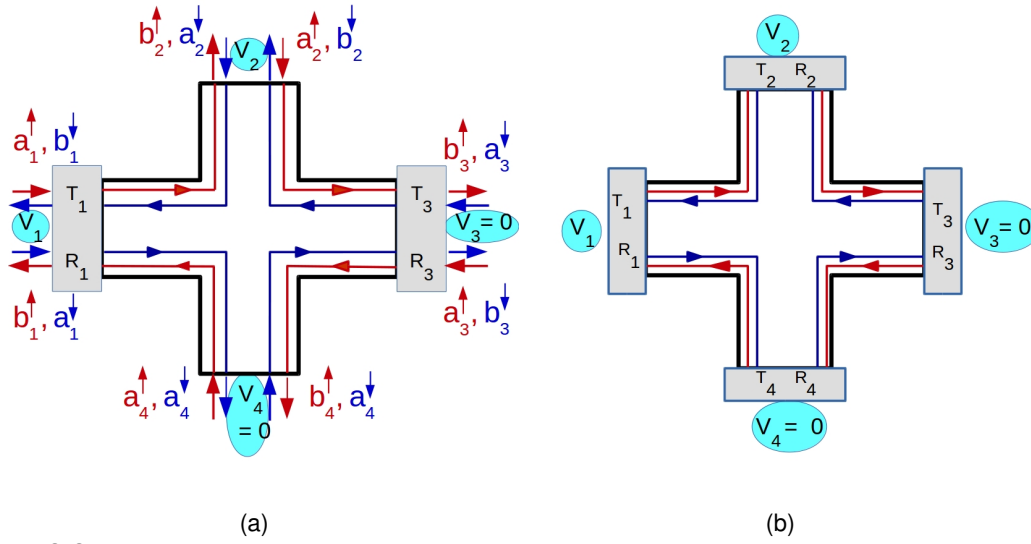
Figure 3.3: Four terminal Quantum Spin Hall bar showing QSH edge modes. These edge modes differ from their QH counterparts since these are spin polarized and helical, contacts 3 and 4 are detectors kept at zero potential. (a) Two disordered contacts and (b) all disordered contacts. $R_i = 1 - T_i$ represents the reflection probability of edge modes from and into contact i with the strength of disorder in contact i ranging from $0 < R_i < 1$. To avoid clutter the edge states are only shown in (a). (b) Have exactly similar edge states to and from the contacts, these aren't shown explicitly.

3.3.3 Quantum spin Hall system with two disordered contacts

The case of two disordered contacts for a QSH sample is depicted in Fig. 3.3(a). The scattering matrix relating the incoming to the outgoing edge states is given as:

$$
\begin{pmatrix} b_1^\uparrow \\ b_1^\downarrow \\ b_2^\uparrow \\ b_2^\downarrow \\ b_3^\uparrow \\ b_3^\downarrow \\ b_4^\uparrow \\ b_4^\downarrow \end{pmatrix} = s \begin{pmatrix} a_1^\uparrow \\ a_1^\downarrow \\ a_2^\uparrow \\ a_2^\downarrow \\ a_3^\uparrow \\ a_3^\downarrow \\ a_4^\uparrow \\ a_4^\downarrow \end{pmatrix}, \text{with } s = \begin{pmatrix} r_1 & 0 & 0 & 0 & 0 & 0 & t_1 & 0 \\ 0 & r_1 & 0 & t_1 & 0 & 0 & 0 & 0 \\ -t_1 & 0 & 0 & 0 & 0 & 0 & r_1 & 0 \\ 0 & 0 & 0 & 0 & 0 & t_3 & 0 & r_3 \\ 0 & 0 & -t_3 & 0 & r_3 & 0 & 0 & 0 \\ 0 & 0 & 0 & 0 & 0 & r_3 & 0 & -t_3 \\ 0 & 0 & r_3 & 0 & t_3 & 0 & 0 & 0 \\ 0 & -t_1 & 0 & r_1 & 0 & 0 & 0 & 0 \end{pmatrix}, \quad (3.9)
$$

with r_i and t_i being the reflection and transmission amplitudes at contact i. There are four contacts in the case described above and the samples have two edge modes on each side- one for spin up and the other for spin down going in the opposite directions (spin-momentum locked), the scattering matrix s is thus a 8×8 matrix. Each element of the total scattering matrix s can be calculated in the following way: suppose an up-spin/down-spin electron incoming in edge state (a_1^σ) can reflect as b_1^σ edge state with amplitude r_1, thus $s_{11}^{\sigma\sigma}$ scattering of an spin up/spin down edge state from contact 1 to itself is r_1. Similarly rest of the elements of the scattering matrix s can be derived. This matrix satisfies the unitarity relation $s^\dagger s = ss^\dagger = I$. Here the potentials are similar to the case of QH systems with two disordered contacts case- $V_1 = V$, $V_2 = V_3 = V_4 = 0$. Further, as before at zero temperature we have the Fermi-Dirac functions as: $f_1 = 1$ and $f_2 = f_3 = f_4 = 0$ for ($0 < E < eV_1$). From Eqs. (3.4), (3.6) one can calculate the nonlocal HBT correlation as-

$$
\begin{aligned}
S_{43}^{\uparrow\uparrow} &= \frac{2e^2}{h} \int dE \sum_{\rho\rho'=\uparrow,\downarrow} \left[A_{12}^{\rho\rho'}(4,\uparrow)A_{21}^{\rho'\rho}(3,\uparrow)f_1(1-f_2) + A_{13}^{\rho\rho'}(4,\uparrow)A_{31}^{\rho'\rho}(3,\uparrow)f_1(1-f_3) \right. \\
&\quad \left. + A_{14}^{\rho\rho'}(4,\uparrow)A_{41}^{\rho'\rho}(3,\uparrow)f_1(1-f_4) \right], \\
&= \frac{2e^2}{h} \sum_{\rho\rho'=\uparrow,\downarrow} \left[e(V_1-V_2)A_{12}^{\rho\rho'}(4,\uparrow)A_{21}^{\rho'\rho}(3,\uparrow) + e(V_1-V_3)A_{13}^{\rho\rho'}(4,\uparrow)A_{31}^{\rho'\rho}(3,\uparrow) \right. \\
&\quad \left. + e(V_1-V_4)A_{14}^{\rho\rho'}(4,\uparrow)A_{41}^{\rho'\rho}(3,\uparrow) \right], \\
&= \frac{2e^2}{h}|eV_1| \sum_{\rho\rho'=\uparrow,\downarrow} \left[s_{41}^{\uparrow\rho\dagger}s_{42}^{\uparrow\rho'}s_{32}^{\uparrow\rho'\dagger}s_{31}^{\uparrow\rho} + s_{41}^{\uparrow\rho\dagger}s_{43}^{\uparrow\rho'}s_{33}^{\uparrow\rho'\dagger}s_{31}^{\uparrow\rho} + s_{41}^{\uparrow\rho\dagger}s_{44}^{\uparrow\rho'}s_{34}^{\uparrow\rho'\dagger}s_{31}^{\uparrow\rho} \right], \\
&= 0.
\end{aligned}
$$

Similarly one can calculate $S_{43}^{\uparrow\downarrow} = S_{43}^{\downarrow\uparrow} = S_{43}^{\downarrow\downarrow} = 0$. Thus $S_{43}^{ch} = S_{43}^{sp} = 0$. This result is identical to QH case.

3.3.4 Quantum spin Hall system with all disordered contacts

Fig. 3.3(b) depicts the all disordered contacts case. The scattering matrix relating the incoming and the outgoing edge states is given as:

$$s = \frac{1}{a}\begin{pmatrix}
r_1 - r_2 r_3 r_4 & 0 & -t_1 t_2 r_3 r_4 & 0 & -t_1 t_3 r_4 & 0 & -t_1 t_4 & 0 \\
0 & r_1 - r_2 r_3 r_4 & 0 & -t_1 t_2 & 0 & -t_1 t_3 r_2 & 0 & -t_1 t_4 r_2 r_3 \\
-t_1 t_2 & 0 & r_2 - r_1 r_3 r_4 & 0 & -t_2 t_3 r_1 r_4 & 0 & -t_2 t_4 r_1 & 0 \\
0 & -t_1 t_2 r_3 r_4 & 0 & r_2 - r_1 r_3 r_4 & 0 & -t_2 t_3 & 0 & -t_2 t_4 r_3 \\
-t_1 t_3 r_2 & 0 & -t_2 t_3 & 0 & r_3 - r_1 r_2 r_4 & 0 & -t_3 t_4 r_1 r_2 & 0 \\
0 & -t_1 t_3 r_4 & 0 & -t_2 t_3 r_1 r_4 & 0 & r_3 - r_1 r_2 r_4 & 0 & -t_3 t_4 \\
-t_1 t_4 r_2 r_3 & 0 & -t_2 t_4 r_3 & 0 & -t_3 t_4 & 0 & r_4 - r_1 r_2 r_3 & 0 \\
0 & -t_1 t_4 & 0 & -t_2 t_4 r_1 & 0 & -t_3 t_4 r_1 r_2 & 0 & r_4 - r_1 r_2 r_3
\end{pmatrix}, \quad (3.10)$$

wherein $a = 1 - r_1 r_2 r_3 r_4$. Each element of the total scattering matrix can be calculated in the following way: suppose an spin up/spin down electron incoming in edge state (a_1^σ) can reflect as spin up/spin down b_1^σ edge state with amplitude r_1, but then, it can also follow a different path by transmitting through contact 1 and then get reflected at contact 2, then again reflected at 3 and then at 4 after which it transmits through contact 1 into b_1^σ state. The amplitude for this path is $-t_1 \times r_2 \times r_3 \times r_4 \times t_1 = -t_1^2 r_2 r_3 r_4$. Following this one can also have a third path with amplitude $-t_1^2 r_1 (r_2 r_3 r_4)^2$ and so on. Summing all these terms we get the scattering amplitude from contact 1 to itself, as $(r_1 - r_2 r_3 r_4)/(1 - r_1 r_2 r_3 r_4)$. Similarly, rest of the elements of the s matrix of the four terminal QSH system can be derived. The above matrix satisfies the unitarity condition- $s^\dagger s = s s^\dagger = I$. Herein the potentials are identical to the two disordered probes case- $V_1 = V$, $V_2 = V_3 = V_4 = 0$. Here again $f_1 = 1$ and $f_2 = f_3 = f_4 = 0$ (for $0 < E < eV_1$). From Eqs. (3.4),(3.6) we can calculate the non-local HBT shot noise cross correlation for both charge as well as spin as-

$$S_{43}^{ch} = S_{43}^{sp} = -\frac{2e^2}{h}|eV|\frac{T_1^2 T_3 T_4 (R_2^2 R_3 + R_4)}{a^4}.$$

Thus both nonlocal charge and spin correlation depends on the disorder at contacts $2, 3$ and 4 which explains why the correlation is zero for two disordered contacts case (disorder
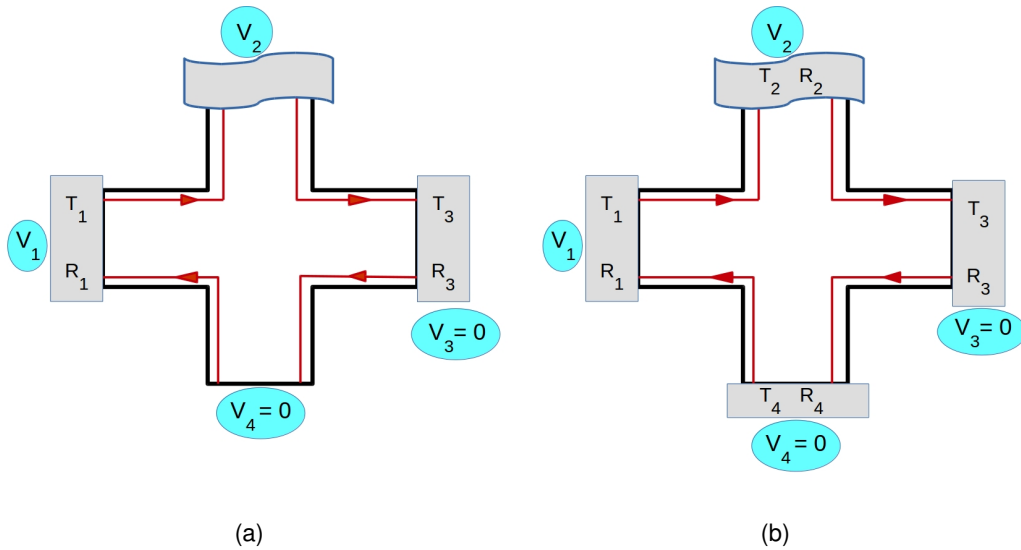
Figure 3.4: (a) Four terminal QH bar with two disordered contacts and inelastic scattering- probe 2 (curvy box) is a voltage probe (with current into it $I_2 = 0$), (b) four terminal QH bar with all disordered contacts and inelastic scattering- probe 2 (curvy box) is a voltage probe (with current into it $I_2 = 0$).

at contacts 1 and 3). This correlation is always negative irrespective of the magnitude of disorder.

3.4 Effect of inelastic scattering on HBT noise in quantum Hall edge modes

In chapter 3 we have used Buttiker voltage probe methods to model inelastic scattering. In chapter 2 we used the method of equilibration of edge modes to model inelastic scattering. Both methods have their advantages and disadvantages. The advantage of Buttiker voltage probe method is that it is very simple to use and calculation done in voltage probe method are not tedious. The disadvantage of using voltage probe method to model inelastic scattering is that herein inelastic scattering only takes place at specific probe or contact. However, inelastic scattering in mesoscopic sample at low temperature generated electron-electron interaction can take place any where in the sample not just a specific place. A better method to model inelastic scattering is via equilibration of edge modes as was done

in chapter 2. The equilibration method model inelastic scattering as taking place any where between two adjacent contacts not restricted to any specific place. However, calculation using equilibration method are tedious for conductance itself as done in chapter 2. For noise calculating scattering matrices between contacts and equilibrating potentials and combining these inelastic matrices is far more difficult although not impossible. Further most of the related theoretical works on shot noise or HBT correlation in both QH as well as QSH edge mode transport use Buttiker voltage probe methods to model inelastic scattering. Since in this chapter we compare the results for helical QSH as well as chiral QH transport to those works we also use Buttiker voltage probe method to model inelastic scattering. Thus, in this chapter inelastic scattering is introduced via replacing the current probe 2 with a voltage probe (shown by a curvy box at contact 2 in Figs. 3.4(a, b)). The difference between a voltage probe and a current probe is that the current through a voltage probe is zero unlike a current probe where it is finite. Whenever a edge state enters a voltage probe from the sample it loses its identity and lost in the reservoir. The current I_2 through the voltage probe is zero. The current through any contact is defined by- $I_\alpha = \frac{1}{e} \int dE \sum_\beta G_{\alpha\beta} f_\beta + \delta I_\alpha$, herein the second term is due to the intrinsic fluctuation[14] (with $S_{\alpha\beta} = \langle \delta I_\alpha \delta I_\beta \rangle$) and the conductance matrix

$$G_{\alpha\beta} = \frac{2e^2}{h} (N_\alpha \delta_{\alpha\beta} - Tr\left[s_{\alpha\beta}^\dagger s_{\alpha\beta}\right]), \tag{3.11}$$

with $N_\alpha =$ No. of edge modes at contact α. We need to fix the fluctuating part of the current at contact 2, $\Delta I_2 = 0$. This condition $\Delta I_2 = 0$ affects the fluctuation of current at other contacts [14] as follows-

$I_\alpha = < I_\alpha > + \Delta I_\alpha,$ with $< I_\alpha >$ the average current in contact α,

Thus, $\dfrac{1}{e} dE \sum_\beta G_{\alpha\beta} f_\beta + \delta I_\alpha = \dfrac{1}{e} \int dE \sum_\beta G_{\alpha\beta} \bar{f}_\beta + \Delta I_\alpha,$

or, $\dfrac{1}{e} \int dE \sum_\beta G_{\alpha\beta} (f_\beta - \bar{f}_\beta) + \delta I_\alpha = \Delta I_\alpha,$

wherein, $\bar{f}_\beta$ is average of the Fermi-Dirac distribution function in contact β.

Now, $\dfrac{1}{e} G_{\alpha 2} (\mu_2 - \bar{\mu}_2) + \delta I_\alpha = \Delta I_\alpha,$ (3.12)

(for contacts $i = 1, 3, 4$ $\mu_i = \bar{\mu}_i$, since these are current probes)

$\mu_2, \bar{\mu}_2$ being chemical potential and average chemical potential at contact 2.

For $\alpha = 2$, we get- $\Delta I_2 = \dfrac{1}{e} G_{22} (\mu_2 - \bar{\mu}_2) + \delta I_2,$ thus, $0 = \dfrac{1}{e} G_{22} (\mu_2 - \bar{\mu}_2) + \delta I_2,$

since contact 2 is a voltage probe, $I_2 = \langle I_2 \rangle = \Delta I_2 = 0,$ $\dfrac{\delta I_2}{G_{22}} = -\dfrac{1}{e} (\mu_2 - \bar{\mu}_2),$

substituting this in Eq. (3.12) we get- $\Delta I_\alpha = \delta I_\alpha - \dfrac{G_{\alpha 2}}{G_{22}} \delta I_2,$ (3.13)

wherein the first term is due to the intrinsic part of the fluctuation and the second term is due to voltage fluctuation at contact 2. Thus, the nonlocal HBT correlation between contacts α, β due to the inelastic scattering is-

$$
\begin{aligned}
S_{\alpha\beta}^{in} &= \; < \Delta I_\alpha \Delta I_\beta > = < (\delta I_\alpha - \frac{G_{\alpha 2}}{G_{22}} \delta I_2)(\delta I_\beta - \frac{G_{\beta 2}}{G_{22}} \delta I_2) >, \\
&= \; < (\delta I_\alpha \delta I_\beta - \frac{G_{\alpha 2}}{G_{22}} \delta I_\beta \delta I_2 - \frac{G_{\beta 2}}{G_{22}} \delta I_\alpha \delta I_2 + \frac{G_{\alpha 2} G_{\beta 2}}{G_{22}^2} \delta I_2 \delta I_2) >, \\
&= \; S_{\alpha\beta} - \frac{G_{\alpha 2}}{G_{22}} S_{\beta 2} - \frac{G_{\beta 2}}{G_{22}} S_{\alpha 2} + \frac{G_{\alpha 2} G_{\beta 2}}{G_{22}^2} S_{22}.
\end{aligned}
$$
(3.14)

3.4.1 Quantum Hall system with two disordered contacts and inelastic scattering

Two contacts are considered to be disordered for this case, see Fig. 3.4(a). The scattering matrix relating the incoming to the outgoing edge state is given as in Eq. (3.7). Here, we have considered source $V_1 = V$ and contacts 3, 4 (with $V_3 = V_4 = 0$) are detectors. As contact 2 is the voltage probe, $I_2 = G_{21}(V_2 - V_1) + G_{24}(V_2 - V_4) = \frac{2e^2}{h}[T_1(V_2 - V_1) + R_1(V_2 - V_4)] = \frac{2e^2}{h}(V_2 - T_1V_1)$, putting $I_2 = 0$, we get- $V_2 = T_1V_1$. The Fermi-Dirac distribution functions at zero temperature in the probes are as follows- $f_1 = 1$, $f_3 = 0$, $f_4 = 0$ (for $0 < E < eV_1$), $f_2 = 1$ (for $0 < E < eV_2$) and $f_2 = 0$ (for $eV_2 < E < eV_1$) as probes 3 and 4 are used as detectors and are at zero voltage. Following Eq. (3.3) the non-local charge correlation between probes 3 and 4 is-

$$
\begin{aligned}
S_{43} &= \frac{2e^2}{h} \int dE \left[A_{12}^4 A_{21}^3 f_1(1 - f_2) + A_{13}^4 A_{31}^3 f_1(1 - f_3) + A_{14}^4 A_{41}^3 f_1(1 - f_4) \right. \\
&\quad \left. + A_{23}^4 A_{32}^3 f_2(1 - f_3) + A_{24}^4 A_{42}^3 f_2(1 - f_4) \right], \\
&= \frac{2e^2}{h} \left[e(V_1 - V_2)A_{12}^4 A_{21}^3 + e(V_1 - V_3)A_{13}^4 A_{31}^3 + e(V_1 - V_4)A_{14}^4 A_{41}^3 \right. \\
&\quad \left. + e(V_2 - V_3)A_{23}^4 A_{32}^3 + e(V_2 - V_4)A_{24}^4 A_{42}^3 \right], \\
&= \frac{2e^2}{h} |eV_1| \left[s_{41}^\dagger s_{42} s_{32}^\dagger s_{31} + s_{41}^\dagger s_{43} s_{33}^\dagger s_{31} + s_{41}^\dagger s_{44} s_{34}^\dagger s_{31} \right. \\
&\quad \left. + T_1(s_{42}^\dagger s_{43} s_{33}^\dagger s_{32} + s_{42}^\dagger s_{44} s_{34}^\dagger s_{32}) \right], \\
&= -\frac{2e^2}{h} |eV|[T_1 T_3 R_3].
\end{aligned}
\tag{3.15}
$$

Similarly, one can calculate $S_{32} = S_{42} = 0$ and $S_{22} = \frac{2e^2}{h}|eV|T_1R_1$ and the conductances (following Eq. (3.11)) are- $G_{42} = -\frac{2e^2}{h}R_3$, $G_{32} = -\frac{2e^2}{h}T_3$ and $G_{22} = \frac{2e^2}{h}$. Following Eq. (3.14) we get the non-local correlation in presence of inelastic scattering as-

$$
S_{43}^{in} = S_{43} - \frac{G_{42}}{G_{22}}S_{32} - \frac{G_{32}}{G_{22}}S_{42} + \frac{G_{32}G_{42}}{G_{22}^2}S_{22} = -\frac{2e^2}{h}|eV|[T_1^2 T_3 R_3].
\tag{3.16}
$$

(a)   (b)
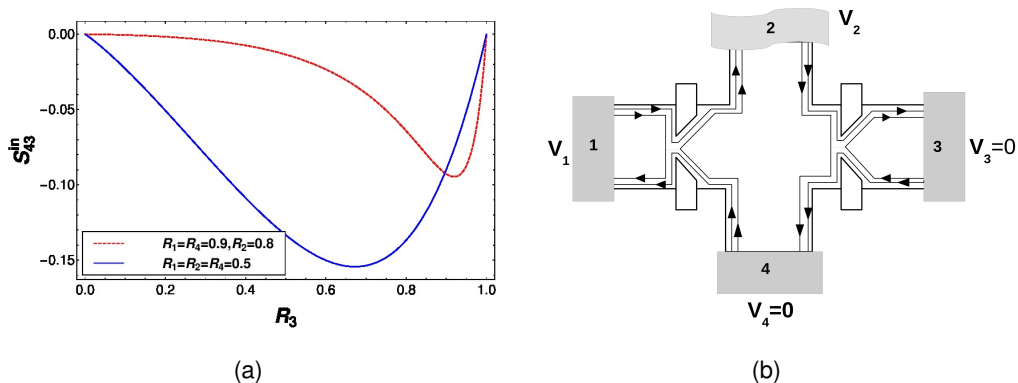
Figure 3.5: (a) Non-local correlation in quantum Hall case S_{43}^{in} vs R_3 for all disordered probes with inelastic scattering with parameters $R_1 = R_2 = R_4 = 0.5$ (solid line) and $R_1 = R_4 = 0.9, R_2 = 0.8$ (dashed line), (b) The Texier, et. al.,/Oberholzer, et. al., set-up as in Refs. [14, 68] to detect positive non-local HBT correlations in a quantum Hall set up. Here, probe 2 is a voltage probe ($I_2 = 0$) while probes 3 and 4 are detectors kept at zero voltage. Note that by using constrictions inside the sample and having edge modes transmitting with different probabilities one can engineer positive non-local correlations. However, in the set-ups we have in this chapter positive non-local correlation in quantum Hall regime are impossible.

If there are multiple no. of edge modes then the correlation is just multiplied by the no. of edge modes and it remains always negative irrespective of the disorder or inelastic scattering for QH case.

3.4.2   Quantum Hall set-up with all disordered contacts and inelastic scattering

All contacts are considered to be disordered for this case. The scattering matrix relating the incoming to the outgoing edge states is given in Eq. (3.8). In the set up of Fig. 3.4(b), only one edge mode is shown. We have considered $V_1 = V$ and $V_3 = V_4 = 0$. As contact 2 is the voltage probe, from Landauer-Buttiker formalism putting $I_2 = 0$ gives $V_2 = \frac{T_1 V_1}{1 - R_1 R_3 R_4}$. The Fermi-Dirac distribution functions are in the zero temperature limit given as follows- $f_1 = 1$, $f_3 = 0$, $f_4 = 0$ (for $0 < E < eV_1$), $f_2 = 1$ (for $0 < E < eV_2$) and $f_2 = 0$ (for $eV_2 < E < eV_1$). From Eq. (3.3) and (3.14) one can calculate the non-local correlation S_{43}^{in} in presence of

inelastic scattering as-

$$S_{43}^{in} = \frac{T_1 T_3 T_4 R_3}{(1 - R_1 R_4 R_3) a^8} [R_1 T_2^3 (1 - R_3 R_4)((1 + R_2)(1 + R_1 R_3 R_4) - 4\sqrt{R_1 R_2 R_3 R_4})$$
$$- 2 R_1 T_2^2 a^2 (R_2 + R_3 R_4 - R_2 R_3 R_4 T_1 - 2\sqrt{R_1 R_2 R_3 R_4})$$
$$- a^4 (1 - R_1 R_2 (1 + T_2) - R_1 R_2^2 R_3 R_4 T_1)],$$

where $a = 1 - r_1 r_2 r_3 r_4$. We plot the shot noise in presence of inelastic scattering obtained from the above equation in Fig. 3.5(a). In Fig. 3.5(a)(dashed line) we see for large disorder at probe $1, 2, 4$ non-local correlation almost vanishes for low levels of disorder at probe 3. This is because the contact with larger disorder behaves as closed for the edge mode, meaning electron cannot transmit into the probe. So it is more probable for the electron to follow a path through a contact with less disorder. This makes the electron behaviour deterministic (particle like behaviour) rather than probabilistic (wave like behaviour), which reduces the noise correlation (almost to zero). As disorder at probe 3 increases electron path becomes more probabilistic and negative correlations appear. One can clearly conclude that probes with same or close to the same disorder will show maximum stochastic nature in the system and will show maximum negative correlation, which is shown in Fig. 3.5(a)(solid line).

3.4.3 Why is shot noise in our quantum Hall set-up always negative but in Texier, et. al., /Oberholzer, et. al., [14, 68] set-ups it can be positive?

Our set-up is different than Texier, et. al./Oberholzer, et. al., set-ups. They considered a constriction/QPC in their sample which can back scatter edge modes and thus creates noise within the system. In our case disorder is relegated to the probe/contact. In our case with disorder at contacts we don't have any back scattering within the sample in contrast

to Texier, et. al.,/Oberholzer, et. al., set-ups of Fig. 3.5(b). Further, in their set-ups they consider two edge modes with different transmission probabilities- one which is completely transmitted while the other is partially transmitted. However, in our case we have identical transmission probabilities for different edge modes arising from a particular contact. Also getting a positive cross correlation in their set-up depends on the no. of edge modes in the sample but in our set-up the results are independent on the no. of edge modes. The shot noise result (with inelastic scattering) derived in Ref. [14] is $S_{43}^{in} = -(e^2/h)|eV|\frac{R_3}{2}[2T_3(1 + T_1) - (1 + T_3)R_1T_1]$, which is positive for $T_3 = 0$, $S_{43}^{in} = +(e^2/h)|eV|R_1T_1/2$ for two edge modes with different transmissions. But if two edge modes have same transmission (lets say the two edge modes are partially transmitted with identical transmittances) then the shot noise result is $S_{43}^{in} = -2(e^2/h)|eV|\frac{R_3}{2}[2T_3T_1 - T_3R_1T_1] = -2(e^2/h)|eV|\frac{T_1T_3R_3}{2}[1 + T_1]$ is completely negative as we see in our case too. The different transmittances for different edge modes arising from a particular contact is the reason why there is a positive correlation. The experimental realization of [14] set-up in Ref. [68] requires QPC's in order to generate different transmittances for different edge modes which for chiral QH samples maybe alright but is quite difficult for helical QSH samples, since in the latter due to Dirac nature of edge states(Klein effect) its extremely difficult to tune their transmittances via a QPC, although not impossible as some recent studies indicative[95]. In this context the set-up we have which does not rely on QPC's but as we will see in next section generates positive correlations for helical edge modes becomes much more relevant for easier experimental implementation. Generating positive non-local correlations is the first step to generating entangled currents, which will have important applications in quantum information processing tasks.
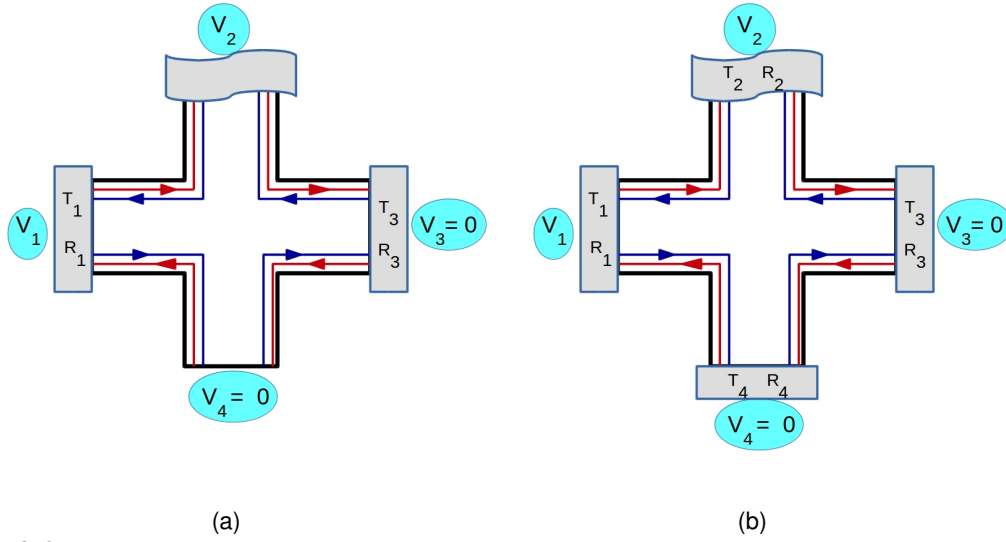
Figure 3.6: Four terminal Quantum Spin Hall bar showing QSH edge modes. (a) Two disordered contacts with inelastic scattering, (b) all disordered contacts with inelastic scattering, (contact 2 is a voltage probe in both (a) and (b) with $I_2 = 0$).

3.5 Effect of inelastic scattering on quantum spin Hall edge modes

To calculate the shot noise in QSH case in presence of both disorder as well as inelastic scattering we generalize the formula obtained for QH case (Eq. (3.14)) by including spin. The non-local charge correlations for QSH case in presence of inelastic scattering then is-

$$
\begin{aligned}
S_{\alpha\beta}^{ch-in} &= S_{\alpha\beta}^{ch} - \frac{G_{\alpha 2}^{ch}}{G_{22}^{ch}} S_{\beta 2}^{ch} - \frac{G_{\beta 2}^{ch}}{G_{22}^{ch}} S_{\alpha 2}^{ch} + \frac{G_{\alpha 2}^{ch} G_{\beta 2}^{ch}}{G_{22}^{ch^2}} S_{22}^{ch}, \\
&= (S_{\alpha\beta}^{\uparrow\uparrow} + S_{\alpha\beta}^{\uparrow\downarrow} + S_{\alpha\beta}^{\downarrow\uparrow} + S_{\alpha\beta}^{\downarrow\downarrow}) - \frac{G_{\alpha 2}^{ch}}{G_{22}^{ch}} (S_{\beta 2}^{\uparrow\uparrow} + S_{\beta 2}^{\uparrow\downarrow} + S_{\beta 2}^{\downarrow\uparrow} + S_{\beta 2}^{\downarrow\downarrow}) \\
&\quad - \frac{G_{\beta 2}^{ch}}{G_{22}^{ch}} (S_{\alpha 2}^{\uparrow\uparrow} + S_{\alpha 2}^{\uparrow\downarrow} + S_{\alpha 2}^{\downarrow\uparrow} + S_{\alpha 2}^{\downarrow\downarrow}) - \frac{G_{\beta 2}^{ch} G_{\alpha 2}^{ch}}{G_{22}^{ch^2}} (S_{22}^{\uparrow\uparrow} + S_{22}^{\uparrow\downarrow} + S_{22}^{\downarrow\uparrow} + S_{22}^{\downarrow\downarrow}). \quad (3.17)
\end{aligned}
$$

Eq. (3.17) can be simplified by separating the individual spin components as follows:

$$S_{\alpha\beta}^{ch-in} = (S_{\alpha\beta}^{\uparrow\uparrow} - \frac{G_{\alpha2}^{ch}}{G_{22}^{ch}}S_{\beta2}^{\uparrow\uparrow} - \frac{G_{\beta2}^{ch}}{G_{22}^{ch}}S_{\alpha2}^{\uparrow\uparrow} + \frac{G_{\alpha2}^{ch}G_{\beta2}^{ch}}{G_{22}^{ch^2}}S_{22}^{\uparrow\uparrow}) + (S_{\alpha\beta}^{\uparrow\downarrow} - \frac{G_{\alpha2}^{ch}}{G_{22}^{ch}}S_{\beta2}^{\uparrow\downarrow} - \frac{G_{\beta2}^{ch}}{G_{22}^{ch}}S_{\alpha2}^{\uparrow\downarrow} + \frac{G_{\alpha2}^{ch}G_{\beta2}^{ch}}{G_{22}^{ch^2}}S_{22}^{\uparrow\downarrow})$$

$$+ (S_{\alpha\beta}^{\downarrow\uparrow} - \frac{G_{\alpha2}^{ch}}{G_{22}^{ch}}S_{\beta2}^{\downarrow\uparrow} - \frac{G_{\beta2}^{ch}}{G_{22}^{ch}}S_{\alpha2}^{\downarrow\uparrow} + \frac{G_{\alpha2}^{ch}G_{\beta2}^{ch}}{G_{22}^{ch^2}}S_{22}^{\downarrow\uparrow}) + (S_{\alpha\beta}^{\downarrow\downarrow} - \frac{G_{\alpha2}^{ch}}{G_{22}^{ch}}S_{\beta2}^{\downarrow\downarrow} - \frac{G_{\beta2}^{ch}}{G_{22}^{ch}}S_{\alpha2}^{\downarrow\downarrow} + \frac{G_{\alpha2}^{ch}G_{\beta2}^{ch}}{G_{22}^{ch^2}}S_{22}^{\downarrow\downarrow}),$$

$$= S_{\alpha\beta}^{\uparrow\uparrow,in} + S_{\alpha\beta}^{\uparrow\downarrow,in} + S_{\alpha\beta}^{\downarrow\uparrow,in} + S_{\alpha\beta}^{\downarrow\downarrow,in}. \tag{3.18}$$

In the above equation $G_{kl}^{ch} = G_{kl}^{\uparrow\uparrow} + G_{kl}^{\uparrow\downarrow} + G_{kl}^{\downarrow\uparrow} + G_{kl}^{\downarrow\downarrow}$ is the conductance summed over all the spin indices's, for example $G_{kl}^{\uparrow\downarrow}$ represents the probability that a spin down electron is transmitted as a spin up electron. The non-local spin correlations is particular to QSH case and can be similarly written as-

$$S_{\alpha\beta}^{sp-in} = S_{\alpha\beta}^{\uparrow\uparrow,in} - S_{\alpha\beta}^{\uparrow\downarrow,in} - S_{\alpha\beta}^{\downarrow\uparrow,in} + S_{\alpha\beta}^{\downarrow\downarrow,in}, \tag{3.19}$$

with $S_{\alpha\beta}^{\sigma\sigma',in}, \sigma, \sigma' =\uparrow, \downarrow$ defined as in Eq. (3.18). We proceed now to calculate the non-local charge and spin correlations in the next sub-section and beyond for QSH edge modes.

3.5.1 Quantum spin Hall set-up with two disordered contacts and in-elastic scattering

For the case of two disordered probes in QSH case, depicted in Fig. 3.6(a). The scattering matrix relating the incoming to outgoing edge states is given as in Eq. (3.9), following

Eq. (3.6) we first calculate $S_{43}^{\uparrow\uparrow}$ as follows-

$$
\begin{aligned}
S_{43}^{\uparrow\uparrow} &= \frac{2e^2}{h}\int dE \sum_{\gamma\gamma'}\sum_{\rho\rho'=\uparrow,\downarrow} Tr\left[A_{\gamma\gamma'}^{\rho\rho'}(4,\uparrow)A_{\gamma'\gamma}^{\rho'\rho}(3,\uparrow)\right]f_\gamma(1-f_{\gamma}'),\\
&= \frac{2e^2}{h}\int dE \sum_{\gamma\gamma'}\sum_{\rho\rho'=\uparrow,\downarrow} Tr\left[s_{4\gamma}^{\uparrow\rho\dagger}s_{4\gamma'}^{\uparrow\rho'}s_{3\gamma'}^{\uparrow\rho'\dagger}s_{3\gamma}^{\uparrow\rho}\right]f_\gamma(1-f_{\gamma}'),\\
&= \frac{2e^2}{h}\sum_{\rho\rho'=\uparrow,\downarrow}\left[Tr\left[s_{41}^{\uparrow\rho\dagger}s_{42}^{\uparrow\rho'}s_{32}^{\uparrow\rho'\dagger}s_{31}^{\uparrow\rho}\right]e(V_1-V_2)+Tr\left[s_{41}^{\uparrow\rho\dagger}s_{43}^{\uparrow\rho'}s_{33}^{\uparrow\rho'\dagger}s_{31}^{\uparrow\rho}\right]e(V_1-V_3)\right.\\
&\quad +Tr\left[s_{41}^{\uparrow\rho\dagger}s_{44}^{\uparrow\rho'}s_{34}^{\uparrow\rho'\dagger}s_{31}^{\uparrow\rho}\right]e(V_1-V_4)+Tr\left[s_{42}^{\uparrow\rho\dagger}s_{43}^{\uparrow\rho'}s_{33}^{\uparrow\rho'\dagger}s_{32}^{\uparrow\rho}\right]e(V_2-V_3)\\
&\quad \left.+Tr\left[s_{42}^{\uparrow\rho\dagger}s_{44}^{\uparrow\rho'}s_{34}^{\uparrow\rho'\dagger}s_{32}^{\uparrow\rho}\right]e(V_2-V_4)\right]=\frac{2e^2}{h}\left[0+0+0+(-T_3R_3eV_2)+0\right],\\
&= -\frac{2e^2}{h}|eV_1|T_1T_3R_3/2.
\end{aligned}
\tag{3.20}
$$

Similarly from Eq. (3.6) and Eq. (3.4), one can calculate $S_{43}^{\uparrow\downarrow}=S_{43}^{\downarrow\uparrow}=S_{43}^{\downarrow\downarrow}=0$ then $S_{43}^{ch}=S_{43}^{\uparrow\uparrow}+S_{43}^{\uparrow\downarrow}+S_{43}^{\downarrow\uparrow}+S_{43}^{\downarrow\downarrow}=-\frac{2e^2}{h}|eV_1|T_1T_3R_3/2$. Now to add the effect of inelastic scattering we have to calculate S_{43}^{ch-in} using Eq. (3.17), further the shot noise cross-correlations S_{32}^{ch}, S_{42}^{ch} and S_{22}^{ch} are determined following Eq. (3.4). Here again we consider $V_1=V$, and $V_3=V_4=0$. As contact 2 is the voltage probe which induces inelastic scattering, substituting $I_2=0$ gives $V_2=T_1V_1/2$. The Fermi-Dirac distribution functions are as follows- $f_1=1$, $f_3=0$, $f_4=0$ (for $0<E<eV_1$), $f_2=1$ (for $0<E<eV_2$) and $f_2=0$ (for $eV_2<E<eV_1$). From Eqs. (3.4), (3.6) and Eq. (3.18), we calculate the non-local charge correlation in presence of inelastic scattering as-

$$
S_{43}^{ch-in}=-\frac{2e^2}{h}|eV|\left[\frac{T_1T_3R_3}{2}-\frac{T_1T_3R_1(R_1+R_3)}{4}\right],
\tag{3.21}
$$

which can be positive for a range of values of T_1 and T_3 as shown in Fig. 3.7(a). Putting $R_3=0$ we get $S_{43}^{ch-in}=\frac{2e^2}{h}|eV|[T_1R_1^2/2]$, which is completely positive for all values of R_1 as shown in Fig. 3.7(b). From Fig. 3.7(a) one can conclude that small values of T_1 (large R_1) and larger values of T_3 (small R_3) help in generating stronger positive cross correlation. In
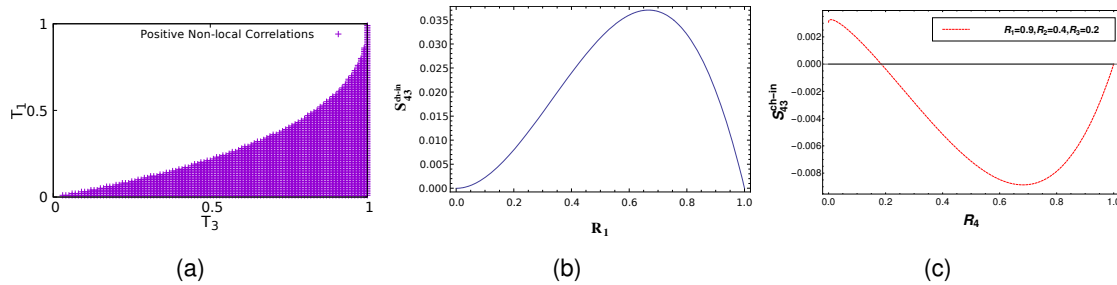
Figure 3.7: S_{43} vs. Disorder. (a) T_1 vs T_3 for two probe disorder with inelastic scattering for QSH (Positive cross correlation), (b) correlation S_{43} vs R_3 for two probe disorder with inelastic scattering for QSH with parameters $R_3 = 0$, (c) Non-local correlation S_{43} vs R_4 for all probe disorder with inelastic scattering for QSH with parameters $R_1 = 0.9$, $R_2 = 0.4$ and $R_3 = 0.2$.

QSH case, inelastic scattering in presence of disorder induces a positive cross correlation in the system which is unexpected for electrons as they are fermions, they should show a negative cross correlation, which is the basis of the famous HBT experiment[106]. We can understand this in this way that QSH edge modes are spin polarized and there are spin up electrons, which after getting out of the probe 2 (voltage probe which redistributes the current) follow one edge of the Hall bar and directly reach the contact 3 (a detector), at the same time spin down electrons after getting out from same contact 2 follow the other edge of the Hall bar reaching contact 4 (another detector) via contact 1- and these two electrons can be correlated positively. Since these two electrons are travelling via two completely different paths and as different probes are disordered with varying degrees of disorder these two paths will have different transmission probabilities. But in QH case (as discussed in section 3.4.2) if there are two edge modes, they do not travel via different paths (one cannot separate the paths taken by the two edge modes from voltage probe to detector) and therefore even if probes are affected with varying degrees of disorder the transmission probabilities of two edge modes will be identical. That's why positive non-local correlation is not observed in the QH set-ups as in section 3.4.2 even in presence of disorder and inelastic scattering.

3.5.2 Quantum spin Hall set-up with all disordered contacts and inelastic scattering

The set-up for this case is depicted in Fig. 3.6(b). The scattering matrix relating the incoming edge states to the outgoing one is given as in Eq. (3.10). Here we have considered $V_1 = V$, and $V_3 = V_4 = 0$. As contact 2 is the voltage probe, substituting $I_2 = 0$ gives $V_2 = \frac{T_1 V_1}{2(1-R_1 R_3 R_4)}$. The Fermi-Dirac distribution functions as usual at zero temperature and with probes 3 and 4 as detectors are as follows- $f_1 = 1$, $f_3 = 0$, $f_4 = 0$ (for $0 < E < eV_1$), $f_2 = 1$ (for $0 < E < eV_2$) and $f_2 = 0$ (for $eV_2 < E < eV_1$). Thus, from Eqs. (3.4),(3.6) and (3.19) one can calculate the non-local correlation S_{43}^{ch-in}, as expressions are large we will analyse them in Fig. 3.7(c). Positive non-local correlations are obtained in this case similar to the two probe case discussed above, while inelastic scattering and the fact that up and spin down edge modes have different transmittances through the sample (due to the difference in their paths) is critical to getting positive correlations, the effect of disorder on these positive correlations is more ambiguous. Some disorder is of course necessary to have noise but other than that there is no clear cut influence of increasing/decreasing disorder on the positive correlations so obtained. Till now we have only considered topological Helical QSH edge modes. Now we ask the question what happens to the positive correlations so obtained if we are not sure of their topological origin. This question has become relevant recently with some papers[43] showing that in a trivial insulator quasi-helical edge modes can also occur, of course they are without any topological protection. In the next section we address this question.

3.6   Topological vs. Trivial quasi-helical quantum spin Hall edge modes

We consider trivial quasi-helical QSH edge modes as shown in Fig. 3.8(a). In Ref. [43] the difference between trivial and topological QSH modes is determined from the non-local resistance. Herein we show the non-local noise (both spin as well as charge) can be very effective in determining the topological origins of QSH edge modes. Since these trivial quasi-helical edge modes are not topologically protected there is a finite probability 'f' that with disorder and inelastic scattering they will scatter to another mode and change their direction and spin. We denote by parameter 'f'- the probability for an electron with a particular spin orientation in a trivial QSH edge mode to change its direction and spin via intra edge scattering. This intra-edge scattering is shown in Fig. 3.8(a) by small arrows connecting two oppositely moving edge modes. Thus, 'linking' up and spin down modes due to the possibility of backscattering because of sample disorder/inelastic scattering. However, we note that in both cases trivial quasi-helical as well as topological helical QSH edge modes (see Fig. 3.3(a)), spin-momentum locking is preserved in absence of any non-magnetic disorder. An up-spin electron is backscattered as a down-spin electron moving in exactly opposite direction.

3.6.1   Trivial QSH set-up with two disordered probes and inelastic scattering

The case represented in Fig. 3.8(a), depicts two disordered probes with inelastic scattering in a trivial QSH set-up. The scattering matrix relating the incoming to the outgoing edge
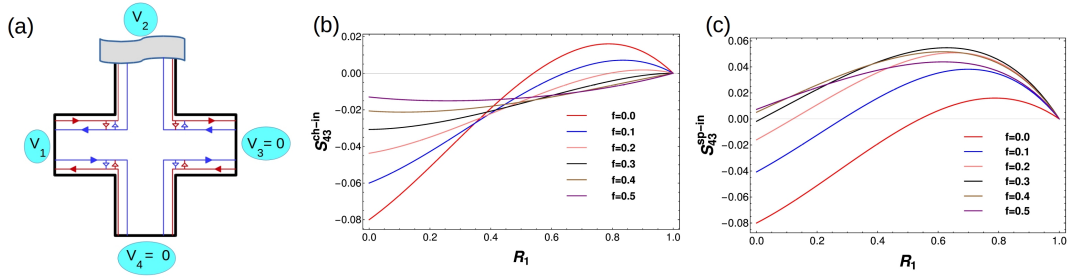
Figure 3.8: (a) QSH sample with trivial quasi-helical edge modes. There are two disordered probes with inelastic scattering included via voltage probe 2, small arrowheads indicate intra edge scattering. The effect of such intra-edge scattering on positive non-local charge(b) and spin(c) correlations. Non-local charge(b) (S_{43}^{ch-in} vs R_1) and spin(c) correlations ($S_{43}^{sp,in}$ vs R_1) in a trivial quasi-helical QSH sample with two disordered probes ($R_3 = 0.2$) and inelastic scattering. Note the exactly opposite behaviour to the nonlocal charge correlations. The intra edge scattering parameter: $f = 0$(topological) (red) and $f = 0.1$ (blue), $f = 0.2$(pink),$f = 0.3$ (black), $f = 0.4$ (brown), $f = 0.5$(purple) in (b) and (c).

states is given as follows:

$$
s = \begin{pmatrix}
\frac{(1+f)r_1}{a_1} & \frac{-it_1^2\sqrt{f}}{a_1} & 0 & \frac{it_1r_1\sqrt{f(1-f)}}{a_1} & 0 & 0 & \frac{t_1\sqrt{1-f}}{a_1} & 0 \\
\frac{-it_1^2\sqrt{f}}{a_1} & \frac{(1+f)r_1}{a_1} & 0 & \frac{t_1\sqrt{1-f}}{a_1} & 0 & 0 & \frac{it_1r_1\sqrt{f(1-f)}}{a_1} & 0 \\
\frac{-t_1\sqrt{1-f}}{a_1} & \frac{-it_1r_1\sqrt{f(1-f)}}{a_1} & 0 & \frac{i(1+R_1)\sqrt{f}}{a_1} & 0 & 0 & \frac{r_1(1-f)}{a_1} & 0 \\
0 & 0 & \frac{i(1+R_3)\sqrt{f}}{a_3} & 0 & \frac{-it_3r_3\sqrt{f(1-f)}}{a_3} & \frac{-t_3\sqrt{1-f}}{a_3} & 0 & \frac{r_3\sqrt{1-f}}{a_3} \\
0 & 0 & \frac{t_3\sqrt{1-f}}{a_3} & 0 & \frac{(1+f)r_3}{a_3} & \frac{-it_3^2\sqrt{f}}{a_3} & 0 & \frac{it_3r_3\sqrt{f(1-f)}}{a_3} \\
0 & 0 & \frac{it_3r_3\sqrt{f(1-f)}}{a_3} & 0 & \frac{-it_3^2\sqrt{f}}{a_3} & \frac{(1+f)r_3}{a_3} & 0 & \frac{t_3\sqrt{1-f}}{a_3} \\
0 & 0 & \frac{r_3\sqrt{1-f}}{a_3} & 0 & \frac{-t_3\sqrt{1-f}}{a_3} & \frac{-it_3r_3\sqrt{f(1-f)}}{a_3} & 0 & \frac{i(1+R_3)\sqrt{f}}{a_3} \\
\frac{-it_1r_1\sqrt{f(1-f)}}{a_1} & \frac{-t_1\sqrt{1-f}}{a_1} & 0 & \frac{r_1(1-f)}{a_1} & 0 & 0 & \frac{i(1+R_1)\sqrt{f}}{a_1} & 0
\end{pmatrix},
$$

$$(3.22)$$

with $a_1 = 1 + fr_1^2, a_3 = 1 + fr_3^2$, whenever there is intra-edge scattering we introduce a $\pi/2$ phase in the scattering amplitude. Here too as before we have $V_1 = V$, and $V_3 = V_4 = 0$. As contact 2 is a voltage probe, putting $I_2 = 0$ gives-

$$
V_2 = \frac{(1 - R_3^2 f^2)T_1(1 + R_1 f)V_1}{2 - R_1^2 f(1+f) - R_3^2 f(1+f) + 2R_1^2 R_3^2 f^3}.
$$

$$(3.23)$$

At zero temperature, the Fermi-Dirac distribution functions are as follows: $f_1 = 1$, $f_3 = 0$, $f_4 = 0$ (for $0 < E < eV_1$), $f_2 = 1$ (for $0 < E < eV_2$) and $f_2 = 0$ (for $eV_2 < E < eV_1$). From Eqs. (3.4), (3.6), and (3.22) one can calculate the non-local charge correlation S_{43}^{ch-in} as

well as spin correlation S_{43}^{sp-in}, as the expressions are large we will analyse them via plots in Figs. 3.8(b) and (c). As intra-edge scattering probability f increases to 0.25, Fig. 3.8(b) the correlation can be positive or negative depending on the disorder at probe 1, and as f increases to 0.5 one can see that non-local charge correlation becomes completely negative irrespective of the disorder. Strong spin flip scattering completely destroys the positive correlation effect induced in the non-local fluctuation by inelastic scattering in the trivial QSH sample. One can also calculate non-local spin shot noise correlation from Eqs. (3.5), (3.6), (3.19), and (3.18). This is plotted in Fig. 3.8(c). In this case we see opposite behaviour to the non-local charge correlation shown in Fig. 3.8(b). The non-local spin correlation turn completely positive with increased intra-edge scattering. Of course the non local charge and spin correlations are identical for QH case as well as for topological QSH samples. The nonlocal HBT spin correlation can thus be a good detector of trivial QSH edge modes.

3.6.2 Distinguishing topological vs trivial quasi-helical edge modes via Fano factor

The Fano factor, like the coefficient of variation, is a measure of the dispersion of the probability distribution of noise. It is basically the signal to noise ratio, named after Ugo Fano. Surprisingly, the noise is usually smaller than a Poisson distribution noise (in which the variance is equal to the mean value, and $F = 1$ for Poisson distributions) and it is called sub-poissonian noise ($F < 1$). If noise is greater than Poisson distribution then it is called super-poissonian noise. The Fano factor is defined by - $F_{ij} = \frac{S_{ij}}{2e|I|}$. The charge Fano factor is $F_{43}^{ch} = \frac{S_{43}^{ch-in}}{2e|I_1^{ch-in}|}$, while spin Fano factor is $F_{43}^{sp} = \frac{S_{43}^{sp-in}}{2e|I_1^{sp-in}|}$. The charge current for trivial quasi-helical QSH system as shown in Fig. 3.8(a) is $I_1^{ch-in} = 2T_1V_1 - \frac{2T_1V_1f+T_1V_2(1-f)}{1-R_1f}$, and the spin current $I_1^{sp-in} = \frac{T_1V_2(1-f)}{1+R_1f}$, where V_2 is defined as in Eq. (3.23). As the expression for S_{43}^{ch-in} and S_{43}^{sp-in} are large, we analyse them via plots in Fig. 3.9. We compare the charge Fano factors in the topological QH and QSH cases in Fig. 3.9(a) while the charge
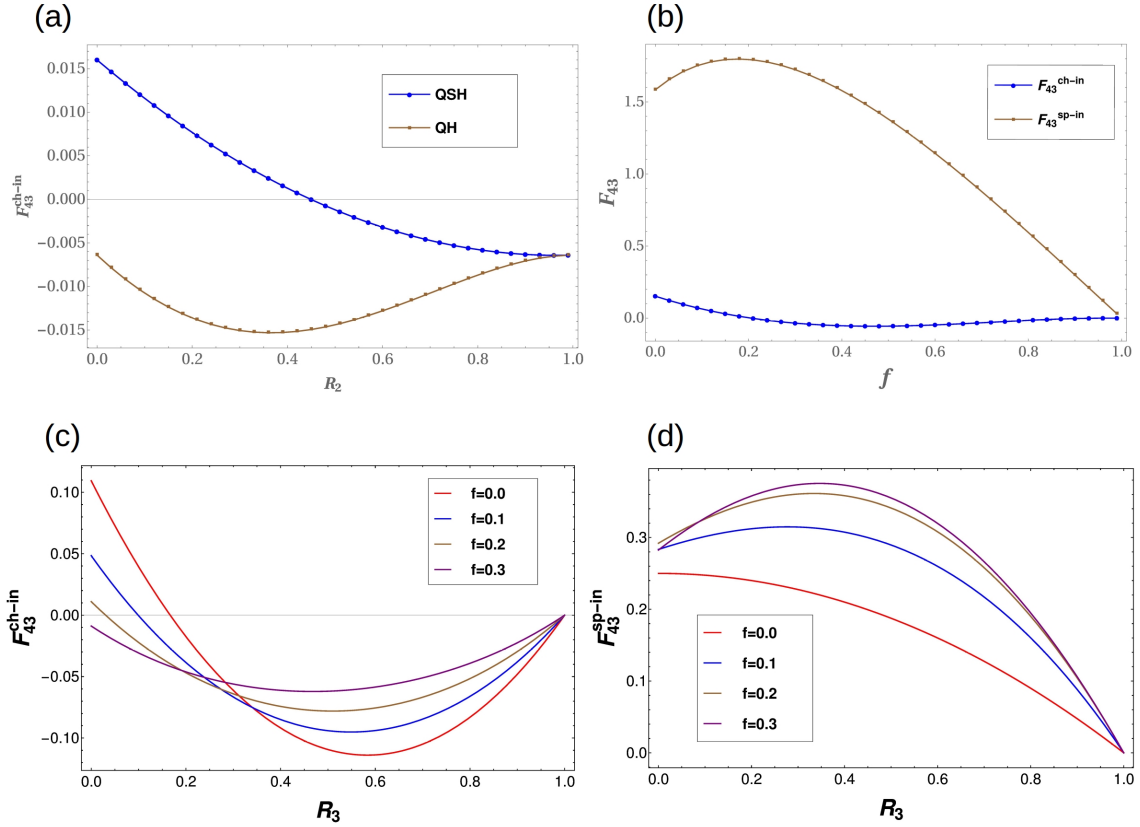
Figure 3.9: The effect of disorder on charge Fano factors (a) Topological QH versus Topological QSH cases, and the effect of intra-edge scattering on Fano factors in (b) for charge and spin Fano factors in trivial QSH phase. The charge Fano factor (c) and spin Fano factor (d) in the trivial phase ($f \neq 0$) are completely distinct from topological ($f = 0$) QSH phase. (a) Non-local charge Fano factors in topological helical QSH and topological chiral QH cases F_{43}^{ch} vs R_2 for all disordered probes ($R_4 = 0, R_3 = 0.2, R_1 = 0.8$) with inelastic scattering. Intra-edge scattering probability: $f = 0$. Note the sub-poissonian behaviour in both cases for the charge Fano factor. (b) Non-local charge Fano factor F_{43}^{ch} and spin Fano factor in trivial quasi-helical QSH sample F_{43}^{sp} vs f (intra-edge scattering probability) for two disordered probes ($R_3 = 0.2, R_1 = 0.8$) with inelastic scattering. Note the super Poissonian behaviour of the spin Fano factor as compared to the charge Fano factor. (c) Non-local charge Fano factors for topological($f = 0$) and trivial($f \neq 0$) QSH edge modes. F_{43}^{ch} vs R_3 for two disordered probes ($R_1 = 0.5$) with inelastic scattering as function of R_3. (d) Non-local spin Fano factors for topological($f = 0$) and trivial($f \neq 0$) QSH edge modes. F_{43}^{sp} vs R_3 for two disordered probes ($R_1 = 0.5$) with inelastic scattering as function of R_3.

and spin Fano factors in the trivial QSH case in Fig. 3.9(b). The charge Fano factor for topological QSH case changes sign while for QH case doesn't as a function of disorder. Further, in case of QSH we have two different Fano factors corresponding to charge and spin. The spin Fano factor is super-Poissonian regardless of whether the edge modes are topological or trivial while the charge Fano factor is sub-Poissonian. Thus, the spin Fano factor can also be a good arbiter of the presence or absence of topological helical edge modes. In Figs. 3.9(c) the charge Fano factors are plotted as function of disorder for increasing intra edge scattering (f), for the topological case while Fano factor changes sign as function of disorder as intra edge scattering increases, i.e., edge modes are in trivial regime, the charge Fano factors turn more and more negative. Thus one can conclude that for trivial quasi-helical edge modes charge Fano factors will be negative. In Fig. 3.9(d) we plot the spin Fano factor, although there is no sign change but entering the trivial regime the spin Fano factor increases in magnitude for increasing intra-edge scattering f. The charge shot noise measured in our case is sub-Poissionian, and the charge Fano factor is well below $1/3$, which is in agreement with the experimental work of Ref. [103] on QSH systems. We summarize the main results on distinction between chiral and helical edge modes and second between topological and trivial origins of QSH edge modes in two Tables 3.1 and 3.2.

3.7 Conclusion

The aim of this chapter was to distinguish topological helical QSH edge modes from chiral QH edge mode via non-local HBT noise measurement rather than present method of conductance measurement. It is also required to identify the topological origin of QSH edge modes via non-local HBT noise measurements since in presence of disorder or inelastic scattering conductance measurements to distinguish them (topological and trivial helical

Table 3.1: Topological Helical vs. Topological Chiral edge modes via non-local HBT correlations.

	QH Edge Mode	QSH Edge Mode	
	Shot Noise	Charge Shot Noise	Spin Shot Noise
Two Probe Disorder	0	0	0
All Probe Disorder	$-\frac{2e^2}{h}\|eV\|\frac{T_1^2 T_3 T_4 R_2^2 R_3}{a^4}$	$-\frac{2e^2}{h}\|eV\|\frac{T_1^2 T_3 T_4 (R_2^2 R_3 + R_4)}{a^4}$	Identical to charge
Two Probe Disorder + Inelastic Scattering	$-\frac{2e^2}{h}\|eV\|[T_1^2 T_3 R_3]$	$-\frac{2e^2}{h}\|eV\|\left[\frac{T_1 T_3 R_3}{2} - \frac{T_1 T_3 R_1 (R_1 + R_3)}{4}\right]$	Identical to charge
All Probe Disorder + Inelastic Scattering	Negative	Positive /Negative	Identical to charge
Charge Fano Factor	sub-poissonian, no sign change	sub-poissonian, changes sign	absent
Spin Fano Factor	absent	sub-poissonian	super-poissonian

edge modes) is not a reliable method as shown in the introduction of this chapter. To fulfil these twin aims, disorder is introduced at the contacts of a four terminal QH and QSH samples as shown in chapter 2 and inelastic scattering via voltage probe 2 rather than within the sample. The results are derived following Buttiker method as shown in Refs. [15, 14] for QH and Ref. [102] for QSH samples. It is shown in this chapter while these non-local HBT noise can be positive with topological helical QSH edge modes but will always be negative with chiral QH edge modes. So, one can differentiate between chiral or helical edge modes just by looking at the sign of HBT noise in those systems rather than its magnitude. Further, it is shown that the difference between the non-local charge and spin correlations can distinguish between the topological or trivial helical edge modes. The non-local charge correlations turn completely negative for trivial quasi-helical edge modes while the non-local spin correlations turn completely positive. In Table 3.1 the results for

Table 3.2: Topological helical vs. Trivial quasi-helical edge modes via non-local HBT correlations.

	Topological Helical	Trivial Helical
Non-local charge noise correlations	positive	turn completely negative
Non-local Spin Noise correlations	maybe positive/negative	turn completely positive
Charge Fano factor	changes sign	No sign change (completely negative)
Spin Fano factor	positive but small	positive and large

the distinction between chiral and Helical edge modes are summarized while in Table 3.2 the differences between trivial and topological QSH edge modes are summarized. To end, it is pointed out that although this chapter exclusively focused on chiral and helical edge modes and their topological origins the detection technique (Non-local HBT correlations) used in this chapter can be a very effective tool to probe helicity and its origin in Weyl semi metals[104] too. Moreover, this positive HBT cross correlation observed in topological QSH edge modes could also be a signature of entanglement in these systems, for which one need to check the violation of Bell's inequality which can confirm whether the edge modes are entangled or not. For this further investigations are needed.

4. Role of helical edge modes in the chiral quantum anomalous Hall state

"In order to describe a particular subculture, you might want to portray people who are typical or representative of that subculture; but to dramatize it, to make it an interesting setting for a story, you want to bring someone anomalous into that setting, to see how she conforms to it, and it to her."

– Jonathan Dee

4.1   Introduction

Quantum anomalous Hall (QAH) effect, the third member of the Hall family, is seen in ferromagnetic topological insulators in absence of magnetic field at low temperatures[44, 47, 49]. QAH edge modes are chiral and spin polarized unlike quantum Hall (QH) edge modes which are chiral but spin-unpolarized. QAH edge modes are either spin up polarized or spin down polarized depending on the magnetization direction in a ferromagnetic topological insulator. The importance of QAH edge modes lies in the fact that they arise in absence of magnetic field which is the main reason for occurrence of QH edge modes. Being chiral and spin polarized QAH edge modes can be used in spintronic devices for spin transport as well as low power information processing[48, 49]. However, experiments to detect a true

QAH effect haven't been completely conclusive. Having said that, the experiment depicted in Ref. [47] is most probably a detection of a single topological chiral quantum anomalous Hall(QAH) edge mode. There have been some other quite recent experiments[48, 49, 44] where it has been reported that QAH edge modes occur in conjunction with quasi helical quantum spin Hall(QSH) edge modes[45]. Quasi-helical QSH edge mode are prone to backscattering and are nothing but QSH edge modes which occur in a trivial insulator[43]. In chapter 3 we looked into the case of quasi-helical edge modes occurring in a trivial insulator. The experiments which "see" QAH edge modes are in fact designed out of QSH edge mode setups in a topological insulator. By applying an extra Ferromagnetic layer or otherwise, an energy gap is sought to be created between the pair of helical edge modes in a QSH sample splitting them away from each other and suppressing one of them, leads to single chiral QAH edge mode transport in a sample. However, contrary to expectation it is not just a chiral QAH mode which was seen in the experiments in Refs. [48, 49, 44]. QAH edge modes seen in Refs. [48, 49, 44] have additional quasi-helical QSH edge modes moving along side[45].

Helical QSH edge modes from which chiral QAH edge modes evolve occur in topological insulators[44, 48, 49]. However, as discussed in chapter 3 and shown in Ref. [43] quasi-helical edge modes occur in a trivial insulator. Applying a similar technique of attaching a ferromagnetic layer to a trivial insulator, one can make quasi-helical edge modes evolve into chiral QAH edge modes. However, in the latter case, the chiral QAH edge mode so produced wont have a topological character and therefore this chiral QAH edge mode won't be protected against backscattering. Now this begs the question how can one be sure of the topological character of QAH edge modes.

Another question which can crop up is, does the topological nature of the QAH edge modes which evolve from helical QSH edge modes in a topological insulator survive the evolution. This "evolution" from helical QSH to chiral QAH edge mode as has been described in

Refs. [48, 49, 44] is via addition of magnetic impurities or a ferromagnetic layer. This may destroy their topological character since helical QSH edge modes are susceptible to spin flip scattering in presence of magnetic impurities. In this context the aim of this chapter is a substantial 'What If?' question- in case QSH edge modes, from which QAH edge modes evolve, are not topologically-protected then the QAH edge modes wont be topologically-protected too and thus unfit for use in any applications, becomes relevant. Further, as a corollary one can also ask if the topological-protection of QSH edge modes does not carry over during the evolution process to QAH edge modes then the 'What if?' scenario becomes apparent again. In those QAH experiments[44, 48, 49] what is quite evident is that the quantization of Hall resistance is attributed to chiral topological QAH edge modes which exist in combination with quasi helical QSH edge modes. What this chapter aims to reveal is that a chiral trivial QAH edge mode which exists in combination with quasi helical QSH edge modes gives the quantization of Hall resistance and not a chiral topological QAH edge mode when occurring with quasi-helical QSH edge modes. Thus, a shadow of doubt creeps up regarding the interpretation of the experiments in Refs. [44, 48, 49].

The focus is specifically on 4 and 6 terminal quantum anomalous Hall samples. Three cases are distinguished one in which there is just a single chiral QAH edge mode which is topological in character (this hasn't been experimentally seen), the second wherein the chiral topological QAH edge mode exists along with a pair of trivial QSH edge modes (this case is the supposed experimental result as in Refs. [48, 49, 45]) and finally the case wherein a trivial QAH edge mode exists with a pair of trivial QSH edge modes (the 'What If?' scenario). Both the 4 terminal and 6 terminal samples are analysed in two distinct regimes-A. when there is disorder but no inelastic scattering and B. when both disorder and inelastic scattering are present in the sample. The disorder considered in our sample is restricted to terminal/contacts while inelastic scattering is present inside the sample and leads to the energy equilibration of the edge modes, see chapter 2 and Refs. [12, 1, 2] for

further details on energy equilibration as applied in different contexts in quantum Hall and quantum spin Hall samples.

4.1.1 This chapter

The structure of this chapter is as follows- beginning with the Landuer-Buttiker formalism for a multi terminal QAH sample in section 4.2, the three cases as explained above- chiral (topological) QAH edge mode in a four terminal QAH sample is discussed in section 4.2.1, chiral (topological) QAH edge mode along with quasi-helical edge modes in a four terminal QAH sample in section 4.2.2 and chiral (trivial) QAH edge mode along with quasi-helical edge modes in a four terminal QAH sample in section 4.2.3. In each of these sections the effect of only disorder and both disorder and inelastic scattering on Hall resistance(R_H), two terminal (local) resistance R_{2T} and finally the non-local resistance R_{NL} are studied. Next the focus is on six terminal QAH sample and herein too the effect of only disorder and both disorder and inelastic scattering on longitudinal resistance (R_L) is studied for the aforesaid three cases in sections 4.3.1, 4.3.2 and 4.3.3 respectively. Then the results of some recent QAH experiments reporting finite longitudinal resistance and a loss of quantization of the Hall resistance as temperature increases is discussed in section 4.4. Finally, the chapter concludes in section 4.5 with a summary of the results.

4.2 Four terminal quantum anomalous Hall sample

In a quantum anomalous Hall (QAH) sample, since edge modes are spin polarized, we can use the Landauer-Buttiker formalism for the quantum spin Hall case. According to this formalism, for a multi-terminal device at zero temperature, the current at contact i is given
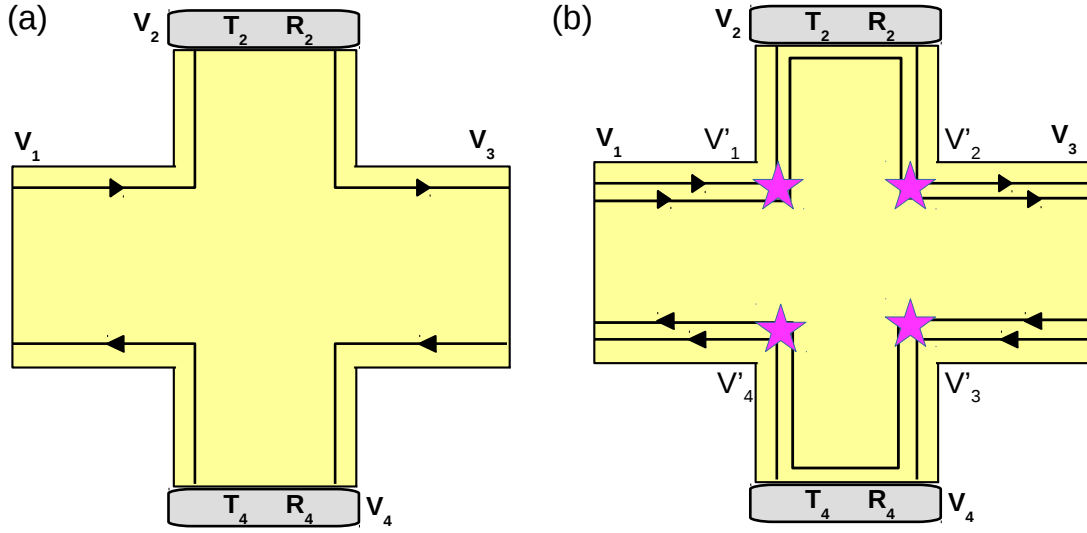
Figure 4.1: Four terminal quantum anomalous Hall bar showing chiral (Topological) QAH edge mode with (a) disorder at contacts 2 and 4, (b) disorder and inelastic scattering: R_2, T_2 and R_4, T_4 represent the reflection and transmission probability of edge modes from and into contact 2 and 4 respectively.

as[33, 10, 12]:

$$I_i = \sum_{\substack{j=1 \\ j\neq i}}^{N} \sum_{\sigma,\sigma'} [G_{ji}^{\sigma\sigma'} V_i - G_{ij}^{\sigma\sigma'} V_j] = \frac{e^2 M}{h} \sum_{\substack{j=1 \\ j\neq i}}^{N} \sum_{\sigma,\sigma'} [T_{ji}^{\sigma\sigma'} V_i - T_{ij}^{\sigma\sigma'} V_j], \qquad (4.1)$$

where $T_{ij}^{\sigma\sigma'}$ is the transmission probability for an electron from contact j to contact i with initial spin σ' to final spin σ, V_i is the potential bias at contact i and M is the number of edge modes.

4.2.1   Chiral topological QAH edge mode

The four terminal sample is shown in Fig. 4.1. We calculate the Hall resistance $R_H = R_{13,24}$, the local (two probe) resistance $R_{2T} = R_{13,13}$ and the non-local resistance $R_{NL} = R_{14,23}$ for various cases starting with just a single chiral(topological) QAH edge mode, then the chiral(topological) QAH edge mode with quasi-helical QSH edge modes and finally the case of chiral(trivial) QAH edge mode with quasi-helical QSH edge modes.

4.2.1.1 Effect of disorder

Herein we consider two of the contacts (2,4) to be disordered, see Fig. 4.1(a). Relations between the currents and voltages at the various terminals can be deduced from the conductance matrix, given below:

$$
G = \frac{e^2 M}{h}
\begin{pmatrix}
1 & 0 & -R_4 & -T_4 \\
-T_2 & T_2 & 0 & 0 \\
-R_2 & -T_2 & 1 & 0 \\
0 & 0 & -T_4 & T_4
\end{pmatrix}.
\tag{4.2}
$$

$R_i = D_i$ and $T_i = 1 - D_i$ (D_i is the strength of disorder at contact i) represent the reflection and transmission probabilities at contact i with $R_i + T_i = 1$ (for $i = 2, 4$). In Fig. 4.1(a), M, the no. of edge modes is one for clarity. Here the diagonal elements G_{ii} is defined as $G_{ii} = \sum_{j \neq i, \sigma, \sigma'} G_{ji}^{\sigma \sigma'}$ and non-diagonal elements $G_{ij} = \sum_{\sigma, \sigma'} G_{ij}^{\sigma \sigma'}$. The diagonal element $G_{11} = \sum_{j=2}^{4} G_{j1}$ where $G_{j1} = \frac{e^2 M}{h} (T_{j1}^{\uparrow\uparrow} + T_{j1}^{\uparrow\downarrow} + T_{j1}^{\downarrow\uparrow} + T_{j1}^{\downarrow\downarrow})$, $j = 2, 3, 4$. From Fig. 4.1(a) we see that an spin up edge state after coming out of contact 1 can either transmit to contact 2 with probability T_2, i.e., $T_{21}^{\uparrow\uparrow} = T_2$ or it can reflect from contact 2 with probability R_2 and transmit to contact 3 without reflection, i.e., $T_{31}^{\uparrow\uparrow} = R_2$. Since only spin up edge state is present in topological QAH case, transmission probability for other spin components are zero. Thus $(1,1)^{th}$ element of the conduction matrix G reduces to $\frac{e^2}{h} M (T_{21}^{\uparrow\uparrow} + T_{31}^{\uparrow\uparrow}) = \frac{e^2}{h} M$ (Since the transmission probabilities $T_{21}^{\uparrow\uparrow} + T_{21}^{\uparrow\uparrow} = T_2 + R_2 = 1$). Similarly rest of the elements of the conduction matrix can be derived. We can check from the conduction matrix- the summation of all the elements of each row or column is zero, which is the necessary condition for the conservation of current. Choosing reference potential $V_3 = 0$, further since 2 and 4 are voltage probes, $I_2 = I_4 = 0$, we thus have $V_2 = V_1$ and $V_3 = V_4 = 0$. So, local (two terminal) resistance $R_{2T}^{QAH} = R_{13,13} = \frac{h}{e^2 M}$. Hall resistance- $R_H^{QAH} = R_{13,24} = \frac{V_2 - V_4}{I_1} = \frac{h}{e^2 M}$. Disorder has no effect on the topological chiral QAH edge mode, the Hall resistance and

local resistance remain the same as in the ideal(zero disorder) case. Finally, to calculate the non-local resistance R_{NL} we consider $2, 3$ as voltage probes and $1, 4$ as current probes, we get $V_2 = V_3$ which gives $R_{NL} = 0$. Thus disorder has no effect on a single chiral(topological) QAH edge mode.

4.2.1.2 Effect of disorder and inelastic scattering

Similar to before, we consider two of the contacts $(2, 4)$ are disordered, see Fig. 4.1(b). Here the inelastic scattering is shown by starry blobs as in Fig. 4.1(b). Inelastic scattering doesn't take place only at a particular point, it can take place any where in the sample: For representation purpose only we put starry blobs. The electrons in-coming from probe 1 with energy $\frac{e^2}{h} R_2 V_1$ are equilibrated with the electrons coming from 2 with energy $\frac{e^2}{h} T_2 V_2$ to a new energy $\frac{e^2}{h}(R_2 + T_2) V_2' = \frac{e^2}{h} V_2'$. Similarly electrons coming from probe 3 are equilibrated with the electrons entering from probe 4 to a new energy as shown below-

$$
\begin{aligned}
\frac{e^2 M}{h} R_2 V_1 + \frac{e^2 M}{h} T_2 V_2 &= \frac{e^2 M}{h} V_2', & \frac{e^2 M}{h} V_1 &= \frac{e^2 M}{h} V_1', \\
\frac{e^2 M}{h} R_4 V_3 + \frac{e^2 M}{h} T_4 V_4 &= \frac{e^2 M}{h} V_4', & \frac{e^2 M}{h} V_3 &= \frac{e^2 M}{h} V_3'.
\end{aligned}
\tag{4.3}
$$

The currents and voltages at the contacts from 1 to 4 are related by the equations-

$$
\begin{aligned}
I_1 &= \frac{e^2 M}{h}(V_1 - V_4'), \\
I_i &= \frac{e^2 M}{h} T_i (V_i - V_{i-1}') \quad \text{for } i = 2, 3, 4.
\end{aligned}
\tag{4.4}
$$

Choosing reference potential $V_3 = 0$ and $I_2 = I_4 = 0$, since 2 and 4 are voltage probes, we thus derive $V_2 = V_1$ and $V_3 = V_4 = 0$. So, local (two probe) resistance $R_{2T}^{QAH} = R_{13,13} = \frac{h}{e^2 M}$. The Hall resistance $R_H^{QAH} = R_{13,24} = \frac{V_2 - V_4}{I_1} = \frac{h}{e^2 M}$. Similarly non-local resistance is derived as before-$R_{NL}^{QAH} = (V_2 - V_3)/I_1 = 0$. So inelastic scattering too, like disorder at voltage
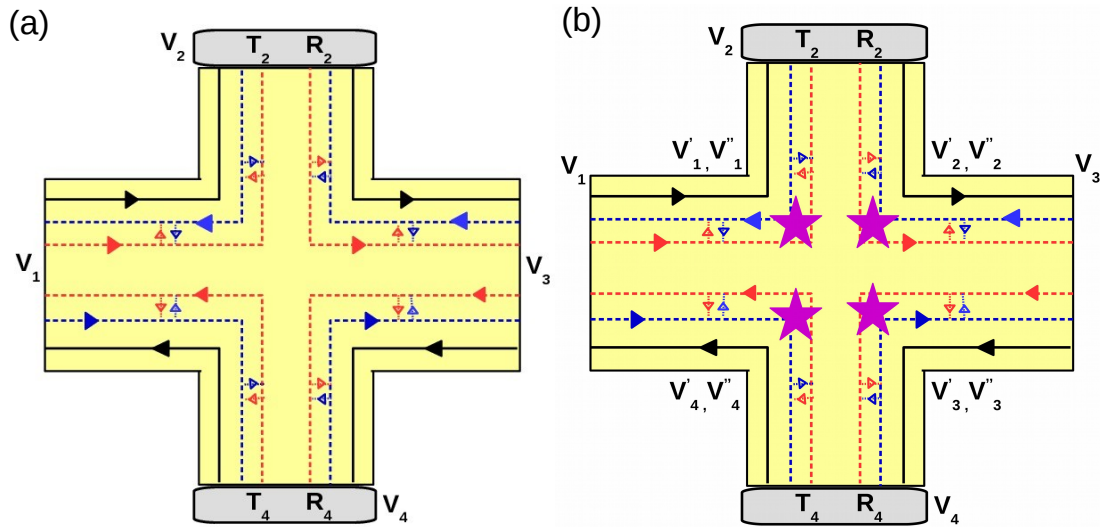
Figure 4.2: Four terminal quantum anomalous Hall bar showing chiral (topological) QAH edge mode with quasi-helical QSH edge modes with (a) disorder at contacts 2 and 4, (b) disorder at contacts $2, 4$ with inelastic scattering in sample represented by starry blobs. R_2, T_2 and R_4, T_4 represent the reflection and transmission probability of edge modes from and into contact 2 and 4 respectively.

probe has no effect on the a single chiral(topological) QAH edge mode.

4.2.2 Chiral (topological) QAH edge mode with quasi-helical edge modes

Herein we calculate first the effect of disorder and then the effect of both disorder and inelastic scattering on chiral (topological) QAH edge modes along with quasi-helical edge modes. Since the chiral QAH edge modes are topological, they aren't prone to backscattering while quasi-helical edge modes can backscatter via spin-flip scattering among themselves. The four terminal system with chiral (topological) QAH edge mode with quasi-helical edge modes is shown in Figs. 4.2(a,b). The solid black line in Fig. 4.2 represents chiral (topological) QAH edge mode while blue and red dotted lines represents spin up and spin down quasi-helical edge modes with small arrows showing the possibility of backscattering between them. Magenta coloured starry blobs shown in Fig. 4.2(b) represents the inelastic scattering via electron-electron or electron-phonon interaction. The spin flip probability between two

quasi-helical edge modes is f.

4.2.2.1 Effect of disorder

Herein, as before we consider two of the contacts 2 and 4 to be disordered, see Fig. 4.2(a). The relations between currents and voltages at the various terminals can be obtained from the conductance matrix below:

$$G = \frac{e^2 M}{h} \begin{pmatrix} T_{11} & -T_{12} & -T_{13} & -T_{14} \\ -T_{21} & -T_{22} & -T_{23} & T_{24} \\ T_{31} & T_{32} & T_{33} & T_{34} \\ T_{41} & T_{42} & T_{43} & T_{44} \end{pmatrix}, \tag{4.5}$$

where

$$
\begin{aligned}
T_{11} &= (3 - 2f - a_1 R_2^2 (1-f)/(a) - R_4^2 (1-f) a_1/(c)), \\
T_{12} &= (1-f)T_2/(1 - R_2 f), \\
T_{13} &= ((1-f)^2 R_2/a + ((1-f)^2 + (1-f)^2)R_4 + R_4^3 a_1^2/c), \\
T_{14} &= ((-2 + f + fR_4)T_4)/(-1 + fR_4), \\
T_{21} &= ((-2 + f + fR_2)T_2)/(-1 + fR_2), \\
T_{22} &= T_2(3 - 2fT_2/(1 - fR_2)), \\
T_{23} &= (1-f)T_2/(1 - R_2 f), \qquad\qquad T^{24} = 0, \tag{4.6}
\end{aligned}
$$

with $a = 1 - R_2^2 f^2, c = 1 - R_4^2 f^2, a_1 = f(1-f)$. By interchanging R_2 and R_4 in the above expressions for T_{11}, $T_{12},..,T_{23}$ rest of the transmission probabilities T_{31} to T_{44} can be deduced. Here the diagonal elements G_{ii} is defined as $G_{ii} = \sum_{j=1, j \neq i, \sigma, \sigma'}^{4} G_{ji}^{\sigma \sigma'}$ and non-diagonal elements $G_{ij} = \sum_{\sigma, \sigma'} G_{ij}^{\sigma \sigma'}$. The non-diagonal element, say $G_{23} = \sum_{\sigma \sigma'} \frac{e^2 M}{h} T_{23}^{\sigma \sigma'}$ can be explained as follows. The transmission probabilities are calculated in this way-

say $T_{23} = \sum_{\sigma\sigma'} T_{23}^{\sigma\sigma'}$, the transmission probability of electron from terminal 3 to 2 can be explained as the sum of paths available from 3 to 2 for one chiral topological edge mode and one pair of trivial helical edge modes. An electron in the topological edge mode coming out of probe 3 has probability zero to reach probe 2. But an electron in the trivial helical edge mode has finite probability to reach probe 2 from 3. An electron coming out of probe 3 can reach probe 2 with probability $T_2(1-f)$, but that is just one path, it can also reach 2 with probability $fR_2T_2(1-f)$ following a second path due to spin flip scattering, similarly a third path is $f^2R_2^2T_2(1-f)$. Thus, we can form an infinite number of paths from probe 3 to 2, these can be summed to get the total transmission probability as $T_{23} = \frac{T_2(1-f)}{(1-R_2f)}$. Similarly, the other transmission probabilities in Eq. (4.6) are obtained. We can check from the conduction matrix- the summation of all the elements of each row or column is zero, which is the necessary condition for the conservation of current. Choosing reference potential $V_3 = 0$, and since 2 and 4 are voltage probes, we derive the local (two probe) resistance in absence of disorder ($R_2 = R_4 = 0$) as $R_{2T}^{Topo} = R_{13,13} = \frac{h}{e^2 M} \frac{3-2f}{5-6f+2f^2}$. The Hall resistance- $R_H^{Topo} = R_{13,24} = \frac{h}{e^2 M} \frac{1}{(5+2f^2-6f)}$. Similarly, as before non-local resistance is deduced as $R_{NL}^{Topo} = \frac{h}{e^2 M} \frac{(2-f)(1-f)(3-2f)}{(5-6f+2f^2)(7-9f+3f^2)}$. For general case (i.e., with disorder) the expressions for R_H, R_{2T} and R_{NL} are too large to be reproduced here, so we will analyse them via plots, see Figs. 4.3(a-d).

4.2.2.2 Effect of disorder and inelastic scattering

Herein we consider the effect of both disorder and inelastic scattering on topological QAH edge modes as shown in Fig. 4.2(b). Here the inelastic scattering is shown by starry blobs as in Fig. 4.2(b). As the QAH edge mode is topological, it will not equilibrate its energy with trivial helical edge modes. Thus, topological chiral edge modes equilibrate only between themselves, these equilibrate to energy V_i'' where i is the contact index from 1 to 4. The
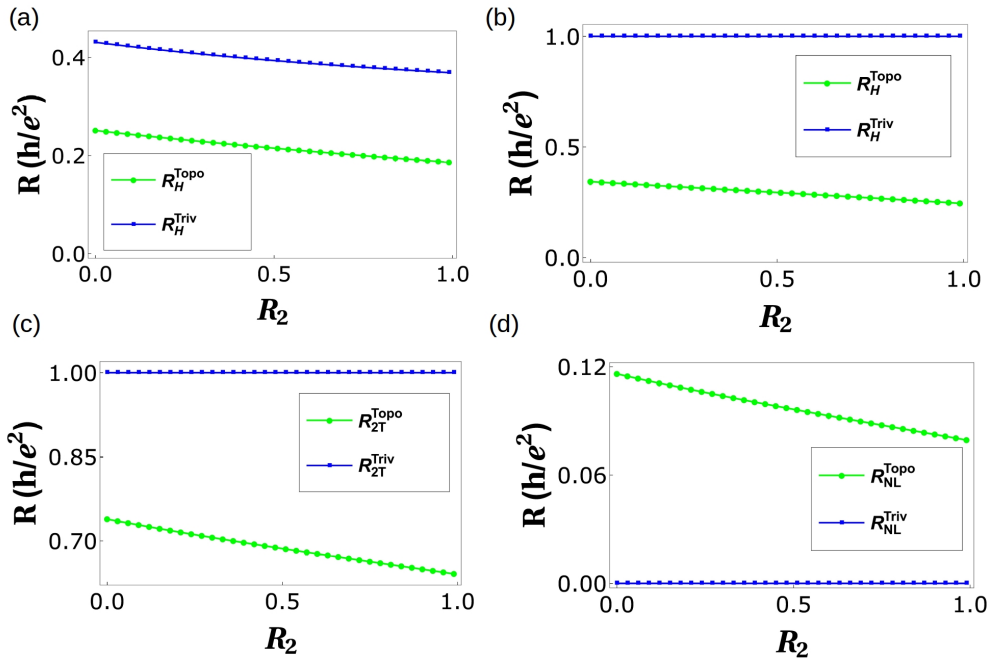
Figure 4.3: R_{NL}, R_{2T} and R_H vs. Disorder. (a) Hall resistance vs. Disorder R_2 with $R_4 = 0.5$ and spin-flip probability $f = 0.3$ and $f_0 = 0.3$, (b) Hall resistance vs. disorder R_2 with $R_4 = 0.5$ and spin-flip probability $f = 0.5$ and $f_0 = 0.5$. (c) Two-terminal resistance vs. Disorder R_2 with $R_4 = 0.5$ and spin-flip probability $f = 0.5$ and $f_0 = 0.5$, (d) Non-local resistance vs. Disorder R_2 with $R_4 = 0.5$ and spin-flip probability $f = 0.5$ and $f_0 = 0.5$.

trivial helical edge modes equilibrate with other helical edge modes and these equilibrate their energy to V_i'. The contacts 2 and 4 are disordered as in the previous case. The currents and voltages at the contacts from 1 to 4 are related by the equations-

$$
\begin{aligned}
I_1 &= \frac{e^2 M}{h}((3-2f)V_1 - V_4'' - (1-f)(V_1' + V_4')), \\
I_2 &= \frac{e^2 M}{h}((3T_2 - \frac{2T_2^2 f}{(1-R_2 f)})V_2 - T_2 V_1'' - \frac{T_2(1-f)}{(1-R_2 f)}(V_1' + V_2')), \\
I_3 &= \frac{e^2 M}{h}((3-2f)V_3 - V_2'' - (1-f)(V_2' + V_3')), \\
I_4 &= \frac{e^2 M}{h}((3T_4 - \frac{2T_4^2 f}{(1-R_4 f)})V_4 - T_4 V_3'' - \frac{T_4(1-f)}{(1-R_2 f)}(V_3' + V_4')),
\end{aligned}
$$

$$(4.7)$$

where the potentials V_i' and V_i'' are related to V_i by-

$$
V_1'' = V_1, \qquad \frac{e^2 M}{h}(R_2 V_1'' + T_2 V_2) = \frac{e^2 M}{h}V_2'',
$$

$$
V_3'' = V_3, \qquad \frac{e^2 M}{h}(R_2 V_3'' + T_2 V_4) = \frac{e^2 M}{h}V_4'',
$$

$$(4.8)$$

and

$$
(1-f)V_1 + \frac{T_2(1-f)}{(1-R_2 f)}V_2 + \frac{R_2(1-f)^2}{a}V_2') = ((1-f) + \frac{T_2(1-f)}{(1-R_2 f)} + \frac{R_2(1-f)^2}{a})V_1',
$$

$$
(1-f)V_3 + \frac{T_2(1-f)}{(1-R_2 f)}V_2 + \frac{R_2(1-f)^2}{a}V_1' = ((1-f) + \frac{T_2(1-f)}{(1-R_2 f)} + \frac{R_2(1-f)^2}{a})V_2',
$$

$$
(1-f)V_3 + \frac{T_4(1-f)}{(1-R_4 f)}V_4 + \frac{R_4(1-f)^2}{c}V_4' = ((1-f) + \frac{T_4(1-f)}{(1-R_4 f)} + \frac{R_4(1-f)^2}{c})V_3',
$$

$$
(1-f)V_1 + \frac{T_4(1-f)}{(1-R_4 f)}V_4 + \frac{R_4(1-f)^2}{c}V_3' = ((1-f) + \frac{T_4(1-f)}{(1-R_4 f)} + \frac{R_4(1-f)^2}{c})V_4',
$$

$$(4.9)$$

with $a = 1 - R_2^2 f^2, c = 1 - R_4^2 f^2$. Choosing reference potential $V_3 = 0$, and the contact 2 and 4 to be voltage probe as before, i.e., $I_2 = I_4 = 0$, we derive local (two probe) resistance
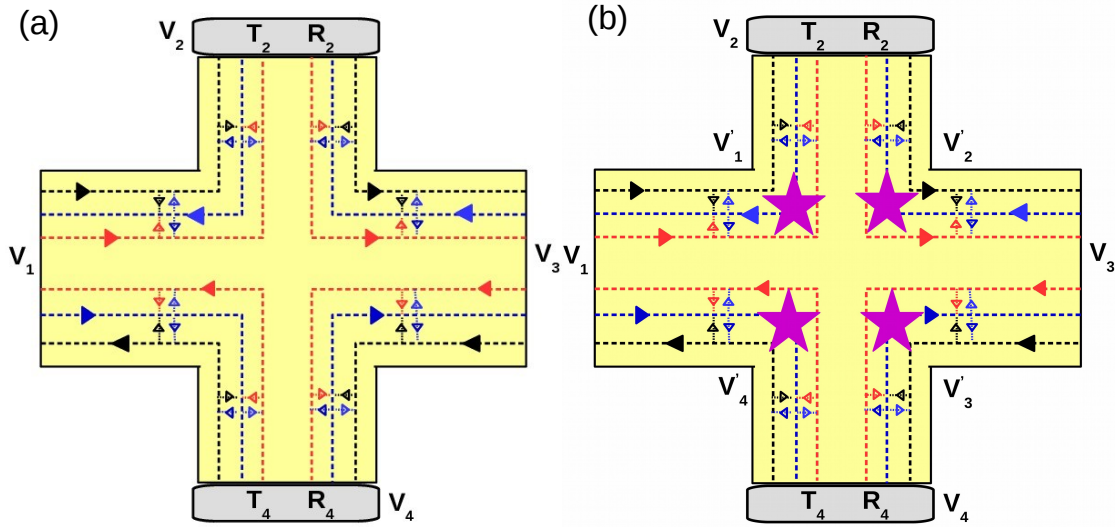
Figure 4.4: Four terminal quantum anomalous Hall bar showing Chiral (trivial) QAH edge mode with quasi-helical QSH edge modes with (a) disorder at contacts 2 and 4, (b) disorder and inelastic scattering: R_2, T_2 and R_4, T_4 represent the reflection and transmission probability of edge modes from and into contact 2 and 4 respectively.

in absence of disorder as $R_{2T}^{Topo} = R_{13,13} = \frac{h}{e^2 M} \frac{4-2f}{5-4f+f^2}$ (for $R_2 = R_4 = 0$). The Hall resistance $R_H^{Topo} = R_{13,24} = \frac{h}{e^2 M} \frac{2}{(5-4f+f^2)}$. For the general case (including disorder) the expressions for R_H, R_{2T} and R_{NL} are again large, hence they are analysed via plots, see Figs. 4.5(a-d).

4.2.3 Chiral (trivial) QAH edge mode with quasi-helical edge modes

Herein too we calculate first the effect of disorder and then the effect of both disorder and inelastic scattering on chiral (trivial) QAH edge modes along with quasi-helical edge modes. Since the chiral QAH edge modes aren't topological, they are prone to backscattering and behaves similar to a quasi-helical edge modes. The four terminal system with chiral (trivial) QAH edge mode with quasi-helical edge modes is shown in Figs. 4.4(a,b). The dashed black line in Fig. 4.4 represents chiral (trivial) QAH edge mode while blue and red dotted lines represents spin up and spin down quasi-helical edge modes with small arrows showing the possibility of backscattering between them. Magenta coloured starry blobs

shown in Fig. 4.4(b) represents the inelastic scattering via electron-electron or electron-phonon interaction. The spin flip probability between chiral (trivial) QAH edge mode and quasi-helical edge modes is f_0 while the same between two quasi-helical edge modes is f.

4.2.3.1 Effect of disorder

Herein as before we consider two of the contacts 2 and 4 to be disordered, see Fig. 4.4(a). The current-voltage relations are derived from the conductance matrix below:

$$
G = \frac{e^2 M}{h}
\begin{pmatrix}
T_{11} & -T_{12} & -T_{13} & -T_{14} \\
-T_{21} & -T_{22} & -T_{23} & T_{24} \\
T_{31} & T_{32} & T_{33} & T_{34} \\
T_{41} & T_{42} & T_{43} & T_{44}
\end{pmatrix},
\tag{4.10}
$$

where

$$
\begin{aligned}
T_{11} &= (3 - 2(f + f_0) - a_1 R_2^2 (1 - f - f_0)/(a) - R_4^2 (1 - f - f_0) a_1/(c)), \\
T_{12} &= ((1 - f - f_0) T_2/a + (1 - f - f_0) T_2 (f + f_0) R_2/a), \\
T_{13} &= ((1 - f - f_0)^2 R_2/a + ((1 - f)^2 + (1 - f_0)^2) R_4 + R_4^3 a_1^2/c), \\
T_{14} &= (T_4 (2 - f - f_0) + (f + f_0) T_4 R_4^2 a_1/c + T_4 R_4 a_1/c), \\
T_{21} &= ((2 - f - f_0) T_2 + T_2 R_2 a_1/a + T_2 R_2^2 a_1 (f + f_0)/a), \\
T_{22} &= (3 T_2 - T_2^2 (f + f_0)/a - T_2^2 R_2 (f + f_0)^2/a - T_2^2 (f + f_0)/a - T_2^2 R_2 (f^2 + f_0^2)/a), \\
T_{23} &= ((1 - f - f_0) T_2 (R_2 (f + f_0)/a + 1/a)), \\
T_{24} &= 0,
\end{aligned}
\tag{4.11}
$$

with $a = 1 - R_2^2 (f^2 + f_0^2), c = 1 - R_4^2 (f^2 + f_0^2), a_1 = f(1 - f) + f_0 (1 - f_0)$. By interchanging R_2 and R_4 in the above Eq. (4.11) rest of the transmission probabilities T_{31} to T_{44} can

be deduced. The non-diagonal element, say $G_{23} = \sum_{\sigma\sigma'} \frac{e^2 M}{h} T_{23}^{\sigma\sigma'}$ can be explained as

follows. The transmission probabilities, say $T_{23} = \sum_{\sigma\sigma'} T_{23}^{\sigma\sigma'}$, the transmission probability

of electron from terminal 3 to 2 can be explained as the sum of probabilities from 3 to

2 for all the edge modes over all possible paths. An electron coming out of probe 3 at

upper edge can reach probe 2 with probability $T_2(1 - f - f_0)$, but that is just one path, it

can also reach 2 with probability $(f + f_0)R_2 T_2(1 - f - f_0)$ following a second path due

to spin flip scattering, similarly probability for a third path is $(f^2 + f_0^2)R_2^2 T_2(1 - f - f_0)$.

These first, third, fifth.. paths form an infinite series with total transmission probability

$\frac{T_2(1-f-f_0)}{a}$ and second, fourth, sixth... paths form a infinite series with total transmission

probability $\frac{(f+f_0)R_2 T_2(1-f-f_0)}{a}$. So, the total transmission probability is sum of the two

and is written as T_{23} as in Eq. (4.11). Similarly, the other transmission probabilities in

Eq. (4.11) are obtained. We can check from the conduction matrix- the summation of

all the elements of each row or column is zero, which is the necessary condition for

the conservation of current. Choosing reference potential $V_3 = 0$, and $I_2 = I_4 = 0$ (as

2 and 4 are voltage probes) we derive local (two probe) resistance in absence of any

disorder as $R_{2T}^{Triv} = R_{13,13} = \frac{h}{e^2 M} \frac{3 - 2(f + f_0)}{5 - 6(f + f_0) + 2(f + f_0)^2}$. The Hall resistance- $R_H^{Triv} = R_{13,24} =$

$\frac{h}{e^2 M} \frac{1}{(5 + 2f^2 + 2(-3 + f_0)f_0 + f(-6 + 4f_0))}$ again for zero disorder. Similarly, as before the non-

local resistance is deduced as $R_{NL}^{Triv} = \frac{h}{e^2 M} \frac{(2 - f - f_0)(1 - f - f_0)(3 - 2f - 2f_0)}{(5 - 6(f + f_0) + 2(f + f_0)^2)(7 - 9(f + f_0) + 3(f + f_0)^2)}$ for zero

disorder. For, general case the expressions for R_H, R_{2T} and R_{NL} are again too large to be

reproduced here, so we will examine them via plots, see Figs. 4.3(a-d).

4.2.3.2 Effect of disorder and inelastic scattering

Herein, we consider the trivial QAH edge modes with both disorder and inelastic scattering

as shown in Fig. 4.4(b). Here the QAH chiral as well as helical both edge modes are in the

trivial phase, i.e., they are all prone to intra edge back scattering due to spin-flips. All the

edge modes interact among themselves leading to their energies being equilibrated to the

potential V_i' ('i' is from 1 to 4). The contacts 2 and 4 are disordered as in the previous case.
The currents and voltages at the contacts from 1 to 4 are related by the equations-

$$I_1 = \frac{e^2 M}{h}([3 - 2(f + f_0)]V_1 - [1 - (f + f_0)]V_1' - [2 - (f + f_0)]V_4'),$$

$$I_2 = \frac{e^2 M}{h}(T_2(3 - \frac{(2(f + f_0 + (f^2 + ff_0 + f_0^2)R_2)T_2)}{(1 - R_2^2(f^2 + f_0^2))})V_2 - \frac{[1 - (f + f_0)][1 + R_2(f + f_0)]T_2}{[1 - R_2^2(f^2 + f_0^2)]}V_2' -$$

$$\frac{[2 - (f + f_0) + ((1 - f)f + (1 - f_0)f_0)R_2 - (f - f_0)^2 R_2^2)T_2}{[1 - R_2^2(f^2 + f_0^2)]}V_1'),$$

$$I_3 = \frac{e^2 M}{h}([3 - 2(f + f_0)]V_3 - [1 - (f + f_0)]V_3' - [2 - (f + f_0)]V_2'),$$

$$I_4 = \frac{e^2 M}{h}(T_2(3 - \frac{(2(f + f_0 + (f^2 + ff_0 + f_0^2)R_4)T_4)}{(1 - R_4^2(f^2 + f_0^2))})V_4 - \frac{[1 - (f + f_0)][1 + R_4(f + f_0)]T_4}{[1 - R_4^2(f^2 + f_0^2)]}V_4' -$$

$$\frac{[2 - (f + f_0) + ((1 - f)f + (1 - f_0)f_0)R_4 - (f - f_0)^2 R_4^2)T_2}{[1 - R_4^2(f^2 + f_0^2)]}V_3'). \tag{4.12}$$

The relations between potentials V_i''s and V_i are written as follows.

$$(2 - f - f_0)V_1 + \frac{[1 - (f + f_0)][1 + (f + f_0)R_2]T_2}{[1 - R_2^2(f^2 + f_0^2)]}V_2 + \frac{R_2(1 - f - f_0)^2}{[1 - R_2^2(f^2 + f_0^2)]}V_2' = [(2 - f - f_0) + \frac{[1 - (f + f_0)][1 + (f + f_0)R_2]T_2}{[1 - R_2^2(f^2 + f_0^2)]}$$

$$+ \frac{R_2(1 - f - f_0)^2}{[1 - R_2^2(f^2 + f_0^2)]}]V_1', \frac{[2 - (f + f_0) + ((1 - f)f + (1 - f_0)f_0)R_2 - (f - f_0)^2 R_2^2)T_2}{[1 - R_2^2(f^2 + f_0^2)]}V_2 + [1 - (f + f_0)]V_3$$

$$+ \frac{(2 + (-2 + f)f + (-2 + f_0)f_0)R_2 + (f - f_0)^2 R_2^3}{[1 - R_2^2(f^2 + f_0^2)]}V_1' = [\frac{[2 - (f + f_0) + ((1 - f)f + (1 - f_0)f_0)R_2 - (f - f_0)^2 R_2^2)T_2}{[1 - R_2^2(f^2 + f_0^2)]} + [1 - (f + f_0)]$$

$$+ \frac{(-2 + f)f + (-2 + f_0)f_0)R_2 + (f - f_0)^2 R_2^3}{[1 - R_2^2(f^2 + f_0^2)]}]V_2', (2 - f - f_0)V_3 + \frac{[1 - (f + f_0)][1 + (f + f_0)R_4]T_4}{[1 - R_4^2(f^2 + f_0^2)]}V_4 + \frac{R_2(1 - f - f_0)^2}{[1 - R_2^2(f^2 + f_0^2)]}V_4'$$

$$= [(2 - f - f_0) + \frac{[1 - (f + f_0)][1 + (f + f_0)R_2]T_2}{[1 - R_2^2(f^2 + f_0^2)]} + \frac{R_2(1 - f - f_0)^2}{[1 - R_2^2(f^2 + f_0^2)]}]V_3',$$

$$\frac{[2 - (f + f_0) + ((1 - f)f + (1 - f_0)f_0)R_4 - (f - f_0)^2 R_4^2)T_4}{[1 - R_4^2(f^2 + f_0^2)]}V_4 + [1 - (f + f_0)]V_1 + \frac{(2 + (-2 + f)f + (-2 + f_0)f_0)R_4 + (f - f_0)^2 R_4^3}{[1 - R_4^2(f^2 + f_0^2)]}V_3'$$

$$= [\frac{[2 - (f + f_0) + ((1 - f)f + (1 - f_0)f_0)R_4 - (f - f_0)^2 R_4^2)T_4}{[1 - R_4^2(f^2 + f_0^2)]} + [1 - (f + f_0)] + \frac{(-2 + f)f + (-2 + f_0)f_0)R_4 + (f - f_0)^2 R_4^3}{[1 - R_2^2(f^2 + f_0^2)]}]V_4'. \tag{4.13}$$

Choosing reference potential $V_3 = 0$, and as before $I_2 = I_4 = 0$ (these are voltage probes),
we derive the local (two probe) resistance $R_{2T}^{Triv} = R_{13,13}$ and the Hall resistance $R_H^{Triv} = R_{13,24}$. Similarly, as before the non-local resistance is deduced as $R_{NL}^{Triv} = R_{14,23}$. The
expressions for R_H, R_{2T} and R_{NL} are large, so again we will analyse them via plots as in
Figs. 4.5(a-d).

In Table 4.1 we tabulate the results obtained so far. One important thing left out of our

Table 4.1: Comparison of chiral(topological) QAH edge modes, chiral(topological) QAH edge mode with quasi-helical QSH edge modes and chiral(trivial) QAH edge mode with quasi-helical QSH edge modes.

		QAH(topological)	QAH(topological) + Trivial QSH	QAH(trivial) + Trivial QSH
R_H	Ideal (zero disorder)	Quantized $\frac{e^2}{h}$ $R_H(\uparrow) = -R_H(\downarrow)$	Not quantized $R_H(\uparrow) = -R_H(\downarrow)$	Not quantized $R_H(\uparrow) = -R_H(\downarrow)$
	Finite disorder	Quantized $\frac{e^2}{h}$ $R_H(\uparrow) = -R_H(\downarrow)$	Not quantized $R_H(\uparrow) = -R_H(\downarrow)$	Not quantized $R_H(\uparrow) = -R_H(\downarrow)$
	Disorder + Inelastic scattering	Quantized $\frac{e^2}{h}$ $R_H(\uparrow) = -R_H(\downarrow)$	Not quantized (Fig. 4.5(a)) $R_H(\uparrow) \neq -R_H(\downarrow)$	Quantized (Fig. 4.5(a)) $R_H(\uparrow) = -R_H(\downarrow)$
R_{2T}	Ideal (zero disorder)	Quantized $\frac{e^2}{h}$ $R_{2T}(\uparrow) = R_{2T}(\downarrow)$	Not quantized $R_{2T}(\uparrow) = R_{2T}(\downarrow)$	Not quantized $R_{2T}(\uparrow) = R_{2T}(\downarrow)$
	Finite disorder	Quantized $\frac{e^2}{h}$ $R_{2T}(\uparrow) = R_{2T}(\downarrow)$	Not quantized (Fig. 4.3(b)) $R_{2T}(\uparrow) = R_{2T}(\downarrow)$	Not quantized (Fig. 4.3(b)) $R_{2T}(\uparrow) = R_{2T}(\downarrow)$
	Disorder + Inelastic scattering	Quantized $\frac{e^2}{h}$ $R_{2T}(\uparrow) = R_{2T}(\downarrow)$	Not quantized (Fig. 4.5(b)) $R_{2T}(\uparrow) \neq R_{2T}(\downarrow)$	Quantized (Fig. 4.5(b)) $R_{2T}(\uparrow) = R_{2T}(\downarrow)$
R_{NL}	Ideal (zero disorder)	0 $R_{NL}(\uparrow) = R_{NL}(\downarrow)$	Finite $R_{NL}(\uparrow) = R_{NL}(\downarrow)$	Finite $R_{NL}(\uparrow) = R_{NL}(\downarrow)$
	Finite disorder	0 $R_{NL}(\uparrow) = R_{NL}(\downarrow)$	Finite (Fig. 4.3(c)) $R_{NL}(\uparrow) = R_{NL}(\downarrow)$	Finite (Fig. 4.3(c)) $R_{NL}(\uparrow) = R_{NL}(\downarrow)$
	Disorder + Inelastic scattering	0 $R_{NL}(\uparrow) = R_{NL}(\downarrow)$	Finite (Fig. 4.5(c, d)) $R_{NL}(\uparrow) \neq R_{NL}(\downarrow)$	0 (Fig. 4.5(d)) $R_{NL}(\uparrow) = R_{NL}(\downarrow)$

Note: In the 4T QAH samples depicted in Figs. 4.1(a,b,c) the magnetization direction is ($\uparrow$) implying the QAH edge mode shown by black solid or dashed line is spin-up polarized. The conductance matrices depicted in Eqs. (4.2), (4.5) and (4.10) as well as the calculations shown in Eqs. (4.4), (4.7), (4.9), (4.12) and the 2T, Hall and non-local resistances derived and plotted in Figs. 4.3, 4.5 are therefore for magnetization ($\uparrow$). We follow similar procedure to calculate the resistances for magnetization direction ($\downarrow$) in which case the QAH edge modes shown by black solid or dashed lines in Figs. 4.6(a-d) will be spin-down polarized and mention the results in this Table.
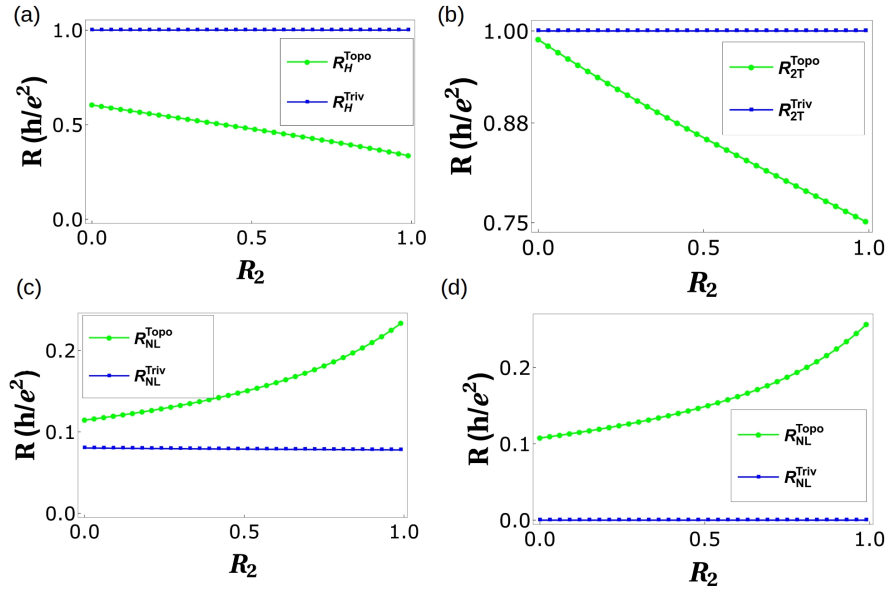
Figure 4.5: R_H, R_{2T} and R_{NL} under the effect of inelastic scattering. (a) Hall resistance vs. Disorder R_2 with parameters $R_4 = 0.5$ and spin-flip probability $f = f_0 = 0.5$, (b) Two terminal resistance vs. Disorder R_2 with parameters $R_4 = 0.5$ and spin-flip probability $f = 0.5$, $f_0 = 0.5$, (c) Non-local resistance vs. Disorder R_2 parameters $R_4 = 0.5$ and spin-flip probability $f = 0.3$, $f_0 = 0.3$, (d) Non-local resistance vs. Disorder R_2 parameters $R_4 = 0.5$ and spin-flip probability $f = 0.5$, $f_0 = 0.5$.

discussion so far has been the role of spin in QAH edge mode. A single chiral (topological) QAH should satisfy the following symmetry relations for $R_H(\uparrow) = -R_H(\downarrow)$ and $R_{NL} = 0$. We see that $R_{NL}(\uparrow) \neq R_{NL}(\downarrow)$ for topological QAH(with quasi helical QSH) while this isn't case for trivial QAH(with quasi helical QSH) edge modes, see Fig. 4.6. Importantly while in case of trivial QAH edge mode $R_{NL}^{Triv}(\uparrow) = R_{NL}^{Triv}(\downarrow) = 0$, for the case of topological QAH edge mode $R_{NL}^{Topo}(\uparrow) \neq R_{NL}^{Topo}(\downarrow) \neq 0$. In fact we see that R_{NL}^{Triv} for the case of disorder and inelastic scattering approaches zero similar to a single chiral QAH edge mode, while for the R_{NL}^{Topo} this doesn't, again leading to a contradiction with the way the experiments of Ref. [48] have been interpreted as in Ref. [45].
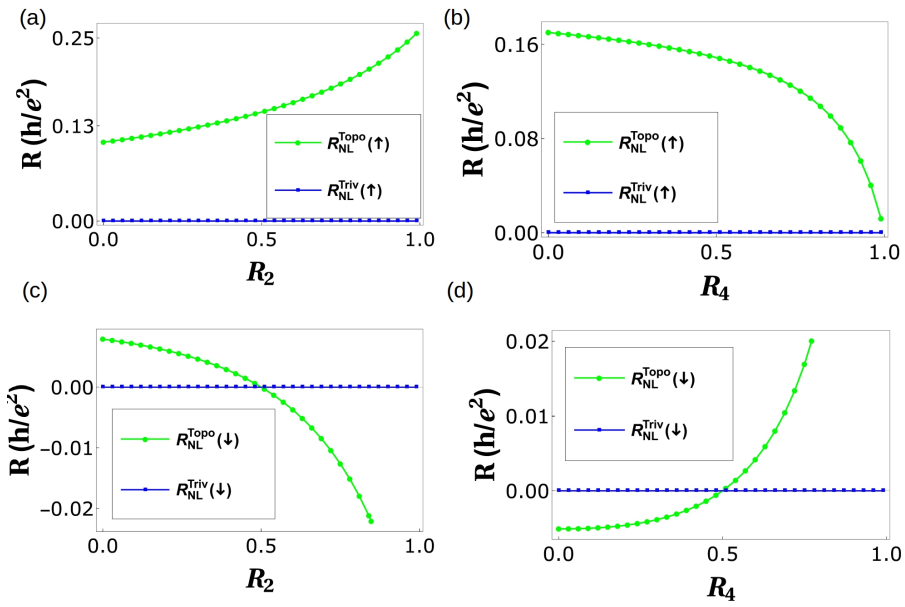
Figure 4.6: Non-local resistances ($R_{NL}(\uparrow)$) for magnetization direction ($\uparrow$) and ($R_{NL}(\downarrow)$) for magnetization direction ($\downarrow$) in presence of both disorder as well as inelastic scattering. (a) $R_{NL}(\uparrow)$ for chiral(topological) QAH edge mode with quasi-helical QSH edge modes and chiral (trivial) QAH edge mode with quasi-helical QSH edge modes for parameters $R_4 = 0.5, f = f_0 = 0.5$, (b) $R_{NL}(\uparrow)$ for chiral(topological) QAH edge mode with quasi-helical QSH edge modes and chiral (trivial) QAH edge mode with quasi-helical QSH edge modes for parameters $R_2 = 0.5, f = f_0 = 0.5$. (c) $R_{NL}(\downarrow)$ for chiral(trivial) QAH edge mode with quasi-helical QSH edge modes and chiral(trivial) QAH edge mode with quasi-helical QSH edge modes for parameters $R_4 = 0.5, f = f_0 = 0.5$, (d) $R_{NL}(\downarrow)$ for chiral(trivial) QAH edge mode with quasi-helical QSH edge modes and chiral(trivial) QAH edge modes with quasi-helical edge modes for parameters $R_2 = 0.5, f = f_0 = 0.5$.
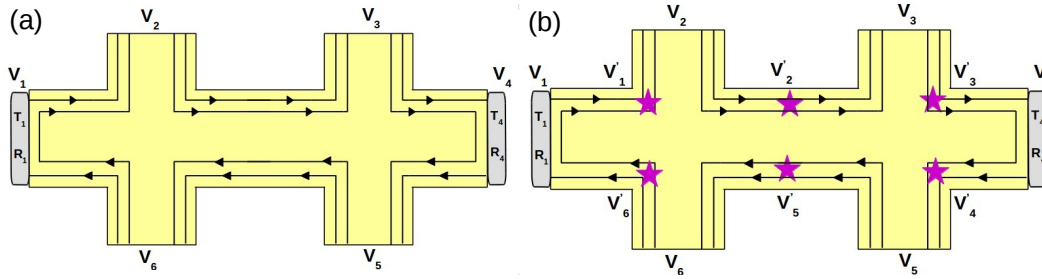
Figure 4.7: Six terminal chiral (Topological) QAH edge mode with (a) disorder at contacts 1, 4, (b) inelastic scattering and disorder at contacts 1, 4.

4.3 Six terminal quantum anomalous Hall bar

In this section we analyse a six terminal QAH bar, we especially focus on the longitudinal resistance R_L. For a single chiral(topological) QAH edge mode $R_L = 0$, but the experiments[48, 49, 44] revealed a finite longitudinal resistance. This result prompted the interpretation of the experiments [48, 49, 44] as seeing not just a chiral(topological) QAH edge mode but in addition also a pair of quasi-helical QSH edge modes[45]. Since a non zero R_L is the hallmark of helical QSH edge modes. Here we probe further by comparing as in sections before the three cases and try to find out if a topological QAH edge mode or a trivial QAH edge mode occurring with quasi-helical edge modes results in a non-zero R_L.

4.3.1 Chiral(topological) QAH edge mode

The six terminal sample is shown in Fig. 4.7. We calculate the longitudinal resistance $R_L = R_{23,14}$ for various cases starting with just a single chiral(topological) QAH edge mode, then the chiral(topological) QAH edge mode with quasi-helical QSH edge modes and finally the case of chiral(trivial) QAH edge mode with quasi-helical QSH edge modes. For each of these cases first we study the effect of disorder and then the effect of both disorder and inelastic scattering similar to four terminal case. The black solid line in Fig. 4.7 represents chiral (topological) QAH edge mode.

4.3.1.1 Effect of disorder

Herein we consider two of the contacts 1 and 4 to be disordered, see Fig. 4.7(a). The relations between the currents and voltages at the various terminals can be derived from the conductance matrix below:

$$G = \frac{e^2 M}{h} \begin{pmatrix} T_1 & 0 & 0 & 0 & 0 & -T_1 \\ -T_1 & 1 & 0 & 0 & 0 & -R_1 \\ 0 & -1 & 1 & 0 & 0 & 0 \\ 0 & 0 & -T_4 & T_4 & 0 & 0 \\ 0 & 0 & -R_4 & -T_4 & 1 & 0 \\ 0 & 0 & 0 & 0 & -1 & 1 \end{pmatrix}. \tag{4.14}$$

R_i and T_i represent the reflection and transmission probabilities at contact i with $R_i + T_i = 1$ (for $i = 1, 4$). In Fig. 4.7(a), M, the no. of edge modes is one for clarity. Here the diagonal elements G_{ii} is defined as $G_{ii} = \sum_{j \neq i, \sigma, \sigma'} G_{ji}^{\sigma\sigma'}$ and non-diagonal elements $G_{ij} = \sum_{\sigma, \sigma'} G_{ij}^{\sigma\sigma'}$. The diagonal element $G_{11} = \sum_{j=2}^{6} G_{j1}$ where $G_{j1} = \frac{e^2 M}{h}(T_{j1}^{\uparrow\uparrow} + T_{j1}^{\uparrow\downarrow} + T_{j1}^{\downarrow\uparrow} + T_{j1}^{\downarrow\downarrow}), j = 2, 3, 4, 5, 6$. From Fig. 4.7(a) we see that an spin up edge state comes out of contact 1 with probability T_2 and enters contact 2 without reflection, i.e., $T_{21}^{\uparrow\uparrow} = T_2$. Since only spin up edge state is present in topological QAH case, transmission probability for other spin components are zero. Thus $(1,1)^{th}$ element of the conduction matrix G reduces to $\frac{e^2}{h} M (T_{21}^{\uparrow\uparrow} = \frac{e^2}{h} M T_1$ (Since the transmission probability $T_{21}^{\uparrow\uparrow} = T_1$). Similarly rest of the elements of the conduction matrix can be derived. We can check from the conduction matrix the summation of all the elements of each row or column is zero, which is the necessary condition for the conservation of current. Choosing reference potential $V_4 = 0$ and $I_2 = I_3 = I_5 = I_6 = 0$ (as these are voltage probes), we get $V_3 = V_2 = \frac{T_1 V_1}{1 - R_1 R_4}$ and $V_3 = V_4 = \frac{T_1 R_4 V_1}{1 - R_1 R_4}$. So the longitudinal resistance $R_L^{QAH} = (V_2 - V_3)/I_1 = 0$. So disorder has no effect on the longitudinal resistance for a single chiral QAH edge mode.

4.3.1.2 Effect of disorder and inelastic scattering

Herein we consider two of the contacts $(1,4)$ to be disordered, see Fig. 4.7(b). The electrons incoming from probe 6 with energy $\frac{e^2 M}{h} R_1 V_6'$ are equilibrated with the electrons incoming from probe 1 with energy $\frac{e^2 M}{h} T_1 V_1$ to a new energy $\frac{e^2 M}{h}(R_1 + T_1)V_1' = \frac{e^2 M}{h}V_1'$. Similarly electrons coming from probe 3 are equilibrated to the electrons coming from probe 4 to a new energy as shown below-

$$
\begin{aligned}
\frac{e^2 M}{h}R_1 V_6' + \frac{e^2}{h}T_1 V_1 &= \frac{e^2 M}{h}V_1', & \frac{e^2 M}{h}V_6 &= \frac{e^2 M}{h}V_6', \\
\frac{e^2 M}{h}R_4 V_3' + \frac{e^2}{h}T_4 V_4 &= \frac{e^2 M}{h}V_4', & \frac{e^2 M}{h}V_3 &= \frac{e^2 M}{h}V_3', \\
\frac{e^2 M}{h}V_5' &= \frac{e^2}{h}V_5, & \frac{e^2 M}{h}V_2' &= \frac{e^2 M}{h}V_2.
\end{aligned}
\tag{4.15}
$$

The currents and voltages at the contacts from 1 to 4 are related by the equations-

$$
\begin{aligned}
I_1 &= \frac{e^2 M}{h}T_1(V_1 - V_6'), & I_2 &= \frac{e^2 M}{h}(V_2 - V_1'), \\
I_3 &= \frac{e^2 M}{h}(V_3 - V_2'), & I_4 &= \frac{e^2 M}{h}T_4(V_4 - V_3'), \\
I_5 &= \frac{e^2 M}{h}(V_5 - V_4'), & I_6 &= \frac{e^2 M}{h}(V_6 - V_5').
\end{aligned}
\tag{4.16}
$$

Choosing the reference potential $V_4 = 0$ and $I_2 = I_4 = I_5 = I_6 = 0$ (as these are voltage probes), we thus derive $V_3 = V_2 = V_1' = V_2'$ which gives the longitudinal resistance $R_L^{QAH} = R_{14,14} = 0$.

4.3.2 Chiral(topological) QAH edge mode with quasi-helical edge modes

Herein too we calculate first the effect of disorder and then the effect of both disorder and inelastic scattering on chiral (topological) QAH edge modes along with quasi-helical edge modes. The solid black line in Fig. 4.8 represents chiral (topological) QAH edge mode while
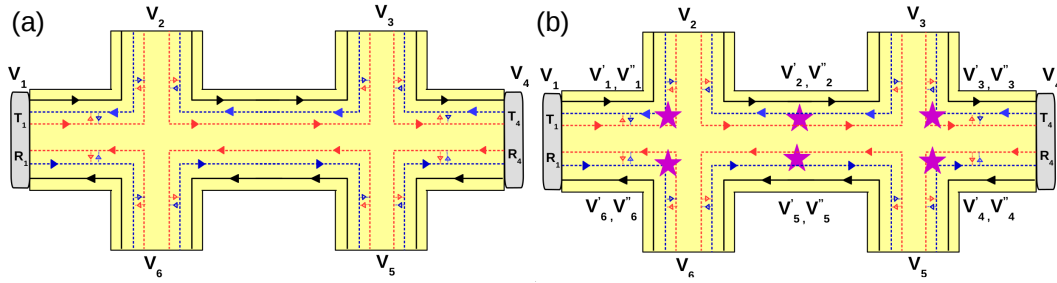
Figure 4.8: Six terminal chiral (Topological) QAH along with quasi-helical QSH edge modes with (c) disorder at contacts 1, 4, (d) inelastic scattering and disorder at contacts 1, 4.

blue and red dotted lines represents spin up and spin down quasi-helical edge modes with small arrows showing the possibility of backscattering between them. Magenta coloured starry blobs shown in Fig. 4.8(b) represents the inelastic scattering via electron-electron or electron-phonon interaction. The spin flip probability between two quasi-helical edge modes is f.

4.3.2.1   Effect of disorder

As before we consider two of the contacts 1 and 4 to be disordered, see Fig. 4.8(a). The relations between currents and voltages at the various terminals can be derived from the conductance matrix below:

$$
G = \frac{e^2 M}{h}
\begin{pmatrix}
T_{11} & -T_{12} & -T_{13} & -T_{14} & -T_{15} & -T_{16} \\
-T_{21} & T_{22} & -T_{23} & -T_{24} & -T_{25} & T_{26} \\
-T_{31} & -T_{32} & T_{33} & -T_{34} & -T_{35} & -T_{36} \\
-T_{41} & -T_{42} & -T_{43} & T_{44} & -T_{45} & -T_{46} \\
-T_{51} & -T_{52} & -T_{53} & T_{54} & T_{55} & -T_{56} \\
-T_{61} & -T_{62} & -T_{63} & -T_{64} & -T_{65} & T_{66}
\end{pmatrix},
\tag{4.17}
$$

where,

$$T_{11} = T_1(3 - f(2 + R_1))/(1 - fR_1),$$

$$T_{12} = T^{61} = T_1(1 - f)/(1 - fR_1),$$

$$T_{13} = 0, \quad T^{14} = 0, \quad T^{15} = 0,$$

$$T_{16} = T^{21} = T_1(2 - f - fR_1)/(1 - fR_1),$$

$$T_{22} = T^{66} = (3 - 2f) + (1 - f^2)fR_1^2/(1 - f^2R_1^2),$$

$$T_{23} = (1 - f), \quad T^{24} = 0, \quad T^{25} = 0,$$

$$T_{26} = (R_1(2 - f(2 - f(1 - R_1^2))))/(1 - f^2R_1^2),$$

$$T_{65} = 1 - f, \quad T^{62} = (1 - f)^2R_1/(1 - f^2R_1^2), \quad T_{63} = T_{64} = 0.$$

(4.18)

Replacing R_1 with R_4 in the above equation rest of the transmission probabilities T_{31} to T_{56} can be deduced. All the elements of the conduction matrix can be calculated in a similar way as done in section 4.2.2 for four terminal sample. Choosing reference potential $V_4 = 0$, and $I_2 = I_3 = I_5 = I_6 = 0$ (as these are voltage probes), we derive longitudinal resistance $R_L^{Topo} = \frac{h}{e^2 M} \frac{2 - 3f + f^2}{9 - 15f + 9f^2 - 2f^3}$ (for zero disorder). For finite disorder, the expression for R_L^{Topo} is quite large, so we plot it in Fig. 4.10(a).

4.3.2.2   Effect of disorder and inelastic scattering

Herein we consider the effect of disorder and inelastic scattering on the various resistances for the sample as shown in Fig. 4.8(b). The contacts 1 and 4 are disordered as in the previous case. The currents and voltages at the contacts from 1 to 6 are related by the

equations-

$$
\begin{aligned}
I_1 &= \frac{e^2 M}{h}\big((3T_1 - 2T_1^2 f/A)V_1 - T_1 V_6 - T_1(1-f)/A(V_1' + V_6')\big), \\[4pt]
I_4 &= \frac{e^2 M}{h}\big((3T_4 - 2T_4^2 f/C)V_4 - T_4 V_3 - T_4(1-f)/C(V_4' + V_3')\big), \\[4pt]
I_2 &= \frac{e^2 M}{h}\big((3-2f)V_2 - (1-f)(V_1' + V_2') - V_1''\big), \\[4pt]
I_3 &= \frac{e^2 M}{h}\big((3-2f)V_3 - (1-f)(V_3' + V_2') - V_2\big), \\[4pt]
I_5 &= \frac{e^2 M}{h}\big((3-2f)V_5 - (1-f)(V_4' + V_5') - V_4''\big), \\[4pt]
I_6 &= \frac{e^2 M}{h}\big((3-2f)V_6 - (1-f)(V_5' + V_6') - V_5\big),
\end{aligned}
$$

$$(4.19)$$

with $A = 1 - R_1 f$ and $C = 1 - R_4 f$, where the potential V_i'' are related to V_i by-

$$
\begin{aligned}
V_2'' &= V_2, \quad V_5'' = V_5, \quad R_1 V_6 + T_1 V_1 = V_1'', \\[4pt]
V_3'' &= V_3, \quad V_6'' = V_6, \quad R_4 V_3'' + T_4 V_4 = V_4''
\end{aligned}
$$

$$(4.20)$$

and the relation between equilibrated potentials V_i' and contact potentials V_i are mentioned as follows.

$$(1-f)(V_2 + V_3) = 2(1-f)V_2', \quad (1-f)(V_5 + V_6) = 2(1-f)V_5',$$

$$(1-f)V_3 + \left(\frac{T_4(1-f)}{(1-R_4^2 f^2)} + \frac{T_4 R_4 f(1-f)}{1-R_4^2 f^2}\right)V_4 + \frac{R_4(1-f)^2}{(1-R_4^2 f^2)}V_4' = \left((1-f) + \left(\frac{T_4(1-f)}{(1-R_4^2 f^2)} + \frac{T_4 R_4 f(1-f)}{1-R_4^2 f^2}\right) + \frac{R_4(1-f)^2}{(1-R_4^2 f^2)}\right)V_3',$$

$$(1-f)V_6 + \left(\frac{T_1(1-f)}{(1-R_1^2 f^2)} + \frac{T_1 R_1 f(1-f)}{1-R_1^2 f^2}\right)V_1 + \frac{R_1(1-f)^2}{(1-R_1^2 f^2)}V_1' = \left((1-f) + \left(\frac{T_1(1-f)}{(1-R_1^2 f^2)} + \frac{T_1 R_1 f(1-f)}{1-R_1^2 f^2}\right) + \frac{R_1(1-f)^2}{(1-R_1^2 f^2)}\right)V_3',$$

$$(1-f)V_5 + \left(\frac{T_4(1-f)}{(1-R_4^2 f^2)} + \frac{T_4 R_4 f(1-f)}{1-R_4^2 f^2}\right)V_4 + \frac{R_4(1-f)^2}{(1-R_4^2 f^2)}V_3' = \left((1-f) + \left(\frac{T_4(1-f)}{(1-R_4^2 f^2)} + \frac{T_4 R_4 f(1-f)}{1-R_4^2 f^2}\right) + \frac{R_4(1-f)^2}{(1-R_4^2 f^2)}\right)V_3',$$

$$(1-f)V_2 + \left(\frac{T_1(1-f)}{(1-R_1^2 f^2)} + \frac{T_1 R_1 f(1-f)}{1-R_1^2 f^2}\right)V_1 + \frac{R_1(1-f)^2}{(1-R_1^2 f^2)}V_6' = \left((1-f) + \left(\frac{T_1(1-f)}{(1-R_1^2 f^2)} + \frac{T_1 R_4 f(1-f)}{1-R_1^2 f^2}\right) + \frac{R_1(1-f)^2}{(1-R_1^2 f^2)}\right)V_3'.$$

$$(4.21)$$
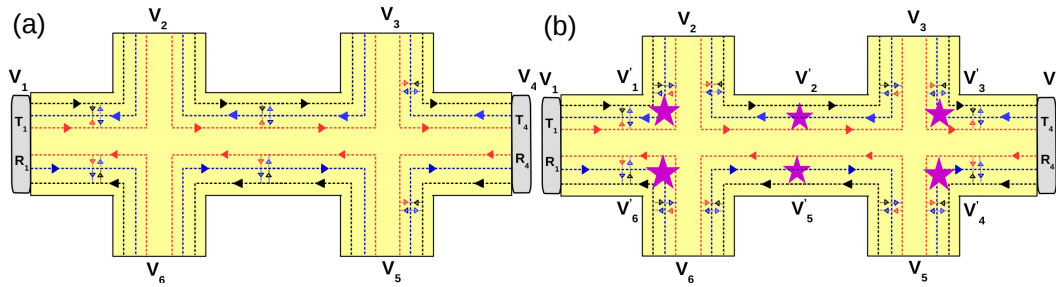
Figure 4.9: Six terminal chiral (Trivial) QAH along with quasi-helical QSH edge modes with (c) disorder at contacts $1, 4$, (d) inelastic scattering and disorder at contacts $1, 4$.

Choosing reference potential $V_4 = 0$, and since 2,3, 5, 6 are voltage probes, $I_2 = I_3 = I_5 = I_6 = 0$ we derive longitudinal resistance $R_L = \frac{h}{e^2 M} \frac{3-4f+f^2}{14-15f+6f^2-f^3}$ for zero disorder but finite inelastic scattering. The expression for R_L in presence of both disorder and inelastic scattering is large so we analyse them via plots as in Fig. 4.10(b).

4.3.3 Chiral(trivial) QAH edge mode with quasi-helical edge modes

Herein too we calculate first the effect of disorder and then the effect of both disorder and inelastic scattering on chiral (trivial) QAH edge modes along with quasi-helical edge modes. The six terminal system with chiral (trivial) QAH edge mode with quasi-helical edge modes is shown in Figs. 4.9(a,b). The dashed black line in Fig. 4.9 represents chiral (trivial) QAH edge mode while blue and red dotted lines represents spin up and spin down quasi-helical edge modes with small arrows showing the possibility of backscattering between them. Magenta colored starry blobs shown in Fig. 4.9(b) represents the inelastic scattering via electron-electron or electron-phonon interaction. The spin flip probability between chiral (trivial) QAH edge mode and quasi-helical edge modes is f_0 while the same between two quasi-helical edge modes is f.

4.3.3.1 Effect of disorder

Herein again we consider two of the contacts 1 and 4 to be disordered, see Fig. 4.9(a). The current voltage relations are derived from the conductance matrix below:

$$
G = \frac{e^2 M}{h}
\begin{pmatrix}
T_{11} & -T_{12} & -T_{13} & -T_{14} & -T_{15} & -T_{16} \\
-T_{21} & T_{22} & -T_{23} & -T_{24} & -T_{25} & T_{26} \\
-T_{31} & -T_{32} & T_{33} & -T_{34} & -T_{35} & -T_{36} \\
-T_{41} & -T_{42} & -T_{43} & T_{44} & -T_{45} & -T_{46} \\
-T_{51} & -T_{52} & -T_{53} & T_{54} & T_{55} & -T_{56} \\
-T_{61} & -T_{62} & -T_{63} & -T_{64} & -T_{65} & T_{66}
\end{pmatrix},
\tag{4.22}
$$

where,

$$
\begin{aligned}
T_{11} &= T_1(3 - 2(f + f_0)T_1/a - 2(f^2 + f_0^2 + ff_0)T_1R_1/a), \\
T_{12} &= ((1 - f - f_0)T_1/a + (1 - f - f_0)R_1T_1(f + f_0)/a), \\
T_{16} &= (T_1(2 - f - f_0) + a_1T_1R_1/a + a_1T_1R_1^2(f + f_0)/a), \\
T_{13} &= T^{14} = T^{15} = 0, \\
T_{22} &= (3 - 2(f + f_0) - (1 - f - f0)R_1^2a_1/a), \\
T_{23} &= (1 - f - f_0), \\
T_{21} &= (T_1(2 - f - f_0) + T_1R_1^2(f + f_0)a_1/a + T_1R_1a_1/a), \\
T_{26} &= (R_1((1 - f)^2 + (1 - f_0)^2) + R_1^3a_1^2/a), \\
T_{25} &= T_{24} = 0,
\end{aligned}
\tag{4.23}
$$

with $a = 1 - R_2^2(f^2 + f_0^2), c = 1 - R_4^2(f^2 + f_0^2), a_1 = f(1 - f) + f_0(1 - f_0)$. Replacing R_1 with R_4 in the above equation rest of the transmission probabilities T_{31} to T_{66} can be deduced. All the elements of the conduction matrix can be calculated in a similar way as
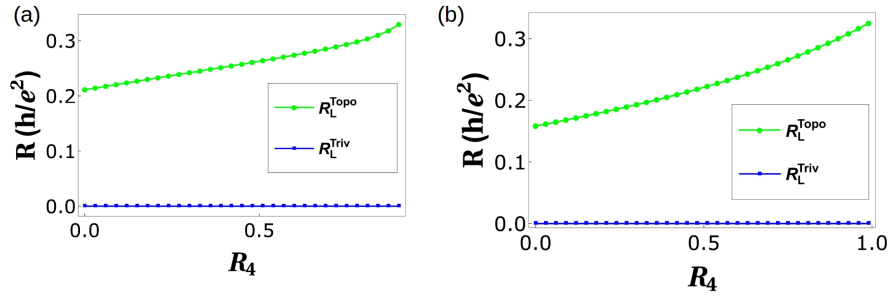
Figure 4.10: (a) Longitudinal resistance R_L vs. Disorder R_4 for parameters $R_1 = 0.5$ and spin-flip probability $f = f_0 = 0.5$, (b) Longitudinal resistance vs. Disorder R_4 in presence of inelastic scattering for parameters $R_1 = 0.5$ and spin-flip probability $f = f_0 = 0.5$. Note the longitudinal resistance vanishes for the trivial case but not for the topological case.

done in section 4.2.3 for four terminal sample. Choosing reference potential $V_4 = 0$, and $I_2 = I_4 = I_5 = I_6 = 0$ (as $5, 2, 3$ and 6 are voltage probes) we derive longitudinal resistance $R_L^{Triv} = R_{23,14} = -\frac{h}{e^2 M}((2 + f^2 - 3f_0 + f_0^2 + f(-3 + 2f_0))/(-9 + 2f^3 + 15f_0 - 9f_0^2 + 2f_0^3 + f^2(-9 + 6f_0) + 3f(5 - 6f_0 + 2f_0^2)))$ for ideal (zero disorder) case. However, in general the expressions for R_L are too large to reproduce here, so we will analyse them via plots as in Fig. 4.10(a).

4.3.3.2 Effect of disorder and inelastic scattering

Herein we consider the trivial QAH edge modes with disorder and inelastic scattering, as shown in Fig. 4.9(b). Here the QAH chiral as well as the QSH helical edge modes are in the trivial phase, i.e. they can scatter from one edge mode to the other. All the edge modes interact with each other and via inelastic scattering equilibrate their energy to a potential V_i' ('i' is from 1 to 6). The contacts 1 and 4 are disordered as in the previous case. The

currents and voltages at the contacts from 1 to 6 are related by the equations-

$$
\begin{aligned}
I_1 &= (3T_1 - 2T_1^2(f+f_0)/a - T_1^2 R_1(f+f_0)^2/a - T_1^2 R_1(f^2+f_0^2)/a)V_1 \\
&\quad - (T_1(1-f-f_0)/a + T_1 R_1(1-f-f_0)(f+f_0)/a)V_1' - (T_1(2-f \\
&\quad - f_0) + T_1 R_1(f(1-f)+f_0(1-f_0))/a + T_1 R_1^2(f(1-f) \\
&\quad + f_0(1-f_0))(f+f_0)/a)V_6', \\
I_2 &= (3-2(f+f_0))V_2 - (2-(f+f_0))V_1' - (1-(f+f_0))V_2', \\
I_3 &= (3-2(f+f_0))V_3 - (2-(f+f_0))V_2' - (1-(f+f_0))V_3', \\
I_5 &= (3-2(f+f_0))V_5 - (2-(f+f_0))V_4' - (1-(f+f_0))V_5', \\
I_6 &= (3-2(f+f_0))V_6 - (2-(f+f_0))V_5' - (1-(f+f_0))V_6'.
\end{aligned}
$$

$$(4.24)$$

The relation between equilibrated potentials V_i''s and contact potentials V_i are given as follows.

$$
\begin{aligned}
&(T_1(2-f-f_0)+T_1 R_1(f(1-f)+f_0(1-f_0))/a+T_1 R_1^2(f+f_0)(f(1-f)+f_0(1-f_0))/a)V_1+(1-f-f_0)V_2 \\
&+(R_1((1-f)^2+(1-f_0)^2)+R_1^3((1-f)f+f_0(1-f_0))^2/a)V_6' = (T_1(2-f-f_0)+T_1 R_1(f(1-f)+f_0(1-f_0))/a \\
&+T_1 R_1^2(f+f0)(f(1-f)+f_0(1-f_0))/a+(1-f-f_0)+R_1((1-f)^2+(1-f_0)^2)+R_1^3((1-f)f+f_0(1-f_0))^2/a)V_1', \\
&(2-f-f_0)V_6+(T_1(1-f-f_0)/a+T_1 R_1(f+f_0)(1-f-f_0)/a)V_1+R_1(1-f-f_0)^2/aV_1' = ((2-f-f_0) \\
&+(T_1(1-f-f_0)/a+T_1 R_1(f+f_0)(1-f-f_0)/a)+R_1(1-f-f_0)^2/a)V_6', \\
&(2-f-f_0)V_2+(1-f-f_0)V_3 = (3-2(f+f_0))V_2', \\
&(2-f-f_0)V_5+(1-f-f_0)V_6 = (3-2(f+f_0))V_5', \\
&(T_4(2-f-f_0)+T_4 R_4(f(1-f)+f_0(1-f_0))/c+T_4 R_4^2(f+f_0)(f(1-f)+f_0(1-f_0))/c)V_4+(1-f-f_0)V_5 \\
&+(R_4((1-f)^2+(1-f_0)^2)+R_4^3((1-f)f+f_0(1-f_0))^2/c)V_3' = (T_4(2-f-f_0)+T_4 R_4(f(1-f)+f_0(1-f_0))/c \\
&+T_4 R_4^2(f+f_0)(f(1-f)+f_0(1-f_0))/c+(1-f-f_0)+R_4((1-f)^2+(1-f_0)^2)+R_4^3((1-f)f+f_0(1-f_0))^2/c)V_4', \\
&(2-f-f_0)V3+(T_4(1-f-f_0)/c+T_4 R_4(f+f_0)(1-f-f_0)/c)V_4+R_4(1-f-f_0)^2/cV_4' = ((2-f-f_0) \\
&+(T_4(1-f-f_0)/c+T_4 R_4(f+f_0)(1-f-f_0)/c)+R_4(1-f-f_0)^2/c)V_3'
\end{aligned}
$$

$$(4.25)$$

Choosing reference potential $V_4 = 0$, and as before $I_2 = I_3 = I_5 = I_6 = 0$ (these are voltage probes), we derive the longitudinal resistance $R_L^{Triv} = R_{23,14}$ in presence of inelastic scattering but for zero disorder as shown below-

$$
\begin{aligned}
R_L^{Triv} &= -(((-3+2f+2f_0)(2+f^2-3f_0+f_0^2+f(-3+2f_0))^2)/(65+2f^6-198f_0 \\
&\quad +255f_0^2-180f_0^3+75f_0^4-18f_0^5+2f_0^6+6f^5(-3+2f_0)+15f^4(5-6f_0+2f_0^2)+ \\
&\quad 20f^3(-9+15f_0-9f_0^2+2f_0^3)+15f^2(17-36f_0+30f_0^2-12f_0^3+2f_0^4) \\
&+\quad 6f(-33+85f_0-90f_0^2+50f_0^3-15f_0^4+2f_0^5))).
\end{aligned} \tag{4.26}
$$

The expression for longitudinal resistance in the general case of arbitrary disorder are quite large so we examine it via plots as in Fig. 4.10(b). One thing is quite clear from Fig. 4.10(b), the case of trivial QAH edge mode with QSH quasi-helical goes over to single chiral(topological) QAH edge mode rather than the topological QAH edge mode with QSH quasi-helical edge modes. This behaviour replicated in the four terminal case too calls for a reinterpretation of the experimental results[48, 49, 45]. In Table 4.2 we tabulate the results obtained for various cases for the longitudinal resistance. We also focus on the change due to change in magnetization from $\uparrow$ to $\downarrow$. There is a symmetry $R_L(\uparrow) = R_L(\downarrow)$ for trivial QAH edge mode which does not hold for a topological QAH edge mode with quasi helical QSH edge modes. This response of the trivial QAH edge mode with a quasi-helical QSH edge modes is again in line with what was experimentally seen.

Table 4.2: Comparison of chiral(topological) QAH edge mode, chiral(topological) QAH edge mode with quasi-helical QSH edge modes and chiral(trivial) QAH edge mode with quasi-helical QSH edge modes, see also Fig. 4.10(a,b).

		QAH(topological)	QAH(topological)+QSH(trivial)	QAH(quasi-helical)+QSH(quasi-helical)
Zero disorder	R_L	0 ($R_L(\uparrow) = R_L(\downarrow)$)	Finite ($R_L(\uparrow) \neq R_L(\downarrow)$)	0 ($R_L(\uparrow) = R_L(\downarrow)$)
Disordered probes	R_L	0 ($R_L(\uparrow) = R_L(\downarrow)$)	Finite ($R_L(\uparrow) \neq R_L(\downarrow)$)	0 ($R_L(\uparrow) = R_L(\downarrow)$)
Disorder +inelastic scattering	R_L	0 ($R_L(\uparrow) = R_L(\downarrow)$)	Finite ($R_L(\uparrow) \neq R_L(\downarrow)$)	0 ($R_L(\uparrow) = R_L(\downarrow)$)

Note: In the 6T QAH sample depicted in Fig. 4.7 the magnetization direction is ($\uparrow$) implying the QAH edge mode shown by black solid or dashed line is spin-up polarized. The conductance matrices depicted in Eqs. (4.14), (4.17), (4.3.3.1) as well as the calculations shown in Eqs. (4.16), (4.19), (4.24) and the longitudinal resistances derived and plotted in Fig. 4.10 are therefore for magnetization ($\uparrow$). We follow similar procedure to calculate the longitudinal resistance for magnetization direction ($\downarrow$) in which case the QAH edge modes shown by black solid or dashed lines in Fig. 4.7 will be spin-down polarized and mention the results in this Table.

4.4   QAH edge modes: Recent experiments

In some recent experiments [5, 47], it has been shown that in observations of the quantum anomalous Hall (QAH) effect the finite longitudinal resistance R_L increases as temperature T increases, while Hall resistance R_H loses its quantization with increase in T. This behaviour was explained in Refs. [5, 47] due to increased thermal fluctuations as T increases, see Figs. 4.11(a,b). A possible question then arises- Is finite temperature the sole reason behind the finite longitudinal resistance or can the presence of quasi-helical QSH edge modes along with the chiral QAH edge mode be a plausible reason? In Ref. [6] this question, is addressed wherein it is shown that similar effects arise in QAH samples with quasi-helical edge modes as disorder increases, in presence of disorder (see Figs. 4.12(a,b)) or both disorder and inelastic scattering even at zero temperature. In Ref. [6] a six terminal QAH bar is examined focusing on longitudinal resistance R_L and Hall resistance R_H at zero temperature. Following Landauer-Buttiker formalism as done in sections 4.2 and 4.3
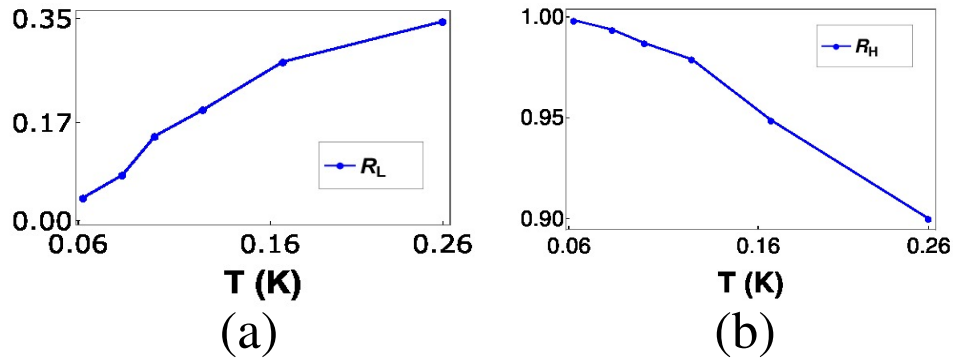
Figure 4.11: (a) The longitudinal resistance and (b) the Hall resistance (both in units of e^2/h) as in Ref. [5] for a six terminal QAH sample, adapted from Figure 3 of Ref. [5].

the resistances at zero temperature are calculated. The longitudinal resistance for the chiral (topological) QAH edge mode with quasi-helical QSH edge modes increases with disorder, while the Hall resistance decreases, which is similar to the behaviour observed as function of temperature. Including both disorder and inelastic scattering in the analysis as in Ref. [6] and studying the system at zero temperature one sees again similar behaviour. The conclusion from Ref. [6] is that experiments of Refs. [5, 47] can not just be interpreted as indication of chiral QAH effect but can also be interpreted as a QAH edge modes occurring with a quasi-helical QSH edge modes. Further, temperature is not the sole reason for seeing finite R_L, the existence of quasi-helical edge modes can also be a plausible reason.

4.5 Conclusion

The aim of this chapter was to identify the topological origin or otherwise of the QAH edge mode observed along with quasi-helical edge modes in QAH experiments. The reason behind the finite longitudinal resistance and non-quantized Hall resistance in QAH experiments as finite temperature fluctuation or due to the presence of quasi-helical edge modes along with the chiral QAH edge mode, see Refs. [5, 47, 45], is also explored. To fulfill these twin aims, disorder is introduced at the contacts of a four and six terminal QAH
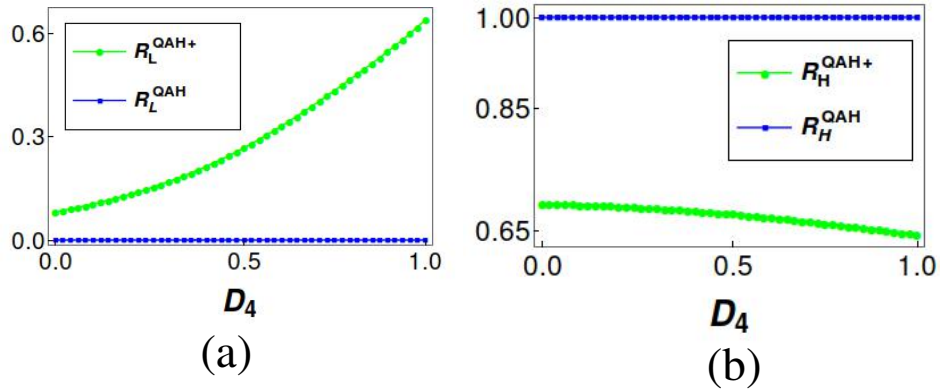
Figure 4.12: (a) The longitudinal resistance and (b) the Hall resistance (both in units of e^2/h) vs disorder (D_4) at contact 4 is shown for a 6 terminal QAH sample at $T = 0$K. The "QAH+" in the superscript of resistance implies that the chiral topological QAH edge mode exists in conjunction with quasi-helical QSH edge modes while 'QAH' implies a single chiral QAH edge mode alone. Parameters are $R_1 = D_1 = 0.5$, spin-flip scattering $f = 0.9$.

samples. The QAH set-ups with disordered contacts are analysed both with and without inelastic scattering. The results are derived following Landauer-Buttiker formalism similarly as shown in Refs. [10, 45]. It is seen in this chapter that trivial(chiral) QAH edge mode with quasi-helical QSH edge modes is more closer to the experimental situation, as interpreted in Ref. [45] than the topological(chiral) QAH edge mode with quasi-helical QSH edge modes case. This implies a reevaluation of the consensus regarding those quantum anomalous Hall experiments[48, 49, 44]. Perhaps, something else is happening and maybe these are not true chiral(topological) quantum anomalous Hall edge modes which were seen, but rather what could be described as chiral(trivial) QAH edge modes. Further, on the second aim we dispel the notion that finite longitudinal resistance and non-quantized Hall resistance are only finite temperature effect in QAH sample (Ref. [5]). Our results show in QAH sample populated with quasi-helical edge modes a finite R_L and non-quantized R_H can also be seen at zero temperature.

5. Thermoelectrics with quantum spin Hall edge modes

"Maybe thermoelectricity will be able to power a tablet someday."

– Ann Makosinski

"Weather systems are natural heat engines, and like all other heat engines, both natural and artificial, they are driven not by temperature per se, but by differences in temperature between one location and another."

– Robert Zubrin

5.1 Introduction

Nano-structured materials are attracting a lot of attention due to their high thermopower and low thermal conductances[99, 53]. High thermo power materials can be used for energy harvesting, i.e., to convert waste heat back into electricity [131]. Another possible use is in refrigeration, i.e., using electrical work to absorb heat from a low temperature region and to dump it in a region at higher temperature[101]. In this chapter the application of a three terminal(3T) quantum spin Hall (QSH) insulator as a quantum heat engine (QHE) and quantum refrigerator will be discussed. Quantum spin Hall(QSH) effect is observed at low temperatures in strong spin-orbit coupling systems like HgTe/CdTe quantum well structures

as discussed in chapters 2, 3. QSH edge states are spin-momentum locked, i.e., if spin up electron is moving in one direction then spin down electron is moving in the opposite direction at one edge of the sample and at the other edge vice-versa. They are helical edge states. 2D edge/surface states are also included in QSH effect but materials where they occur differ like e.g., Bi_2Se_3, Bi_2Te_3, $Bi_{1-x}Sb_x$, etc. Since this chapter deals with 1D QSH edge modes, our candidate materials are HgTe/CdTe quantum well structures. Using the helical properties of the 1D edge modes a powerful quantum heat engine as well as a quantum refrigerator is proposed. In Refs. [36, 18] a 3T quantum Hall (QH) system is shown to work as a QHE with the aid of quantum interference or quantum point contacts (QPC). Multi-terminal QH heat engines have broken time-reversal (TR) symmetry and thus either the Seebeck coefficient (defined previously in Eq. (1.38) of chapter 1) finite and Peltier coefficient (Eq. (1.38)) zero or vice-versa due to the nature of chiral QH edge modes. The asymmetric parameter(AP)- ratio of Seebeck to Peltier coefficient, in QH quantum heat engines therefore is either zero or infinity. AP is intimately related to the working of a heat engine as refrigerator. The fact that AP is either zero or infinity reduces the ability of QH heat engines to be used as a refrigerator, see Ref. [17]. In contrast for a QSH system TR symmetry is not broken and thus AP is unity, which implies that the upper bound of coefficient of performance (COP) (see Eq. (1.38) of chapter 1) of a QSH refrigerator is equal to the Carnot efficiency (Eq. (1.38)) of the refrigerator. The main aim of this chapter is to show that a 3T QSH system (see Fig. 5.1) can work both as QHE as well as refrigerator operating at full power.

5.1.1 This chapter

The structure of this chapter is as follows, beginning with the theory required to explain the working of a QSH heat engine in section 5.2, the focus is on the quantum heat engine in section 5.2.1 and then on quantum refrigerator in section 5.2.2. Next the discussion
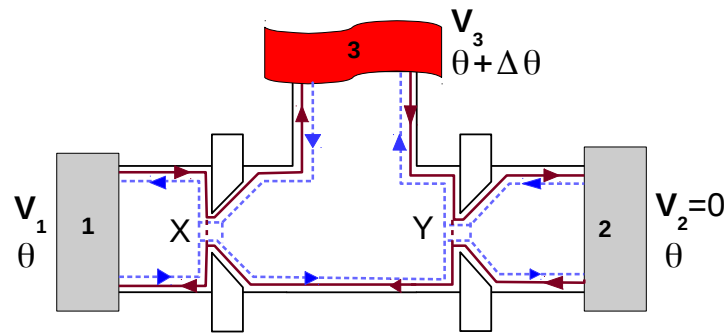
Figure 5.1: 3T QSH thermoelectric system. Blue dashed line represents spin up and maroon solid line represents spin down edge mode. Voltage bias ΔV is applied between terminals 1 and 2. Thermal gradient is applied at terminal 3 which acts as a voltage probe too.

dwells on the focus is on designing a 3T QSH system with energy dependent transmissions through constrictions X,Y (see Fig. 5.1). The two constrictions can be modeled by QPC's or antidots [18] and are studied in section 5.3. The focus then shifts to the analysis of the performance of the 3T QSH system both as a quantum heat engine as well as a quantum refrigerator in section 5.3.1. The analysis is done via few plots of the conduction and Seebeck coefficients in section 5.3.1.1, charge power (see Eq. (1.42)) and spin power in section 5.3.1.2. Efficiencies for charge (Eq. (1.43)) and spin based QSH heat engine are discussed in section 5.3.1.2 while the coefficient of performance and cooling power for QSH refrigerator are analysed in section 5.3.1.3. The experimental realization of the QSH system as both a QHE and refrigerator is discussed in section 5.3.2. The performance and characteristics of the QSH heat engine and refrigerator are compared with chiral QH heat engine proposals in Tables 5.1 and 5.2 in section 5.4. Finally, the chapter concludes in section 5.5 with a perspective on future investigations on this topic.

5.2 Theoretical modeling

In two terminal heat engines as seen in chapter 1, the flow of heat energy and electric currents are through the same terminals, so its not possible to control separately the flow

of heat and charge current via tuning the transmission function at different terminals. In multi-terminal heat engines, however the separate flow of heat energy and electric current is possible through different terminals.

5.2.1   Three terminal quantum heat engine

Herein we discuss the theoretical approaches needed to describe a general three terminal quantum spin heat engines where not only charge but also spin of the electrons take part in converting heat to energy unlike quantum heat engine described in section 1.4 in the introduction of this thesis. For simplicity, we have considered only one spin up edge mode shown by blue dashed line and one spin down edge mode by maroon solid line, see Fig. 5.1. The terminals 1 and 2 are at same temperature θ, while the terminal 3 is at a higher temperature $\theta_3 = \theta + \Delta\theta$ with respect to the other terminals. We describe the problem via Landauer-Buttiker formalism, i.e., the electric and heat currents transported from one terminal to another are defined via the transmission probabilities as long as we are in the linear response regime[52]. In linear response regime, the electric ($I_i^{e,s}$) and heat currents ($I_i^{h,s}$) can be written in terms of the driving forces, i.e., bias voltage and temperature difference, as [18, 52]-

$$\begin{pmatrix} I_i^{e,s} \\ I_i^{h,s} \end{pmatrix} = \frac{1}{h} \sum_j \int_{-\infty}^{\infty} dE [\delta_{ij} - T_{ij}^s(E)](-\frac{df}{dE}) \begin{pmatrix} e^2 & eE/\theta \\ eE & E^2/\theta \end{pmatrix} \begin{pmatrix} \Delta V_j \\ \Delta \theta_j \end{pmatrix}, \qquad (5.1)$$

where $T_{ij}^s(E)$ is the energy dependent transmission from terminal j to i for spin $s =\uparrow / \downarrow$ electrons, f is the Fermi-Dirac distribution with Fermi energy $E_F = 0$, and $I_i^{e,s}, I_i^{h,s}$ define the electric and heat currents at terminal i for spin 's' electrons and $\Delta\theta_3 = \Delta\theta$ with $\Delta\theta_1 = \Delta\theta_2 = 0$ is the thermal bias applied only at terminal 3. Since terminal 3 is a voltage probe, electric charge current, $I_{ch,3}^e = I_3^{e,\uparrow} + I_3^{e,\downarrow}$, through it is zero. From conservation of current we thus have $I_{1,ch}^e = -I_{2,ch}^e$, and as temperature difference is applied only at terminal 3, we

can rewrite Eq. (5.1) in terms of Onsager coefficients, see [52] as-

$$
\begin{pmatrix} I^{e,s} \\ I_3^{h,s} \end{pmatrix} = \begin{pmatrix} L_{eV}^s & L_{e\theta}^s \\ L_{hV}^s & L_{h\theta}^s \end{pmatrix} \begin{pmatrix} \Delta V \\ \Delta \theta_3 \end{pmatrix}, \tag{5.2}
$$

where $L_{eV}^s = G^s$ is the electric and $L_{h\theta}^s$ is the thermal conductance respectively for spin 's' electrons, while the off-diagonal elements are the thermoelectric responses. Since in this chapter, we do not have any spin-flip scattering, from Eq. (5.2), one can define charge/spin Seebeck ($S_{ch/sp}$) and Peltier coefficients ($P_{ch/sp}$) as-

$$
S_{ch} = \frac{S^\uparrow + S^\downarrow}{2}, \quad S_{sp} = S^\uparrow - S^\downarrow, \text{ with } S^s = \frac{L_{e\theta}^s}{L_{eV}^s}, \tag{5.3}
$$

$$
P_{ch} = \frac{P^\uparrow + P^\downarrow}{2}, \quad P_{sp} = P^\uparrow - P^\downarrow, \text{ with } P^s = \frac{L_{hV}^s}{L_{eV}^s}. \tag{5.4}
$$

Summing over spin s of the electrons, in Eq. (5.2), we can write the charge $I_{ch}^e = I_1^{e,\uparrow} + I_1^{e,\downarrow}$, spin $I_{sp}^e = I_1^{e,\uparrow} - I_1^{e,\downarrow}$ electric currents at terminal 1 and the heat $I_{ch}^h = I_3^{h,\uparrow} + I_3^{h,\downarrow}$ current at terminal 3 in terms of the driving forces V_{ch}, V_{sp} and $\Delta\theta$ as follows[16]-

$$
\begin{pmatrix} I_{ch}^e \\ I_{sp}^e \\ I_{ch}^h \end{pmatrix} = \begin{pmatrix} G_{ch} & G_{sp} & L_{e\theta}^+ \\ G_{sp} & G_{ch} & L_{e\theta}^- \\ L_{hV}^+ & L_{hV}^- & L_{h\theta}^+ \end{pmatrix} \begin{pmatrix} V_{ch} \\ V_{sp}/2 \\ \Delta\theta \end{pmatrix}, \tag{5.5}
$$

where $V_{ch} = \frac{V^\uparrow + V^\downarrow}{2}$ and $V_{sp} = V^\uparrow - V^\downarrow$ are the charge and spin voltages at terminal 1, $G_{ch} = G^\uparrow + G^\downarrow$ and $G_{sp} = |G^\uparrow - G^\downarrow|$ are the charge and spin conductances respectively. The thermoelectric responses are defined as $L_k^\pm = L_k^\uparrow \pm L_k^\downarrow$, where $k = hV$, $h\theta$ or $e\theta$. In our setup we apply only a charge voltage bias $V_1 - V_2 = \Delta V = V_1$, thus $V_{sp} = 0$ and $V_{ch} = V_1$.

This gives the output power for charge current at terminal 1 as-

$$\mathcal{P}_{ch} = -I_{ch}^e V_1 = -(G_{ch}V_1^2 + L_{e\theta}^+ V_1 \Delta\theta). \tag{5.6}$$

The maximum charge output power can be calculated by differentiating $\mathcal{P}_{ch}$ with respect to V_1 and equating it to zero, $\frac{d\mathcal{P}_{ch}}{dV_1} = 0$. This gives the maximum output charge power at $V_1 = -\frac{L_{e\theta}^+}{2G_{ch}}\Delta\theta$. Similarly, the output power for spin current-

$$\mathcal{P}_{sp} = -I_{sp}^e V_1 = -(G_{sp}V_1^2 + L_{e\theta}^- V_1 \Delta\theta), \tag{5.7}$$

can also be set to maximum via $\frac{d\mathcal{P}_{sp}}{dV_1} = 0$, which gives the maximum at $V_1 = -\frac{L_{e\theta}^-}{2G_{sp}}\Delta\theta$. The maximum charge/spin output power at terminal 1 can thus be calculated from Eqs. (5.6) and (5.7) as-

$$\mathcal{P}_{ch}^{max} = \frac{1}{4}\frac{(L_{e\theta}^+)^2}{G_{ch}}(\Delta\theta)^2 \text{ and } \mathcal{P}_{sp}^{max} = \frac{1}{4}\frac{(L_{e\theta}^-)^2}{|G_{sp}|}(\Delta\theta)^2. \tag{5.8}$$

Following from Eq. (5.8), the charge/spin efficiency at that maximum charge/spin power can be calculated by substituting $V_1 = -\frac{L_{e\theta}^+}{2G_{ch}}\Delta\theta$ for charge currents and $V_1 = -\frac{L_{e\theta}^-}{2G_{sp}}\Delta\theta$ for spin currents in expressions for $\mathcal{P}_{ch}^{max}$ and P_{sp}^{max} as follows-

$$\begin{aligned} \eta(\mathcal{P}_{ch}^{max}) &= \frac{\mathcal{P}_{ch}^{max}}{I_{ch}^h} = \theta\frac{\eta_c}{2}\frac{(L_{e\theta}^+)^2}{2G_{ch}L_{h\theta}^+ - L_{e\theta}^+ L_{hV}^+}, \\ \eta(\mathcal{P}_{sp}^{max}) &= \frac{\mathcal{P}_{sp}^{max}}{I_{ch}^h} = \theta\frac{\eta_c}{2}\frac{(L_{e\theta}^-)^2}{2G_{sp}L_{h\theta}^+ - L_{e\theta}^- L_{hV}^+}. \end{aligned} \tag{5.9}$$

Eqs. (5.8), (5.9) are the main working formulas for the QSH heat engine. Next we explore how to turn our model into a quantum refrigerator for both charge as well as spin.

5.2.2 Three terminal quantum refrigerator

For our model depicted in Fig. 5.1 to work as a quantum refrigerator, first we need to define the co-efficient of performance (COP)[17]. COP is the ratio of heat current extracted by the system from cooler terminal to the electrical work done on the system. Here, the terminals 1 and 2 are both at the same temperature, i.e., cooler than terminal 3. So, heat is absorbed from terminals 1 and 2 and dumped into terminal 3. Mathematically, COP is defined as- $\eta_{ch}^r = \frac{J^Q}{W_{ch}}$ for charge currents, wherein $J^Q = I_{ch}^h = -\sum_s [(I_1^{h,s} + I_2^{h,s})] = \sum_s I_3^{h,s}$, see Eq. (5.1). The charge output power $W_{ch} = P_{ch}$ is the electrical work done on the system via charge currents with I_{ch}^e defined as in Eq. (5.5). Similarly in case of spin, we can define COP(spin) given by[8]- $\eta_{sp}^r = \frac{J^Q}{W_{sp}}$, where $W_{sp} = I_{sp}^e V_1$ is the spin work done on the system via spin currents with I_{sp}^e is given in Eq. (5.5). COP of the system can be set to maximum for given charge/spin currents by allowing for $\frac{d\eta_{ch(sp)}^r}{dV} = 0$, which is maximum for charge current (considering $J^Q < 0$ and $W_{ch} < 0$) at [53]-

$$V = -\frac{L_{h\theta}^+}{L_{hV}^+} \left(1 + \sqrt{\frac{det\mathbb{L}^+}{G_{ch}L_{h\theta}^+}} \right) \Delta\theta, \text{where } \mathbb{L}^+ = \begin{pmatrix} G_{ch} & L_{e\theta}^+ \\ L_{hV}^+ & L_{h\theta}^+ \end{pmatrix} \tag{5.10}$$

and $det\mathbb{L}^+$ refers to determinant of matrix $\mathbb{L}^+$. The maximum COP and the cooling power J^Q for the charge currents are -

$$\eta_{ch}^{r,max} = \frac{\eta_c^r}{x} \frac{\sqrt{y+1}-1}{\sqrt{y+1}+1}, \qquad \text{with } y = \frac{L_{hV}^+ L_{e\theta}^+}{det\mathbb{L}^+}, \quad x = \theta\frac{L_{e\theta}^+}{L_{hV}^+},$$

$$\text{and } J^Q(\eta_{ch}^{r,max}) = L_{h\theta}^+ \left(\sqrt{\frac{det\mathbb{L}^+}{G_{ch}L_{h\theta}^+}} \right) \Delta\theta, \tag{5.11}$$

while COP for spin currents is maximum at -

$$V = \frac{L_{h\theta}^+}{L_{hV}^+}\left(-1 - \sqrt{\frac{det\mathbb{L}^-}{G_{sp}L_{h\theta}^+}}\right)\Delta\theta, \text{where } \mathbb{L}^- = \begin{pmatrix} G_{sp} & L_{e\theta}^- \\ L_{hV}^+ & L_{h\theta}^+ \end{pmatrix} \tag{5.12}$$

and $det\mathbb{L}^-$ refers to determinant of matrix $\mathbb{L}^-$. The maximum COP and cooling power at that maximum COP for spin current is-

$$\eta_{sp}^{r,max} = \frac{\eta_c^r}{x}\frac{\sqrt{y'+1}-1}{\sqrt{y'+1}+1}, \qquad \text{with} \quad y' = |\frac{L_{hV}^+ L_{e\theta}^-}{det\mathbb{L}^-}|,$$

$$\text{and } J^Q(\eta_{sp}^{r,max}) = L_{h\theta}^+\left(\sqrt{\frac{det\mathbb{L}^-}{G_{sp}L_{h\theta}^+}}\right)\Delta\theta, \tag{5.13}$$

where, $\eta_c^r = \theta/\Delta\theta$ is the Carnot efficiency of refrigerators. The QSH system depicted in Fig. 5.1 can work both as a quantum heat engine as well as a quantum refrigerator as it does not break TR symmetry. This is a major advantage of the 3T quantum spin Hall heat engine in comparison to quantum Hall heat engines which are difficult to convert for refrigeration. For systems with broken TR symmetry the asymmetry parameter(AP) $x = \theta\frac{L_{e\theta}^+}{L_{hV}^+}$(ratio of Seebeck to Peltier coefficient), deviates from unity. The more AP deviates from unity, more the upper bound of COP goes below the Carnot efficiency η_c^r[17].

5.3   Helical thermoelectrics and refrigeration

A 3T QSH system is shown in Fig. 5.1. The transmissions between the terminals, is modulated by constrictions at X, Y. The transmission through these constrictions is energy dependent, which is the main criteria to get a finite thermoelectric response. Here, we discuss two kinds of transmission (see [18])-a) QPC like: the transmission below a certain energy is zero, and above a particular energy is unity and in between it is par-
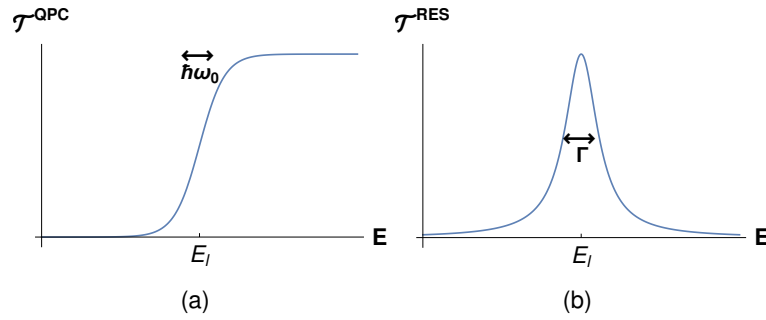
Figure 5.2: Two types of energy dependent transmission-a) QPC type- described by a saddle point potential, b) resonant tunnelling type- due to the presence of an antidot.

tially transmitting, mathematically, $\mathcal{T}_l^{QPC}(E) = [1 + exp(-2\pi(E - E_l)/\hbar\omega_0)]^{-1}$ and b)

resonant tunnelling like: only at a particular energy range the transmission is finite, oth-

erwise zero, mathematically, $\mathcal{T}_l^{RES}(E) = \Gamma_l^2[\Gamma_l^2 + 4(E - E_l)^2]^{-1}$. Here, E_l is the position

of the step at constriction $l = X, Y$, while ω_0 and Γ_l are the width of the same for QPC

and resonant tunnelling respectively. The first kind of transmission is present in case of

QPC constrictions, and the second kind is present in case of antidot constrictions [18].

Depending on what kind of transmission is present at which constriction, there are four

possible configurations. Configuration 1 consists of two QPC's at X and Y, configuration 2

consists of a QPC at X and an antidot (resonant tunnelling) at Y. Configuration 3 consists

of an antidot at X and a QPC at Y while configuration 4 consist of two antidots at X, Y. To

calculate maximum power and efficiency at that maximum power, first we need to calculate

the conduction G_s and Seebeck coefficient S_s for spin s electrons. The thermoelectric re-

sponse is generated due to the energy dependent transmission through the QPC's/antidots

between the terminals[107] and is calculated below. The conduction of spin up and spin

down electrons can be calculated in a 3T QSH bar following Landauer-Buttiker formalism.

For a multi-terminal setup with thermoelectric transport, the spin dependent electric and

heat currents are given below[108]-

$$I_i^{e,s} = \sum_j G_{ij}^s V_j + \sum_j L_{ij,e\theta}^s \Delta\theta_j,$$

$$I_i^{h,s} = \sum_j L_{ij,hV}^s V_j + \sum_j L_{ij,h\theta}^s \Delta\theta_j, \tag{5.14}$$

where, $G_{ij}^s = \frac{e^2}{h} \int_{-\infty}^{\infty} dE [M_i^s \delta_{ij} - T_{ij}^s(E)](-\frac{df}{dE})$, $L_{ij,e\theta}^s = \frac{e}{h\theta} \int_{-\infty}^{\infty} dE (E-\mu)[M_i^s \delta_{ij} - T_{ij}^s(E)]$ $(-\frac{df}{dE}) = L_{ij,hV}^s/\theta$ and $L_{ij,h\theta}^s = \frac{1}{\theta h} \int_{-\infty}^{\infty} dE (E-\mu)^2 [M_i^s \delta_{ij} - T_{ij}^s(E)](-\frac{df}{dE})$ with $M_i^s =$ the no. of edge modes at contact 'i' for spin 's' electron, T_{ij}^s is the transmission probability from terminal 'j' to terminal 'i' for spin 's' electrons, μ is the Fermi energy, 'E' is energy of electrons and 'f' is the Fermi-Dirac distribution, $\Delta\theta$ is the temperature bias applied at terminal 3. The spin polarized conductances G_{ij}^s are related to the the constriction conductances G_l with $l = X, Y$ where

$$G_l = \frac{e^2}{h} \int_{-\infty}^{\infty} dE \, \mathcal{T}_l(E)(-\frac{df}{dE}), \tag{5.15}$$

with $\mathcal{T}_l(E)$, the transmission probability through constriction $l = X, Y$. T_{11}^s is the probability of a electron coming out of terminal 1 and going again back to the same terminal after reflection at constrictions X. Thus, $1 - T_{11}^s$ implies an electron coming out of terminal 1 but not going back into the same terminal, i.e., the transmission probability to transmit through constriction X without getting scattered, which is defined by G_{11}^s. So, $G_{11}^\uparrow = G_{11}^\downarrow = G_X$, the constriction conductance. The conductance G_{12}^s is related to the transmission probability T_{12}^s of a spin 's' electron to transmit from terminal 2 to 1. $T_{12}^\uparrow$, the transmission probability of spin up electron from terminal 2 to 1, shown by the blue dashed line in Fig. 5.1, is zero due to helical transport. We have spin up edge modes moving from left to right at the bottom edge while spin down edge modes move from right to left at top edge. Thus $G_{12}^\uparrow = 0$, but $T_{12}^\downarrow$ the transmission probability for spin down electron from terminal 2 to terminal 1, shown

by the maroon solid line in Fig. 5.1, is equal to the product of the transmission probabilities at constrictions X and Y because a spin down electron emitted from terminal 2 passes the constriction Y with probability $\mathcal{T}_Y(E)$ and then constriction X with probability $\mathcal{T}_X(E)$ to enter terminal 1. So, $T_{12}^\downarrow = \mathcal{T}_X(E)\mathcal{T}_Y(E)$ and $G_{12}^\downarrow = -J_1$ (minus sign is due to the current flowing in a clockwise direction), where

$$J_n = A_n \int_{-\infty}^{\infty} dE(E-\mu)^{n-1}\mathcal{T}_X(E)\mathcal{T}_Y(E)(-\frac{df}{dE}), \tag{5.16}$$

with $A_1 = \frac{e^2}{h}, A_2 = \frac{e}{\theta h}, A_3 = \frac{1}{\theta h}$. The thermopower S_l generated across the QPC's/antidots at constriction 'l' is defined as-

$$S_l = \frac{e}{\theta h G_l} \int_{-\infty}^{\infty} dE(E-\mu)(-\frac{df}{dE})\mathcal{T}_l(E). \tag{5.17}$$

Similarly, $L_{13,e\theta}^\uparrow$ depends on the transmission probability $T_{13}^\uparrow$ of a spin up electron from terminal 3 to terminal 1 (see the expression for $L_{ij,e\theta}^s$ below Eq. (5.20)). The spin up electron emitted from terminal 3 enters terminal 1 after passing through the constriction X, thus, $T_{13}^\uparrow = \mathcal{T}_X(E)$ and $L_{13,e\theta}^\uparrow = -G_X S_X$. The rest of the conductances $G_{i,j}^s$ and thermoelectric responses, $L_{ij,k}^s$'s too depend on the transmission probability from terminal j to i in a similar fashion. Thus, electric current and voltages at the three terminals are related as follows-

$$\begin{pmatrix} I_1^{e,\uparrow} \\ I_1^{e,\downarrow} \\ I_3^{e,\uparrow} \\ I_3^{e,\downarrow} \end{pmatrix} = \begin{pmatrix} G_X & 0 & -G_X & -G_X S_X \\ G_X & -J_1 & -G_X+J_1 & -G_X S_X+J_2 \\ -G_X+J_1 & -G_Y & G_X+G_Y-J_1 & G_X S_X+G_Y S_Y-J_2 \\ -G_X & -G_Y+J_1 & G_Y+G_Y-J_1 & G_X S_X+G_Y S_Y-J_2 \end{pmatrix} \begin{pmatrix} V_1 \\ V_2 \\ V_3 \\ \Delta\theta \end{pmatrix}. \tag{5.18}$$

Since the third terminal is an ideal voltmeter, electric charge current through this terminal is zero $I_{ch,3}^e = 0$ and as terminal 2 is grounded, $V_2 = 0$. So, the total electric current $I_{ch,3}^e = I_3^{e,\uparrow}+I_3^{e,\downarrow} = 0 \Rightarrow V_3 = \frac{2G_X-J_1}{2(G_X+G_Y-J_1)}V_1 - \frac{G_X S_X+G_Y S_Y-J_2}{G_X+G_Y-J_1}\Delta\theta$. Substituting this value in

Eq. (5.18), we get-

$$I_1^{e,\uparrow} = G^{\uparrow}V_1 + L_{e\theta}^{\uparrow}\Delta\theta, \quad \text{and} \quad I_1^{e,\downarrow} = G^{\downarrow}V_1 + L_{e\theta}^{\downarrow}\Delta\theta, \tag{5.19}$$

wherein,

$$
\begin{aligned}
G^{\uparrow} &= \frac{G_X(2G_Y - J_1)}{2(G_X + G_Y - J_1)}, \qquad G^{\downarrow} = \frac{2G_XG_Y + G_XJ_1 - J_1^2}{2(G_X + G_Y - J_1)}, \\
L_{e\theta}^{\uparrow} &= \frac{G_XG_Y}{G_X + G_Y - J_1}(S_Y - S_X) + \frac{G_X}{G_X + G_Y - J_1}(J_1S_X - J_2), \\
L_{e\theta}^{\downarrow} &= \frac{G_XG_Y}{G_X + G_Y - J_1}(S_Y - S_X) - \frac{G_Y}{G_X + G_Y - J_1}(J_1S_Y - J_2),
\end{aligned} \tag{5.20}
$$

for spin up and down electric currents. The first term in the thermoelectric responses- $L_{e\theta}^s$, $(s = \uparrow, \downarrow)$ in Eq. (5.20) is proportional to the difference between the thermopower generated at the two constrictions. The second term is related to the coherent transport between the respective terminals and the sign of this term is related to the helicity of the different spins. Spin up electrons are moving in counter clockwise direction, which is opposite to that of spin down electrons which are moving in clockwise direction. So, different spins have opposite effect on the thermoelectric responses as shown in the second term. Similarly, the heat conductance of spin up and spin down electrons can be calculated in a 3T QSH bar following Landauer-Buttiker formalism. For a multi-terminal setup with thermoelectric transport, the heat currents using Landauer-Buttiker formalism are given as follows[108]-

$$I_i^{h,s} = \sum_j L_{ij,hV}^s V_j + \sum_j L_{ij,h\theta}^s \Delta\theta_j, \tag{5.21}$$

where $L_{ij,hV}^s = \frac{e}{h}\int_{-\infty}^{\infty} dE(E - \mu)(-\frac{df}{dE})[M_i^s\delta_{ij} - T_{ij}(E)]$ and $L_{ij,h\theta}^s = \frac{1}{\theta h}\int_{-\infty}^{\infty} dE\ (E - \mu)^2$ $[M_i^s\delta_{ij} - T_{ij}(E)](-\frac{df}{dE})$. The Peltier term $L_{11,hV}^s$ depends on the probability $(1 - T_{11}^s)$ (see the expression for $L_{ij,hV}^s$) for spin s electrons. T_{11}^s is the probability of a spin 's' electron

emitted from terminal 1 to again go back to same terminal, after getting reflected at the constrictions X. For spin up electron, probability $(1 - T_{11}^{\uparrow})$ defines the transmission for spin up electron coming out of terminal 1 and not going back to the same terminal (see the blue dashed line in Fig. 5.1), i.e., after coming out of terminal 1, it is transmitted through the constriction X, so $(1 - T_{11}^{\uparrow}) = \mathcal{T}_X(\mathcal{E})$. Thus, $L_{11,hV}^{\uparrow} = L_{11,hV}^{\downarrow} = G_X S_X \theta = \frac{e}{h} \int dE (E - \mu)(-\frac{df}{dE}) \mathcal{T}_X(E)$. Similarly, the thermal conductance $L_{13,h\theta}^{\uparrow}$ depends on the transmission of thermal current from terminal 3 to 1, i.e. on the transmission function $T_{13}^{\uparrow} = \mathcal{T}_X(E)$ (see the blue dashed line in Fig. 5.1) for spin up electron, so $L_{13,h\theta}^{\uparrow} = -N_X$, where

$$N_l = \frac{1}{\theta h} \int_{-\infty}^{\infty} dE \, \mathcal{T}_l(E)(E - \mu)^2 (-\frac{df}{dE}), \tag{5.22}$$

is the thermal conductance across the QPC/antidot at constriction 'l' with $l = X, Y$. Each of the entries in matrix (Eq. (5.23)) can be explained in this way.

$$
\begin{pmatrix} I_1^{h,\uparrow} \\ I_1^{h,\downarrow} \\ I_2^{h,\uparrow} \\ I_2^{h,\downarrow} \\ I_3^{h,\uparrow} \\ I_3^{h,\downarrow} \end{pmatrix} = \begin{pmatrix} G_X S_X \theta & 0 & -G_X S_X \theta & -N_X \\ G_X S_X \theta & -J_2 \theta & -(G_X S_X - J_2)\theta & -(N_X - J_3) \\ -J_2 \theta & G_Y S_Y \theta & -(G_Y S_Y - J_2)\theta & -(N_Y - J_3) \\ 0 & G_Y S_Y \theta & -(G_Y S_Y)\theta & -N_Y \\ -(G_X S_X - J_2)\theta & -G_Y S_Y \theta & (G_X S_X + G_Y S_Y - J_2)\theta & (N_X + N_Y - J_3) \\ -G_X S_X \theta & -(G_Y S_Y - J_2)\theta & (G_X S_X + G_Y S_Y - J_2)\theta & (N_X + N_Y - J_3) \end{pmatrix} \begin{pmatrix} V_1 \\ V_2 \\ V_3 \\ \Delta\theta \end{pmatrix} \tag{5.23}
$$

In our setup, we need only the heat current $I_3^{h,\uparrow}$ and $I_3^{h,\downarrow}$ at terminal 3 in terms of the potential bias and thermal bias, by putting the value of V_3 in terms of V_1 and $\Delta\theta$ we get-

$$I_3^{h,\uparrow} = L_{hV}^{\uparrow} V_1 + L_{h\theta}^{\uparrow} \Delta\theta,$$

$$I_3^{h,\downarrow} = L_{hV}^{\downarrow} V_1 + L_{h\theta}^{\downarrow} \Delta\theta, \tag{5.24}$$
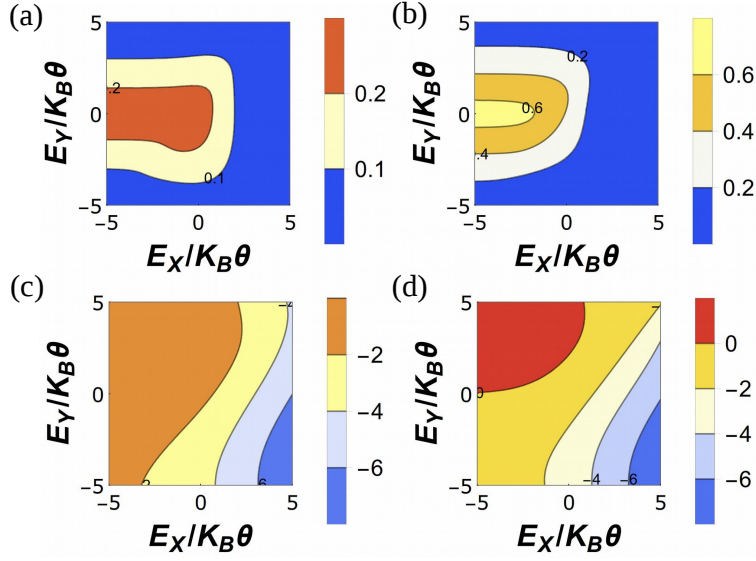
Figure 5.3: (a) Spin up and (b) spin down conductances (in unit of $\frac{e^2}{h}$) are shown for QPC at constriction X and resonant tunnelling at constriction Y. (c) Spin up and (d) spin down Seebeck coefficients (in unit of $\frac{k_B}{e}$) ($S^{\uparrow}$ and $S^{\downarrow}$) are shown for QPC at constriction X and resonant tunnelling at constriction Y. Parameters are $\hbar\omega_0 = 0.1 k_B\theta$, $\Gamma = 2k_B\theta$ and $\theta = 0.1K$.

where,

$$
\begin{aligned}
L_{hV}^{\uparrow} &= \theta L_{e\theta}^{\downarrow} = \frac{\theta G_X G_Y}{G_X + G_Y - J_1}(S_Y - S_X) - \frac{\theta G_Y}{G_X + G_Y - J_1}(J_1 S_Y - J_2), \\
L_{hV}^{\downarrow} &= \theta L_{e\theta}^{\uparrow} = \frac{\theta G_X G_Y}{G_X + G_Y - J_1}(S_Y - S_X) + \frac{\theta G_X}{G_X + G_Y - J_1}(J_1 S_X - J_2), \\
L_{h\theta}^{\uparrow} &= L_{h\theta}^{\downarrow} = (N_1 + N_2 - J_3) - \theta\frac{(G_X S_X + G_Y S_Y - J_2)^2}{(G_X + G_Y - J_1)}.
\end{aligned}
\tag{5.25}
$$

From Eq. (5.25) we see that $(L_{hV}^{\uparrow} + L_{hV}^{\downarrow}) = \theta(L_{e\theta}^{\uparrow} + L_{e\theta}^{\downarrow})$, which implies that the TR symmetry is preserved in three terminal QSH systems unlike in three terminal QH systems, see Ref. [18]. $N_l = \frac{1}{\theta h}\int_{-\infty}^{\infty} dE \mathcal{T}_l(E)(E-\mu)^2(-\frac{df}{dE})$ is the thermal conductance across the QPC/antidot at constriction 'l'. From Eq. (5.25) we see that $L_{hV}^{+} = \theta L_{e\theta}^{+}$, which implies TR symmetry is preserved in 3T QSH systems unlike in 3T QH systems, see Ref. [18]. Since TR symmetry is preserved in a QSH system, which is also seen from the Onsager relations between the off-diagonal coefficients, we have high Peltier coefficients along with high

Seebeck coefficient. A high Seebeck coefficient is a necessary condition to get a QHE with large power, a high Peltier coefficient is required condition to get a quantum refrigerator with large cooling power [17].

5.3.1 Onsager Coefficients

Our aim is to design a powerful QSH heat engine as well as a good refrigerator. For these twin purposes we need to have a large Seebeck as well as large Peltier coefficient. Seebeck and Peltier coefficients are related to the off-diagonal elements of the Onsager matrix, $L_{e\theta}^{s}$ and L_{hV}^{s} respectively, as shown in Eq. (5.2). First we discuss the conditions required to have a powerful QSH heat engine. To have large charge power (P_{ch}^{max}) we need a large thermoelectric response $L_{e\theta}^{+}$ with small charge conductance G_{ch}, as in Eq. (5.8). The efficiency at that charge power (see Eq. (5.9)) will be large only when the thermal conductance $L_{h\theta}^{+}$ is small along with the condition for large power. For each of the four configurations explained before (see paragraph above Eq. (5.14)), we have analysed the results. From the thermoelectric properties, maximum power and efficiency for each of these configurations we find that those properties depending on charge currents are best seen for configuration 2 (QPC at X and antidot at Y), while properties related to spin currents are best seen for configuration 1 (QPC at both X and Y). Hence, we have shown the maximum power and efficiency of charge current for configuration 2 (see Figs. 5.4(a,b)) and the same of spin current for configuration 1 (see Figs. 5.4(c,d)).

5.3.1.1 Conductance and Seebeck coefficient

For transport through QPC if, $-E_l >> \hbar\omega_0$ then it is open, i.e., the transmission through QPC is 1, but if $|E_l| \leq \hbar\omega_0$ then it is noisy, i.e., electrons are partially transmitted through QPC, else if $E_l > \hbar\omega_0$ the QPC is closed. For transport through antidot, if $|E_l| >> \hbar\omega_0$ then
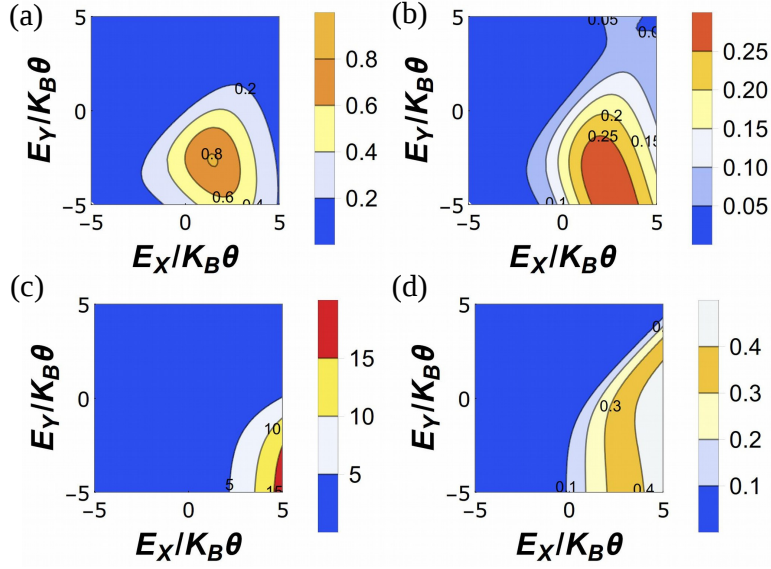
Figure 5.4: (a) Maximum power for charge currents P_{ch}^{max} in unit of $\frac{(k_B\Delta\theta)^2}{h}$ and (b) Efficiency at that power in unit of η_c for both in configuration 2. (c) Maximum power for spin currents P_{sp}^{max} in unit of $\frac{(k_B\Delta\theta)^2}{h}$ and (d) efficiency at that power in unit of η_c for both in configuration 1. Parameters are $\hbar\omega_0 = 0.1k_B\theta$ and θ=0.1K.

it is closed, but if $|E_l| < \hbar\omega_0$ then it is partially open. In Figs. 5.3 (a, b), for configuration 2, we see that spin up and down conductances are maximum when constriction at Y is partially open, i.e., $|E_Y| \leq \hbar\omega_o$ and at X is open. In Figs. 5.3 (c,d), for the same configuration, the spin up Seebeck coefficient $|S^{\uparrow}|$ is maximum when constriction at X is closed and at Y is open. Similarly, the spin down Seebeck current $|S^{\downarrow}|$ is maximum when constriction at X is closed and Y is open.

5.3.1.2 Power and efficiency of QSH heat engine

In Fig. 5.4 (a), we see the maximum charge power as large as $0.25(k_B\Delta\theta)^2/h$ with efficiency at that power equal to $0.8\eta_c$ (for configuration 2), as shown in Fig. 5.4 (b). We see these large power and efficiency occurs at the same parameter value where the Seebeck coefficients $|S^{\uparrow}|$ and $|S^{\downarrow}|$ are maximum, as in Eqs. (5.3), (5.8). The power and efficiency both are maximum when constriction at X is partially open and at Y is open. The maximum power

delivered by our system is double that of a quantum Hall(QH) system, due to presence of helical edge modes rather than chiral, although the efficiency generated at that maximum power is comparable to the QH system[18]. The use of QSH system to design a quantum spin heat engine is only possible because of the presence of spin up/down edge modes. This is exclusive to the QSH heat engine. In Fig. 5.4 (c), we see that a large spin power $15(k_B\Delta\theta)^2/h$ is obtained in case of spin currents with efficiency at that spin power $0.4\eta_c$ (for configuration 1), as shown in Fig. 5.4(d). The maximum power and efficiency for spin currents are maximum when constriction at X is closed while that at Y is open. Due to quantum effects and in the non-linear transport regime there is an upper limit to how much heat energy can be carried by each channel/edge mode, see Ref. [105]. As a result, it also limits the efficiency achieved at maximum power by any heat engine irrespective of whether it is two/three terminal heat engine or TR symmetry is broken or not. Though this kind of bound will not affect our results in this chapter as we are in linear transport regime where the temperature difference applied between the two terminals is small and the heat energy carried by each edge mode will always be less than this upper bound.

5.3.1.3 Coefficient of performance(COP) and cooling power of refrigerator

The use of the quantum spin Hall system as a charge or spin refrigerator is the subject of this subsection. In Figs. 5.5 (a,b), the cooling power $(J^Q(\eta_{ch}^{max}))$ (see Eq. (5.11)) for charge currents of around $3.5(k_B\Delta\theta)^2/h$ with a COP $0.2\eta_c^r$ is observed for configuration 2. We see that the cooling power $(J^Q(\eta_{ch}^{max}))$ is maximum when both constrictions at X and Y are open, although the coefficient of performance for charge currents is maximum when constriction at X is partially open while at Y is open. In Figs. 5.5 (c,d), the cooling power $(J^Q(\eta_{sp}^{max}))$ for spin currents is shown in (c), which is around $20(k_B\Delta\theta)^2/h$ and maximum COP (η_{sp}^{max}) of around 0.15 η_c^r is shown in Fig. 5.5(d) for configuration 2. The cooling power and COP for spin currents are maximum when constriction at X is closed and at Y is open.
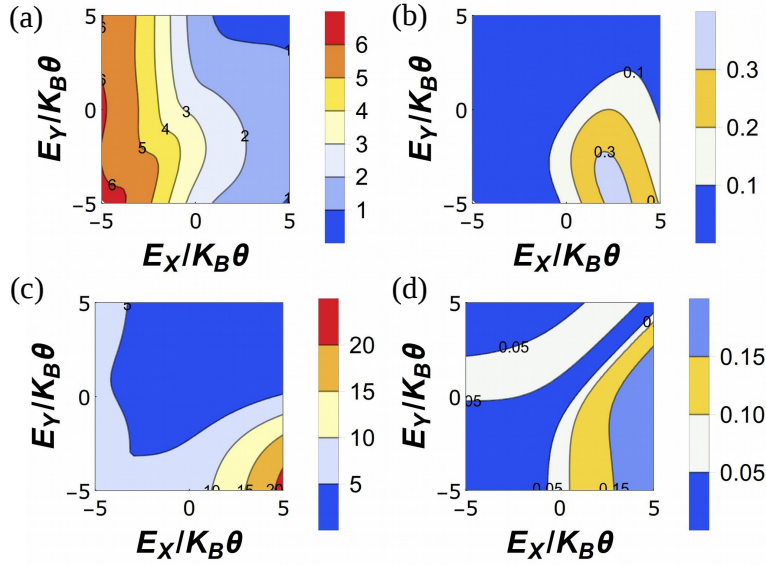
Figure 5.5: (a) Maximum cooling power for charge currents $J^Q(\eta_{ch}^{r,max})$ in unit of $\frac{(k_B\Delta\theta)^2}{h}$ and (b) maximum efficiency $\eta_{ch}^{r,max}$ in unit of η_c^r for configuration 2. (c) Maximum cooling power for spin currents $J^Q(\eta_{sp}^{r,max})$ in unit of $\frac{(k_B\Delta\theta)^2}{h}$ and (d) maximum efficiency $\eta_{sp}^{r,max}$ in unit of η_c^r for configuration 1. Parameters are $\hbar\omega_0 = 0.1k_B\theta$ and θ=0.1K.

Again because of the preservation of TR symmetry in our system, it can act as a very good refrigerator with giant cooling power of 3.5 $(k_B\Delta\theta)^2/h$ for charge refrigeration which is more than 150 times than that seen in the quantum dot (QD) refrigerators (see Table 5.2) [110, 109].

5.3.2 Experimental Realization

2D QSH samples are well known topological insulators, known for their dissipation less spin transport. These helical edge modes have been experimentally realized, see Refs. [40, 111]. Though the design of a QPC in a QSH insulator is not so easy, very recently they have been experimentally realized in Ref. [95]. Realization of resonant tunnelling in QSH system can be done by an antidot[112]. Thus, the experimental realization of our model would not be that difficult. Spin power of our system can also be converted to charge power by using inverse spin Hall effect or spin valve to do electrical work by the system, as

shown in Ref. [16].

5.4   Chiral vs Helical thermoelectrics

The performance of the quantum spin Hall system as a quantum heat engine as well as a refrigerator is discussed in section 5.3. Herein a comparison is made between the performance of quantum spin Hall heat engine with that of other quantum Hall heat engines in Table 5.1. Since there are no refrigerators based on chiral quantum Hall systems, the helical QSH refrigerator is compared with quantum dot refrigerators in Table 5.2. From Table 5.1, one can see that the maximum power for charge currents for a 3-terminal quantum spin Hall heat engine is $0.8(k_B\Delta\theta)^2/h$ which is double than that of a 3-terminal quantum Hall heat engine based on quantum point contacts[18], but much larger than that of a 3-terminal quantum Hall heat engine based on Mach-Zehnder interferometers [36]. The efficiency at maximum power for the QSH heat engine is $0.28\eta_c$ which is comparable to that seen in [18] but much larger than what is seen in [36]. Further, it can also be seen from Table 5.1 that if a 1 cm^2 area is fabricated with quantum spin Hall heat engines (area of each nano-scale QSH heat engine is say 100 nm^2) then a huge output power of around 0.08 Watt can be generated which is much larger than that seen in Refs. [18, 36]. Thus it is clear from Table 5.1 that quantum spin Hall heat engines outperform quantum Hall heat engines quite easily. From Table 5.2, one can see that a quantum spin Hall refrigerator too outperforms other quantum dot refrigerators with large cooling power of $3.5(k_B\Delta\theta)^2/h$ and co-efficient of performance of $0.2\eta_c^r$.

Table 5.1: How does the QSH heat engine compare with quantum Hall heat engine proposals?

Heat Engines	Maximum power P_{max} $(k_B\Delta\theta)^2/h$	Efficiency at maximum power $\eta(P_{max})$	Power generated in $1cm^2$ area fabricated by nano engines
QH (MZI)(3T)[36]	0.14	0.042 η_c	0.04 Watt
QH (QPC) [18]	0.4	0.3 η_c	0.06 Watt
QSH heat engine (3T)	0.8	0.28η_c	0.08 Watt

Note: The power and efficiencies are based on charge transport, see Eqs. (1.42), (1.43) and Figs. 5.4(a, b).

Table 5.2: Comparison with quantum dot (QD) refrigerators

Quantum refrigerator	Cooling Power J^Q at maximum COP in units of $(k_B\Delta\theta)^2/h$	Maximum COP in units of η_c^r
QD refrigerator[110]	0.002	0.4
Magnon QD refrigerator [109]	0.025	0.2
QSH refrigerator (3T)	3.5	0.2

Note: The cooling power and coefficient of performance are based on charge transport, see Eq. (5.11) and Figs. 5.5(a, b).

5.5 Conclusion

The aim in this chapter was to design a powerful quantum spin Hall (QSH) heat engine. The ability of the helical QSH system to work as an efficient quantum refrigerator is also explored. Besides designing a charge based heat engine, a powerful spin based heat engine can also be modelled in the QSH system. To fulfil these twin aims, two QPC's/antidots are introduced at the two junctions X, Y of a 3T QSH system (as discussed in section 5.3). The results are derived following Landauer-Buttiker formalism in section 5.3. It is shown that for configuration 2 (QPC at constriction X and antidot at constriction Y) the charge power and efficiency for charge current are maximum for QSH heat engine and refrigerator. The power and efficiency for spin currents are maximum for configuration 1 (QPC at both the

constrictions X and Y). Further, it is shown that the performances of QSH heat engine is better than that of quantum Hall (QH) heat engines[36, 18] in section 5.4. The performance of QSH system as a refrigerator too is better than quantum dot refrigerators. Herein only a 3-terminal QSH system is analysed both as a quantum heat engine as well as a quantum refrigerator. In future this can be extended to multi-terminal (more than 3-terminal) QSH heat engines to improve their performance further and more interesting effects like spin Nernst effect could be explored in multi-terminal QSH systems.

6. Thermoelectrics in strained graphene

"What is important about graphene is the new physics it has delivered."

– Andre Geim

"The concept of graphene came along in 1947, but nobody paid much attention to it. I was fascinated because it had a linear E versus K while everything else that people were working on at that time had a quadratic dispersion relationship. I wondered why this was and what was so special about it. That was my fascination."

– Mildred S. Dresselhaus

6.1   Introduction

The aim of this chapter is to design both a powerful quantum heat engine as well as a quantum refrigerator using ballistic modes in a monolayer graphene system. Graphene is a allotrope of carbon and it consists of a single layer of carbon atoms arranged in a hexagonal lattice[122]. It is a semi-metal with zero band gap. In chapter 5, the application of edge modes in thermoelectrics is discussed. In this chapter, the use of ballistic modes in graphene to thermoelectric application is probed and compared with the edge modes in chapter 5. The reason for comparing ballistic modes in graphene to edge modes in

QH or QSH heat engines is that graphene is available in its pure form very easily and even in presence of impurity scattering it has perfectly conducting ballistic channels[50] similar to edge modes observed in QH or QSH systems. The efficacy of quantum heat engines(QHE) at the nanoscale has been made more than obvious in the past half decade [113]. From being useful in schemes for removal of excess heat in nanosystems to novel nano heat engines which produce huge amounts of power they have been one of the most productive areas of research [16]. Graphene as a thermoelectric material has a very small thermoelectric figure of merit ZT around $0.1 - 0.01$, which is much smaller than the most efficient thermoelectric material Bi_2Te_3, see Refs. [114, 115]. This is due to its large thermal conductance and absence of any band gap. In some recent works, a moderate improvement of the thermoelectric figure of merit ZT is noticed in graphene based systems. This improved thermoelectric figure of merit ZT of around $2.5 - 3$ has been observed in 2D graphene systems with disorder [116, 117] or isotopes[117] or nanopores[118] or by nano-patterning the graphene surface[114]. This thermoelectric figure of merit observed in 2D graphene system is still smaller than that of the heat engine based on spin wave ferromagnetic system, see Ref. [16]. In this chapter a recipe is provided to design a graphene spin heat engine and refrigerator using spin polarized ballistic modes in strained graphene. Giant thermoelectric factors of around 50 for both charge as well as spin transport are seen in the graphene spin heat engine.

There have been a few papers on marrying spin transport into heat engines, mention may be made of Ref. [16] wherein both the spin as well as charge thermoelectric factors are calculated along with the power and efficiency of both charge as well as spin heat engines. In Ref. [42], charge/spin thermoelectric properties of a carbon atomic chain sandwiched between two ferromagnetic zigzag graphene nanoribbon is studied at various temperature (ranges from $0 - 400$ K). In Ref. [52] the spin and charge thermoelectric figure of merits for a ferromagnetic graphene based QHE is calculated. Finally, in Ref. [119] the

authors calculate the thermoelectric figure of merit as well as power output in a graphene based heat engine with spin polarized edge modes. In Ref. [119] it is mentioned that a thermoelectric figure of merit (around 3) is obtained in the device. In this chapter a charge thermoelectric figure of merit $10 - 20$ times the number obtained in Ref. [119] is predicted in a graphene based system. The giant thermoelectric figure of merit for charge is not unique us, in Ref. [16] a thermoelectric figure of merit of around 100 is seen. However, what is unique to this model is that the same graphene based heat engine under strain and doped with a magnetic impurity can work as a highly efficient charge as well as spin heat engine with giant thermoelectric figure of merits for not only charge but also spin. The graphene device considered generates a charge power almost twice than what is seen in it's closest competitor, see Ref. [119]. Further, the graphene device exhibits excellent characteristics (coefficient of performance) when used as a charge or spin refrigerator. In some of the recent works, see Refs. [152, 153, 154], the possibility of graphene to work as spin caloritronic devices is studied, where graphene nanoribbon devices are engineered to generate large spin currents on application of a temperature difference at the two opposite edges of the system.

Further, in this chapter, a huge charge/spin thermoelectric figure of merit ($ZT_{ch/sp}$) is observed in a graphene system in presence of strain and a magnetic impurity. In Refs. [52, 119], which are based on a graphene system, this huge charge/spin thermoelectric figure of merit is not observed. In Ref. [16], a large charge thermoelectric figure of merit is observed, but it's not a graphene based system but a ferromagnetic system. The aim in this chapter is to design a graphene based quantum heat engine and refrigerator. The prospect for the device realization of a graphene based quantum heat engine is quite high. Since in graphene, electronic transport can be very easily tuned by a gate voltage alone. The huge ZT_{sp} seen in the graphene spin heat engine of this chapter is not seen in any (graphene/non-graphene) system till date. The graphene system considered can work as a quantum

refrigerator as well with huge charge/spin co-efficient of performances(COP). In Ref. [18], it is demonstrated that a quantum dot heat engine, coupled to two ferromagnetic metals and a ferromagnetic insulator, can convert heat to spin polarized charge current as well as pure spin current depending on the spin orientation directions of the two ferromagnetic metal reservoirs. In the model graphene spin heat engine, by optimizing the parameters, heat can be converted to a spin polarized charge current as well as a pure spin current similar to Ref. [18]. In this chapter, not only charge and spin based heat engines are considered but the model is extended to charge and spin based refrigerators based on the same graphene based system. A large coefficient of performance is observed for the graphene spin refrigerator in both charge as well as spin domains too.

6.1.1 This chapter

The structure of this chapter is as follows, beginning with the theoretical description required to operate a 2-terminal graphene quantum spin heat engine in section 6.2, the spin Seebeck coefficient is described in section 6.2.1, the maximum power and efficiency for charge as well as spin currents are derived in section 6.2.2 and then the coefficient of performance, cooling power are derived in section 6.2.3. Next in section 6.3 the model of graphene quantum spin heat engine is described. Herein the focus is on our model which consists of strained graphene system embedded with a magnetic impurity as in section 6.3.1. Then the Hamiltonian of the system is described and wave functions are solved using the boundary conditions in section 6.3.2. The charge/spin conductances and Seebeck coefficient are calculated in section 6.3.3. Next the focus is on the performance of the system to work as an efficient quantum heat engine in section 6.3.4. Next in section 6.3.5 a comparison is made between graphene spin heat engine with related proposals in Table 6.1. In sections 6.4 the special case of graphene quantum heat engine when magnetic impurity is absent is also discussed. Next the conductance, Seebeck coefficient of graphene quantum heat

engine are discussed in section 6.4.1 and maximum power, efficiency at that power are discussed in section 6.4.2. Then the focus is on the performance of the graphene spin system to work as a quantum refrigerator in section 6.5. Again the special case when the magnetic impurity is absent is discussed in section 6.5.1 for graphene refrigerator. The experimental realization of this model is discussed in section 6.6. A comparison between the performance of the graphene quantum spin heat engine based on ballistic modes with that of quantum heat engines based on quantum spin Hall edge modes (as described in chapter 5 of this thesis) is done in section 6.7 (Tables. 6.2, 6.3 and 6.4). Finally, the chapter concludes in section 6.8.

6.2 Theory of the quantum spin heat engine and refrigerator

6.2.1 Onsager coefficients

The aim of this chapter as stated in the introduction is to design a quantum spin heat engine and refrigerator using a strained graphene layer embedded with a magnetic impurity. It goes without saying that our device acts as a quantum charge heat engine too. For this we begin by defining the thermoelectric properties of our graphene system in the linear transport regime- the electric and heat currents are linearly proportional to the applied biases be it electric or thermal. As is well known electrons in graphene can be both valley (K/K') polarized as well as spin ($\uparrow$ / $\downarrow$) polarized[90, 121]. The linear dependencies can be expressed as follows [52, 53, 36]-

$$
\begin{pmatrix} j_s^v \\ j_s^{q,v} \end{pmatrix} = \begin{pmatrix} L_s^{11,v} & L_s^{12,v} \\ L_s^{21,v} & L_s^{22,v} \end{pmatrix} \begin{pmatrix} -\mathscr{E} \\ -\Delta\theta \end{pmatrix},
$$

(6.1)

where j^v_s and $j^{q,v}_s$ are the electric and heat currents for spin 's' electrons ($s \in \uparrow, \downarrow$) respectively, and v is for K/K' valley, L_{ij} with $i, j \in 1, 2$ represents the Onsager coefficients for a two terminal thermo-electric system. The electric response due to a finite temperature difference $\Delta\theta$ across the graphene layer is denoted as the Seebeck coefficient while the heat current generated due to the applied bias voltage $\mathcal{E}$ across graphene layer is denoted as Peltier coefficient. Using Eq. (6.1) these aforesaid coefficients can be expressed as-

$$S^v_s = -\frac{L^{12,v}_s}{L^{11,v}_s}, \quad \text{and} \quad P^v_s = \frac{L^{21,v}_s}{L^{11,v}_s}. \tag{6.2}$$

Due to the additional spin(s) and valley(v) degrees of freedom for electrons in graphene the charge(S^v_{ch}) and spin Seebeck(S^v_{sp}) and Peltier coefficients(P^v_{ch}, P^v_{sp}) for any valley ($v = K/K'$) can be written as[16]-

$$S^v_{ch} = \frac{G^v_\uparrow S^v_\uparrow + G^v_\downarrow S^v_\downarrow}{G^v_\uparrow + G^v_\downarrow} \text{ and } S^v_{sp} = \frac{G^v_\uparrow S^v_\uparrow - G^v_\downarrow S^v_\downarrow}{G^v_\uparrow + G^v_\downarrow}, \tag{6.3}$$

$$P^v_{ch} = \frac{G^v_\uparrow P^v_\uparrow + G^v_\downarrow P^v_\downarrow}{G^v_\uparrow + G^v_\downarrow} \text{ and } P^v_{sp} = \frac{G^v_\uparrow P^v_\uparrow - G^v_\downarrow P^v_\downarrow}{G^v_\uparrow + G^v_\downarrow}. \tag{6.4}$$

The sum over both valleys (K and K') gives the total charge/spin Seebeck and Peltier co-efficients-

$$S_{ch} = S^K_{ch} + S^{K'}_{ch} \text{ and } S_{sp} = S^K_{sp} + S^{K'}_{sp}, \tag{6.5}$$

$$P_{ch} = P^K_{ch} + P^{K'}_{ch} \text{ and } P_{sp} = P^K_{sp} + P^{K'}_{sp}. \tag{6.6}$$

To simplify matters, the Onsager co-efficient matrix in Eq. (6.1), relating electric and heat currents to temperature difference and applied electric bias, can be rewritten as follows

[52, 122, 55]-

$$
\begin{pmatrix} L_s^{11,v} & L_s^{12,v} \\ L_s^{21,v} & L_s^{22,v} \end{pmatrix} = \begin{pmatrix} \mathcal{L}_s^{0,v} & \mathcal{L}_s^{1,v}/e\theta \\ \mathcal{L}_s^{1,v}/e & \mathcal{L}_s^{2,v}/e^2\theta \end{pmatrix},
\tag{6.7}
$$

$$
\text{with, } \mathcal{L}_s^{\alpha,v} = G_0 \int_{-\pi/2}^{\pi/2} d\phi \cos\phi \int_{-\infty}^{\infty} d\varepsilon (-\frac{\partial f}{\partial \varepsilon}) \frac{|\varepsilon|}{\hbar v_f} (\varepsilon - \mu)^{\alpha} \mathcal{T}_s^{v}(\varepsilon, \phi),
\tag{6.8}
$$

herein $G_0 = (e^2/\hbar)(W/\pi^2)$, with W being the width of graphene layer in $y-$ direction,

$\mathcal{L}_s^{0,v} = G_s^v$ is conductance of graphene electrons with spin s, in valley v [55]. ϕ is the

angle at which the electron is incident, ε is the energy of the electron, f is the Fermi-Dirac

distribution, μ is the Fermi energy and $\mathcal{T}_s^v(\varepsilon, \phi)$ is the transmission probability for spin s

electrons through strained graphene for valley v. To calculate the Onsager coefficients

$L_s^{ij,v}$ in Eq. (6.1), one first has to calculate the transmission probability $\mathcal{T}_s^v(\varepsilon, \phi)$ and then

after calculating the Onsager coefficients $L_s^{ij,v}$ in Eq. (6.1), we calculate efficiency and

power of our quantum spin heat engine. To do that we need to write the response matrix

in terms of electric charge(J_{ch}) and spin(J_{sp}) currents as well as heat current (J_Q), which

can be calculated from Eq. (6.1) by using the relations- $J_{ch} = j_\uparrow + j_\downarrow$, $J_{sp} = j_\uparrow - j_\downarrow$ and

$J_Q = j_\uparrow^q + j_\downarrow^q$ as follows [16]-

$$
\begin{pmatrix} J_{ch} \\ J_{sp} \\ J_Q \end{pmatrix} = G_{ch} \begin{pmatrix} 1 & P & S_{ch} \\ P & 1 & P'S_{ch} \\ S_{ch}T & P'S_{ch} & \mathcal{K}/G_{ch} \end{pmatrix} \begin{pmatrix} -\mathcal{E} \\ -\mathcal{E}_{sp} \\ -\Delta\theta \end{pmatrix}.
\tag{6.9}
$$

In the above Eq. (6.9), $\mathcal{E}$ is the applied electric field while the spin voltage applied $\mathcal{E}_{sp} = 0$ in

our system. Here we have summed the contribution of two valleys such that the total electric

charge conductance $G_{ch} = G_\uparrow + G_\downarrow$ and spin conductance $G_{sp} = |G_{ch}P|$, with $G_s = \sum_v G_s^v$

and $S_s = \frac{1}{2}\sum_v S_s^v$ with $s = \uparrow, \downarrow$, S_{ch} and S_{sp} are the charge and spin Seebeck co-efficients

respectively, P is the polarization of spin conductance while P' is the polarization of the

product of Seebeck coefficient and conductance [16, 113] which are defined as follows:

$$S_{ch} = \frac{G_\uparrow S_\uparrow + G_\downarrow S_\downarrow}{G_\uparrow + G_\downarrow}, \quad P = \left| \frac{G_\uparrow - G_\downarrow}{G_\uparrow + G_\downarrow} \right|, \quad P' = \left| \frac{G_\uparrow S_\uparrow - G_\downarrow S_\downarrow}{G_\uparrow S_\uparrow + G_\downarrow S_\downarrow} \right|. \quad (6.10)$$

Similarly $S_{sp} = S_{ch}P'$. The spin polarization also affects the thermal conductance which are defined as-

$$\mathcal{K} = \kappa + \frac{1 + P'^2 - 2PP'}{(1 - P^2)} G_{ch} S_{ch}^2 T = \kappa + G_\uparrow S_\uparrow^2 T + G_\downarrow S_\downarrow^2 T, \quad (6.11)$$

with κ being the thermal conductivity in absence of any electrical charge or spin conductivity[16], defined as-

$$\kappa = \kappa_\uparrow + \kappa_\downarrow, \quad \kappa_s = \frac{L_s^{11} L_s^{22} - L_s^{12} L_s^{21}}{L_s^{11}}, \quad (6.12)$$

with $L_s^{ij} = \sum_v L_s^{ij,v}$ as in Eq. (6.1).

6.2.2 Efficiency and power of quantum spin heat engine

The charge(spin) power[53] defined as usual as the product of electric current and volatge applied then can be written as-

$$\mathcal{P}_{ch(sp)} = -J_{ch(sp)}\mathcal{E} = -(G_{ch(sp)}\mathcal{E} + G_{ch}S_{ch(sp)}\Delta\theta)\mathcal{E}. \quad (6.13)$$

The above equation is maximized by $\frac{d\mathcal{P}_{ch(sp)}}{d\mathcal{E}} = 0$, at $\mathcal{E} = -\frac{G_{ch}S_{ch(sp)}}{2G_{ch(sp)}}\Delta\theta$, which gives maximum power as-

$$P_{ch}^{max} = \frac{1}{4}S_{ch}^2 G_{ch}(\Delta\theta)^2 \text{ and } P_{sp}^{max} = \frac{1}{4}S_{sp}^2 \frac{G_{ch}^2}{G_{sp}}(\Delta\theta)^2. \quad (6.14)$$

The efficiency at maximum power is defined as the ratio of maximum power to the heat current transported and can be derived as follows[53]-

$$\eta(\mathcal{P}_{ch}^{max}) = \frac{\mathcal{P}_{ch}^{max}}{J_Q} = \frac{\eta_c}{2} \frac{G_{ch}S_{ch}^2\theta/(\mathcal{K} - G_{ch}S_{ch}^2\theta)}{2 + G_{ch}S_{ch}^2\theta/(\mathcal{K} - G_{ch}S_{ch}^2\theta)} = \frac{\eta_c}{2} \frac{ZT|_{ch}}{2 + ZT|_{ch}}, \tag{6.15}$$

$$\eta(\mathcal{P}_{sp}^{max}) = \frac{\mathcal{P}_{sp}^{max}}{J_Q} = \frac{\eta_c}{2} \frac{G_{ch}^2 S_{sp}^2\theta/(G_{sp}\mathcal{K} - G_{ch}^2 S_{ch}S_{sp}\theta)}{2 + G_{ch}^2 S_{ch}S_{sp}\theta/(G_{sp}\mathcal{K} - G_{ch}^2 S_{ch}S_{sp}\theta)} = \frac{\eta_c}{2} P' \frac{ZT|_{sp}}{2 + ZT|_{sp}}, \tag{6.16}$$

at $\mathcal{E}_{ch(sp)} = -\frac{G_{ch}S_{ch(sp)}}{2G_{ch(sp)}}\Delta\theta$, which is the condition for maximum power. Herein, η_c is the Carnot efficiency defined by $\frac{\Delta\theta}{\theta}$ and $ZT|_{ch/sp}$ is the figure of merit, a dimensionless quantity, defined as-

$$ZT|_{ch} = \frac{G_{ch}S_{ch}^2\theta}{\mathcal{K} - G_{ch}S_{ch}^2\theta}, \tag{6.17}$$

$$ZT|_{sp} = \frac{P'G_{ch}S_{ch}^2\theta}{P\mathcal{K} - P'G_{ch}S_{ch}^2\theta}. \tag{6.18}$$

Similarly, efficiency η can be written as[53]-

$$\eta_{ch} = \frac{\mathcal{P}_{ch}}{J_Q} = \frac{(G_{ch}\mathcal{E} + G_{ch}S_{ch}\Delta\theta)\mathcal{E}}{(G_{ch}S_{ch}\theta\mathcal{E} + \mathcal{K}\Delta\theta)}, \tag{6.19}$$

$$\eta_{sp} = \frac{\mathcal{P}_{sp}}{J_Q} = \frac{(G_{sp}\mathcal{E} + G_{ch}S_{sp}\Delta\theta)\mathcal{E}}{(G_{ch}S_{ch}\theta\mathcal{E} + \mathcal{K}\Delta\theta)}. \tag{6.20}$$

To calculate maximal efficiency for the charge transported we need to calculate $\frac{d\eta_{ch}}{d\mathcal{E}} = 0$ in Eq. (6.19), this with the condition $J_Q > 0$, gives-

$$\mathcal{E} = \frac{\mathcal{K}}{G_{ch}S_{ch}\theta}\left(-1 + \sqrt{1 - \frac{G_{ch}S_{ch}^2\theta}{\mathcal{K}}}\right)\Delta\theta,$$

Thus, substituting $\mathcal{E}$ in Eq. (6.19)- $\quad \eta_{ch}^{max} = \eta_c \frac{\sqrt{ZT|_{ch} + 1} - 1}{\sqrt{ZT|_{ch} + 1} + 1}. \tag{6.21}$

Similarly, to calculate the maximal efficiency for spin transport we need to calculate $\frac{d\eta_{sp}}{d\mathcal{E}} = 0$ in Eq. (6.20), this again with the condition $J_Q > 0$, gives-

$$\mathcal{E} = \frac{\mathcal{K}}{G_{ch}S_{ch}\theta}(-1 + \sqrt{1 - \frac{P'}{P}\frac{G_{ch}S_{ch}^2\theta}{\mathcal{K}}})\Delta\theta,$$

Thus, substituting $\mathcal{E}$ in Eq. (6.20)- $\quad \eta_{sp}^{max} = \eta_c P'\frac{\sqrt{ZT|_{sp}+1}-1}{\sqrt{ZT|_{sp}+1}+1}.$ (6.22)

After determining the expressions for the quantities (both charge as well as spin) like Seebeck coefficient, Thermoelectric figure of merit, maximum power output and efficiency of respective heat engines at maximum power, we plot them in sections 6.3.3 and 6.3.4. We also discuss and analyse the aforesaid plots in the same section.

6.2.3   Coefficient of Performance of quantum charge/spin refrigerator

To use our model as a quantum refrigerator, we have to find the coefficient of performance of our system. The co-efficient of performance of the refrigerator is defined by the ratio of heat current extracted from the hot reservoir to the electrical power $\mathcal{P}$, such as for charge transport [17]-

$$\eta_{ch}^r = \frac{J^Q}{\mathcal{P}_{ch}},$$ (6.23)

which is maximum (considering $J^Q < 0$ and $\mathcal{P}_{ch} < 0$) for -

$$\mathcal{E} = \frac{\mathcal{K}}{G_{ch}S_{ch}\theta}(-1 - \sqrt{1 - \frac{G_{ch}S_{ch}^2\theta}{\mathcal{K}}})\Delta\theta.$$ (6.24)

Thus, substituting $\mathcal{E}$ in Eq. (6.23)- $\quad \eta_{ch}^{r,max} = \eta_c^r\frac{\sqrt{ZT|_{ch}+1}-1}{\sqrt{ZT|_{ch}+1}+1},$ (6.25)

where $\eta_c^r = \frac{\theta}{\Delta\theta}$ is the efficiency of an ideal refrigerator. The reason we have the condition $J_Q < 0, P_{ch} < 0$ when deriving $\eta_{ch}^{r,max}$ is because we intend to use it as a refrigerator. A refrigerator to describe it crudely converts work done to heat ($J_Q < 0$) or for a refrigerator work is done on the refrigerator system and it results in lowering of temperature and transfer of heat to environment, this is opposite to what a heat engine does for which $J_Q > 0$. Similarly we can calculate the coefficient of performance of a spin dependent refrigerator via the ratio of heat current extracted to spin power supplied,

$$\eta_{sp}^r = \frac{J^Q}{\mathscr{P}_{sp}}, \tag{6.26}$$

which is again maximum (considering $J^Q < 0$ and $\mathscr{P}_{sp} < 0$) for-

$$\mathscr{E} = \frac{\mathscr{K}}{G_{ch}S_{ch}\theta}\left(-1 - \sqrt{1 - \frac{P'}{P}\frac{G_{ch}S_{ch}^2\theta}{\mathscr{K}}}\right)\Delta\theta,$$

Thus, substituting $\mathscr{E}$ in Eq. (6.26)- $\quad \eta_{sp}^{r,max} = \frac{\eta_c^r}{P'}\frac{\sqrt{ZT|_{sp} + 1} - 1}{\sqrt{ZT|_{sp} + 1} + 1}. \tag{6.27}$

For the systems with broken time-reversal(TR) symmetry, the upper bound of the refrigerator coefficient of performance (COP) $\eta_{ch}^{r,max}$ is always less than the Carnot limit η_c^r , and it decreases with the deviation of asymmetric parameter $x = \frac{L^{12}}{L^{21}}$ from 1, see Ref. [17]. For systems with conserved TR symmetry, the upper bound of the corresponding maximum COP $\eta_{ch}^{r,max}$ equals η_c^r at $ZT|_{ch} \to \infty$ for giant thermoelectric figure of merit [53]. This is the advantage of multiterminal quantum heat engine systems with time reversal symmetry preserved, these systems can be converted to work as a refrigerator with larger COP than multi-terminal quantum heat engine systems with broken TR symmetry. Since our quantum heat engine system is a two terminal system, it always conserves the TR symmetry due to current conservation, see Ref. [126] and thus works as a highly efficient refrigerator with large COP.
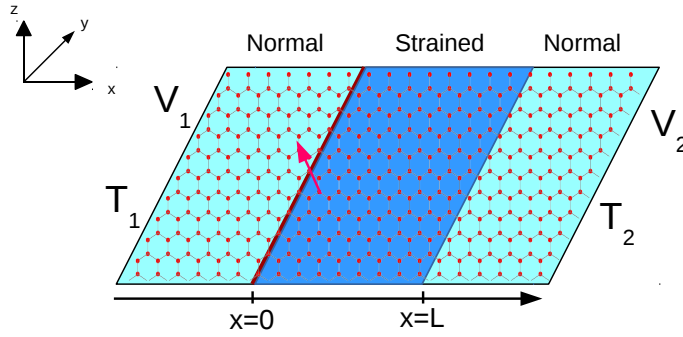
Figure 6.1: Monolayer graphene with a magnetic impurity at $x = 0$ denoted by thick maroon line. The middle portion is strained region while the two side portions are normal graphene regions. Voltages V_1 and V_2 are applied to the two sides which are at temperatures T_1 and T_2 respectively.

6.3 Graphene spin heat engine

6.3.1 Model

A graphene sheet is lying in the $x - y$ plane, a strain is applied as before to the region $0 < x < L$, see Fig. 6.1, with a magnetic impurity at $x = 0$. The in-plane uniaxial strain impacts the hopping between nearest neighbours and is generally delineated via a gauge vector which takes opposing signs in the two valleys (K and K') of graphene [138]. In the Landau gauge, the vector potential corresponding to the strain is $\vec{A} = (0, A_y)$. The system is then defined by the Hamiltonian-

$$\mathcal{H}_{K/K'} = H_{K/K'} + J\mathbf{s}.\mathbf{S}\delta(x) \tag{6.28}$$

with $H_K = \hbar v_f \sigma.(k - t)$ and $H_{K'} = \hbar v_f \sigma^*.(k + t)$. Strain is denoted as $t = A_y/\hbar v_f[\Theta(x) - \Theta(x - L)]$ with Θ the Heaviside step function and v_F the Fermi velocity. The first term in Eq. (6.28) represents the kinetic energy in graphene with $\sigma = (\sigma_x, \sigma_y)$ - the Pauli matrices that operate on the sublattices A or B and $\mathbf{k} = (k_x, k_y)$ the 2D wave vector. The second term in Eq. (6.28) denotes the exchange interaction between Dirac electron and magnetic impurity with J representing the strength of the exchange interaction. The spin of Dirac

electron is denoted by $\mathbf{s}$, while $\mathbf{S}$ represents spin of the magnetic impurity and m its magnetic moment, while magnetic moment of Dirac electrons is $1/2$ (spin up) or $-1/2$ (spin down). For better understanding of our model we have compared our delta potential magnetic impurity with a rectangular potential barrier magnetic impurity in Fig. 6.2. There is a single magnetic impurity located along the line $x = 0$. A solid black color line is shown at $x = 0$ in Fig. 6.2(a). The magnetic impurity is lying along this line. The magnetic impurity is modelled as a delta potential in $x-$, but is uniform in the $y-$direction. A magnetic quantum dot doped with few Mn^+ ions can be thought of as a magnetic impurity, see Refs. [127, 128]. It is assumed to have a finite width with a translational invariance in the $y-$direction. This can be understood with an analogy to a rectangular potential barrier in graphene. Klein tunnelling in graphene is a 2D scattering problem, see Ref. [129]. The Klein setup has a rectangular potential barrier between $x = 0$ and $x = L$ with translational invariance in the $y-$direction, as shown in Fig. 6.2(c). The potential barrier affects the transmission of incident particles in the $x-$direction but doesn't affect the transmission in $y-$direction because the transmitting particle cannot feel the potential change in the $y-$direction. As one reduces the length L of the potential barrier, it becomes similar to a delta potential located at $x = 0$, see Ref. [130]. Similarly, a magnetic impurity can have a finite width between $x = 0$ and $x = L$ with a translational invariance in the $y-$direction, as shown in Fig. 6.2(b), see Ref. [127]. If one decreases the width L of the impurity, it reduces to a delta function like profile affecting the transmission in the $x-$direction but not in the $y-$direction, see Fig. 6.2(a). All electrons passing through the system interact with the impurity. Refs. [90, 121, 134, 135, 127, 128] too have a magnetic impurity embedded into a graphene monolayer very similar to us. The analysis as done in Refs. [90, 121, 127], is used in this chapter also. In Ref. [127], a delta potential approximation of a rectangular barrier magnetic impurity in a graphene monolayer shows that for a range of incident angles from $-\pi/6$ to $\pi/6$ the difference between the transmissions through delta potential magnetic impurity and that of the rectangular barrier
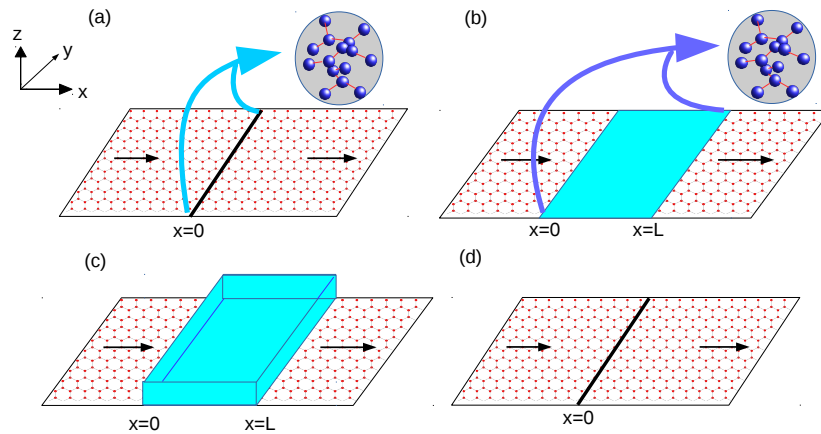
Figure 6.2: 2D graphene monolayer with (a) a delta potential magnetic impurity, (b) rectangular barrier magnetic impurity, (c) a rectangular potential barrier and (d) a delta potential barrier. A rectangular barrier magnetic impurity(b) models a magnetic quantum dot (see Ref. [127]) the transmission through which approximates that of a delta potential magnetic impurity(a) to a great extent. Similarly, a rectangular potential barrier(c) approximates a delta potential(d) in modelling the Klein paradox (see Refs. [129, 130]).

magnetic impurity is quite small. In Ref. [127], the delta potential magnetic impurity is an approximation for a magnetic quantum dot with spin.

We consider a magnetic impurity as the prototype of a magnetic quantum dot doped with few Mn^+ ions, oriented by an external magnetic field and put in a specific state with spin S and spin magnetic moment in z-direction m, see Refs. [127, 128]. It can be oriented such that only a particular state-defined by S, m is occupied. Two types of scattering can happen: 1. with spin-flip (same S but $m \to m \pm 1$) or 2. without spin-flip (same S as well as m) of magnetic impurity. The rest of the states would have zero occupation probability as shown in the analysis of the scattering of electrons due to the magnetic impurity in the next subsection, see also Refs. [127, 90, 121].

6.3.2   Wave functions and boundary conditions

To calculate the transmission probability and from it the Onsager coefficients and the thermoelectric factors we consider a spin-up electron with energy E incident at the strained graphene interface at $x = 0$ at an incident angle ϕ . At the interface itself we also have a

magnetic impurity. The incident electron thus can be scattered due to the strained region. Further, its spin can also be affected because of the magnetic impurity. The incident electron thus can be scattered as a spin up or down electron depending on the spin and magnetic moment of the magnetic impurity. The wave function for A-sublattice in each region (normal and strained) for K- valley can be written as:

For $x < 0$-

$$\psi_A^1(x,y) = \begin{bmatrix} (e^{ik_x x} + r_\uparrow e^{-ik_x x})\chi_m \\ -r_\downarrow e^{-ik_x x}\chi_{m+1} \end{bmatrix}, \tag{6.29}$$

$$\psi_B^1(x,y) = \begin{bmatrix} (e^{ik_x x + i\phi} + r_\uparrow e^{-ik_x x - i\phi})\chi_m \\ -r_\downarrow e^{-ik_x x - i\phi}\chi_{m+1} \end{bmatrix}, \tag{6.30}$$

in region $0 < x < L$-

$$\psi_A^2(x,y) = \begin{bmatrix} (a_\uparrow e^{iq_x x} + b_\uparrow e^{-iq_x x})\chi_m \\ (a_\downarrow e^{iq_x x} - b_\downarrow e^{-iq_x x})\chi_{m+1} \end{bmatrix}, \tag{6.31}$$

$$\psi_B^2(x,y) = \begin{bmatrix} (a_\uparrow e^{iq_x x + i\gamma} + b_\uparrow e^{-iq_x x - i\gamma})\chi_m \\ (a_\downarrow e^{iq_x x + i\gamma} - b_\downarrow e^{-iq_x x - i\gamma})\chi_{m+1} \end{bmatrix}, \tag{6.32}$$

and for $x > L$-

$$\psi_A^3(x,y) = \begin{bmatrix} t_\uparrow e^{ik_x x}\chi_m \\ t_\downarrow e^{ik_x x}\chi_{m+1} \end{bmatrix}, \tag{6.33}$$

$$\psi_B^3(x,y) = \begin{bmatrix} t_\uparrow e^{ik_x x + i\phi}\chi_m \\ t_\downarrow e^{ik_x x + i\phi}\chi_{m+1} \end{bmatrix}. \tag{6.34}$$

The x component of the wave-vector in strained region is $q_x = \sqrt{(E/\hbar v_F)^2 - (k_y - t)^2}$, whereas in the normal region q_x is substituted with k_x , wherein $k_x = E\cos\phi/\hbar v_F$, and the phase factor in strained region is given by $\tan\gamma = (k_y - t)/q_x$. χ_m is the eigen state of $z-$component of spin operator of magnetic impurity S_z with $S_z\chi_m = m\chi_m$, m being the corresponding eigen-value. The spin flipping mechanism is considered elastic and the sum of the $z-$components of the spin magnetic moment of impurity(m) and of electron($m' = \pm 1/2$), i.e., $M = m + m'$ remains conserved before and after spin-flip scattering. Following Ref. [143], one obtains the boundary conditions at $x = 0$:

$$i\hbar v_F[\psi_B^2(x=0) - \psi_B^1(x=0)] = \frac{J}{2}s.S[\psi_A^1(x=0) + \psi_A^2(x=0)], \tag{6.35}$$

$$i\hbar v_F[\psi_A^2(x=0) - \psi_A^1(x=0)] = \frac{J}{2}s.S[\psi_B^1(x=0) + \psi_B^2(x=0)] \tag{6.36}$$

and at $x = L$ as-

$$\psi_A^2(x=L) = \psi_A^3(x=L) \text{ and } \quad \psi_B^2(x=L) = \psi_B^3(x=L). \tag{6.37}$$

The spin flip process is attributed to the interaction between the spin of electron $(\mathbf{s})$ and the spin of magnetic impurity $(\mathbf{S})$, with $\mathbf{s}.\mathbf{S} = s_z S_z + \frac{1}{2}(s^- S^+ + s^+ S^-)$, where $s^- S^+ \begin{bmatrix} 1 \\ 0 \end{bmatrix} \chi_m = F \begin{bmatrix} 0 \\ 1 \end{bmatrix} \chi_{m+1}$ and $s^+ S^- \begin{bmatrix} 0 \\ 1 \end{bmatrix} \chi_m = F' \begin{bmatrix} 1 \\ 0 \end{bmatrix} \chi_{m-1}$ with $F = \sqrt{(S-m)(S+m+1)}$ and $F' = \sqrt{(S+m)(S-m+1)}$. Here, s_z with $s_z \begin{bmatrix} 1 \\ 0 \end{bmatrix} = \frac{1}{2} \begin{bmatrix} 1 \\ 0 \end{bmatrix}$ and S_z are the z-components of the spin operator of electron and magnetic impurity, respectively. $S_\pm = S_x \pm iS_y$, where S_+ and S_- are the spin raising and spin lowering operators for magnetic impurity, and $s_\pm = s_x \pm is_y$ are the same for electrons. After substituting the wave functions (6.29)-(6.34)

in Eqs. (6.35)-(6.37), at $x = 0$ we get-

$$a_\uparrow(e^{i\gamma} + i\alpha m) - b_\uparrow(e^{-i\gamma} - i\alpha m) - (e^{i\phi} - i\alpha m) + r_\uparrow(e^{-i\phi} + i\alpha m) + i\alpha F(a_\downarrow + b_\downarrow + r_\downarrow) = 0,$$

$$a_\downarrow(e^{i\gamma} - i\alpha(m+1)) - b_\downarrow(e^{-i\gamma} + i\alpha(m+1)) + r_\downarrow(e^{i\phi} - i\alpha(m+1)) + i\alpha F(a_\uparrow + b_\uparrow + r_\uparrow + 1) = 0,$$

$$a_\uparrow(1 + i\alpha m e^{i\gamma}) + b_\uparrow(1 - i\alpha m e^{-i\gamma}) - (1 - i\alpha m e^{i\phi}) - r_\uparrow(1 + i\alpha m e^{-i\phi}) + i\alpha F(a_\downarrow e^{i\gamma} - b_\downarrow e^{-i\gamma}$$

$$- r_\downarrow e^{-i\phi}) = 0, a_\downarrow(1 - i\alpha(m+1)e^{i\gamma}) + b_\downarrow(1 + i\alpha(m+1)e^{-i\gamma)}) - r_\downarrow(1 - i\alpha(m+1)e^{-i\phi}) + i\alpha F(a_\uparrow e^{i\gamma}$$

$$- b_\uparrow e^{-i\gamma} + e^{i\phi} - r_\uparrow e^{-i\phi}) = 0, \tag{6.38}$$

and at $x = L$ we get-

$$t_\uparrow e^{ikL} = a_\uparrow e^{iqL} + b_\uparrow e^{-iqL}, \qquad t_\downarrow e^{ikL} = a_\downarrow e^{iqL} + b_\downarrow e^{-iqL},$$

$$t_\uparrow e^{ikL+i\phi} = a_\uparrow e^{iqL+i\gamma} - b_\uparrow e^{-iqL-i\gamma}, \qquad t_\downarrow e^{ikL+i\phi} = a_\downarrow e^{iqL+i\gamma} + b_\downarrow e^{-iqL-i\gamma}. \tag{6.39}$$

In the above equations $\alpha = J/(4\hbar v_f)$. Eqs. (6.38), (6.39) consist of 8 unknowns $a_\uparrow$, $a_\downarrow$, $b_\uparrow$, $b_\downarrow$, $r_\uparrow$, $r_\downarrow$, $t_\uparrow$ and $t_\downarrow$ satisfy the probability conservation- $|r_\uparrow|^2 + |t_\uparrow|^2 + |r_\downarrow|^2 + |t_\downarrow|^2 = 1$. Similarly, for spin down incident electron from the left side we can derive the scattering amplitudes. Further, for K' valley too solving the Hamiltonian one can get the transmission amplitude (t_s) and reflection amplitude (r_s) with $s = \uparrow, \downarrow$ again in a nod to probability conservation satisfying $|r_\uparrow|^2 + |t_\uparrow|^2 + |r_\downarrow|^2 + |t_\downarrow|^2 = 1$ for K' valley also. Since there is no inter valley scattering, our results remain identical for K' valley after integrating over both energy and the incident angle. So we focus on the transmission probability $\mathcal{T}_s = |t_s|^2$ in one valley $v = K$ only. Since the expression for $\mathcal{T}_s$ is large we only analyse the thermoelectric properites via plots in Figs. 6.3-6.10. We get a simplified transmission probability of an electron for only $J = 0$ case (considering no magnetic impurity at $x = 0$), which is
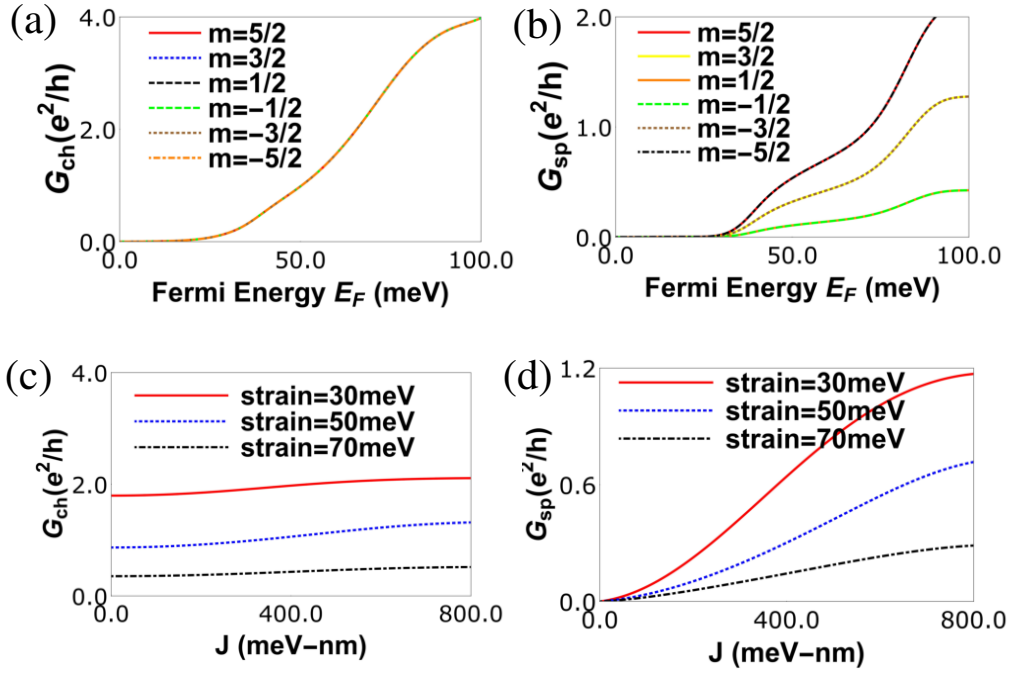
Figure 6.3: (a) Charge Conductance (G_{ch}) vs. E_F (Fermi energy) for various values of magnetic moment m, length of strained graphene layer $L = 40nm$ and width $W = 20$ nm, strain $t = 50meV$, temperature $\theta = 30K$ with spin of magnetic impurity $S = 5/2$ and $J = -600meV$, (b) Spin Conductance (G_{sp}) vs. E_F (Fermi energy) for various values of magnetic moment m, length of strained graphene layer $L = 40nm$, strain $t = 50meV$, temperature $\theta = 30K$ with spin of magnetic impurity $S = 5/2$ and $J = -600meV$, (c) Charge conductance (G_{ch}) vs J (impurity coupling strength) for various strains at Fermi energy $E_F = 50meV$, length of strained graphene layer $L = 60nm$, temperature $\theta = 30K$ with spin of magnetic impurity $S = 5/2$ and spin magnetic moment $m = -5/2$. (d)Spin conductance (G_{sp}) vs. J (impurity coupling strength) for various strains at Fermi energy $E_F = 50meV$, length of strained graphene layer $L = 60nm$, temperature $\theta = 30K$ with spin of magnetic impurity $S = 5/2$ and spin magnetic moment $m = -5/2$.

$(\mathcal{T}_\uparrow + \mathcal{T}_\downarrow = \mathcal{T})$-

$$\mathcal{T}(\varepsilon, \phi) = \frac{1}{\cos^2[q_x L] + \sin^2[q_x L](\frac{1 - \sin[\theta]\sin[\phi]}{\cos[\theta]\cos[\phi]})^2}. \tag{6.40}$$

6.3.3 Onsager coefficients

In Figs. 6.3 (a) and (b) we plot the charge and spin conductance for various m values (spin magnetic moment in z-direction) of magnetic impurity. We see that though different magnetic orientations have no effect on the charge conductance, the spin conductance

increases as the magnitude of m increases, but it is unaffected by the direction of m. Decreasing the spin magnetic moment m of the magnetic impurity reduces the transmission probability of spin up electrons, but increases the transmission probability for spin down electrons. The total charge conductance remains unaffected by the changing m, but the spin conductance increases as the difference between spin up current and spin down current increases. Similar effects on the charge/spin conductances are observed when the exchange interaction J is altered. In Fig. 6.3 (c) we see that the charge conductance is almost constant as function of the exchange interaction (J), however the spin conductance increases as shown in Fig. 6.3 (d). If an electron is incident at the interface of strained and unstrained region, it is refracted to the strained region with a refraction angle $\gamma = \tan^{-1}(k_y - t)/q_x$ in K valley. So, if one increases the strain t, electrons with incident angle 0 to $\pi/2$ will refract close to the normal to the interface between the two regions and thus their transmission probability increases, but electrons with incident angle 0 to $(-\pi/2)$ will refract away from the normal to interface reducing the transmission probability more and thus reducing the overall transmission (after integrating over incident angle ϕ) in the the K valley. In the K' valley, the electrons refract in the opposite direction to that of the K valley with a refraction angle $\gamma = tan^{-1}(k_y + t)/q_x$, but overall transmission probability (after integrating over incident angle ϕ) reduces with strain and is always equal to the K valley unless a magnetic field is applied at the interface to create a valley polarization, see Ref. [132]. Increasing strain decreases both the charge as well as spin conductances. Similar to Fig. 6.3, in Fig. 6.4 we see the effect of the orientation of the magnetic impurity in $z-$ direction (m) and strain on the charge and spin Seebeck coefficients. In Figs. 6.4 (a) and (b) we see that impurity orientation m has no effect on the charge Seebeck coefficient, but it has a huge impact on the spin Seebeck coefficient. In Figs. 6.4 (c) and (d) we see that charge and spin Seebeck coefficients both increase with increasing strain, which is opposite to the effect on charge and spin conductances. This can be understood as follows- A
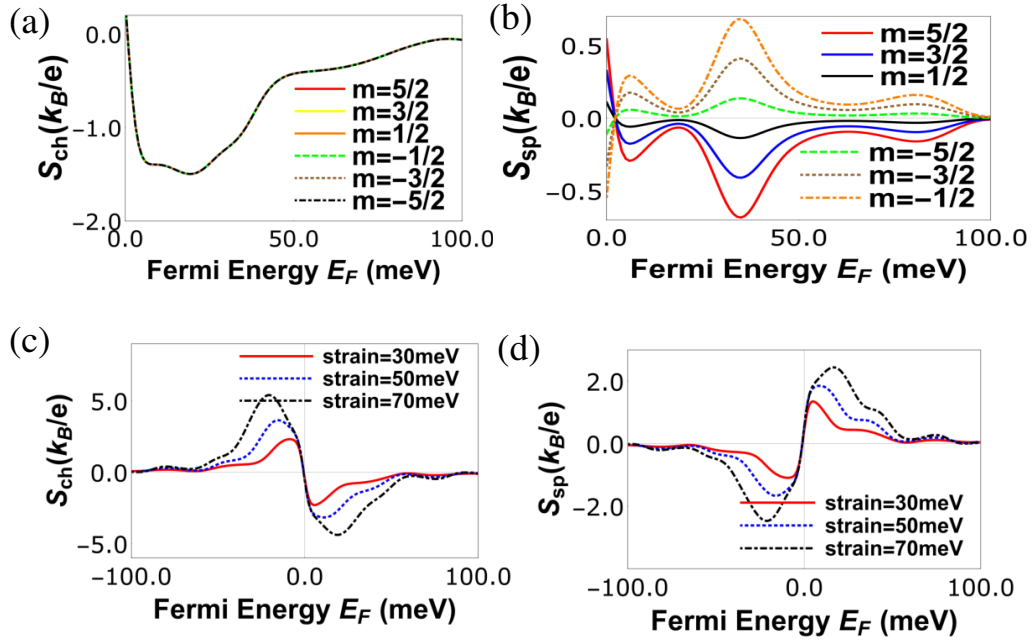
Figure 6.4: (a) Charge Seebeck coefficient (S_{ch}) vs. Fermi energy for various m of magnetic impurity at $T = 30K, J = -600$ meV-nm, strain (t)=50 meV and spin $S = 5/2$ and length of strained graphene region $L = 40nm$ and width $w = 20$ nm and (b) Spin Seebeck coefficient S_{sp} vs. Fermi energy E_F in meV for various m of magnetic impurity, length of strained graphene layer $L = 40$ nm, strain $= 50meV$, temperature $\theta = 30K$ with spin of magnetic impurity $S = 5/2$ and $J = -600meV$. (c) Charge Seebeck coefficient (S_{ch}) vs Fermi energy for various strains at $J = 600meV - nm$, length of strained graphene layer $L = 60nm$, temperature $\theta = 30K$ with spin of magnetic impurity $S = 5/2$ and spin magnetic moment $m = -5/2$, (d) Spin Seebeck coefficient (S_{sp}) vs Fermi energy for various strains with parameters same as (c).

bandgap in a nanostructured material can increase the Seebeck coefficient significantly. In graphene, due to its gapless bandstructure the Seebeck coefficient is very small, see Ref. [55]. Applying strain in a graphene device can shift the Dirac points in opposite direction by opening a conduction gap without opening a bandgap. This conduction gap increases with increasing strain and so also the charge/spin Seebeck coefficients.

From Fig. 6.4 (b), it's evident that spin Seebeck coefficient depends on the sign (orientation) of the magnetic impurity m, i.e., $S_{sp}|_m = -S_{sp}|_{-m}$, unlike the spin conductance which is independent, since $G_{sp} = |G_\uparrow - G_\downarrow|$. In Fig. 6.5(a) we see that exchange interaction strength J has no effect on charge Seebeck coefficient S_{ch} at zero strain, while the spin Seebeck coefficient S_{sp} increases with J, as shown in Fig. 6.5(b). In presence of strain, the effect of J on S_{ch} is negligible. One thing to note in Figs. 6.4 and 6.5 is that both spin
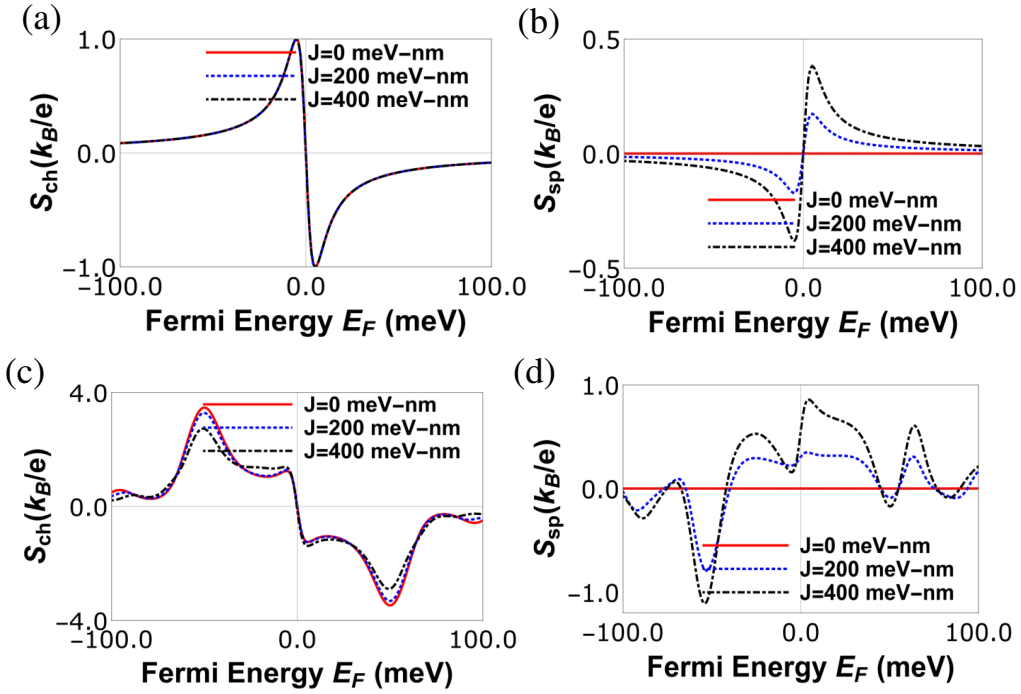
Figure 6.5: (a) Charge Seebeck coefficient S_{ch} vs. Fermi energy (E_F) for various exchange coupling strength J with parameters at $L = 40$ nm, strain $t = 0$ meV, $\theta = 30$ K, $S = 5/2$, $m = -5/2$, (b) spin Seebeck coefficient S_{sp} vs. Fermi energy (E_F) for various exchange coupling strength J with parameters at $L = 40$ nm, strain $t = 0$ meV, $\theta = 30$K, $S = 5/2$, $m = -5/2$, (c) charge Seebeck coefficient S_{ch} vs. Fermi energy (E_F) for various exchange coupling strength J with parameters at $L = 40$ nm, strain $t = 100$ meV, $\theta = 30$K, $S = 5/2$, $m = -5/2$, (d) spin Seebeck coefficient S_{sp} vs. Fermi energy (E_F) for various exchange coupling strength J with parameters at $L = 40$ nm, strain $t = 100$ meV, $\theta = 30$K, $S = 5/2$, $m = -5/2$.

as well as charge Seebeck coefficients are anti-symmetric as function of Fermi energy (E_F), i.e., $S_{ch/sp}(E_F) = -S_{ch/sp}(-E_F)$ at zero strain. In presence of finite strain while $S_{ch}(E_F) = -S_{ch}(-E_F)$, S_{sp} has no symmetry with respect to sign reversal of Fermi energy, in effect change of charge carriers from electrons to holes. All this is in contrast to the spin and charge conductances which are symmetric, $G_{ch/sp}(E_F) = G_{ch/sp}(-E_F)$, to reversal of charge carriers.

The sign change seen in Fig. 6.5(a) for the charge Seebeck coefficient S_{ch} near the charge neutrality point or Dirac point is because the charge carriers switch from electrons to holes. The origin of second peak in Fig. 6.5(c) is solely strain. On the other hand the first peak seen in Fig. 6.5(c) which appears close to the Dirac point is due to the asymmetric contribution
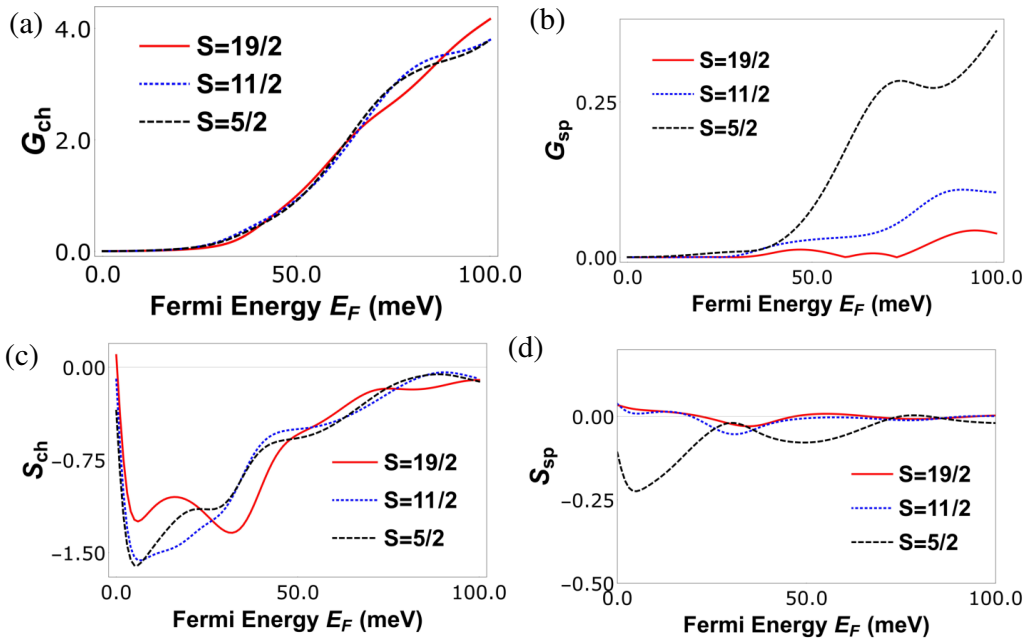
Figure 6.6: (a) Charge conductance G_{ch} vs. Fermi energy (E_F) for various spin S and magnetic moment m of the magnetic impurity with parameters at $L = 40$ nm, $W = 20$ nm, strain $t = 50$ meV, $\theta = 30$K, and exchange coupling $J = 600$ meV, (b) spin conductance G_{sp} vs. Fermi energy (E_F) for various spin S with fixed magnetic moment $m = 1/2$ of the magnetic impurity with parameters same as (a), (c) charge Seebeck coefficient S_{ch} vs. Fermi energy (E_F) for various spin S and magnetic moment $m = 1/2$ of the magnetic impurity with parameters same as (a), (d) spin Seebeck coefficient S_{sp} vs. Fermi energy (E_F) for various spin S and magnetic moment $m = 1/2$ of the magnetic impurity with parameters same as (a).

to the Seebeck current from electrons and holes, which arises due to the unique energy dependent density of states of graphene. The first peak is always present in graphene even in absence of strain, see Figs. 6.5(a) and (b) and Ref. [149]. In presence of strain, in addition to this unique energy dependent density of states of graphene, an asymmetry is created in the transmission probability as function of energy and that gives rise to the second peak in Fig. 6.5(c). See also Ref. [7], where a similar peak is observed due to strain in graphene. It should be noted that the position of the first peak is always fixed, i.e., close to the Dirac point but changing the parameters like length of the strained region one can change the position of the second peak and thus these two peaks may merge to form a single large peak, see Figs. 6.4(c) and (d) which in turn leads to large power and efficiency. It is to be noted from Figs. 6.5 (c) and (d) that at the Dirac point the charge Seebeck coefficient is exactly zero, while the spin Seebeck coefficient is finite, leading to the generation of pure spin current within the system due to temperature difference only. In Fig. 6.6, we have shown the effect of large spin S of the magnetic impurity on the charge/spin conductances and Seebeck coefficients. In Fig. 6.6 (a), we see that the charge conductance is not affected much by the high spin state of the magnetic impurity while the spin conductance is maximum when the spin of the magnetic impurity is small, as shown in Fig. 6.6(b). In Fig. 6.6 (c), we see that the S_{ch} is large for small S—the spin state of the magnetic impurity with the magnetic moment in the $z-$direction fixed while in Fig. 6.6 (d), we see that the spin Seebeck coefficient S_{sp} too is large for small values of S. For this reason, we have used a relatively lower value of spin $S = 5/2$ of magnetic impurity to get the maximum charge/spin Seebeck coefficient and conductances.

Recently, there have been some interesting works on quantum heat engines concentrating on the weakly non-linear regime, see Refs. [133, 131]. In the weakly non-linear regime, the
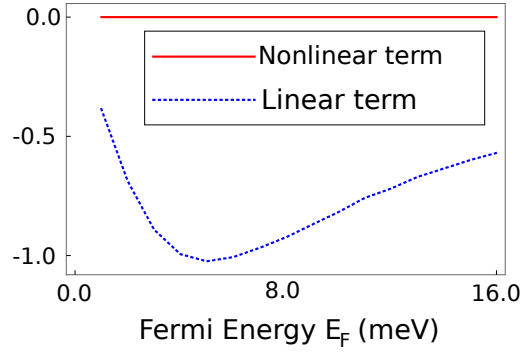
Figure 6.7: Linear and non-linear contribution to the charge Seebeck coefficient vs the Fermi energy. Parameters are as follows- Length of the strain region $L = 40$ nm, strain $t = 100$ meV, $\theta = 30$ K, spin configuration of the magnetic impurity $S = 5/2$, $m = -5/2$ and exchange interaction $J = 200$ meV-nm. (The same parameters as in Fig. 6.5(c).)

charge Seebeck coefficient can be written as-

$$
\begin{aligned}
S'_{ch} &= S_{ch} + S^1_{ch}\Delta\theta + O(\Delta\theta^2), \\
\text{with } S_{ch} &= -\frac{L_{11}}{G_{11}}, \\
\text{and } S^1_{ch} &= -\frac{1}{G_{11}}[G_{111}L_{11}^2 + L_{111}G_{11}^2 + G_{11}L_{11}(M_{121} - M_{111})], \qquad (6.41)
\end{aligned}
$$

where, S_{ch} is the linear contribution to the Seebeck coefficient, same as defined in Eq. (6.3) above and S^1_{ch} is the first order correction to the Seebeck coefficient in a two terminal system, i.e., the nonlinear contribution to the Seebeck coefficient. Here, G_{11} and G_{111} define the charge conduction of the system in the linear and non-linear regime respectively, and L_{11} and L_{111} define the Seebeck current in the linear and non-linear regime respectively. The terms M_{111} and M_{121} define the other non-linear contributions, see Refs. [131, 133]. The linear terms G_{11} and L_{11} are equal to $\sum_s L_s^{11}$ and $\sum_s L_s^{12}$, respectively, i.e., G_{11}(of Ref. [131])$= L_\uparrow^{11} + L_\downarrow^{11}$(of this chapter)$= G_\uparrow + G_\downarrow = G_{ch}$ and L_{11}(of Ref. [131])$= L_\uparrow^{12} + L_\downarrow^{12}$(of this chapter)$= G_\uparrow S_\uparrow + G_\downarrow S_\downarrow$ as in Eq. (6.3)(above). The nonlinear terms $G_{111}, L_{111}, M_{121}$

and M_{111} are defined as follows-

$$
\begin{aligned}
G_{111} &= \sum_{s,v}\left(2\frac{\partial L_s^{11,v}}{\partial \Delta V} + G_0 e \int_{-\pi/2}^{\pi/2} d\phi \cos\phi \int_{-\infty}^{\infty} d\varepsilon \left(-\frac{\partial f}{\partial \varepsilon}\right)\frac{|\varepsilon|}{\hbar v_f}\frac{\partial \mathcal{T}_s^v(\varepsilon,\phi)}{\partial \varepsilon}\right), \\
L_{111} &= \sum_{s,v}\left(2\frac{\partial L_s^{12,v}}{\partial \Delta \theta} + \frac{G_0}{e} \int_{-\pi/2}^{\pi/2} d\phi \cos\phi \int_{-\infty}^{\infty} d\varepsilon \left(-\frac{\partial f}{\partial \varepsilon}\right)\frac{|\varepsilon|}{\hbar v_f}\frac{(\varepsilon-\mu)^2}{\theta^2}\frac{\partial \mathcal{T}_s^v(\varepsilon,\phi)}{\partial \varepsilon}\right), \\
M_{111} &= \sum_{s,v}\left(\frac{\partial L_s^{12,v}}{\partial \Delta V} + \frac{\partial L_s^{11,v}}{\partial \Delta \theta} + G_0 \int_{-\pi/2}^{\pi/2} d\phi \cos\phi \int_{-\infty}^{\infty} d\varepsilon \left(-\frac{\partial f}{\partial \varepsilon}\right)\frac{|\varepsilon|}{\hbar v_f}\frac{(\varepsilon-\mu)}{\theta}\frac{\partial \mathcal{T}_s^v(\varepsilon,\phi)}{\partial \varepsilon}\right), \\
M_{121} &= \sum_{s,v}\left(-\frac{\partial L_s^{12,v}}{\partial \Delta V} + \frac{\partial L_s^{11,v}}{\partial \Delta \theta}\right).
\end{aligned}
\tag{6.42}
$$

If the nonlinear contribution, S_{ch}^1 is much smaller than the linear contribution S_{ch}, then we can neglect the nonlinear contribution. In Fig. 6.7, we have compared the nonlinear term S_{ch}^1 to the linear term S_{ch} and found that for our graphene spin heat engine the linear term is much larger than the nonlinear term, around eight orders of magnitude large. Thus, all the calculations including that of Seebeck coefficient are done in this chapter in the linear response regime only. Finally, we have neglected the phonon contribution in our calculations since the phonon contribution to the thermal conductance of graphene is quite small (almost absent) at low temperatures $0-30K$, see Figs. 2,3 of Ref. [54] and Fig. 5 of Ref. [151]. Beyond $25-30K$ range, the phonon contribution increases linearly with temperature, as shown in Refs. [54, 151]. Thus, the phonon contribution to the thermal conductance can be neglected at the temperature range $20-30K$ as discussed in this chapter.
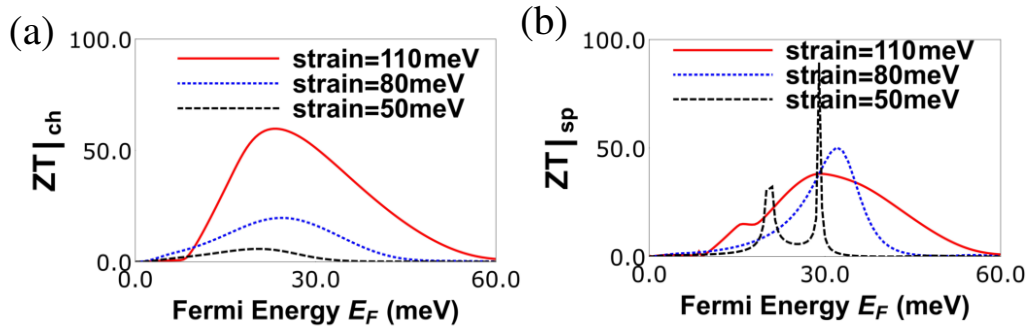
Figure 6.8: (a) Charge thermoelectric figure of merit ($ZT|_{ch}$) vs. Fermi energy for various strains with parameters $T = 30$ K, $J = 232$ meV-nm and $L = 80$ nm, $w = 20$ nm and spin $S = 5/2$, magnetic moment $m = -5/2$ of magnetic impurity, (b) Spin thermoelectric figure of merit $ZT|_{sp}$ vs. Fermi energy for various strains with parameters $\theta = 30$K, $J = 232$ meV-nm and $L = 80$ nm, $w = 20$ nm and spin $S = 5/2$, magnetic moment $m = -5/2$ of magnetic impurity.

6.3.4 Thermoelectric figure of merit, power and efficiency of graphene spin heat engine

To get large efficiency for our charge and spin heat engines we need a large charge and spin thermoelectric figure of merit ($ZT|_{ch}$ and $ZT|_{sp}$). From Eq. (6.17) we see that charge thermoelectric figure of merit is proportional to the product of square of the charge Seebeck coefficient S_{ch} and charge conductance G_{ch}, i.e., $S_{ch}^2 G_{ch}$, while spin thermoelectric figure of merit ($ZT|_{sp}$) is proportional to the product of charge and spin Seebeck (S_{ch} and S_{sp}) coefficients with charge conductance G_{ch}, i.e., $S_{ch} S_{sp} G_{ch} = P' G_{ch} S_{ch}^2$ as in Eq. (6.18).

In Fig. 6.8, charge and spin thermoelectric figure of merits are plotted as function of Fermi energy for various strains. In Fig. 6.8 (a) we see that charge figure of merit $ZT|_{ch}$ increases with strain, while spin figure of merit ZT_{sp} decreases as shown in Fig. 6.8 (b). $ZT|_{ch}$ takes values around 50 which is quite large and similar to those obtained in Ref. [16]. Further, $ZT|_{sp}$ approaches 100 which is completely unheard of. These giant charge and spin thermoelectric factors are crucial for designing highly efficient quantum charge and spin heat engines and are one of the main novelties of this chapter.

According to Eq. (6.15), this large ZT_{ch} will give rise to a large efficiency at maximum power,

(a)

(b)
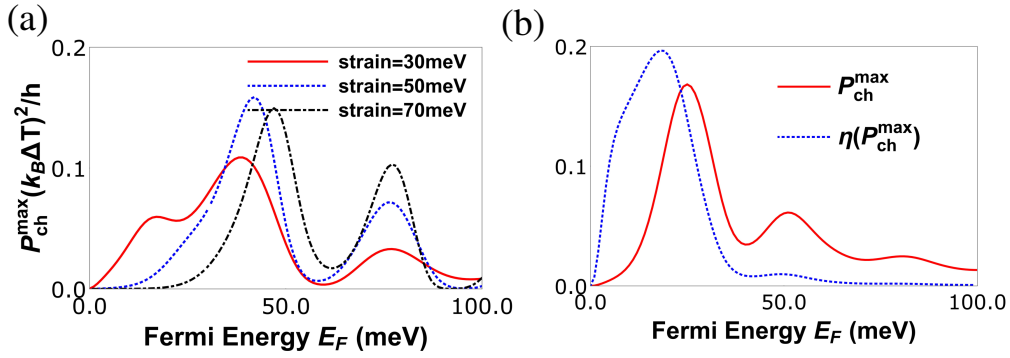
Figure 6.9: (a) Maximum power for charge current (P_{ch}^{max}) vs. Fermi energy (E_F) in meV for various strains at $J = 600$ meV-nm, length of strained graphene layer $L = 60$ nm, width $W = 20$ nm, temperature $T = 30$ K with spin of magnetic impurity $S = 5/2$ and spin magnetic moment $m = -5/2$, (b) Efficiency at maximum power vs. Fermi energy (E_F) in meV for strain $t = 30$ meV, $L = 70$ nm, $W = 20$ nm, $\theta = 30$ K, $J = 232$ meV-nm and spin $S = 5/2$, magnetic moment $m = -5/2$ of magnetic impurity.

$\eta(P_{ch}^{max}) = 0.48\eta_C$, corresponding to this value of ZT_{ch} the maximum power delivered by our graphene spin heat engine is $0.02(k_b\Delta\theta)^2/h$, which is quite small. This is the remarkable trade off between power and efficiency in a quantum heat engine, that when efficiency is maximum the corresponding power is minimum. That's why, we choose a set of parameters where power and efficiency both are moderately large to give the optimal performance. With a certain set of parameters, we obtain $ZT_{ch} \sim 2$ for which we get the efficiency at maximum power $\eta_{maxP} = 0.166\eta_C$ and maximum power delivered $\equiv 0.16\frac{(k_B\Delta\theta)^2}{h}$, which is a large value compared with some other charge QHE's, see Table 6.1.

(a)

(b)
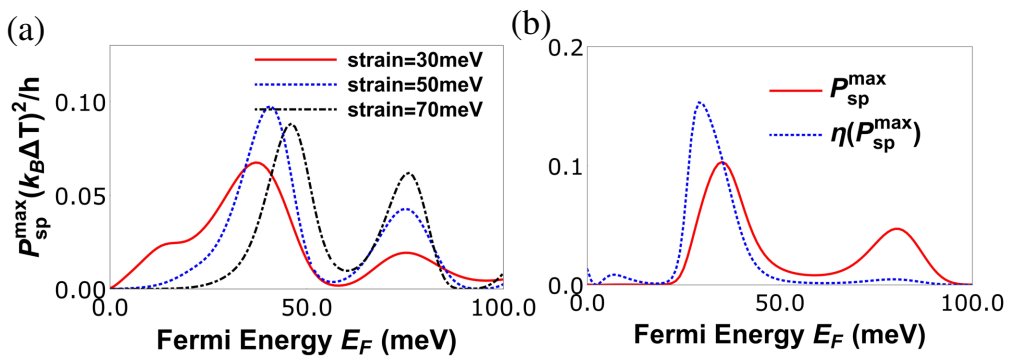
Figure 6.10: (a) Maximum power for spin current (P_{sp}^{max}) vs. Fermi energy (E_F) for various strains with parameters $J = 600$ meV-nm, $L = 60$ nm, $W = 20$ nm, $T = 30$ K, $S = 5/2$, $m = -5/2$, (b) Maximum spin power (P_{sp}^{max}) and efficiency at maximum power ($\eta(P_{sp}^{max})$) in units of η_c vs. Fermi energy (E_F) at $L = 40$ nm, $W = 20$ nm, $\theta = 30$ K, $J = -600$ meV-nm, strain $t = 50$ meV, $S = 5/2$, $m = -5/2$.

In Fig. 6.9 we plot the maximum power for charge heat engine at various strains, we see that there are two peaks in P_{ch}^{max}. The first peak in P_{ch}^{max} (which is proportional to $S_{ch}^2 G_{ch}$) is observed when the charge conductance G_{ch} dominates over the charge Seebeck coefficent S_{ch}, which can be seen at strain ($t = 50$ meV). The second peak appears when the charge Seebeck coefficient S_{ch} dominates over the charge conductance G_{ch}, this can be verified easily because the second peak increases with increasing strain. In Fig. 6.9(b) we plot both maximum power(P_{ch}^{max}) and the efficiency at maximum power ($\eta(P_{ch}^{max})$) as function of the Fermi energy (E_F). We see that $\eta(P_{ch}^{max})$ goes to almost $0.2\eta_c$, this is also a very large value as compared to other similar heat engines. The efficiency at maximum charge power as derived from Eq. (6.15) depends only on $ZT|_{ch}$. Since in our case $ZT|_{ch}$ takes quite high values its not surprising that we have a highly efficient charge heat engine. Further, we see that the efficiency $\eta(P_{ch}^{max})$ is maximum ($0.2\eta_c$) for $E_F = 18meV$ but at this Fermi energy the maximum power delivered is around $0.1(k_B\Delta\theta)^2/h$. However, at Fermi energy close to $23.5meV$ the efficiency although slightly lower at $0.16\eta_c$ the maximum power output is $0.16(k_B\Delta\theta)^2/h$. We not only need high efficiency but we need to deliver large output power too, balancing these two needs implies operating the charge heat engine at $E_F = 23.5meV$ will satisfy both our needs. Similarly, in Fig. 6.10 we plot the maximum power for spin heat engine for various strains, we see that there are two peaks in P_{sp}^{max} also. The first peak in P_{sp}^{max} (which is proportional to $S_{sp}^2 \frac{G_{ch}^2}{G_{sp}}$) is observed when the factor $\frac{G_{ch}^2}{G_{sp}}$ dominates over the spin Seebeck coefficient S_{sp}, which can be seen at strain $t = 50meV$. The second peak appears when the spin Seebeck coefficient S_{sp} dominates over the factor $\frac{G_{ch}^2}{G_{sp}}$, this can be again verified as the second peak increases with increasing strain. In Fig. 6.10(b) we plot both maximum power(P_{sp}^{max}) and efficiency at maximum power ($\eta(P_{sp}^{max})$) as function of the Fermi energy (E_F). We see that $\eta(P_{sp}^{max})$ goes to almost $0.15(k_B\Delta\theta)^2/h$. The efficiency at maximum spin power as derived from Eq. (6.22), depends on two factors $ZT|_{sp}$ and P'. Since in our case $ZT|_{sp}$ takes quite large values its not surprising that we have a highly

efficient spin heat engine in addition to a highly efficient charge based one too. Further, we see that the efficiency $\eta(P_{sp}^{max})$ is maximum $0.15\eta_c$ for $E_F = 30 meV$ but at this Fermi energy the maximum spin power delivered is around $0.07(k_B\Delta\theta)^2/h$. However, at Fermi energy close to $35 meV$ the efficiency although slightly lower at $0.1\eta_c$ the maximum spin power output is $0.1(k_B\Delta\theta)^2/h$. As stated before, we not only need high efficiency but we need to deliver large output spin power too balancing these two needs implies that operating the spin heat engine at $E_F = 35 meV$ will satisfy both our needs.

6.3.5 Comparison of graphene spin heat engine with related proposals

In Table 6.1 $\eta(P_{ch}^{max}), \eta(P_{sp}^{max}), P_{ch}^{max}, P_{sp}^{max}, ZT|_{ch}$ and $ZT|_{sp}$ and the maximum charge power generated in $1 cm^2$ area in this graphene spin heat engine with some other related works are compared, which can work both as a charge and spin QHE. It can be seen that our model system has excellent characteristics compared to other works like the maximum charge and spin thermoelectric figure of merit $ZT|_{ch/sp}$ achieved in our model is more than most of the other works, see Refs. [52, 16, 119]. Although the model spin heat engine of Ref. [16], has a larger $ZT|_{ch}$ it has but a smaller $ZT|_{sp}$. As efficiency $\eta_{ch/sp}^{max}$ is proportional to the $ZT|_{ch/sp}$, a large $ZT|_{ch/sp}$ leads to a large efficiency $\eta_{ch/sp}^{max}$ (not shown in Table 6.1). From Ref. [52] we have calculated the P_{ch}^{max} to be $0.09(K_B\Delta\theta)^2$ and $\eta(P_{ch}^{max})$ to be $0.06\eta_c$ for charge based heat engine and thus they are smaller than what is obtained for this graphene spin heat engine. In Ref. [16] only $ZT|_{ch/sp}$ is calculated but P_{ch}^{max} and $\eta(P_{ch}^{max})$ are missing. In Ref. [119], a large value for the maximum charge power P_{ch}^{max} is obtained more than that seen in our model, although, $\eta(P_{ch}^{max})$ is comparable to our's. The reason for this is explained below. The maximum charge power P_{ch}^{max} observed in our system is greater than that in Ref. [52] but less than that of Ref. [119]. Although the maximum charge power generated in Ref. [119] is larger than that generated in our graphene spin heat engine,

however, the system dimensions of the quantum heat engine(QHE) of Ref. [119] are much larger than ours too. In our case, the area of our graphene spin heat engine is $1200nm^2$ with dimensions used in plot for maximum charge power (Fig. 6.9(a))- length $L \sim 60nm$ while width $W \sim 20nm$, however in Ref. [119] the area of their QHE system is $8316nm^2$ with dimensions of length $L \sim 1350nm$ and width $W \sim 6.16nm$ making the area of the QHE of Ref. [119] around 7 times larger then our graphene spin heat engine. Thus, if a $1cm^2$ area is fabricated with these small quantum heat engines then for those systems whose dimensions are small, more can be fitted in this area and more the charge power generated. We have found that under these circumstances the total charge power generated in our system is twice that of Ref. [119], see Table 6.1. The maximum spin power obtained in our graphene spin heat engine is not discussed in any other QHE before.

Table 6.1: Comparison of graphene spin heat engine with related models

	Ramsheti, et. al., Ref. [52]	Bauer, et. al., Ref. [16]	Po-Hao Chang, et. al., Ref. [119]	This model
$ZT\vert_{ch}$	0.3	100	3	55
$ZT\vert_{sp}$	1.5	0.9	N.A.	50
P_{ch}^{max}	$0.09\frac{(K_B\Delta\theta)^2}{h}$	N.A.	$0.5\frac{(K_B\Delta\theta)^2}{h}$	$0.16\frac{(K_B\Delta\theta)^2}{h}$
Maximum charge power generated in $1cm^2$ area	N.A.	N.A.	$1.7*10^{-3}$ W	$3.8*10^{-3}$ W
P_{sp}^{max}	N.A.	N.A.	N.A.	$0.1\frac{(K_B\Delta\theta)^2}{h}$
$\eta(P_{ch}^{max})$	$0.06\eta_c$	N.A.	$0.3\eta_c$	$0.48\eta_c$
$\eta(P_{sp}^{max})$	N.A.	N.A.	N.A.	$0.1\eta_c$

N.A.-This property is not addressed in the paper. Note: Ref. [119] includes phonon contribution too, while Refs. [16, 52] as also our model ignore it since we are in the temperature regime $0-30K$. $ZT\vert_{ch} = 3$ seen in Ref. [119] is at 40 K, in the regime $0-30$ K where phonon contribution is negligible, $ZT\vert_{ch} < 3$ in Ref. [119].
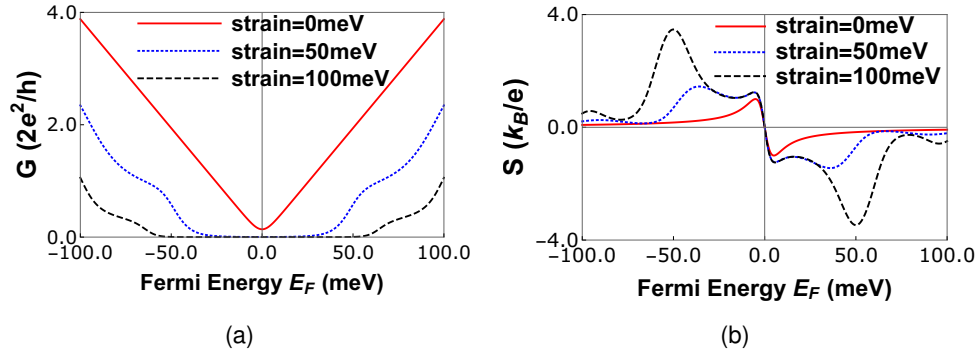
Figure 6.11: (a) Charge conductance (in units of "$2e^2/h$") at 30 K for various values of strain with $L = 40$ nm and width $W = 20$ nm, (b) charge Seebeck co-efficient S in units of (k_b/e) at 30 K for different values of strain with $L = 40$ nm and width $W = 20$ nm.

6.4   Graphene quantum heat engine

In this section we consider the special case of $J = 0$ (Eq. (6.28)), i.e., absence of magnetic impurity. For $J = 0$ case there is no spin transport only charge transport. Therefore in this section we identify the Onsager coefficients, Power, efficiency of graphene quantum heat engine of graphene quantum heat engine by the charge only and thus we omit the subscript ch from these coefficients. It has to be remembered that all quantities plotted in various figures in this section are based on the graphene quantum heat engine working in the charge domain. Now, we discuss the model of graphene quantum heat engine. The model consists of an uniaxial strain applied in the x direction as shown in Fig. 6.1 in absence of magnetic impurity. The Hamiltonian of this model is similar to that shown in Eq. (6.28) (with absence of magnetic impurity). This system is described by the Hamiltonian, which is given for K and K' valleys as-

$$\mathcal{H}_K = \hbar v_f \sigma(k - t), \quad \mathcal{H}_{K'} = -\hbar v_f \sigma^*(k + t). \tag{6.43}$$

In Eq. (6.43), $t = \frac{A_y}{\hbar v_f}[\Theta(x) - \Theta(x-L)]$ is the applied strain, $\sigma = (\sigma_x, \sigma_y)$ are the Pauli matrices operating on the graphene sublattices A and B with σ^* being the complex conjugate, $k(=\{k_x, k_y\})$ is the 2D wave vector, Θ being the Heaviside step function and v_f the Fermi velocity.

6.4.1 Onsager coefficients

From Eq. (6.43) and wave functions Eqs. (6.29)-(6.34) and putting $J = 0$ in the boundary conditions Eqs. (6.35)-(6.37) we get a system of equations. This system of equations is solved to get the conductance, Seebeck coefficient, maximum power and efficiency for the graphene system in absence of magnetic impurity. In Figs. 6.11(a, b) the conductance and Seebeck coefficient are plotted. Increasing strain reduces the electrical conductance, see Fig. 6.11(a), but increases the Seebeck coefficient, as in Fig. 6.11(b), which is also seen in Ref. [55]. As strain is increased the total transmission probability of electrons decreases, thus reducing the electrical conductance. From Fig 6.11(a), we see that increasing strain opens a gap in the conduction, which is due to the shift of the Dirac cones by the strain in the Brillouin zone. A band gap opens for strain beyond 20 percent (540 meV) in pristine graphene [142], so we will restrict ourselves only to a maximum of 15 percent strain (400 meV). A sign change in Fig. 6.11(b) is observed in the Seebeck co-efficient near the charge neutrality point (CNP) ($E_F = 0$), which is due to switch between the current carriers from hole to electron. The first peak, close to the CNP, is due to the imbalance in electron and hole contribution to the thermo-electric co-efficient $L^{12} = \sum_v L^{12,v}$ (see Eqs. (6.7), (6.8)), which is present at zero strain, but dies at a distance from the CNP. The origin of the second peak in the Seebeck co-efficient (blue line in Fig. 6.11(b)) is solely strain. As a result of applied strain transmission probability becomes a function of energy and gives rise to a large Seebeck co-efficient, which leads to large power with a finite efficiency.

6.4.2 Power and efficiency of graphene quantum heat engine

At lower values of strain ($t = 50$ meV) our engine achieves maximum power, i.e., 0.2 $(k_b \Delta\theta)^2/h = 0.057$ pico-Watts at $30K$ for a $40nm$ strained region, considering $\Delta\theta = 1K$, see Figs. 6.12(a, b), which is more than two and three terminal quantum Hall heat engine at maximum power [36]. From Fig. 6.11(b) we see with applied strain transmission probability becomes a function of energy and give rise to a large Seebeck co-efficient, which leads to a large power with a finite efficiency. At lower values of strain ($t = 50$ meV) our engine achieves maximum power, i.e., 0.2 $(k_b \Delta\theta)^2/h = 0.057$ pico-Watts at $30K$ for a $40nm$ strained region, considering $\Delta\theta = 1K$, see Figs. 6.12(a) and 6.12(b), which is more than two and three terminal quantum Hall heat engine at maximum power [36]. The efficiency at maximum power $\eta(P_{max})$ is $0.1\eta_c$, which is also good enough as compared to the other QHE's, see Fig. 6.12(c). Efficiency at maximum power can also be increased to a large value(more than 0.4 η_c), as in Fig. 6.13(a), but then maximum power P_{max} reduces to less than 0.03 $(k_b \Delta\theta)^2/h$. This is because while power depends on both Seebeck co-efficient and electrical conductance, see Eq. (6.14) the two factors so conspire to reduce the maximum power. On the other hand, the overall efficiency at maximum power again though dependent on Seebeck co-efficient (S), conductance G and thermal conductance κ, effectively increases with increasing strain. Individually, S increases with increasing strain, while for G and κ it is the opposite. Although the maximum efficiency $\eta(P_{max})$ and maximum power P_{max} are good for this system, the dimension of the heat engine is large, equal to 20×40 nm^2. A effective QHE should deliver a high power with high efficiency and its dimensions should be as small as possible, so that in less area more number of nano heat engines can be fabricated, and thus good amount of power can be generated. From Fig. 6.13 (b) we see that with increasing strain ($150meV$), while decreasing length ($L = 21nm$) large power and efficiency can be generated. The performance of the heat engine can be increased more by tuning one more variable, the Fermi velocity v_f. Till

now, we have considered the Fermi velocity of Dirac electrons to be equal to 10^6m/s, but increasing strain can reduce the Fermi velocity to 6×10^5m/s [125], then performance of the heat engine can be increased more, such as- maximum power as well as efficiency at maximum power both can be increased to a value as high as 0.268 $(k_b\Delta\theta)^2/h$ and $0.1\eta_c$ respectively, see Fig. 6.13 (c). This can be understood better as, if $1cm^2$ area is fabricated by this quantum nano heat engines in parallel, then $0.06 Watts$ total power can be generated with efficiency 0.1 η_c, which is better than quantum Hall heat engines but comparable to quantum dot heat engines, see Table 6.2 below.

(b)   (c)
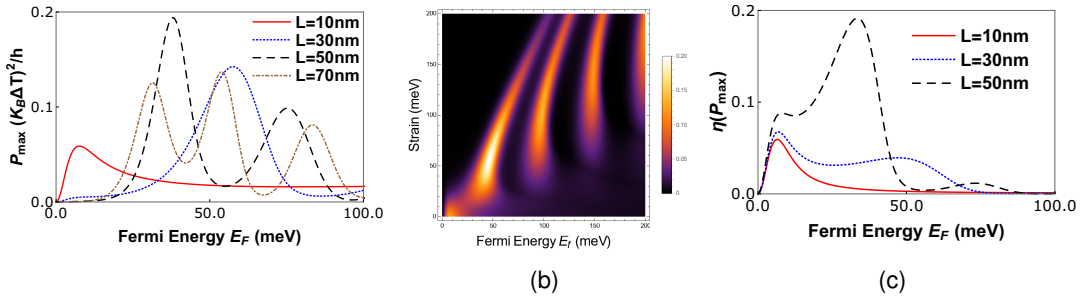
Figure 6.12: (a) Maximum Power (P_{max}) in units of $((k_B\Delta\theta)^2/h)$ at 30 K for different lengths(L) of strained region with strain $=$ 50 meV and width(W) of strained region $=$ 20 nm, (b) Maximum Power (P_{max}) in units of $((k_B\Delta\theta)^2/h)$ at $\theta = 30$ K, where strain is along the y direction and Fermi energy E_f is along the x direction with $L = 40$ nm and width $W = 20$ nm, (c) Efficiency at maximum power in units of (η_c) at 30 K with strain $=$ 50 meV and width $W = 20$ nm.

(b)   (c)
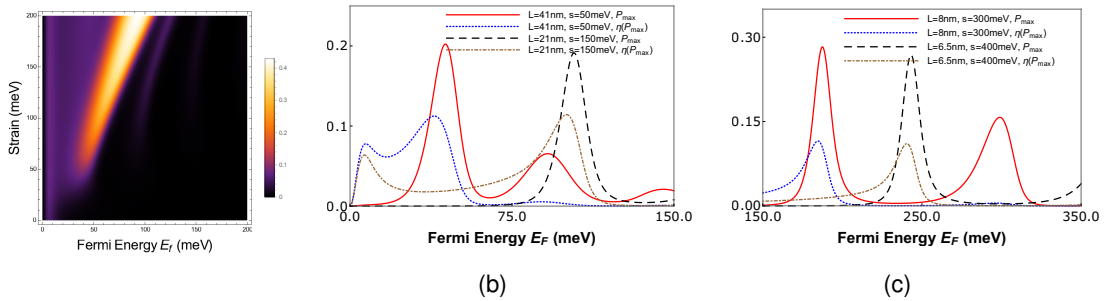
Figure 6.13: (a) Efficiency at maximum power ($\eta(P_{max})$) in units of (η_c) at $\theta = 30$ K with width $W = 20$ nm and $L = 40$ nm, (b) Maximum Power P_{max} in units of $((k_B\Delta\theta)^2/h)$ and $\eta(P_{max})$ in units of (η_c) at 30 K, for $v_f = 10^6$ m/s and (c) Maximum Power P_{max} in units of $((k_B\Delta\theta)^2/h)$ and $\eta(P_{max})$ in units of (η_c) at 30 K, $v_f = 6 \times 10^5$ m/s with width $W = 20$ nm.

6.5 Graphene quantum spin refrigerator

Herein, we explain the working of graphene spin heat system as a refrigerator. Again, one needs to have a large coefficient of performance as defined in Eq. (6.23) for the charge refrigerator and in Eq. (6.27) for the spin refrigerator to work. In Figs. 6.14(a) and (b) we plot the coefficient of performance at various strains for charge and spin refrigerators respectively. We see that for both charge and spin refrigerators the coefficient of performance increases with strain. In Fig. 6.14(a) we see that a high coefficient of performance for charge based refrigerator $\eta_{ch}^{r,max} = 0.47\eta_c^r$ is obtained at strain $t = 80$ meV, which is expected as it depends only on $ZT|_{ch}$. Similarly in Fig. 6.14 (b) we see that coefficient of performance $(\eta_{sp}^{r,max})$ for spin based refrigerator too is large $0.9\eta_c^r$. The reason however is different than that for charge based refrigerator. Here, $ZT|_{sp}$ does not increase with increase in strain, the increase in $\eta_{sp}^{r,max}$ is because of the decrease of P', see (Eq. (6.27)) with strain. However, one has to note that strain moderates the peaks of $ZT|_{sp}$, while at lower strains peaks appear in $ZT|_{sp}$, as strain increases the peaks disappear.
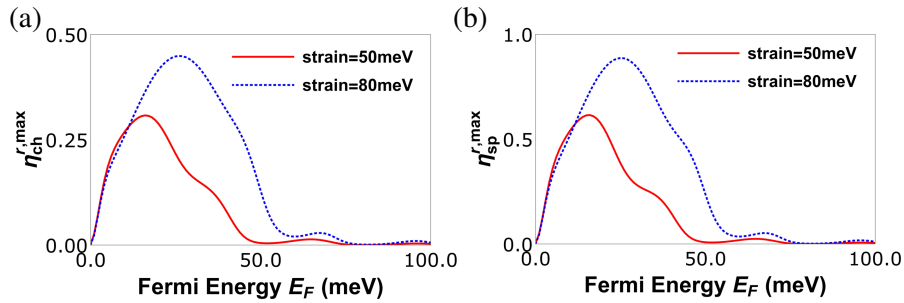
Figure 6.14: (a) Coefficient of performance $(\eta_{ch}^{r,max})$ in units of η_c^r for charge based refrigerator vs. Fermi energy (E_F) for various strains with parameters $J = 800$ meV-nm, $L = 70$ nm, $\theta = 30$ K, $S = 5/2$, $m = -5/2$, (b) Coefficient of performance $(\eta_{sp}^{r,max})$ in units of η_c^r for spin based refrigerator vs. Fermi energy (E_F) for various strains with parameters $J = 600$ meV-nm, $L = 60$ nm, $\theta = 30$ K, $S = 5/2$, $m = -5/2$.

6.5.1 Graphene quantum refrigerator

Finally, we discuss the use of our model as a quantum refrigerator for the special case of $J = 0$, i.e., absence of magnetic impurity and discuss the coefficient of performance and cooling power. Since we are in charge domain exclusively we do not identify the thermoelectric coefficients with subscript 'ch'. However these are all calculated and plotted for graphene refrigerator working in charge domain only. As in our model external magnetic field is absent, so Time-Reversal (TR) symmetry is not broken. The co-efficient of performance of the refrigerator is defined by the ratio of heat current extracted from the hot reservoir to the electrical power $\mathcal{P}$, such as -

$$\eta^r = \frac{j^q}{\mathcal{P}},\tag{6.44}$$

which is maximum, considering $j^q < 0$ and $\mathcal{P} < 0$, for -

$$\mathcal{E} = \frac{L^{22}}{L^{21}}(-1 - \sqrt{\frac{L^{11}L^{22} - L^{12}L^{21}}{L^{11}L^{22}}})\Delta\theta,\tag{6.45}$$

$$\text{and,} \quad \eta^r_{max} = \eta^r_c\frac{\sqrt{ZT+1}-1}{\sqrt{ZT+1}+1}, \quad J^Q = L^{22}\sqrt{\frac{L^{11}L^{22} - L^{12}L^{21}}{L^{11}L^{22}}}\Delta\theta,\tag{6.46}$$

where $\eta^r_c = \frac{\theta}{\Delta\theta}$ is the efficiency of an ideal refrigerator. For systems with broken TR symmetry, the upper bound of the refrigerator efficiency η^r_{max} decreases from η^r_c as the asymmetric parameter $x = \theta L^{12}/L^{21}$ deviates from one (1) [17]. For systems with conserved TR symmetry, the asymmetric parameter x becomes unity, and the upper bound of the corresponding maximum efficiency η^r_{max} equals η^r_c. This is the advantage of systems with conserved TR symmetry, that it can work as both quantum heat engine as well as quantum refrigerator with higher bound on the efficiency. For systems with broken TR symmetry, this upper bound reduce from η^r_c, when used as quantum refrigerators.

6.6   Experimental realization

Our proposal of a quantum heat engine based on a strained monolayer graphene layer doped with a magnetic impurity (or in absence of a magnetic impurity) is experimentally realizable. There are many theoretical (see Ref. [138] which initiated the field of straintronics in graphene and Ref. [147] for a recent review) works which are based on strained graphene. There are experimental works (see Refs. [139, 140]) which deal with uniaxial strain in monolayer graphene system. Thus, there should not be much difficulty in realizing strain in a graphene system. A graphene quantum heat engine without magnetic impurity could be realizable with ease. In addition, there are theoretical works which deal with effects of magnetic impurities on electronic transport in graphene, see Refs. [90, 128, 127]. In Ref. [127], it is shown that a delta potential approximation of a rectangular barrier magnetic impurity in graphene can be a very effective model of a magnetic quantum dot(a quantum dot with spin). For a range of incident angles from $-\pi/6$ to $\pi/6$, it is seen that the difference between the transmissions through delta potential magnetic impurity and that through a rectangular barrier magnetic impurity in graphene is quite small. The graphene based system in Ref. [127] is very similar to our set-up, and the problem too is solved similar to ours, only difference being that there is no strain in Ref. [127]. In Refs. [144, 145], an extended line defect has been studied in a graphene nanostructure experimentally. These line defects can be replaced by a magnetic quantum dot doped with Mn^+ ions to realize a magnetic impurity, see Refs. [127, 128]. Ref. [128] is an experimental work which shows how doping Mn^+ ions into semiconductor quantum dots realizes magnetic quantum dots. Further, magnetic quantum dots have been experimentally realized in graphene recently, see Ref. [148]. Since in the aforesaid papers, people have worked on similar systems, thus the applied aspect of our model is evidently realizable. The amount of strain applied in our system is very small. The maximum strain used in our system is $110 meV$, which is equivalent to 4% strain in graphene. In pristine graphene, maximum 20% strain can be

reached without opening a band gap. All the numerical values of different parameters are physically realizable and are used in other works also, see Refs. [138, 55, 90].

6.7   Edge vs ballistic modes in quantum thermoelectrics

In this section a comparison is made between the performance of quantum heat engines discussed in this chapter, based on ballistic modes in strained graphene systems (either in presence or absence of magnetic impurity) with that of quantum heat engines based on edge modes like quantum spin Hall heat engine (discussed in chapter 5) or quantum Hall heat engine (see Ref. [36]). The reason for comparing ballistic modes in graphene to edge modes in QH or QSH heat engines is that graphene is available in its pure form very easily and even in presence of impurity scattering it has perfectly conducting ballistic channels[50] similar to edge modes observed in QH or QSH systems. First, strained graphene quantum spin heat engine ($J \neq 0$ case, i.e., in presence of magnetic impurity) is compared with the quantum spin Hall heat engine (discussed in chapter 5 of this thesis), in Table 6.2. Next, graphene spin refrigerator ($J \neq 0$ case) is compared with quantum dot refrigerators in Table 6.3 and then finally strained graphene heat engine ($J = 0$ case, i.e., in absence of magnetic impurity) is compared with quantum Hall heat engine [36] in Table 6.4. From Table 6.2, it is seen that the maximum power and efficiency at that power for charge currents in graphene spin heat engine is $0.16(k_B\Delta\theta)^2/h$ and $0.16\eta_c$ respectively, which are much less than that of the quantum spin Hall heat engine (maximum power $0.8(k_B\Delta\theta)^2/h$ and efficiency at maximum power $0.28\eta_c$). Further, maximum power and efficiency for spin currents for graphene spin heat engine are $0.1(k_B\Delta\theta)^2/h$ and $0.1\eta_c$ which are also less than that of the quantum spin Hall heat engine. One can conclude from Table 6.2 that the performance of graphene quantum spin heat engine based on ballistic modes is not better than that of the quantum spin Hall heat engine based on edge modes. For our model as

graphene spin refrigerator too the cooling power and efficiency for charge currents are $0.7(k_B\Delta\theta)^2/h$ and $0.1\eta_c^r$ respectively, which is much less than that of the quantum spin Hall refrigerators, see Table 6.3. From Table 6.4, it can be seen that the maximum power generated in the 2-terminal strained graphene quantum heat engine is 0.268 $(k_B\Delta\theta)^2/h$ which is much greater than that of the chaotic cavity heat engine and almost double than the 2-terminal quantum Hall heat engine based on Mach-Zehnder interferometer[36]. Even for 3-terminal quantum Hall heat engine the maximum power generated is much less than that of our model. Although, in our model efficiency at maximum power is $0.1\eta_c$, larger than that of chaotic cavity heat engine and 3-terminal quantum Hall heat engine, it is same for a 2-terminal quantum Hall heat engine. It can also be seen from Table 6.4 that if a 1cm^2 area is fabricated with these nano heat engines, then also the output power generated in that area is 0.06 Watts for graphene quantum heat engine which is huge compared to 2-terminal, 3-terminal quantum Hall and chaotic cavity heat engines. Thus it is clear from Table 6.4 that 2-terminal strained graphene quantum heat engine based on ballistic modes is more efficient than quantum Hall heat engines based on chiral edge modes. However, helical quantum heat engines discussed in Table 6.2 and helical quantum refrigerator discussed in Table 6.3 are better than their strained graphene counterparts.

Table 6.2: Comparison of quantum spin heat engine based on QSH (Chapter 5) and ballistic mode in graphene (Chapter 6)

Heat Engines	Ballistic mode in graphene	QSH edge modes
Charge power	0.16 (Fig. 6.9(b))	0.8 (Fig. 5.4(a))
Efficiency	0.16 (Fig. 6.9(b))	0.28 (Fig. 5.4(b))
Spin power	0.1 (Fig. 6.10(b))	10 (Fig. 5.4(c))
Spin efficiency	0.1 (Fig. 6.10(b))	0.4 (Fig. 5.4(d))

Table 6.3: Comparison of quantum refrigerator based on QSH (chapter 5) and ballistic mode in graphene (chapter 6)

Refrigerator	Ballistic mode in graphene	QSH edge modes
Cooling power	0.7	3.5 (Fig. 5.5(a))
C.O.P.	0.1	0.2 (Fig. 5.5(b))

Note: Charge power, spin power and cooling power are in the same unit $(k_B\Delta\theta)^2/h$ while efficiency (for charge currents), spin efficiency (for spin current) are in unit of η_c and coefficient of performance in unit of η_c^r.

Table 6.4: How does the strained graphene QHE ($J = 0$) compare with related proposals?

Heat Engines	Maximum Power P_{max} in units of $(k_B\Delta\theta)^2/h$	Efficiency at maximum Power $\eta(P_{max})$	Power generated in 1 cm^2 area fabricated by nano engines
Quantum Hall Heat Engine(two terminal)[36]	0.14	0.10 η_c (Fig. 3) of Ref. [36]	0.04 Watts
Quantum Hall Heat Engine(three terminal) [36]	0.14 (Fig. 2(b)) of Ref. [36]	0.042 η_c	0.04 Watts
Chaotic Cavity[150]	0.0066	0.01 η_c	0.00189 Watts
Strained Graphene QHE($J = 0$)	0.268 (Fig. 6.13(b))	0.1 (Fig. 6.13(b)) η_c	0.06 Watts

6.8 Conclusion

The aim of this chapter was to design an efficient graphene spin heat engine using uniaxial strain in a monolayer graphene system embedded with a magnetic impurity between strained and unstrained region at $x = 0$. Beside this it is also required to check the ability of the same graphene model to work as a graphene spin refrigerator. Finally the main reason behind this chapter was to compare the performance of a quantum heat engine and a quantum refrigerator based on ballistic modes in graphene to that of a quantum heat engine and a quantum refrigerator based on edge modes in QH and QSH samples. To fulfil

these aims, an uni-axial strain is introduced between the region $x = 0$ and $x = L$ ($L =$ the length of the strained region) and a magnetic impurity at $x = 0$, see Fig. 6.1. The results are derived following Onsager matrix relations similarly as also shown in Refs. [52, 16]. In this chapter it is shown that a strained graphene layer embedded with a magnetic impurity can act both as charge as well spin heat engine with better performance characteristics like high efficiency than many other systems operating as charge as well as spin heat engines. In this system though strain and magnetic impurity are present, since it is a two terminal system none of them breaks TR symmetry, so it can act as both heat engine as well as refrigerator. In Table 6.1 $\eta(P_{ch}^{max}), \eta(P_{sp}^{max}), P_{ch}^{max}, P_{sp}^{max}, ZT|_{ch}$ and $ZT|_{sp}$ and the maximum charge power generated in $1cm^2$ area in this graphene spin heat engine and compared with some other related works, which can work both as a charge and spin QHE. It can be seen that our model system (graphene spin heat engine) has excellent characteristics compared to other models like the maximum charge and spin thermoelectric figure of merit $ZT|_{ch/sp}$ achieved in our model is more than most of the other models, see Refs. [52, 16, 119]. Although the model spin heat engine of Ref. [16], has a larger $ZT|_{ch}$ it has smaller $ZT|_{sp}$. As efficiency $\eta_{ch/sp}^{max}$ is proportional to the $ZT|_{ch/sp}$, a large $ZT|_{ch/sp}$ leads to a large efficiency $\eta_{ch/sp}^{max}$ (not shown in Table 6.1). From Ref. [52] P_{ch}^{max} is calculated to be $0.09(K_B\Delta\theta)^2$ and $\eta(P_{ch}^{max})$ to be $0.06\eta_c$ for charge based heat engine and thus they are smaller than what is obtained for this graphene spin heat engine. In Ref. [119], a large value for the maximum charge power P_{ch}^{max} is obtained more than that seen in our graphene spin heat engine, although, $\eta(P_{ch}^{max})$ is comparable to it. The maximum charge power P_{ch}^{max} observed in the graphene spin heat engine is greater than that in Ref. [52] but less than that of Ref. [119]. Although the maximum charge power generated in Ref. [119] is larger than that generated in our graphene spin heat engine, however, the system dimensions of the quantum heat engine(QHE) of Ref. [119] are much larger than the graphene spin heat engine too. In this chapter, the area of the graphene spin heat engine is $1200nm^2$

with dimensions used in plot for maximum charge power (Fig. 6.9(a))- length $L \sim 60nm$ while width $W \sim 20nm$, however in Ref. [119] the area of their QHE system is $8316nm^2$ with dimensions of length $L \sim 1350nm$ and width $W \sim 6.16nm$ making the area of the QHE of Ref. [119] around 7 times larger then the graphene spin heat engine. Thus, if a $1cm^2$ area is fabricated with these small quantum heat engines then for those systems whose dimensions are small, more can be fitted in this area and more the charge power generated. It is shown that under these circumstances the total charge power generated in the graphene spin heat engine system is twice that of Ref. [119], see Table 6.1. The maximum spin power obtained in our graphene spin heat engine is not discussed for any other quantum heat engine before. Further, the efficiency at maximum power for spin too is only calculated in this chapter on graphene spin heat engine. In addition, the power and efficiency are calculated for our graphene based quantum spin heat engine(QSHE). The spin power generated in our graphene spin heat engine can be converted to charge power by using a suitable method, like inverse spin Hall effect or spin valve method[16]. The graphene spin heat engine discussed in this chapter not only displays excellent characteristics as a charge/spin quantum heat engine, it also doubles up as a charge/spin refrigerator with high coefficient of performance. Finally, the device can generate a pure spin current too. On the other hand, the performance of graphene quantum heat engine (with $J = 0$, i.e., absence of magnetic impurity) is also better than 2-terminal/3-terminal quantum Hall heat engines [36] (see Table 6.4), implying ballistic modes are better suited than chiral edge modes in quantum heat engine/quantum refrigerator applications. However, in comparison to helical edge modes, spin polarized ballistic modes in graphene aren't that effective in quantum thermoelectrics as seen in Tables 6.2 and 6.3 of this chapter.

7. Conclusion

"A conclusion is the place where you get tired of thinking."

– Arthur Bloch

This thesis compared the chiral quantum Hall (QH), helical quantum spin Hall (QSH) and quantum anomalous Hall (QAH) edge modes as regards their proclivity to disorder and inelastic scattering via conductance measurements, non-local HBT shot noise measurements and investigated the applicability of these edge modes in thermoelectrics. In the first chapter of this thesis the origin of chiral QH, helical QSH and chiral QAH edge modes is dealt with and then the characteristics of these edge modes are discussed. In the same chapter the basic theory required to understand a two-terminal quantum heat engine and quantum refrigerator is also discussed. The introduction also focuses on the reasons behind studying these edge modes and their application in quantum heat engines and quantum refrigerators. In the second chapter of this thesis the effect of disorder and inelastic scattering on Hall resistance (R_H), longitudinal resistance (R_L), 2-terminal resistance (R_{2T}) and non-local resistance (R_{NL}) have been studied and it is shown that while in quantum Hall regime non-local transport is not affected by disorder and inelastic scattering, in quantum spin Hall regime non-local and local transport both are strongly affected by disorder and inelastic scattering. This result raises a question about the usefulness of non-local quantum spin Hall transport in low-power information processing as reported in several works. Chapter 2 also brings out the fact that the widely used quantized non-local conductance as a tool

238

to detect helical edge mode transport has serious deficiencies especially in presence of disorder and inelastic scattering. In short, the non-local conductance in helical (QSH) edge mode transport does not retain its quantization and so would be unable to detect helicity in presence of contact disorder and inelastic scattering. In presence of either disorder or both disorder and inelastic scattering the quantization is lost in quantum spin Hall samples and it will be difficult to distinguish between topological QSH edge modes and quasi-helical QSH edge modes in their presence. Non-local HBT shot noise could be a saviour in distinguishing the topological or otherwise, i.e., trivial, origin of helical edge modes and this is discussed in chapter three of this thesis. In chapter three of the thesis it is shown that non-local charge Hanbury-Brown and Twiss (HBT) correlations turn completely negative while the non-local spin correlations turn completely positive for quasi-helical edge modes. Further, non-local HBT charge cross correlations can be positive for topological helical QSH edge modes but will always be negative for chiral quantum Hall edge mode transport. Thus, non-local HBT cross correlations can distinguish between topological chiral QH and topological helical QSH edge modes. In chapter four of this thesis the experimental observation of finite longitudinal resistance in some recent experiments in QAH samples has been discussed. The origin of this finite longitudinal resistance has been explained by introducing quasi-helical QSH edge modes along with topological QAH edge mode in Ref. [45]. In chapter four of this thesis it is shown that the trivial(chiral) QAH edge mode with quasi-helical QSH edge modes is more closer to the experimental situation, as interpreted in Ref. [45] than the topological(chiral) QAH edge mode with quasi-helical QSH edge modes is. This implies a re-evaluation of the consensus regarding those quantum anomalous Hall experiments[48, 49, 44]. Perhaps, something else is happening and maybe these are not true chiral(topological) quantum anomalous Hall edge modes which were seen. This concludes the first part of this thesis which deals with the robustness, identification of topological origin and the characteristics of QH, QSH and QAH edge modes.

In second part of this thesis the application of these edge modes in thermoelectrics is discussed utilizing the characteristics of these edge modes established in the first part of this thesis. In chapter five of this thesis it is shown that a topological insulator (quantum spin Hall insulator) can work both as a charge/spin heat engine as well as a charge/spin refrigerator which uses charge/spin currents to extract heat from a cooler region of the system to dump it into a hotter region of the system. It is also shown that the maximum output power and efficiency at that maximum charge power generated in helical QSH heat engine are much larger than the chiral QH heat engine as reported in Refs. [36, 18]. Further, when adapted as a quantum refrigerator too its performance is better than other quantum refrigerators. It is shown that the maximum charge coefficient of performances (COP) of this model is comparable to other models but the cooling power of our model is huge compared to other proposals. The performance of a quantum heat engine based on helical QSH edge modes is compared with a quantum heat engine based on ballistic modes in strained graphene systems in chapter six of this thesis. It is shown in chapter six of this thesis that while the maximum power and efficiency generated in a strained graphene system can be larger than a two terminal chiral quantum Hall system, it is still smaller than that of a helical QSH heat engine. In strained graphene spin heat engine a huge thermoelectric figure of merit is also observed which is larger than most other quantum heat engines. The spin power generated in the helical QSH and graphene spin heat engines can be converted to charge power by using a suitable method, like inverse spin Hall effect or spin valve method[16]. The helical QSH and graphene spin heat engines shown in chapters five and six of this thesis not only display excellent characteristics as a charge/spin quantum heat engine, they also double up as a charge/spin refrigerator with high coefficient of performance. Finally, in the graphene spin heat engine pure spin current generation is also possible. This thesis concludes with the realization that the use of QSH edge modes in low power information processing could be doubtful owing to its fragility to disorder and inelastic scattering, but its application as a

quantum heat engine and/or quantum refrigerator could be more fructuous.

8. Appendix

8.1 Mathematica program to calculate spin polarized conductance and Seebeck coefficients for chapter 5 on helical thermoelectrics and refrigeration

The following Mathematica code is used to calculate the charge/spin thermoelectric properties of a three terminal quantum spin Hall heat engine in the linear transport regime with a potential bias ΔV applied at contact 1, while a temperature difference $\Delta\theta$ applied at contact 3. Thus contacts 1 and 3 are at lower temperature θ and contact 2 is grounded, i.e., $V_2 = 0$. In our model contact 3 served as a voltage probe, which implies that the electric current through contact 3 is zero, i.e., $I_3^e = 0$. For simplicity, we have considered only one spin up edge mode shown by blue dashed line and one spin down edge mode by maroon solid line, see Fig. 8.1. The electric ($I_i^{e,s}$) and heat ($I_i^{h,s}$) currents in our system are related to the
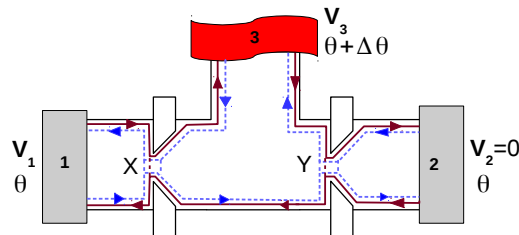
Figure 8.1: 3T QSH thermoelectric system. Blue dashed line represents spin up and maroon solid line represents spin down edge mode. Voltage bias ΔV is applied between terminals 1 and 2. Thermal gradient is applied at terminal 3 which acts as a voltage probe too.

applied potential bias ΔV and temperature difference $\Delta\theta$ via Onsager matrix as shown in Eq. (5.1) in chapter 5 of this thesis, which is-

$$\begin{pmatrix} I_i^{e,s} \\ I_i^{h,s} \end{pmatrix} = \frac{1}{h}\sum_j \int_{-\infty}^{\infty} dE[\delta_{ij} - T_{ij}^s(E)](-\frac{df}{dE}) \begin{pmatrix} e^2 & eE/\theta \\ eE & E^2/\theta \end{pmatrix} \begin{pmatrix} \Delta V_j \\ \Delta\theta_j \end{pmatrix} \tag{8.1}$$

$$= \begin{pmatrix} L_{eV}^s & L_{e\theta}^s \\ L_{hV}^s & L_{h\theta}^s \end{pmatrix} \begin{pmatrix} \Delta V_j \\ \Delta\theta_j \end{pmatrix} \tag{8.2}$$

Substituting $I_3^e = 0$ since it is a voltage probe, we have already solved Eq. (8.2) and derived the Onsager coefficients L_{eV}^s, $L_{e\theta}^s$, L_{hV}^s, $L_{h\theta}^s$ in Eqs. (5.20), (5.25). The Mathematica program described below calculates the spin polarized conductances and Seebeck coefficients. The time required to run this Mathematica program is less than 5 minutes. Herein, Fig. 5.3 of chapter 5 of this thesis is generated via the Mathematica program below.

$h = 6.634 * 10^\wedge(-34);$ h=Planck constant

$hb = 1.05 * 10^\wedge(-34);$ hb=h/2π

$e = 1.6 * 10^\wedge(-19);$ e=electric charge

$ae = 1.6 * 10^\wedge(-22);$ 1meV=ae

$kb = 1.38 * 10^\wedge(-23);$ kb=Boltzmann constant

SetSharedVariable[list]   list is shared by all the kernels, needed for parallel programming

list $= \{\};$ A list is created where the generated data will be stored

$\pmb{\mu o} = 0; \Gamma = 2.1a;$ μo=Fermi energy, Γ=bandwidth of resonant tunnelling transmission

$\textbf{T} = 0.1; \textbf{kbT1} = \textbf{T} * \textbf{kb}; \pmb{M} = \pmb{h}/(4(\textbf{kb}^\wedge 2));$ T=temperature

$\pmb{G} =.; \omega 1 = 0.1\textbf{kb*T}/(\textbf{hb}); \omega 2 = 0.1\textbf{kb*T}/(\textbf{hb}); \pmb{a} = \textbf{kb*T};$ ω1=ω2=width of the step function

M is a constant;

ParallelDo$[\{$ Do loop for parallel programming

$\textbf{For}[\varepsilon 1 = -5a, \varepsilon 1 \leq 5a, \varepsilon 1 = \varepsilon 1 + .5a,$

$\{$

no = −0.1 ∗ ae; n1 = 0.1 ∗ ae;

no and n1 are initial and final limit of the integration to calculate the elements of onsager matrix;

T1 = 1./(1 + Exp[−2Pi(G − ε1)/(hb ∗ ω1)]);   T1=QPC like tunnelling;

T2 = Γ^2/(Γ^2 + 4(G − ε2)^2);   T2=resonant tunnelling, Γ=width of the resonant tunnelling;

df = Exp[(G − μo)/(kbT1)]/((Exp[(G − μo)/(kbT1)] + 1)^2 a);

 df=derivative of the Fermi-Dirac distribution;

G1 = e^2/(h)NIntegrate[T1 ∗ df, {G, no, n1}, Method → "LocalAdaptive"];

G1=conductance for junction 1;

G2 = e^2/(h) NIntegrate[T2 ∗ df, {G, n2, n3}, Method → "LocalAdaptive"];

G2=conductance for junction 2;

J1 = e^2/(h) NIntegrate[T1 ∗ T2 ∗ df, {G, no, n1}, Method → "LocalAdaptive"];

J2 = e/(Th) NIntegrate[T1 ∗ T2 ∗ G ∗ df, {G, no, n1}, Method → "LocalAdaptive"];

J3 = 1/(Th) NIntegrate[T1 ∗ T2 ∗ G^2 ∗ df, {G, no, n1}, Method → "LocalAdaptive"];

N1 = 1./(h ∗ T)NIntegrate[T1 ∗ G^2 ∗ df, {G, no, n1}, Method → "LocalAdaptive"];

N1=heat conductance through junction 1;

N2 = 1./(h ∗ T)NIntegrate[T2 ∗ G^2 ∗ df, {G, no, n1}, Method → "LocalAdaptive"];

N2=heat conductance through junction 2;

S1 = e/(h ∗ T ∗ G1) NIntegrate[G ∗ T1 ∗ df, {G, no, n1}, Method → "LocalAdaptive"];

S1= Seebeck coefficient for junction 1;

S2 = e/(h ∗ T ∗ G2) NIntegrate[G ∗ T2 ∗ df, {G, n2, n3}, Method → "LocalAdaptive"];

S2=Seebeck coefficient for junction 2;

Gu = (G1)(2G2 − J1)/(2(G1 + G2 − J1));

Gu=Spin up conductance for 3T QSH system;

Gd = (2G1G2 + G1J1 − J1^2)/(2(G1 + G2 − J1));

Gd=Spin down conductance for 3T QSH system;

GG = G1 ∗ G2/(G1 + G2 − J1);

$\chi 1u = GG/G2(S1 * J1 - J2);$

$\chi 2u = GG/G1(S2 * J1 - J2);$

$\chi 1d = GG/G2(S1 * J1 - J2);$

$\chi 2d = GG/G1(S2 * J1 - J2);$

LeVu = Gu;   LeVu=spin up component of (1,1) element Onsager matrix;

LeVd = Gd;   LeVd=spin down component of (1,1) element Onsager matrix;

LeTu = (GG(S2 − S1) + $\chi 1u$);   LeTu=spin up component of (1,2) element Onsager matrix;

LeTd = (GG(S2 − S1) − $\chi 2d$);   LeTd=spin down component of (1,2) element Onsager matrix;

LhVu = TLeTd;   LhVu=spin up component of (2,1) element Onsager matrix;

LhVd = TLeTu;   LhVu=spin down component of (2,1) element Onsager matrix;

LhTu = (N1 + N2 − J3) − T(G1 * S1 + G2 * S2 − J2)^2/(G1 + G2 − J1);

LhTd = LhTu;   spin up/down component of (2, 2) element Onsager matrix;

κch = (LhTu + LhTd);   charge heat conductance;

Su = LeTu/(LeVu);   Spin up Seebeck coefficient;

LhTa = κch;

Sd = LeTd/(LeVd);   Spin down Seebeck coeffcient;

Gch = Gu + Gd;   Charge conductance ;

Gsp = Abs[Gu − Gd];   Spin condctance;

LeTa = (LeTu + LeTd); LeVa = (LeVu + LeVd); LhVa = (LhVu + LhVd);

ηmaxP = TLeTa^2/(2(2LeVa * LhTa − LeTa * LhVa));

Efficiency at maximum power;

Pmax = LeTa^2/LeVa * M;

Maximum powerfor charge curents;

detLa = LeVa * LhTa − LeTa * LhVa;

y = **Abs[LhVa * LeTa/(detLa)];**

$\eta r = (\text{Sqrt}[y+1]-1)/(\text{Sqrt}[y+1]+1);$

Coefficient of performances for charge currents;

$\text{JQ} = \text{LhTa}(\text{Sqrt}[\text{detLa}/(\text{LeVa}*\text{LhTa})])*h/\text{kb}^\wedge 2;$

Cooling power for charge currents;

$\text{LeVb} = \text{Abs}[(\text{LeVu}-\text{LeVd})]; \text{LeTb} = \text{Abs}[(\text{LeTu}-\text{LeTd})];$

$\text{detLb} = \text{LeVb}*\text{LhTa}-\text{LeTb}*\text{LhVa};$

$\text{y1} = \text{Abs}[\text{LhVa}*\text{LeTb}/(\text{detLb})];$

$\eta\text{rsp} = (\text{Sqrt}[\text{y1}+1]-1)/(\text{Sqrt}[\text{y1}+1]+1);$

Coefficient of performances for spin currents;

$\text{JQsp} = \text{LhTa}(\text{Sqrt}[\text{detLb}/(\text{LeVb}*\text{LhTa})])*h/\text{kb}^\wedge 2;$

Cooling power for spin currents;

$\text{Pmaxsp} = 1./4*\text{LeTb}^\wedge 2/\text{LeVb}*M;$

Maximum power for spin curents;

$\eta\text{maxsp} = T\text{LeTb}^\wedge 2/(2(2\text{LeVb}*\text{LhTa}-\text{LeTb}*\text{LhVa}));$

Efficiency at maximum powerfor spin currents;

$\text{list} = \text{AppendTo}[\text{list}, \{\epsilon 2/a, \epsilon 1/a, \text{LeVu}*(h/(e^\wedge 2)), \text{LeVd}*(h/(e^\wedge 2)), \text{Su}*e/\text{kb}, \text{Sd}*e/\text{kb}\}]$

$\}];$

$\}, \{\epsilon 2, -5*a, 5a, .5a\}]; //\text{AbsoluteTiming}$

$\text{list} = \text{Sort}[\text{list}]; \text{Export}[\text{``check1.dat''}, \text{list}]$

Export generated data to a output file

$\{\text{``27.618''}, \text{Null}\}$

check1.dat

Import data from output stored file

$\text{data} = \text{Import}[\text{``check1.dat''}, \text{``Table''}][[\text{All}, \{2,1,3\}]];$

$\text{data1} = \text{Import}[\text{``check1.dat''}, \text{``Table''}][[\text{All}, \{2,1,4\}]];$

$\text{data2} = \text{Import}[\text{``check1.dat''}, \text{``Table''}][[\text{All}, \{2,1,5\}]];$

data3 = Import["check1.dat", "Table"][[All, {2, 1, 6}]];

Plot data in a grid view

A = ListDensityPlot[data, ImageSize → 145, ColorFunction → ColorData

["TemperatureMap"], PlotLegends → Automatic];

B = ListDensityPlot[data1, ImageSize → 180, ColorFunction → "TemperatureMap",

PlotLegends → Automatic, PlotRange → Automatic,

FrameLabel → {None, Style ["E_2/K_BT", 20]}];

c = ListDensityPlot[data2, ImageSize → 145, ColorFunction → "TemperatureMap",

PlotLegends → Automatic, PlotRange → Automatic,

FrameLabel → {Style ["E_1/K_BT", 20] , None}];

d = ListDensityPlot[data3, ImageSize → 175, ColorFunction → "TemperatureMap",

PlotLegends → Automatic, PlotRange → Automatic,

FrameLabel → {Style ["E_1/K_BT", 20] , Style ["E_2/K_BT", 20]}];

e = Grid[{{A, B}, {c, d}}]

Export["helical_con_Seebeck.jpeg", e, ImageResolution → 300]

helical_con_Seebeck.jpeg
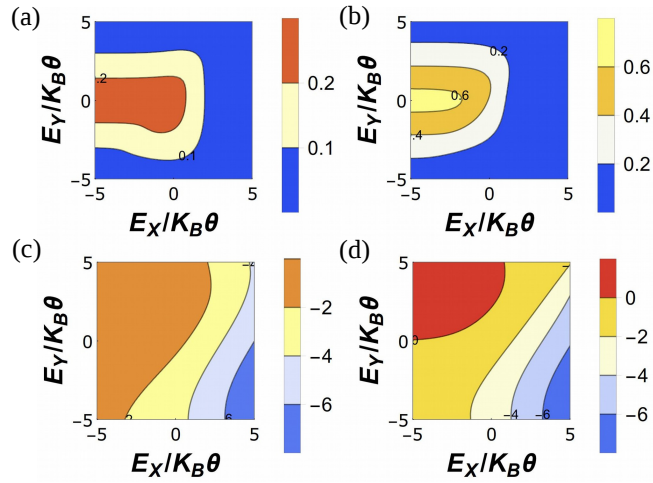
Figure 8.2: (a) Spin up and (b) spin down conductances (in unit of $\frac{e^2}{h}$) are shown for QPC at constriction X and resonant tunnelling at constriction Y. (c) Spin up and (d) spin down Seebeck coefficients (in unit of $\frac{k_B}{e}$) ($S^\uparrow$ and $S^\downarrow$) are shown for QPC at constriction X and resonant tunnelling at constriction Y. Parameters are $\hbar\omega_0 = 0.1 k_B\theta$, $\Gamma = 2 k_B\theta$ and $\theta = 0.1 K$. This figure corresponds to Fig. 5.3 in chapter 5 of this thesis.

8.2 Mathematica program to calculate charge conductance for graphene spin heat engine

The following program is used to calculate the charge/spin thermoelectric properties of a two terminal graphene quantum spin heat engine in the linear transport regime. A graphene sheet is lying in the x-y plane, a strain is applied to the region $0 < x < L$, see Fig. 8.3, with a magnetic impurity at $x = 0$. The in-plane uniaxial strain impacts the hopping between nearest neighbors and is generally delineated via a gauge vector which takes opposing signs in the two valleys (K and K') of graphene [138]. In the Landau gauge, the vector potential corresponding to the strain is $\vec{A} = (0, A_y)$. The system is then defined by the Hamiltonian-

$$\mathcal{H}_{\mathcal{K}/\mathcal{K}'} = H_{K/K'} + J\mathbf{s}.\mathbf{S}\delta(x),$$ (8.3)
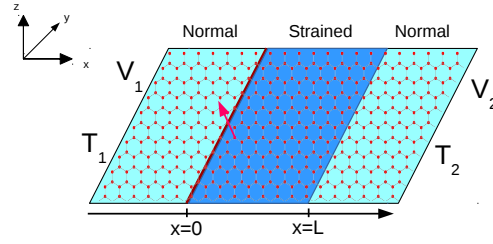
Figure 8.3: Monolayer graphene with a magnetic impurity at $x = 0$ denoted by thick maroon line. The middle portion is strained region while the two side portions are normal graphene regions. Voltages V_1 and V_2 are applied to the two sides which are at temperatures T_1 and T_2 respectively.

with $H_K = \hbar v_f \sigma.(k-t)$ and $H_{K'} = \hbar v_f \sigma^*.(k+t)$, . Strain is denoted as $t = A_y/\hbar v_f[\Theta(x) - \Theta(x-L)]$ with Θ the Heaviside step function and v_F the Fermi velocity. The first term in Eq. (8.3) represents the kinetic energy in graphene with $\sigma = (\sigma_x, \sigma_y)$ - the Pauli matrices that operate on the sublattices A or B and $\mathbf{k} = (k_x, k_y)$ the 2D wave vector. The second term in Eq. (8.3) denotes the exchange interaction between Dirac electron and magnetic impurity with J representing the strength of the exchange interaction. The spin of Dirac electron is denoted by $\mathbf{s}$, while $\mathbf{S}$ represents spin of the magnetic impurity and m its magnetic moment, while magnetic moment of Dirac electrons is $1/2$ (spin up) or $-1/2$ (spin down). The Mathematica program described below calculates the charge conductance for system shown in Fig. 8.3. Time required to run this Mathematica program ranges from 5 minutes to 1 hour depending on the strength of strain parameter. For higher value of strain it takes longer time because larger strain increases the refraction angle for electron to close to $90°$ which increases the integration time. Herein, Fig. 6.3(a) of chapter 6 of this thesis is generated with this Mathematica program.

$S = 5/2;$ Total spin of the magnetic impurity

$m = -5/2;$ Spin component of the magnetic impurity in the z direction

$F = \text{Sqrt}[(S-m)(S+m+1)];$

$F1 = \text{Sqrt}[(S+m)(S-m+1)];$

a1=.;a2=.;b1=.;b2=.;r1=.;r2=.;t1=.;t2=.;γ=.;ky=.;qy=.;

sol = Solve[{a1(Exp[$I\gamma$] + $I\alpha m$) + b1($-$Exp[$-I\gamma$] + $I\alpha m$)

$-$(Exp[$I\phi$] $-$ $I\alpha m$) + r1(Exp[$-I\phi$] + $I\alpha m$) + $I\alpha F$(a2 + b2 + r2) == 0,

a2(Exp[$I\gamma$] $-$ $I\alpha(m+1)$) $-$ b2(Exp[$-I\gamma$] + $I\alpha(m+1)$)+

r2(Exp[$-I\phi$] $-$ $I\alpha(m+1)$) + $I\alpha F$(a1 + b1 + 1 + r1) == 0,

a1(1 + $I\alpha m$Exp[$I\gamma$]) + b1(1 $-$ $I\alpha m$Exp[$-I\gamma$]) $-$ (1 $-$ $I\alpha m$Exp[$I\phi$])

$-$r1(1 + $I\alpha m$Exp[$-I\phi$]) + $I\alpha F$(a2Exp[$I\gamma$] $-$ b2Exp[$-I\gamma$] $-$ r2Exp[$-I\phi$]) == 0,

a2(1 $-$ $I\alpha(m+1)$Exp[$I\gamma$]) + b2(1 + $I\alpha(m+1)$Exp[$-I\gamma$])$-$

r2(1 $-$ $I\alpha(m+1)$Exp[$-I\phi$]) + $I\alpha F$(a1Exp[$I\gamma$] $-$ b1Exp[$-I\gamma$]

+Exp[$I\phi$] $-$ r1Exp[$-I\phi$]) == 0,

a1Exp[$IqxL$] + b1Exp[$-IqxL$] == t1Exp[$IkxL$],

a2Exp[$IqxL$] + b2Exp[$-IqxL$] == t2Exp[$IkxL$],

a1Exp[$IqxL + I\gamma$] $-$ b1Exp[$-IqxL - I\gamma$] == t1Exp[$IkxL + I\phi$],

a2Exp[$IqxL + I\gamma$] $-$ b2Exp[$-IqxL - I\gamma$] == t2Exp[$IkxL + I\phi$]

}, {a1, a2, b1, b2, r1, r2, t1, t2}];

Solving above equations we get the transmission amplitudes for an incident spin up electron

tuu = t1/.sol[[1]];

Transmission amplitude for an electron with initial spin up to final spin up

tdu = t2/.sol[[1]];

Transmission amplitude for an electron with initial spin up to final spin down

sol = Solve[{a1(Exp[$I\gamma$] + $I\alpha(m-1)$) + b1($-$Exp[$-I\gamma$] + $I\alpha(m-1)$)+

r1(Exp[$-I\phi$] + $I\alpha(m-1)$) + $I\alpha F$(a2 + b2 + 1 + r2) == 0, a2(Exp[$I\gamma$] $-$ $I\alpha(m)$)

$-$b2(Exp[$-I\gamma$] + $I\alpha(m)$) + r2(Exp[$-I\phi$] $-$ $I\alpha(m)$)+

$I\alpha F$(a1 + b1 + r1) == Exp[$I\phi$] + $I\alpha(m)$, a1(1 + $I\alpha(m-1)$Exp[$I\gamma$])+

b1(1 $-$ $I\alpha(m-1)$Exp[$-I\gamma$]) $-$ r1(1 + $I\alpha(m-1)$Exp[$-I\phi$])+

$I\alpha F$(a2Exp[$I\gamma$] $-$ b2Exp[$-I\gamma$] + Exp[$I\phi$] $-$ r2Exp[$-I\phi$]) == 0,

a2(1 $-$ $I\alpha(m)$Exp[$I\gamma$]) + b2(1 + $I\alpha(m)$Exp[$-I\gamma$]) $-$ r2(1 $-$ $I\alpha(m)$Exp[$-I\phi$])

$+I\alpha F(\text{a1}\,\text{Exp}[I\gamma] - \text{b1}\,\text{Exp}[-I\gamma] - \text{r1}\,\text{Exp}[-I\phi]) == 1 + I\alpha(m)\text{Exp}[I\phi],$

$\text{a1}\,\text{Exp}[I\text{qxL}] + \text{b1}\,\text{Exp}[-I\text{qxL}] == \text{t1}\,\text{Exp}[I\text{kxL}],$

$\text{a2}\,\text{Exp}[I\text{qxL}] + \text{b2}\,\text{Exp}[-I\text{qxL}] == \text{t2}\,\text{Exp}[I\text{kxL}],$

$\text{a1}\,\text{Exp}[I\text{qxL} + I\gamma] - \text{b1}\,\text{Exp}[-I\text{qxL} - I\gamma] == \text{t1}\,\text{Exp}[I\text{kxL} + I\phi],$

$\text{a2}\,\text{Exp}[I\text{qxL} + I\gamma] - \text{b2}\,\text{Exp}[-I\text{qxL} - I\gamma] == \text{t2}\,\text{Exp}[I\text{kxL} + I\phi]$

$\}, \{\text{a1}, \text{a2}, \text{b1}, \text{b2}, \text{r1}, \text{r2}, \text{t1}, \text{t2}\}];$

Solving above equations we get the transmission amplitudes for an incident spin down electron

$\text{tud} = \text{t1}/.\text{sol}[[1]];$

Transmission amplitude for an electron with initial spin down to final spin up

$\text{tdd} = \text{t2}/.\text{sol}[[1]];$

Transmission amplitude for an electron with initial spin down to final spin down

$h = 6.634 * 10^{\wedge}(-34);$ h=Planck constant

$\text{hb} = 1.05 * 10^{\wedge}(-34);$ hb=h/2π

$e = 1.6 * 10^{\wedge}(-19);$ e=electronic charge

$\text{ae} = 1.6 * 10^{\wedge}(-22);$ ae=1 meV

$\text{vf} = 1. * 10^{\wedge}6;$ vf=Fermi velocity

$\text{kb} = 1.38 * 10^{\wedge}(-23);$ kb=Boltzmann constant

$n = \text{hbvf};$

SetSharedVariable[list]

$\text{list} = \{\};$

$z = \text{ae} * 10^{\wedge}(-9)/n;$

$\mu\text{o}=.;$

$L = 40 * 10^{\wedge}(-9); T = 30.0; J = 50 * z; \text{kbT1} = T * \text{kb};$

L=length of strained region, T=temperature, J=coupling strength between

 magnetic impurity and electron

$f = 0.005\text{Pi}; t = 100 * \text{ae}; M = h/(4(\text{kb}^{\wedge}2));$

t=Strength of strain

$G=.;$

$\phi=.; W = 2*(20)*10^\wedge(-9)*e^\wedge 2/(h*\text{Pi});$

W=width of our system

ϕ=Angle of incident electron;

$F = \text{Sqrt}[5]; F1 = \text{Sqrt}[0]; m = -5/2; \alpha = J; d = e/\text{kb};$

$\textbf{ParallelDo}[\{$

$\gamma = \text{ArcSin}[\text{Sin}[\phi] - t/G];$

γ=Angle of refracted electron;

$\text{kx} = (G/n)\text{Cos}[\phi];$

kx=Wave vector in un-strained region;

$\text{qx} = (G/n)\text{Cos}[\gamma];$

qx=Wave vector in strained region;

$\text{T11} = \text{tuutuu}^*;$

Transmission probability of incident spin up electron as a up-spin electron;

$\text{T21} = \text{tudtud}^*;$

Transmission probability of incident spin down electron as a up-spin electron;

$\text{df} = \text{Exp}[(G-\mu\text{o})/(\text{kbT1})]/((\text{Exp}[(G-\mu\text{o})/(\text{kbT1})]+1)^\wedge 2\text{kbT1});$

Derivativeof the Fermi-Dirac distribution function;

$\rho = \text{Abs}[G]/((\text{hbvf}));$

Density of states;

$\text{T3} = \text{tdutdu}^*;$

Transmission probability of incident spin up electron as a down-spin electron;

$\text{T4} = \text{tddtdd}^*;$

Transmission probability of incident spin down electron as a down-spin electron;

$\text{no} = \mu\text{o} - 50*\text{ae}; \text{n1} = \mu\text{o} + 50*\text{ae};$

sum1 $=$ **WNIntegrate[df** $*\rho*$ **(T11** $+$ **T21)** $*$ **Cos[ϕ]**, $\{G,$**no**, **n1**$\}$

$,\{\phi,-$**Pi**$/2+f,$**Pi**$/2-f\}$**]**;

Spin up component of (1,1) element of Onsager matrix;

suum1 $=$ **WNIntegrate[df** $*\rho*$ **(T11** $+$ **T21)** $*(G-\mu$**o**$)*$ **Cos[ϕ]**, $\{G,$**no**, **n1**$\}$

$,\{\phi,-$**Pi**$/2+f,$**Pi**$/2-f\}$**]**;

Spin up component of (1,2) element of Onsager matrix;

suuum1 $=$ **WNIntegrate[df** $*\rho*$ **(T11** $+$ **T21)** $*(G-\mu$**o**$)^{\wedge}2*$ **Cos[ϕ]**, $\{G,$**no**, **n1**$\}$

$,\{\phi,-$**Pi**$/2+f,$**Pi**$/2-f\}$**]**;

Spin up component of (2,2) element of Onsager matrix;

sum2 $=$ **WNIntegrate[df** $*\rho*$ **(T3** $+$ **T4)** $*$ **Cos[ϕ]**, $\{G,$**no**, **n1**$\}$

$,\{\phi,-$**Pi**$/2+f,$**Pi**$/2-f\}$**]**;

Spin down component of (1,1) element of Onsager matrix;

suum2 $=$ **WNIntegrate[df** $*\rho*$ **(T3** $+$ **T4)** $*(G-\mu$**o**$)*$ **Cos[ϕ]**, $\{G,$**no**, **n1**$\}$

$,\{\phi,-$**Pi**$/2+f,$**Pi**$/2-f\}$**]**;

Spin down component of (1,2) element of Onsager matrix;

suuum2 $=$ **WNIntegrate[df** $*\rho*$ **(T3** $+$ **T4)** $*(G-\mu$**o**$)^{\wedge}2*$ **Cos[ϕ]**, $\{G,$**no**, **n1**$\}$

$,\{\phi,-$**Pi**$/2+f,$**Pi**$/2-f\}$**]**;

Spin down component of (2,2) element of Onsager matrix;

SS1 $=-$**Re[suum1]**$/(e*T)$;

SS2 $=-$**Re[suum2]**$/(e*T)$;

suuum1 $=-$**Re[suuum1]**$/(e*e*T)$;

suuum2 $=-$**Re[suuum2]**$/(e*e*T)$;

S1 $=$ **sum1**; **S2** $=$ **sum2**;

A1 $=$ **SS1**$/($**S1**$)$;

Spin up Seebeck coefficient;

A2 $=$ **SS2**$/($**S2**$)$;

Spin down Seebeck coefficient;

list = AppendTo[list, {μo/ae, σch $* h/e^{\wedge}2$, σsp $* h/e^{\wedge}2$, A1 $* d$, A2 $* d$}]

(*}];*)

}, {μo, 0 $*$ ae, 100 $*$ ae, 1 $*$ ae}]; //AbsoluteTiming

list = Sort[list];

Export["check2.dat", list]

Needs["PlotLegends"]

data = Import["check1.dat", "Table"][[All, {1, 2}]];

ListLinePlot[data, PlotLegend $\rightarrow$ {Style["m=-5/2", Bold, 24]}, LegendPosition $\rightarrow$ {.002, -0.3},

PlotRange $\rightarrow$ {{0, 100}, Automatic}, Frame $\rightarrow$ True,

FrameTicks $\rightarrow$ {{{0, "0.0"}, {02, "2.0"}, {04, "4.0"}}, None}, {{{0, "0.0"}, {100, "100.0"},

{50.0, "50.0"}}, None}}, PlotRange $\rightarrow$ {0, 80}, FrameLabel $\rightarrow$ {Style["Fermi Energy

E_F (meV)", 24, Bold, Black], Style ["G_{ch} $(e^2$/h)", 28, Bold, Black]}, FrameTicksStyle

$\rightarrow$ Directive["Label", Black, 20], PlotStyle $\rightarrow$ {Red, Thick}]
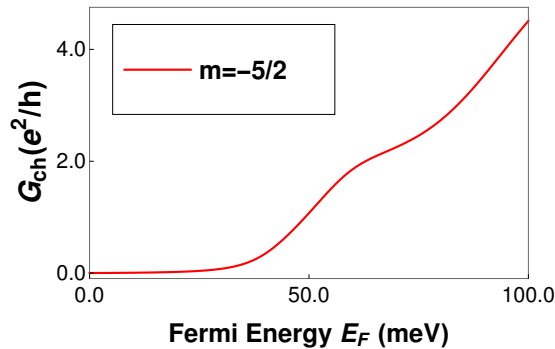
Figure 8.4: Charge Conductance (G_{ch}) vs. E_F (Fermi energy) for magnetic moment $m = -5/2$, length of strained graphene layer $L = 40nm$ and width $W = 20$ nm, strain $t = 50meV$, temperature $T = 30K$ with spin of magnetic impurity $S = 5/2$ and $J = -600meV$. This figure corresponds to Fig. 6.3(a) in chapter 6 of this thesis.

Bibliography

[1] Arjun Mani, Colin Benjamin, Are quantum spin Hall edge modes more resilient to disorder, sample geometry and inelastic scattering than quantum Hall edge modes? J. Phys.: Condens. Matter 28, 145303 (2016).

[2] Arjun Mani, Colin Benjamin, Fragility of Nonlocal Edge-Mode Transport in the Quantum Spin Hall State, Phys. Rev. Applied 6, 014003.

[3] Arjun Mani, Colin Benjamin, Probing helicity and the topological origins of helicity via non-local Hanbury-Brown and Twiss correlations, Scientific Reports 7: 6954 (2017).

[4] Arjun Mani, Colin Benjamin, Role of helical edge modes in the chiral quantum anomalous Hall state, Scientific Reports 8: 1335 (2018).

[5] A. J. Bestwick, et. al., Precise Quantization of the Anomalous Hall Effect near Zero Magnetic Field, Phys. Rev. Lett. 114, 187201 (2015).

[6] Arjun Mani, Colin Benjamin, Are thermal fluctuations the sole reason for finite longitudinal resistance in quantum anomalous Hall experiments?, arXiv:1803.04995.

[7] Arjun Mani, Colin Benjamin, Strained graphene based highly efficient quantum heat engine operating at maximum power, Phys. Rev. E 96, 032118 (2017).

[8] Arjun Mani, Colin Benjamin, Designing a quantum spin heat engine and refrigerator in strained graphene with giant theromoelectric figure of merit, arXiv: 1707.07159v1;

[9] Arjun Mani, Colin Benjamin, Helical thermoelectrics and refrigeration, Phys. Rev. E 97, 022114(2018).

[10] M. Buttiker, Absence of Backscattering in The Quantum Hall effect in Multiprobe Conductors, Phys. Rev. B 38, 9375 (1988), Surface Science 229, 201 (1990).

[11] A. Narayan, S. Sanvito, Multiprobe Quantum Spin Hall Bars, Eur. Phys. J. B 87, 43 (2014).

[12] Jens Nikolajsen, Bachelors project, Edge States and Contacts in the Quantum Hall Effect, Nanoscience center, Niels Bohr Institute, Faculty of Science, Univ. of Copenhagen, Denmark.

[13] M. Buttiker, Small normal-metal loop coupled to an electron reservoir, Phys. Rev. 32, R1846 (1985).

[14] C. Texier and M. Buttiker, Effect of incoherent scattering on shot noise correlations in the quantum Hall regime, Phys. Rev. B 62, 7454 (2000).

[15] Ya. M. Blanter, M. Buttiker, Shot noise in mesoscopic con- ductors, Phys. Reports 336, 1 (2000).

[16] A. B. Cahaya, O. A. Tretiakov and G.E. W. Bauer, Spin Seebeck Power Conversion, IEEE Trans. Magn. 51, 0800414 (2015).

[17] K. Brandner, et. al., Strong Bounds on Onsager Coefficients and Efficiency for Three-Terminal Thermoelectric Transport in a Magnetic Field, Physical Rev. Lett. 110, 070603 (2013).

[18] R. Sanchez, et. al., Chiral Thermoelectrics with Quantum Hall Edge States, Phys. Rev. Lett. 114, 146801 (2015).

[19] Edwin Hall, On a New Action of the Magnet on Electric Currents, American Journal of Mathematics. 2 (3), 287 (1879).

[20] M. I. Dyakonov and V. I. Perel, Possibility of orientating electron spins with current, Sov. Phys. JETP Lett. 13: 467 (1971).

[21] C. L. Kane, E. J. Mele, Quantum Spin Hall Effect in Graphene, Phys. Rev. Lett. 95:226801 (2005).

[22] B. A. Bernevig, S. C. Zhang, Quantum Spin Hall Effect, Phys. Rev. Lett. 96:106802 (2006).

[23] M. König, et al., Quantum Spin Hall Insulator State in HgTe Quantum Wells, Science 318:766–70 (2007).

[24] M. O. Goerbig, Quantum Hall effects, arXiv:0909.1998.

[25] J. Maciejko, T. L. Hughes and S-C Zhang, The quantum spin Hall effect, Annu. Rev. Condens. Matter Phys. 2, 31(2011).

[26] J. Asboth, L. Oroszlany and A. Palyi, A Short Course on Topological Insulators: Band-structure topology and edge states in one and two dimensions, Lecture Notes in Physics, 919 (2016).

[27] K. v. Klitzing, et. al., New Method for High-Accuracy Determination of the Fine-Structure Constant Based on Quantized Hall Resistance, Phys. Rev. Lett. 45, 494 (1980).

[28] R. Seshadri, et. al., Edge states, spin transport, and impurity-induced local density of states in spin-orbit coupled graphene, Phys. Rev. B 93, 035431 (2016).

[29] T. P. Cysne, et. al., Quantum Hall effect in graphene with interface-induced spin-orbit coupling, Phys. Rev. B 97, 085413 (2018).

[30] Z. Jiang, et. al., Quantum Hall effect in graphene, Solid State Communications 143, 14–19 (2007).

[31] Yuanbo Zhang, et. al., Experimental observation of the quantum Hall effect and Berry's phase in graphene, Nature, 438, 201–204 (2005).

[32] S. K. Maiti, et. al., Integer quantum Hall effect in a square lattice revisited, Phys. Lett. A 376, 1366–1370 (2012).

[33] S. Datta, Electron transport in mesoscopic systems, Cambridge university press (1995).

[34] A. Roth, et. al., Nonlocal Transport in the Quantum Spin Hall State, Science 325, 294 (2009); C Brune, et. al., Nature Physics, 8, 485 (2012).

[35] Ke He, The Quantum Hall Effect Gets More Practical, Physics 8, 41 (2015).

[36] P. P. Hofer, B. Sothmann, Quantum heat engines based on electronic Mach-Zehnder interferometers, Phys. Rev. B 91, 195406 (2015).

[37] H. Min., et. al., Intrinsic and Rashba spin-orbit interactions in graphene sheets, Phys. Rev. B 74, 165310 (2006).

[38] Y. Yao.,et. al., Spin-orbit gap of graphene: First-principles calculations, Phys. Rev. B 75, 041401(R) (2007).

[39] B. A. Bernevig ,T. L. Hughes, S. C. Zhang, Quantum spin Hall effect and topological phase transition in HgTe quantum wells, Science 314:1757 (2006).

[40] J. Maciejko, et. al., The Quantum Spin Hall Effect, Annu. Rev. Condens. Matter Phys. 2 (1), 31 (2011).

[41] Shun-Qing Shen, Topological Insulators- Dirac Equation in Condensed Matter, (Springer, 2013).

[42] Yu-Shen Liu, et. al., Spin-resolved Fano resonances induced large spin Seebeck effects in graphene-carbon-chain junctions, App. Phys. Lett., 104, 242412 (2014).

[43] F. Nichele, et. al., Edge transport in the trivial phase of inas/gasb. New J. Phys. 18, 083005 (2016).

[44] J. Wang, et. al., Anomalous Edge Transport in the Quantum Anomalous Hall State, Phys. Rev. Lett. 111, 086803 (2013).

[45] J. Wang, et. al., Quantum anomalous Hall effect in Magnetic topological insulators, Phys. Scr. T164, 014003 (2015).

[46] C. X. Liu, et. al., Quantum Anomalous Hall Effect in $Hg_{1-y}Mn_yTe$ Quantum Wells, Phys. Rev. Lett. 101, 146802 (2008).

[47] C. Z. Chang, et. al., High-precision realization of robust quantum anomalous Hall state in a hard ferromagnetic topological insulator, Nat. Mat. 14, 473 (2015).

[48] Kou, et. al., Scale-Invariant Quantum Anomalous Hall Effect in Magnetic Topological Insulators beyond the Two-dimensional Limit, Phys. Rev. Lett. 113, 137201(2014).

[49] Checkelsky, et. al., Trajectory of Anomalous Hall Effect toward the Quantized State in a Ferromagnetic Topological Insulator, Nature Physics 10, 731 (2014).

[50] K. Wakabayashi, et. al., Edge Effect on Electronic Transport Properties of Graphene Nanoribbons and Presence of Perfectly Conducting Channel, CARBON(Elsevier), 47, 124 (2009).

[51] G. Benenti, G. Casati, K. Saito, R. S. Whitney, Fundamental aspects of steady state conversion of heat to work at the nanoscale, Phys. Rep, 694, 1 (2017).

[52] B. Z. Rameshti, A. G. Moghaddam, Spin-dependent Seebeck effect and spin caloritronics in magnetic graphene, Phys. Rev. B 91, 155407 (2015).

[53] G. Benenti, K. Saito, G. Casati, Thermodynamics Bounds on Efficiency for systems with Broken Time-Reversal Symmetry, Phys. Rev. Lett. 106, 230602 (2011).

[54] F. Mazzamuto, et. al., Enhanced thermoelectric properties in graphene nanoribbons by resonant tunneling of electrons, Phys. Rev. B 83, 235426 (2011).

[55] M. C. Nguyen, et. al., Enhanced Seebeck effect in graphene devices by strain and doping engineering, Physica E. 73, 207 (2015).

[56] Ville T. Lahtinen and Jiannis K. Pachos, A short introduction to topological quantum computation, Sci. Post Phys. 3, 021 (2017).

[57] J. Alicea, New direction in the pursuit of Majorana fermions in the solid state systems, Rep. Prog. Phys. 75, 076501 (2012).

[58] C. Benjamin, J. K. Pachos, Detecting Majorana bound states, Phys. Rev. B 81, 085101 (2010).

[59] J. Li, R-L Chu, J. K. Jain and S-Q Shen, Topological Anderson Insulator, Phys. Rev. Lett. 102, 136806 (2009).

[60] P. Delplace, J. Li and M. Buttiker, Magnetic-Field-Induced Localization in 2D Topological Insulators, Phys. Rev. Lett. 109, 246803 (2012).

[61] P. Sternativo, F. Dolcini, Effects of disorder on electron tunneling through helical edge states, Phys. Rev. B 90, 125135 (2014).

[62] K. Kobayashi, et al., Probe-Configuration-Dependent Decoherence in an Aharonov-Bohm Ring, J. Phys. Soc. Jpn., 71, 2094 (2002).

[63] G. Seelig, et. al., Probe-configuration-dependent dephasing in a mesoscopic interferometer, Phys. Rev. B 68, 161310(R) (2003).

[64] F. Qu, et. al., Electric and magnetic tuning between the trivial and topological phases in inas/gasb double quantum wells. Phys. Rev. Lett. 115, 036803 (2015).

[65] C. Brune, et. al., Spin polarization of the quantum spin Hall edge states. Nature Physics 8, 485 (2012).

[66] A. P. Protogenov, V. A. Verbus and E. V. Chulkov, Nonlocal Edge State Transport in Topological Insulators, Phys. Rev. B 88, 195431 (2013).

[67] M. Buttiker, Edge-State Physics Without Magnetic Fields, Science 325, 278 (2009).

[68] S. Oberholzer, et. al., Positive Cross Correlations in a Normal-Conducting Fermionic Beam Splitter, Phys. Rev. Lett. 96, 046804 (2006)

[69] Y. Imry, Introduction to mesoscopic physics, second edition, Oxford University Press (2001).

[70] P. Adroguer, et. al., Probing the helical edge states of a topological insualtor by cooper-pair injection. Phys. Rev. B 82, 081303 (R) (2010).

[71] J. I Vayrynen, T. Ojanen, Electrical manipulation and measurement of spin properties of quantum spin hall edge states. Phys. Rev. Lett. 106(7), 076803 (2011).

[72] C.-Y. Hou, et. al., Corner junction as a probe of helical edge states. Phys. Rev. Lett. 102, 076602 (2009).

[73] S. Das, S. Rao, Spin-polarized scanning-tunneling probe for helical luttinger liquids. Phys. Rev. Lett. 106, 236403 (2011).

[74] J. C. Teo, C. L. Kane, Critical behavior of a point contact in a quantum spin hall insulator. Phys. Rev. B 79, 235321 (2009).

[75] T. L. Schmidt, Current correlations in quantum spin hall insulators. Phys. Rev. Lett. 107, 096602 (2011).

[76] Y.-W. Lee, Y.-L., C.-H. Chung, Nonequilibrium noise correlations in a point contact of helical edge states. Phys. Rev. B 86, 235121 (2012).

[77] F. Dolcini, Noise and current correlations in tunnel junctions of quantum spin hall edge states. Phys. Rev. B 92, 155421 (2015).

[78] P. P. Aseev, K. Nagaev, Shot noise in the edge states of two-dimensional topological insulators. Phys. Rev. B 94, 045425 (2016).

[79] J. I. Vyryen, L. I. Glazman, Current noise from a magnetic moment in a helical edge. Phys. Rev. Lett. 118, 106802 (2017).

[80] W. Chen, et. al., π spin berry phase in a quantum-spin-hall-insulator-based interferometer: Evidence for the helical spin texture of the edge states. Phys. Rev. Lett. 117, 076802 (2016).

[81] D. Ferraro, et. al., Electronic hong-ou-mandel interferometry in two-dimensional topological insulators. Phys. Rev. B 89, 075407 (2014).

[82] D. Pikulin, et. al., Disorder and magnetic-field-induced breakdown of helical edge conduction in an inverted electron-hole bilayer. Phys. Rev. B 89, 161403 (2014).

[83] J. Edge, et. al., z_2 peak of noise correlations in a quantum spin hall insulator. Phys. Rev. Lett. 110, 246601 (2013).

[84] A. Strom, H. Johanneson, Tunneling between edge states in a quantum spin hall system. Phys. Rev. Lett. 102, 096806 (2009).

[85] R. Santos, et. al., Phase diagram of two interacting helical states. Phys. Rev. B 93, 235436 (2016).

[86] R. Hanbury Brown, R. Twiss, A new type of interferometer for use in radio astronomy. Philos. Mag. Ser. 7 45, 663 (1954).

[87] M. Henny, et. al., The fermionic hanbury brown and twiss experiment. Science 284, 296 (1999).

[88] W. Oliver, et. al., Hanbury brown and twiss-type experiment with electrons. Science 284, 299 (1999).

[89] B. Z. Rameshti, A. G. Moghaddam,Spin-dependent Seebeck effect and spin caloritronics in magnetic graphene, Phys. Rev. B 91, 155407 (2015).

[90] SK Firoz Islam and Colin Benjamin, A scheme to realize the quantum spin-valley Hall effect in monolayer graphene, Carbon 110, 304 (2016).

[91] Cui-Zu Chang, et. al., Zero Field Dissipationless Chiral Edge Transport and the Nature of Dissipation in the Quantum Anomalous Hall State, Phys. Rev. Lett. 115, 057206 (2015).

[92] R. Scanchez, et. al., Heat diode and engine based on quantum Hall edge states, New J. Phys. 17, 075006 (2015).

[93] Gil-Ho Lee, et. al., Inducing Superconducting Correlation in Quantum Hall Edge States, Nat. Phys. 13, 693 (2017).

[94] Z.-Wei Zuo, et. al., Detecting Majorana fermions by use of superconductor-quantum Hall liquid junctions, Euro. Phys. Lett 114, 27001 (2016).

[95] M. Muhlbauer, et. al., Nanolithography on Mercury Telluride, Dissertation, University at Wurzburg (2015).

[96] V. M. Pereira and A. H. Castro Neto, Strain Engineering of Graphene's Electronic Structure, Phys. Rev. Lett. 103, 046801 (2009).

[97] D. Tong, Lectures on the Quantum Hall Effect, arXiv:1606.06687.

[98] M. Buttiker, Edge-State Physics Without Magnetic Fields, Science 325, 278 (2009).

[99] D.M. Rowe, Thermoelectrics Handbook: Macro to Nano, CRC Press, Boca Raton, FL, (2006).

[100] D. Sánchez, R. López, Scattering Theory of Nonlinear Thermoelectric Transport, Phys. Rev. Lett. 110, 026804 (2013).

[101] R. Kosloff, A. Levy, Quantum Heat Engines and Refrigerators: Continuous Devices, Annu. Rev. Phys. Chem, 65, 365 (2014).

[102] R. L. Dragomirova, B. K. Nikolic, Shot noise of spin-polarized charge currents as a probe of spin coherence in spin-orbit coupled nanostructures. Phys. Rev. B 75, 085328 (2007).

[103] E. S. Tikhonov, et. al., Shot noise of the edge transport in the inverted band hgte quantum wells. JETP Lett. 101, 708 (2015).

[104] T. Morimoto, A. Furusaki, Weyl and dirac semimetals with Z_2 topological charge. Phys. Rev. B 89, 235127 (2014).

[105] R. S. Whitney, Quantum Coherent Three-Terminal Thermoelectrics: Maximum Efficiency at Given Power Output, Entropy 18, 208 (2016).

[106] M. Buttiker, et. al., Entangled hanbury brown twiss effects with edge states. Physica E 20, 33 (2003).

[107] R. Sanchez, et. al., Heat diode and engine based on quantum Hall edge states, New J. Phys. 17, 075006 (2015).

[108] D. Sanchez and L. Serra, Thermoelectric transport of mesoscopic conductors coupled to voltage and thermal terminals, Phys. Rev. B. 84, 201307(R) (2011).

[109] Y. Wang, et. al., Magnon-driven quantum dot refrigerators, Phys. Lett. A 379, 3054-3058 (2015).

[110] Y. Zhang, et. al., Three-terminal quantum-dot refrigerators, Phys. Rev. E 91, 052118 (2015).

[111] M. Kónig, et. al., The Quantum Spin Hall Effect: Theory and Experiment, J. Phys. Soc. Jpn. 77, 031007 (2008).

[112] H. Maier, et. al., Ballistic geometric resistance resonances in a single surface of a topological insulator, Nat. Comm. 8, 2023 (2017).

[113] G. E. W. Bauer, E. Saitoh and B. J. van Wees, Spin caloritronics, Nature Materials 11, 391 (2012).

[114] J. Yun Kim and J. C. Grossman, High-Efficiency Thermoelectrics with Functionalized Graphene, Nano Lett. 15, 2830(2015).

[115] Y. M. Zuev, et. al., Thermoelectric and Magnetothermoelectric Transport Measurements of Graphene, Phys. Rev. Lett. 102, 096807 (2009).

[116] Y. Anno, et. al., Enhancement of graphene thermoelectric performance through defect engineering, 2D Matter. 4, 025019(2017).

[117] V.-T. Tran, et. al., Optimizing the thermoelectric performance of graphene nanoribbons without degrading the electronic properties, Sci. Rep. 7, 2313 (2017).

[118] H. Sadeghi, et. al., Enhancing the thermoelectric figure of merit in engineered graphene nanoribbons, Beilstein J. Nanotechnol. 6, 1176 (2015).

[119] Po-Hao Chang, M. S. Bahramy, N. Nagaosa, and B. K. Nikolic, Giant Thermoelectric Effect in Graphene-Based Topological Insulators with Heavy Adatoms and Nanopores, Nano Letters 14, 3779-3784 (2014).

[120] B. Sothmann, M. Buttiker, Magnon-driven quantum-dot heat engine, Euro. Phys. Lett. 99, 27001 (2012).

[121] F. Islam, C. Benjamin, Adiabatically twisting a magnetic molecule to generate pure spin currents in graphene, J. Phys.: Condens. Matter 28 035305 (2016).

[122] S. Shafraniuk, Graphene Fundamentals, Devices and Applications, Pan Stanford publishing (2014).

[123] D. Dragoman, M. Dragoman, Giant thermoelectric effect in graphene, App. Phys. Lett. 91, 203116 (2007).

[124] F. Ghahari, et. al., Enhanced Thermoelectric Power in Graphene: Violation of the Mott Relation by Inelastic Scattering, Phys. Rev. Lett. 116, 136802 (2016).

[125] H. Behera, G. Mukhopadhyay, Fermi Velocity Modulation in Graphene by Strain Engineering, AIP Conference Proceedings, 1512, 1 (2013).

[126] K. Brandner, et. al., Multi-terminal thermoelectric transport in a magnetic field: bounds on Onsager coefficients and efficiency, New J. Phys.15, 105003 (2013).

[127] G. Cordourier-Maruri, et. al., Graphene-enabled low-control quantum gates between static and mobile spins, Phys. Rev. B 89, 075426 (2014).

[128] R. M. Abolfath, et. al., Electronic states of magnetic quantum dots, New J. Phys. 9, 353 (2007).

[129] M. I. Katsnelson, et. al., Chiral tunnelling and the Klein paradox in graphene, Nature Phys. 2, 620-625 (2006).

[130] M. Barbier, et. al., Kronig-Penney model on bilayer graphene: spectrum and transmission periodic in the strength of the barriers, Phys. Rev. B 82, 235408 (2010).

[131] D. Sanchez and R. López, Scattering Theory of Nonlinear Thermoelectric Transport, Phys. Rev. Lett. 110, 026804 (2013).

[132] C. Yesilyurt, et. al., Perfect valley filter in strained graphene with single barrier region, AIP Advances 6, 056303 (2016).

[133] J. Meair and P. Jacquod, Scattering theory of nonlinear thermoelectricity in quantum coherent conductors, J. Phys.: Condens. Matter 25, 082201(2013).

[134] Xiang-Guo Li, et. al., Single-molecule magnet Mn_{12} on graphene, Phys. Rev. B 90, 125447 (2014).

[135] Feng-Xia Zu, et. al., Efficient spin filter and spin valve in a single-molecule magnet Fe_4 between two graphene electrodes, App. Phys. Lett. 107, 252403 (2015).

[136] C. J. Milios, et. al., Spin Switching via Targeted Structural Distortion, J. Am. Chem. Soc.129-6547 (2007).

[137] A. Prescimone, et. al., Mn_6 under Pressure: A Combined Crystallographic and Magnetic Study, Angew. Chem. Int. Ed.47-2828(2008).

[138] V. M. Pereira, A. H. Castro Neto, Strain Engineering of Graphene's Electronic Structure, Phys. Rev. Lett. 103, 046801 (2009).

[139] T.M.G. Mohiuddin, et. al., Uniaxial strain in Graphene by Raman spectroscopy: G peak splitting, Gruneisen parameters and sample orientation, Phys. Rev. B, 79, 205433 (2009).

[140] M. Chhikara, et. al., Effect of uniaxial strain on the optical Drude scattering in graphene, 2D Materials 4, 025081 (2017).

[141] S. P. Milovanovic, F. M. Peeters, Strain controlled valley filtering in multi-terminal graphene structures, App. Phys. Lett. 109, 203108 (2016).

[142] V. M. Pereira, A. H. Castro Neto, Tight-binding approach to uniaxial strain in graphene, Phys. Rev. B. 80, 045401 (2009).

[143] O.L.T. de Menezes and J.S. Helman, Spin flip enhancement at resonant transmission, American Journal of Physics 53, 1100 (1985).

[144] J. Lahiri, et. al., An extended defect in graphene as a metallic wire, Nature Nanotechnology 5, 326 (2010).

[145] J.-H. Chen, et. al., Controlled growth of a line defect in graphene and implications for gate-tunable valley filtering, Phys. Rev. B 89, 121407(R) (2014).

[146] M. Yang, J. Wang, Fabry-Perot states mediated quantum valley-Hall conductance in a strained graphene system, New J. Phys. 16 113060 (2014).

[147] C. Si, et. al., Strain engineering of graphene: a review, Nanoscale 8, 3207 (2016).

[148] Y. Sun, et. al., Magnetism of graphene quantum dots, npj Quantum Materials 2, 5 (2017).

[149] Y. M. Zuev, et. al., Thermoelectric and Magnetothermoelectric Transport Measurements of Graphene, Phys. Rev. Lett. 102, 096807 (2009).

[150] B. Sothmann, et. al., Phys. Rev. B 85, 205301 (2012).

[151] Y. Xu, et. al., Thermal and Thermoelectric Properties of Graphene, Small 10, 2182 (2014).

[152] M. Zeng, et. al., Graphene-based Spin Caloritronics, Nano Lett. 11, 1369 (2011).

[153] Xiao-Qin Tang, et. al., Metal-free magnetism, spin-dependent Seebeck effect, and spin-Seebeck diode effect in armchair graphene nanoribbons, Sci. Rep. 8, 927 (2018).

[154] Yun Ni, et. al., Spin Seebeck Effect and Thermal Colossal Magnetoresistance in Graphene Nanoribbon Heterojunction, Sci. Rep. 3, 1380 (2013).